High Spin Structures of Transitional Nuclei Around Mass 100

A. D. Yamamoto

A thesis submitted in partial fulfillment of the School of Electrical and Physical Sciences in the University of Surrey for the degree of Doctor of Philosophy.

September 28, 2003

High Spin Structures of Transitional Nuclei Around Mass 100

A. D. Yamamoto

A thesis submitted in partial fulfillment of the School of Electrical and Physical Sciences in the University of Surrey for the degree of Doctor of Philosophy.

September 28, 2003

Abstract

Equilibrium shape fluctuations with respect to both the proton and the neutron numbers in slightly neutron-rich nuclei around mass 100 are due to shape co-existence/competition phenomena associated with the strong n-p interaction between orbitals with a large spatial overlap, and are the subject of this thesis. In particular, the alignment systematics of the $\nu h_{11/2}$ configurations in even-N, $^{96-102}_{42}$Mo isotopes and N = 57 isotones in this mass region have been interpreted using a self-consistent cranked-mean-field calculations employing a Woods-Saxon potential.

Experimental data were obtained following a $^{96}_{40}Zr_{56}$ + 46 MeV $^{9}_{4}Be_{5}$ fusion-evaporation reaction using the YRASTBALL Ge detector array, and a $^{100}_{42}Mo_{58}$ + 700 MeV $^{136}_{54}Xe_{82}$ binary reaction utilising the GAMMASPHERE Ge detector array plus the heavy-ion detector, CHICO. Results from the former experiment extended the yrast and positive parity structures in $^{101}_{44}$Ru and $^{102}_{44}$Ru up to tenative spin/parity of $(\frac{45}{2}^{+})$ and (20^{+}), respectively, while the latter experiment extended the $^{100}_{42}$Mo and $^{102}_{42}$Mo nuclei up to (20^{+}) and (14^{+}), respectively. All the above yrast and positive parity structures, bar $^{102}_{42}$Mo, have been observed to undergo a backbend, consistent with the crossing of an aligned $(\nu h_{11/2})^2$ configuration. The unobserved bandcrossing in $^{102}_{42}$Mo marks the shape transition for nuclei with N $\geq$ 60. The $\nu h_{11/2}$ bands in $^{99}_{42}$Mo, $^{101}_{42}$Mo, and $^{101}_{44}$Ru have also been extended to tenative spin/parity of $(\frac{39}{2}^{-})$, $(\frac{35}{2}^{-})$, and $(\frac{47}{2}^{-})$, respectively, and the structures are interpreted as the rotational alignment of a pair of mid-shell $g_{9/2}$ protons.

The present work established the alignment properties in this mass region to arise from the population of the deformation-driving, $\nu h_{11/2}$ orbital, coupled with the competing influences from the $\pi g_{9/2}$ and $\nu g_{7/2}$ orbitals that strongly depend on the particle number. The rotationally-based cranked Shell Model calculations were also found to reproduce consistent results in this vibrational-rotational transitional region.

Acknowledgements

Firstly, I would like to thank Dr. P.H. Regan and Prof. W. Gelletly for allowing me to join the Nuclear Physics group at the University of Surrey. They have also been my greatest inspiration to the subject throughout the degree course. The author thanks the EPSRC (U.K.) for financial support.

E veryone at the Physics department has been most supportive and kind, for which I would like to express my sincere appreciation. In particular, I would like to thank Dr. C. Pearson for his help on advanced computing, J.J. Valiente-Dobon for the general programming in C, the departmental secretary ,Beth Herbert, on the general administrative work, and all the postdocs (Zsolt, Stuart, Carl, Qiang) for the general knowledge on the nuclear physics. Moreover, this work could not be possible without the kind help I have received from Prof. F.R. Xu for all the CSM calculations performed for this thesis, and Dr. C.Y. Wu and Adam Hayes of the Rochester University for the GAMMASPHERE and CHICO data analysis.

I would like also to thank Prof. R.F. Casten for allowing me to stay for a year at the WNSL, Yale university, and to take part in his lectures. The knowledge I have gained from his lectures constitute a large part of what I know about the nuclear physics theory now, and for which I am most grateful. During that time, I also owe thanks for all the kindest help I received regarding everyday matters to the Secretaries at the WNSL, headed by Mary-Ann.A big Thank-You also goes to Gulhan and the postdocs there, Drs. Jo Ressler and Hannan Amro, for their kindest assistance.

At more social level, my particular thanks go to Paddy (again!), Alvaro, Becca, Bruno, Des, Jo, Jose Javier, Libby, Nico, Russel, Sareh, Scott, Steve, and Tamara. You guys made my PhD student days more enjoyable than I could have ever imagined.

Lastly, but certainly not least, I am most grateful to my parents for everything.

Contents

List of Figures

Chapter 1

Introduction

1.1 Transitional Nuclei Around A $\simeq$ 100

Atomic nuclei are quantum mechanical many-body systems, comprised of a finite number of strongly interacting fermions. Their observed structures ultimately result from the attractive and short-ranged nuclear force appropriate for fermionic nucleons, and hence do not allow simple perturbation and many-body theories to be utilised. Given such a complex form of the force involved, our knowledge of the nuclear structure can only be derived through regularities in the empirical evidence, interpretation of which often requires phenomenological models. They contain paradigm shifts, and aim to provide simpler physical insights, while accommodating all known and underlying physical laws. Models incorporating such shifts can be spectacularly successful, given the ability of the deformed shell model to provide a microscopic basis for the existence of rotational and vibrational collective motions. Physical insights provided from this particular model have already been proven useful in understanding neutron-rich A $\simeq$ 100 nuclei, where their observed rapid phase changes and shape competition phenomena are found

to be sensitive to shell effects, as well as their microscopic configurations in a single-particle spectrum (see figure 1.1) [1].

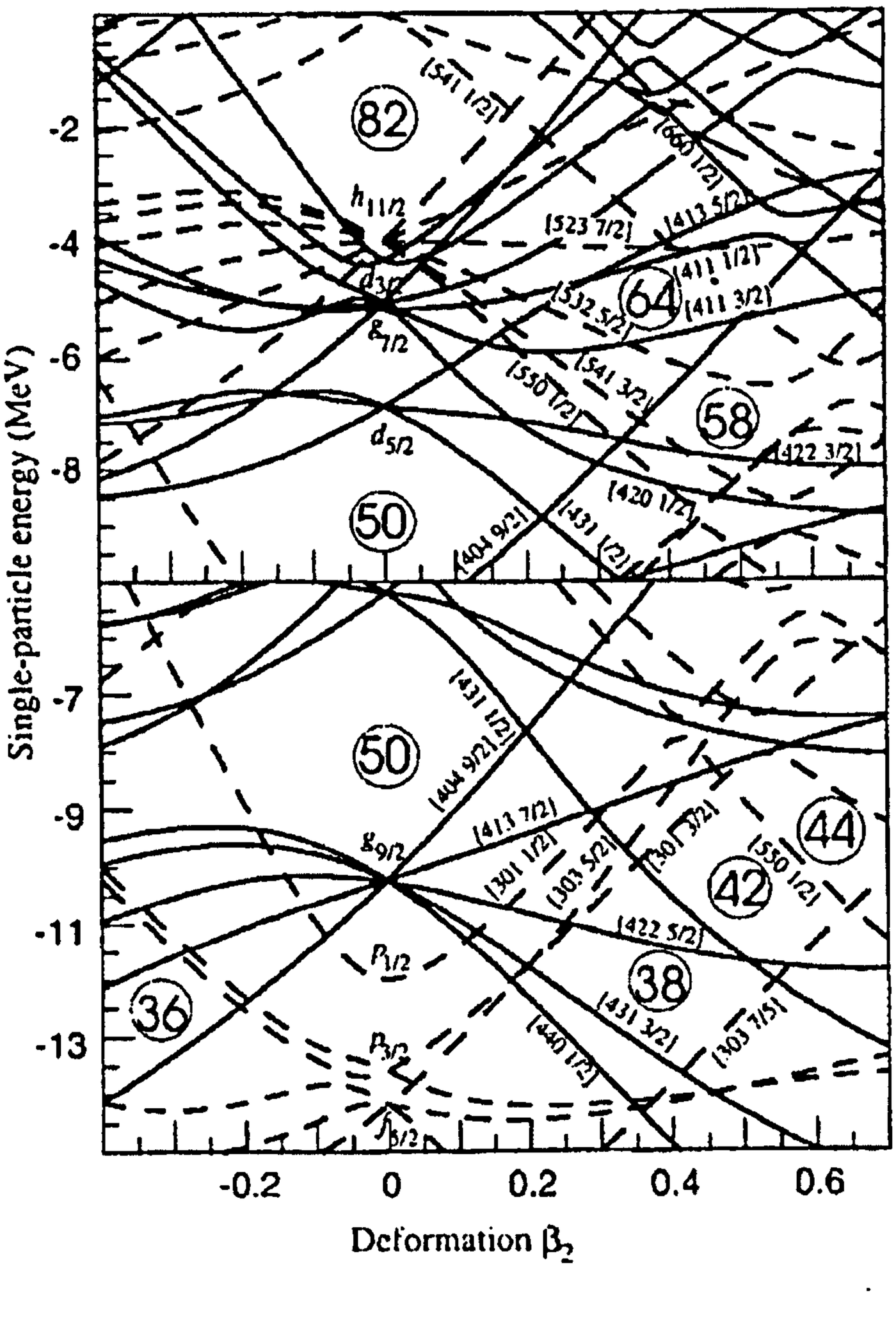

Figure 1.1: Single-particle spectra obtained for (top) neutrons (bottom) protons in the A $\simeq$ 100 nuclei using a Nilsson-Strutinsky calculations of Ref [1].

Systematics of the first 2^+ excited level of the even-even nuclei, as well as the energy ratio, $E(4_1^+)/\ E(2_1^+)$, in the A $\simeq$ 100 mass region have characteristics shown in figure 1.2 and 1.3, respectively, and represent transitions

from vibrational to γ-soft and/or rotational nuclear collectivity. The most dramatic changes in structure are observed for $_{38}$Sr and $_{40}$Zr isotopes, manifested in figure 1.2 by a factor of $\sim$5.7 drop in the 2_1^+ energy as neutron number, N, increases from 58 to 60, and by a sudden rise in the energy ratio (figure 1.3) from approximately 1.6 (vibrational) for N $\leq$ 58, to near 2.6 (γ-soft) at N = 60, and $\sim$3.15 (rotational) for N > 60. Similar, but more gradual changes in the E(2_1^+) values occur for $_{42}$Mo isotopes (figure 1.4), indicating a transition from an anharmonic vibrational limit for $^{94-96}$Mo to a rotational limit in $^{102-104}$Mo [2]. In addition, the ^{100}Mo nucleus is predicted to possess significant γ-softness at low spin, but is predicted to form a superdeformed band at high spin ($I\sim$22 $\hbar$) [1].

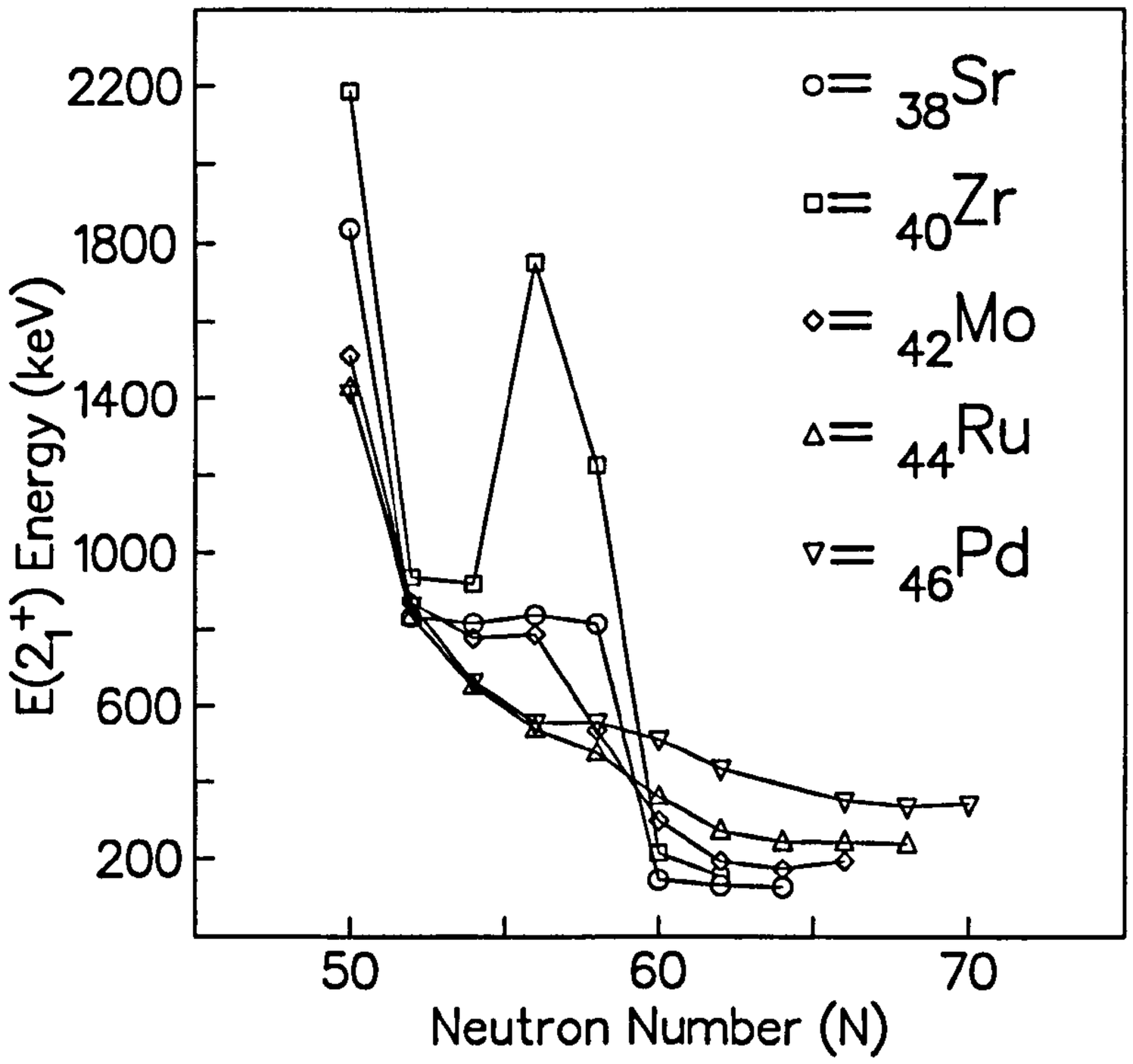

Figure 1.2: Systematics of the E(2_1^+) states for nuclei around A $\simeq$ 100.

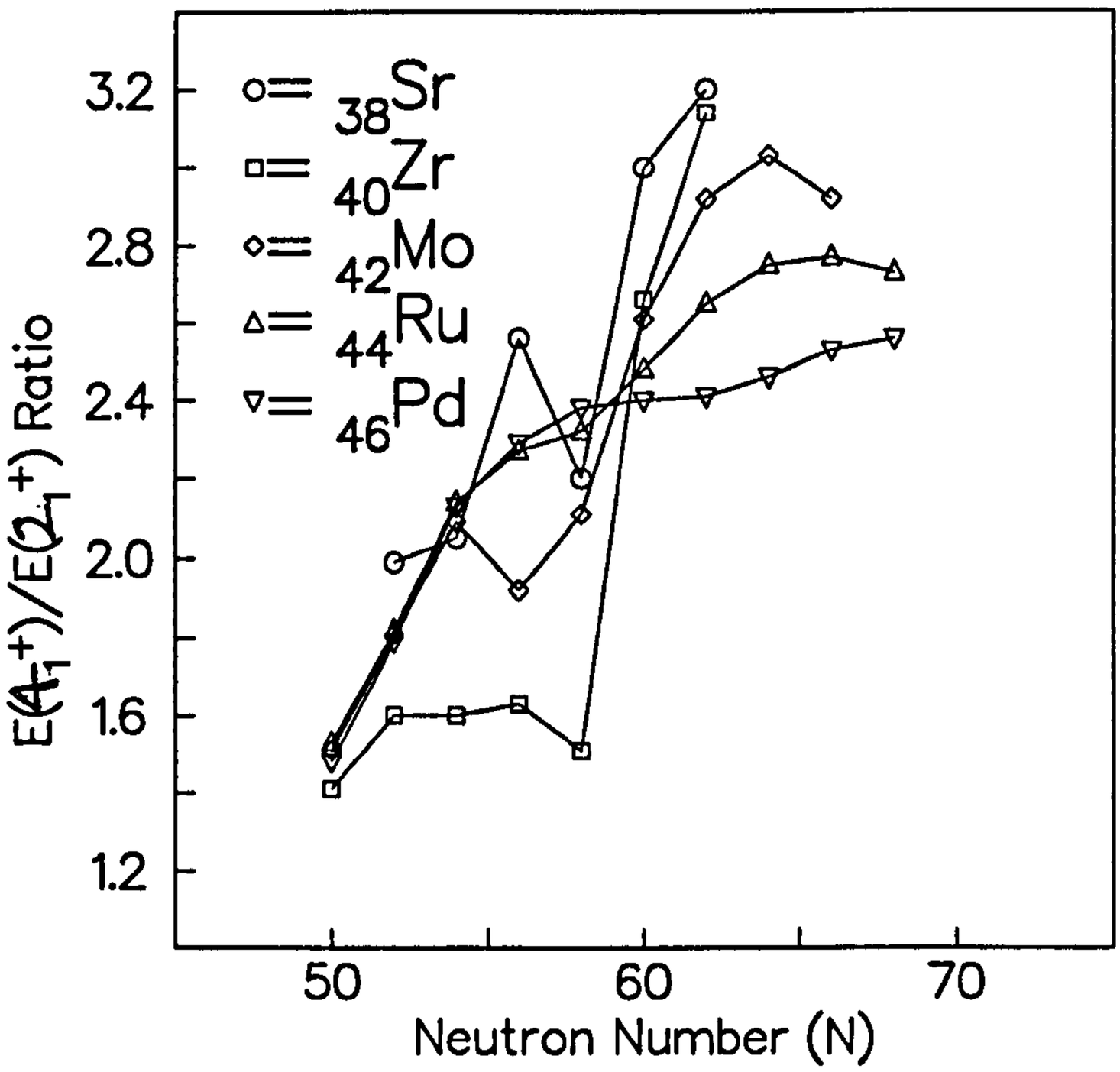

Figure 1.3: Systematics of the $E(4_1^+)/E(2_1^+)$ ratio for the nuclei around the $A \simeq 100$ region.

However, the information on the high-spin states in the near-stable nuclei in this mass region is still limited, and the details on the yrast structures of $_{42}$Mo-isotopes are investigated in the current work. The experiment studied was performed using the GAMMASPHERE HPGe array and the CHICO detector, which allowed to observe reaction fragments from binary reactions between $^{100}_{42}$Mo and $^{136}_{54}$Xe. Previously, high spin studies in this mass region were primarily performed using spontaneous fission sources with a backed or thick target, limiting the possible angular momentum observations to below $\sim$14 $\hbar$. Studies by Takai *et. al.* [3] concerning the spin generation in the heavy-ion binary reactions however suggested the possibility for populating high

spin states using such reactions. The present study thus aims also to provide additional information on the usefulness of the above-barrier binary reactions for the study of yrast/near-yrast, high-spin states in neutron-rich nuclei.

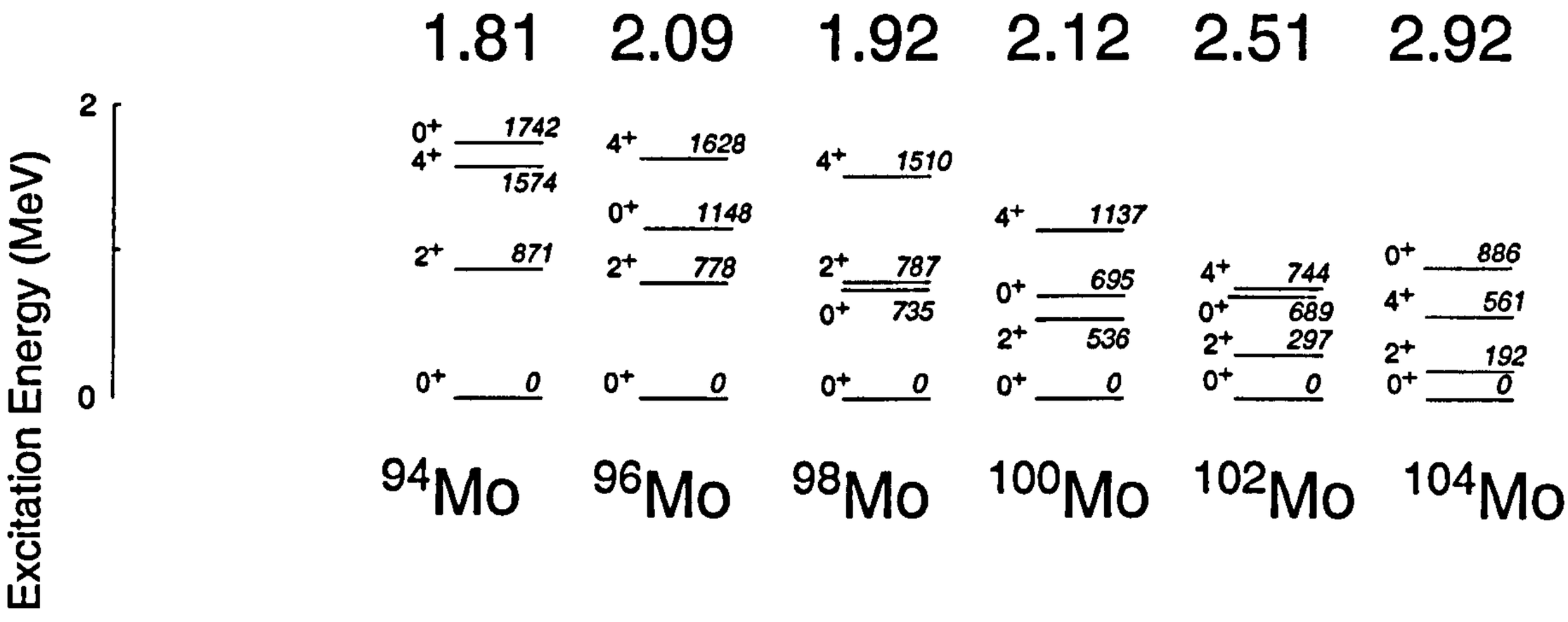

Figure 1.4: Systematics of the $E(2_1^+)$ and $E(4_1^+)$ levels in the A $\simeq$ 100 Mo-isotopes. The numbers shown above each of the bands are the $\frac{E(4_1^+)}{E(2_1^+)}$ ratio, and the level energies are in keV.

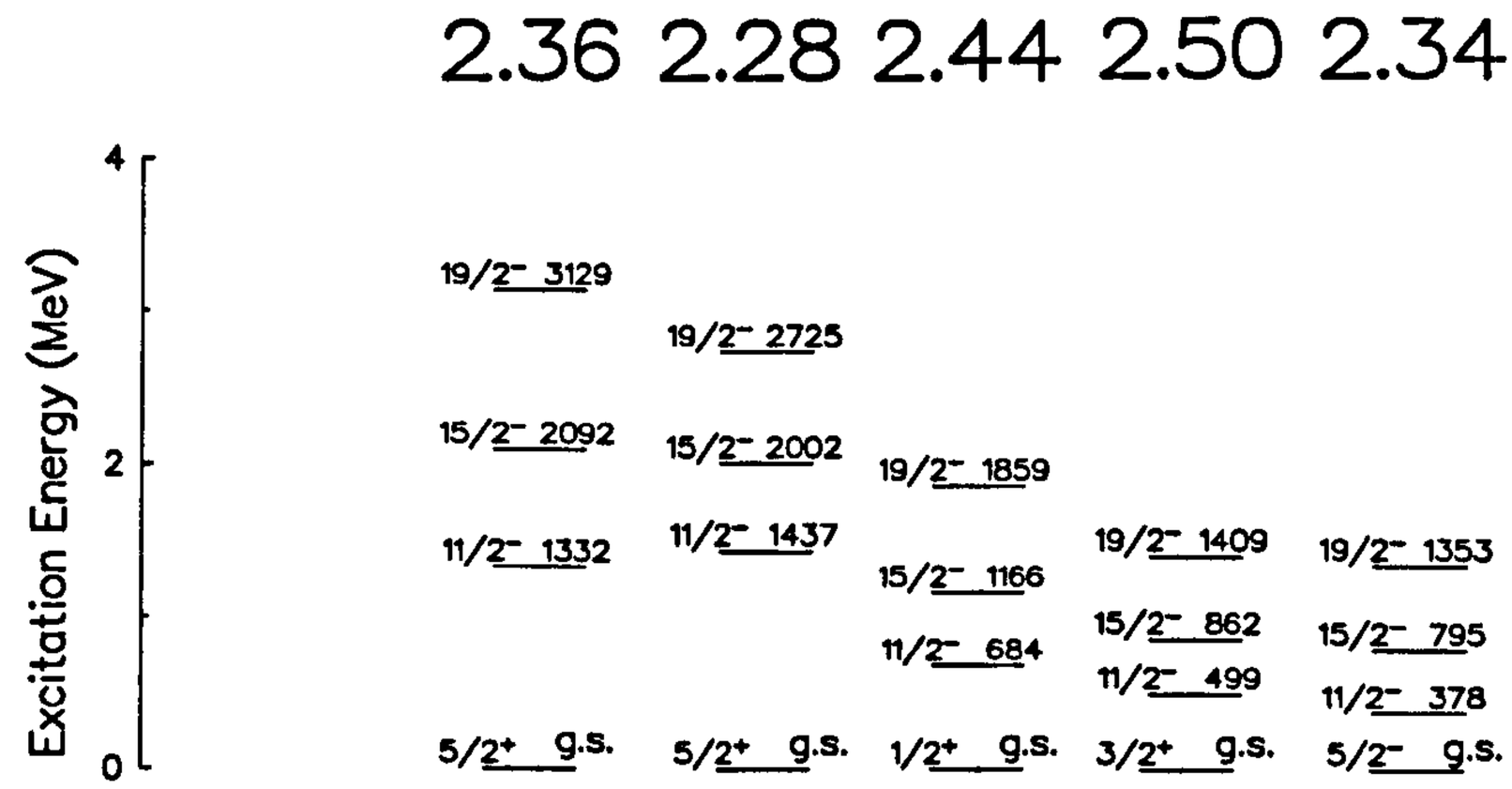

Figure 1.5: Systematics of $\nu h_{11/2}$ bands in the odd-N Mo-isotopes. The numbers shown above each of the bands are the $\frac{E(\frac{19}{2}^- \rightarrow \frac{11}{2}^-)}{E(\frac{15}{2}^- \rightarrow \frac{11}{2}^-)}$ ratio, and the level energies are in keV.

The previously described abrupt onset of deformation in A $\simeq$ 100 region has been described as a manifestation of the existence of low-lying intruder states, which compete in energy with the regular, near spherical ground state. A microscopic explanation for this rapid onset of deformation and the existence of low-lying excited 0_2^+ states has been given by Federman and Pittel [4, 5, 6, 7]. Crucial to their argument is the strongly attractive neutron-proton interaction between orbitals with a large spatial overlap, which in this mass region is between the $\nu g_{7/2}$ and $\pi g_{9/2}$ (e.g. figure 1.1). The ability of the neutron-proton interaction to cause significant deformation requires not only that such set of orbitals are lying close to the Fermi surface prior to deformation, but that orbitals with a large spatial overlap to occur at the Fermi surface once the nucleus becomes deformed. The Nilsson-Strutinsky calculations [1] indicate that a large component of the $\nu h_{11/2}$ orbitals indeed lies below the Fermi surface for N $\geq$ 60 [8, 9, 10, 11], but plays an increasingly dominant role over $\nu g_{7/2}$ orbitals, as it also has a significant spatial overlap with the $\pi g_{9/2}$ orbitals, driving the core to permanent quadrupole deformation. Given such significance of the deformed subshell closure at N = 58 (see figure 1.1), the bands containing high-spin states in N = 57 isotones are considered an appropriate testing ground for Coriolis effects in weakly deformed nuclei [12, 13, 14]. The situation seems to be more complicated, however, thanks to the γ-softness observed in the Ruthenium nuclei around N = 60 [1]. It can be seen from figure 1.6 that all of the N = 57 isotones between $40 < Z < 50$ shell closures show systematic behavior associated with weakly coupled harmonic vibrators [2], with the $\frac{E(\frac{19}{2}^- \rightarrow \frac{11}{2}^-)}{E(\frac{15}{2}^- \rightarrow \frac{11}{2}^-)}$ value for all four nuclei lying close to the γ-soft limit of approximately 2.5. Already, in a recent study of the low-lying states in ^{100}Ru, Genilloud *et. al.* [15] identified the signatures of a quasi-γ vibrational band, with energy spacings consis-

tent with a γ-unstable nucleus [16]. The question of the effect and clear signature of triaxial deformation at high-spins remains a major question in nuclear structure physics. Motivated by these aspects, the current work also presents yrast/near-yrast states of nuclei around A$\simeq$ 100, populated through a light-ion induced fusion-evaporation reaction.

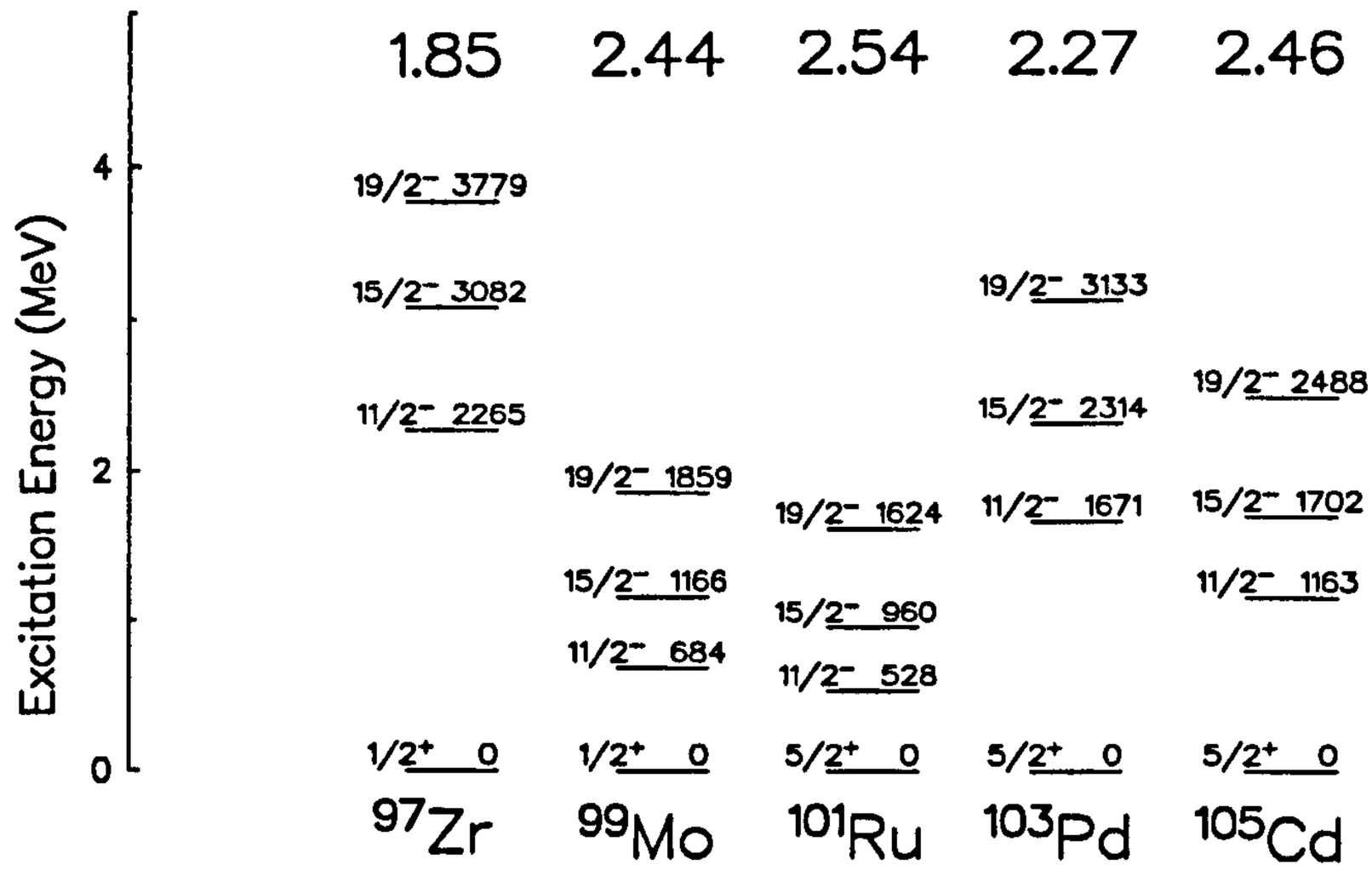

Figure 1.6: Systematics of $\nu h_{11/2}$ bands in the N = 57 isotones. The numbers shown above each band are the $\frac{E(\frac{19}{2}^- \rightarrow \frac{11}{2}^-)}{E(\frac{15}{2}^- \rightarrow \frac{11}{2}^-)}$ ratio, and the level energies are in keV.

1.2 Gamma-Ray Spectroscopy

1.2.1 Properties of Electromagnetic Radiation

An energetically elevated nuclear state $|i\rangle$ may decay to a lower (excited) state $|f\rangle$ by emitting a photon with energy

$$\hbar\omega = E_i - E_f. \tag{1.1}$$

However, since a nuclear state has a definite angular momentum **j**, its component m, and parity π, the emitted photon must also carry an angular momentum **J** with its eigenvalue λ, component μ, and parity π, in accordance with the conservation laws appropriate for these quantities [17];

$$\begin{aligned} \mathbf{J} &= \mathbf{j}_i - \mathbf{j}_f, \\ \pi &= \pi_i \times \pi_f. \end{aligned} \tag{1.2}$$

Semi-classically, a photon with wavelength λ carries away 1 $\hbar$ of angular momentum when emitted at an impact parameter r, where

$$r = \lambda/p, \tag{1.3}$$

and,

$$r \approx \lambda = \frac{\hbar c}{E} = \frac{197}{E(MeV)} fm, \tag{1.4}$$

so that the above relations (1.3) and (1.4) suggest decreasing photon emission probability with increasing multipole order. In a nuclear system, however, photoemission involves the re-arrangement of the entire nucleus, and often results in the emission of higher multipole radiations.

Parity change between initial and final states due to nuclear re-arrangements leads to two types of electromagnetic radiation being emitted with a multiplicity λ, and parity π, as

$$\begin{aligned} Electric\ 2^\lambda &- pole\ (E\lambda)\ radiation: \\ \pi_i\pi_f &= (-1)^\lambda, \end{aligned} \tag{1.5}$$

$$\begin{aligned} Magnetic\ 2^\lambda &- pole\ (M\lambda)\ radiation: \\ \pi_i\pi_f &= (-1)^{\lambda+1}. \end{aligned} \tag{1.6}$$

In addition, since the total angular momentum of a state, **J**, is a vector sum of the orbital (**L**) and spin (**S**) angular momenta,

$$\mathbf{J} = \mathbf{L} + \mathbf{S}, \tag{1.7}$$

with its eigenfunction $\mathbf{J}^2$ and J_z, it has a corresponding electromagnetic radiation eigenvalue $\lambda(\lambda+1)$ and a component μ as

$$\mathbf{J}^2\mathbf{X}^{\mu}_{\lambda lm} = \lambda(\lambda+1)\mathbf{X}^{\mu}_{\lambda lm}, \tag{1.8}$$

$$J_z\mathbf{X}^{\mu}_{\lambda lm} = \mu\mathbf{X}^{\mu}_{\lambda lm}, \tag{1.9}$$

where,

$$\mathbf{X}^{\mu}_{\lambda l1} = \Sigma^{1}_{m=-1}\langle l\mu-m, 1m \mid \lambda\mu\rangle Y_l^{\mu-m}(\theta,\phi)\epsilon_m. \tag{1.10}$$

For each value of $J^2 = \lambda(\lambda+1)$ with $\lambda \geq 1$, the l takes three values, $l = \lambda$, $\lambda\pm1$, and ϵ represents the elements of spherical basis for the spin of the emitted photon.

1.2.2 Transition Probability

The transition probability, $T(\sigma\lambda\mu)$, for a γ-ray decay from initial spin state j_i to final spin state j_f with energy E_γ, multipolarity λ, and component μ is [18]

$$T(\sigma\lambda\mu) = \frac{8\pi(\lambda+1)}{\hbar\lambda((2\lambda+1)!!)^2}\left(\frac{E_\gamma}{\hbar c}\right)^{2\lambda+1} B(\sigma\lambda\mu), \tag{1.11}$$

where $B(\sigma\lambda\mu)$ is the reduced transition probability

$$B(\sigma\lambda\mu) = \frac{2j_f+1}{2j_i+1} \mid < J_f \| M(\sigma\lambda\mu) \| J_i > \mid^2. \tag{1.12}$$

In the above equation (1.12), the $M(E)$ operator corresponds to the 2^λ-pole charge distribution and the $M(M)$ operator includes (i) the orbital motion of a charged particle and (ii) the intrinsic magnetisation. Note that while $T(\sigma\lambda\mu)$ has a transition energy dependency of $E^{2\lambda+1}$, the reduced transition probability does not. Therefore, the $B(\sigma\lambda\mu)$ value is often quoted to compare decay rates between different nuclei.

1.2.3 Weisskopf Single Particle Estimates

Determination of the transition rates often allows the relative single particle or collective nature of a state to be estimated, frequently by way of comparing with a theoretical limit. One particular approach for the single particle estimate assumes a proton that moves around in an average central potential, changing orbit between the state with $l = 0$ and a value l. In this particular approach, the transition probability may be expressed as [18]

$$T(El) = \frac{2(l+1)}{l[(2l+1)!!]^2}\left(\frac{3}{l+3}\right)^2\left(\frac{\hbar}{mcR}^2\right)\frac{e^2}{\hbar c}(kR)^{2l}\omega \qquad (1.13)$$

for an electric transition, and

$$T(Ml) = \frac{20(l+1)}{l[(2l+1)!!]^2}\left(\frac{3}{l+3}\right)^2\left(\frac{\hbar}{mcR}^2\right)\frac{e^2}{\hbar c}(kR)^{2l}\omega \qquad (1.14)$$

for a magnetic transition, where the nucleon mass m is $mc^2 \approx 938$ MeV and the nuclear radius R is $R \approx 1.2A^{1/3}$. Past data on the transition rate find the $B(El)$ values to scale roughly as R^{2l}, so that the transition rate will depend on l as $(kR)^{2l}$. In the limit of long wavelength for the emitted photon, it is assumed that $kr << 1$, so that the lowest multipole is the most dominant.

The numerical estimates obtained from the above relations (1.13) and (1.14) are known as *Weisskopf estimates*, and are given in table 1.1. A measured transition probability much greater than the Weisskopf estimates indicates similar wavefunctions for the initial and final states, while much reduced transition probability for a transition suggests it to be 'forbidden' due to quantum mechanical selection rules.

Transition Rate	Weisskopf Estimates
$T(E1)=1.587x10^{15}\ E^3\ B(E1)$	$B(E1)=6.446x10^{-2}\ A^{2/3}$
$T(E2)=1.223x10^{9}\ E^5\ B(E2)$	$B(E2)=5.940x10^{-2}\ A^{4/3}$
$T(E3)=5.689x10^{2}\ E^7\ B(E3)$	$B(E3)=5.940x10^{-2}\ A^{2}$
$T(E4)=1.649x10^{-4}\ E^9\ B(E4)$	$B(E4)=6.285x10^{-2}\ A^{8/3}$
$T(E5)=3.451x10^{-11}\ E^{11}\ B(E5)$	$B(E5)=6.928x10^{-2}\ A^{10/3}$
$T(M1)=1.779x10^{13}\ E^3\ B(M1)$	$B(M1)=6.446$
$T(M2)=1.371x10^{7}\ E^5\ B(M2)$	$B(M2)=1.650\ A^{2/3}$
$T(M3)=6.387x10^{0}\ E^7\ B(M3)$	$B(M3)=1.650\ A^{4/3}$
$T(M4)=1.889x10^{-6}\ E^9\ B(M4)$	$B(M4)=1.746\ A^{2}$
$T(M5)=3.868x10^{-13}\ E^{11}\ B(M5)$	$B(M5)=1.924\ A^{8/3}$

Table 1.1: Transition probabilities T(sec^{-1}) expressed by $B(EL)$ in ($e^2(fm)^{2L}$) and $B(ML)$ in (($\frac{e\hbar}{2mc}^2(fm)^{2L-2}$). E is the γ-ray energy, measured in MeV. Taken from [19].

Chapter 2

Theoretical Considerations

2.1 Spherical Shell Model

The Spherical Shell Model (SSM) describes a nucleus as a system of A - independent fermions, interacting with each other through many-body nucleon-nucleon forces. The present lack of a fundamental theoretical basis for these quantum many-body forces however encourages one to express the nuclear mean-field system in terms of an average one-body potential instead.

Empirically observed conservation of parity, total angular momentum, J, and the third component of the isoscalar, τ_{i3}, preserves the symmetry laws of the nucleon-nucleon interaction, including angular momentum $\mathbf{l}_i$, spin σ_i, and parity π_i, of each nucleon i. As such, any chosen mean-field should possess rotational invariance associated with the conservation of total angular momentum (i.e. $[\mathrm{H}_{tot},\mathrm{J}_{tot}] = 0$), and should allow occupation of proton and neutron single-particle levels separately. The SSM employs as its Hamiltonian H,

$$H = \sum_{i=1}[T_i + U(i)] + \frac{1}{2}\sum_{i\neq j}\nu(ij), \tag{2.1}$$

and is comprised of the unperturbed hamiltonian,

$$H_0 = \sum_{i=1}[T_i + U(i)] = \sum h(i), \tag{2.2}$$

as well as the two-body residual interaction, $\nu(ij)$, which acts on the H_0 as a first order perturbation to break the symmetries embodied within. In many cases, the study of such configuration-mixing interactions yields valuable information on the underlying nuclear structure. However, extraction of the details on the residual interaction from the total Hamiltonian requires a model-dependent form of $U(i)$, which is often taken as the phenomenological Woods-Saxon potential, V_{ws},

$$V_{ws} = \frac{-V_0}{1 + exp(r - R_0/a)}, \tag{2.3}$$

where $V_0 \sim 50$ MeV, $R_0 \sim 1.2\ A^{1/3}$ fm, and $a \sim 0.6$ fm. It was realised, however, that the use of such a phenomenological potential alone cannot even reproduce the empirical shell closures without the inclusion of a 'spin-orbit' coupling term, $\mathbf{l}_i \cdot \mathbf{s}_i$, contributed by Mayer *et. al.* [21]. Application of the Schrödinger equation to the zeroth-order (i.e. no $\nu(ij)$) hamiltonian plus the coupling term,

$$\left(-\frac{\hbar^2}{2M}\nabla^2 + U(i) + C(\mathbf{l}_i \cdot \mathbf{s}_i)\right)\Psi = E\Psi, \tag{2.4}$$

then yields the independent single-particle levels and the observed magic numbers (low level densities at Z = N = 2, 8, 20, 50, 82, and 126 in figure 2.1). In this model, a particle-hole excitation refers to the promotion of a nucleon from an occupied to an unoccupied level. The level scheme of figure 2.1 derived from the equations 2.3 and 2.4 is expected to vary if (i) different form of $U(i)$ is assumed, and (ii) residual interactions $\nu(ij)$ are included. In particular, the accumulative nature of the residual interaction $\nu(ij)$ means

the exact location of magic numbers can be altered, and may lead to various stable configurations for nuclei which are not spherically symmetric.

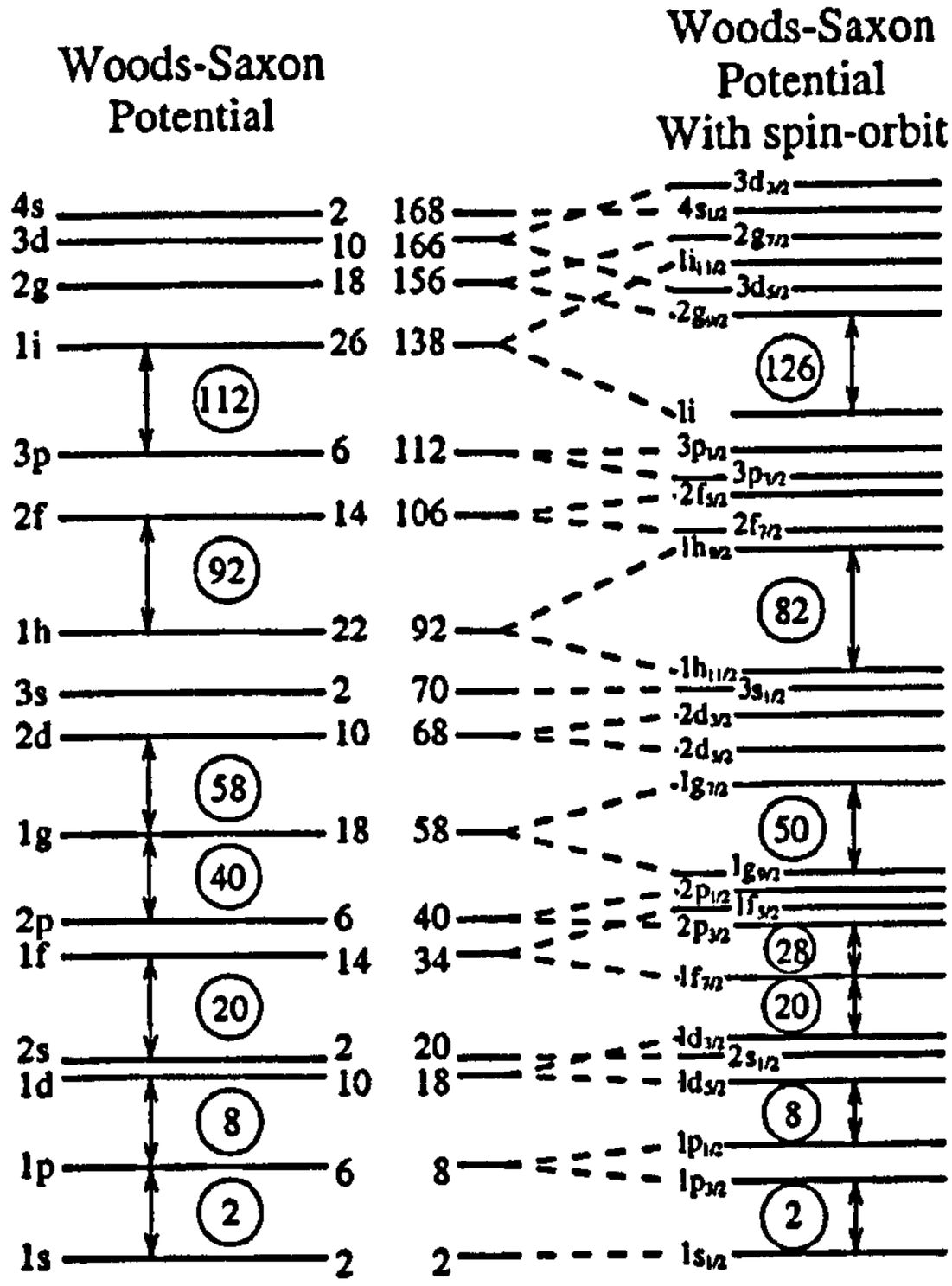

Figure 2.1: Calculated energy levels using (left) the Woods-Saxon potential of equation 2.3. The effect of the spin-orbit interaction in the level ordering is also shown (right). Figure taken from Ref [17].

This effect is further exaggerated by the ever-increasing level densities for nuclei with large nucleon numbers, which lead to the failure of the assumption of a configuration that can be characterised by a unique set of angular and spin variables. A well known example of this was shown by Talmi [22], who demonstrated that there are $\sim 3\times10^{14}$, 2^+ states which can be constructed for the $^{154}_{62}Sm_{92}$ nucleus with a proton and a neutron basis encompassing single-particle levels between Z = 50-82 and N = 82-126 closed shells.

2.2 Nuclear Shape Parametrisation

The importance of such degeneracy-breaking residual interactions between the increasing number of valence nucleons introduces nuclear collectivity, including static and dynamic deformations. In geometric models, such as the unified collective model, nuclear shapes are often parametrised in terms of a spherical harmonic multipole expansion, and are related to the observed nuclear moments or the transition rate in a model dependent way. The length of a radius vector $R(\theta, \phi)$ pointing from the origin to the nuclear surface is given by [20]

$$R(\theta, \phi) = R_0[1 + \sum_{\lambda=1}^{\lambda_{max}} \sum_{\nu-\lambda}^{\lambda} \alpha_{\lambda,\nu} Y(\theta, \phi)], \tag{2.5}$$

where R_0 is a radius of sphere with the equal volume. In many cases, nuclear shapes are assumed to be invariant with respect to the three symmetry planes, so that

$$\alpha_{\lambda,\nu} = \alpha_{\lambda,-\nu}, \tag{2.6}$$

$$\alpha_{\lambda,\nu} = 0. \quad (\lambda = odd \; and/or \; \nu = odd) \tag{2.7}$$

For axially symmetric shapes with respect to the major axis (z-axis in figure 2.3), all deformation parameters except $\nu = 0$ disappear, and the remaining deformation parameters $\alpha_{\lambda,0}$ are described as β_λ, i.e. $\beta_\lambda = \alpha_{\lambda,0}$.

The quadrupole deformations ($\lambda = 2$) are usually the most important of the shape parameters: three of the five quadrupole deformation parameters determine the orientation of a nucleus in space,

$$\alpha_{2,1} = \alpha_{1,2} = \alpha_{2,2} - \alpha_{2,-2} = 0, \tag{2.8}$$

and the remaining two quadrupole deformations, $\alpha_{2,0}$ and $\alpha_{2,2}$ may be written in terms of the Hill-Wheeler polar coordinates (β,γ) [25] as

$$\alpha_{2,0} = \beta_2 \cos\gamma, \tag{2.9}$$

$$\alpha_{2,2} = \alpha_{2,-2} = -\frac{1}{\sqrt{2}}\beta_2 \sin\gamma. \quad (2.10)$$

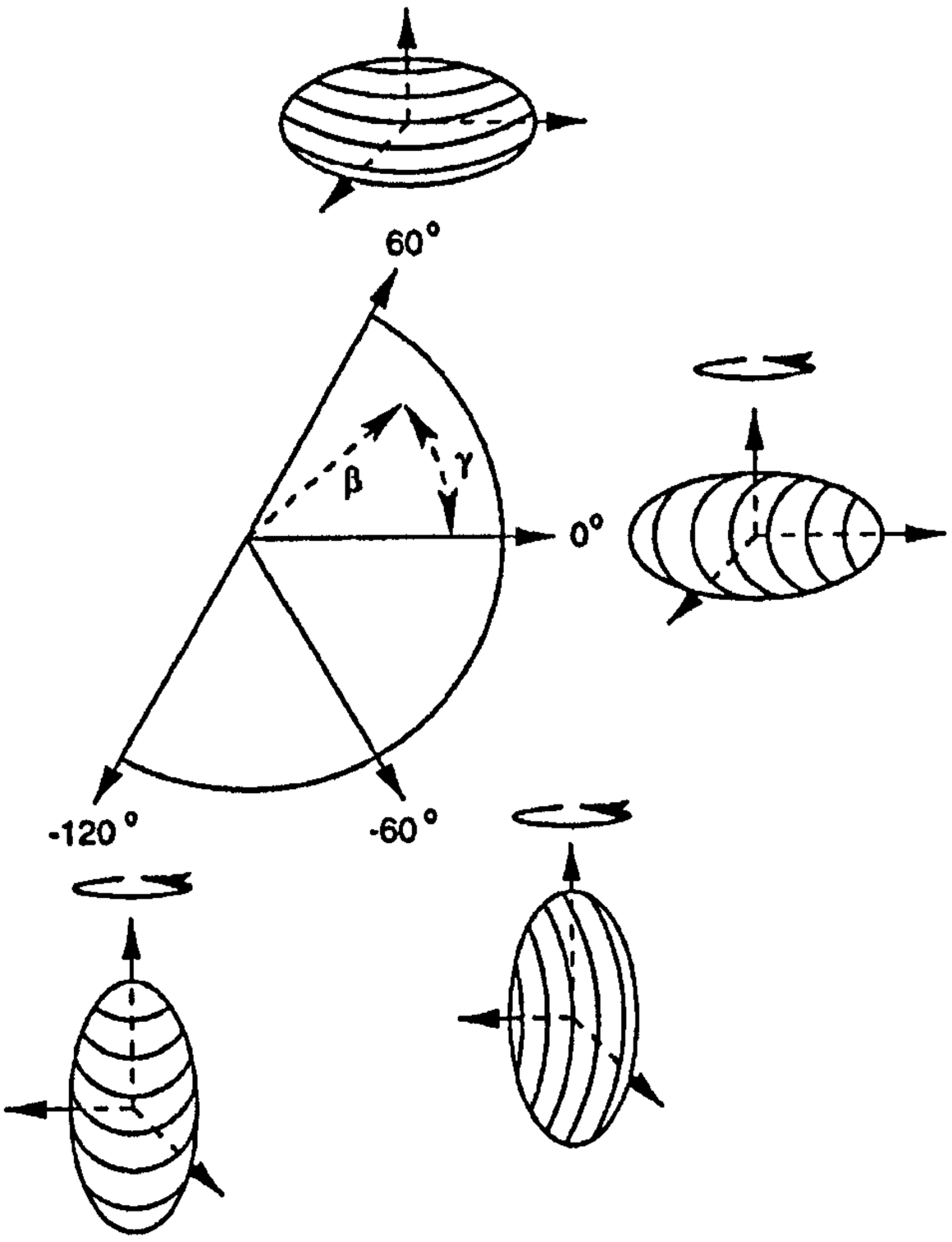

Figure 2.2: The 'Lund Convention' for nuclear shape parametrisation. Figure taken from Ref [23].

In this representation, the nuclear shapes are axial if $\beta > 0$ and γ is a multiple of 60°, and γ-soft/triaxial if the γ is not a multiple of 60°.

2.3 The Nilsson Model

The relative success of the spherical shell model close to the shell closures encouraged Nilsson [26] to construct a modified shell model hamiltonian to explain the microscopic structures of deformed nuclei. Limited only to the harmonic-oscillator potential, the zeroth order Hamiltonian, H_{intr}, can be expressed as

$$H_{intr} = -\sum_i \frac{\hbar^2}{2M}\nabla_i^2 + \frac{1}{2}M\sum_i [w_x^2(x_i^2 + y_i^2) + w_z^2 z_i^2], \qquad (2.11)$$

where $\omega_{x,y,z}$ are the oscillator frequencies in x-, y-, z-direction. The energy corresponding to the above Hamiltonian is [27]

$$E(N, n_z, \delta) = \hbar\omega_x(N - n_z + 1) + \hbar\omega_z(n_z + \frac{1}{2}), \qquad (2.12)$$

where $N = n_x + n_y + n_z$ and is the total number of harmonic quanta in x-, y-, z-direction.

The number of oscillator quanta can be set to be a function of deformation δ [27], so that

$$(w_x + w_y) = w_\delta \approx w_0[1 + \frac{1}{3}\delta],\ w_z \approx w_0[1 - \frac{2}{3}\delta],\ \delta = \frac{\Delta R}{R_0}. \qquad (2.13)$$

The above relations illustrate that for a spherical single-particle configuration, i.e. $\frac{\Delta R}{R_0} = 0$, $N = n_x + n_y + n_z$ is degenerate and the shell gaps appear in the single particle spectrum as the usual magic numbers. As the potential becomes deformed, i.e. $\frac{\Delta R}{R_0} > 0$, this degeneracy is lost, but a high degree of degeneracy reappears whenever the ratio of rotational frequencies, $\omega_{x,y} : \omega_z$, are simple integers. This is a general feature of the anisotropic

harmonic oscillator potential of equation 2.11, which leads to the deformed magic numbers.

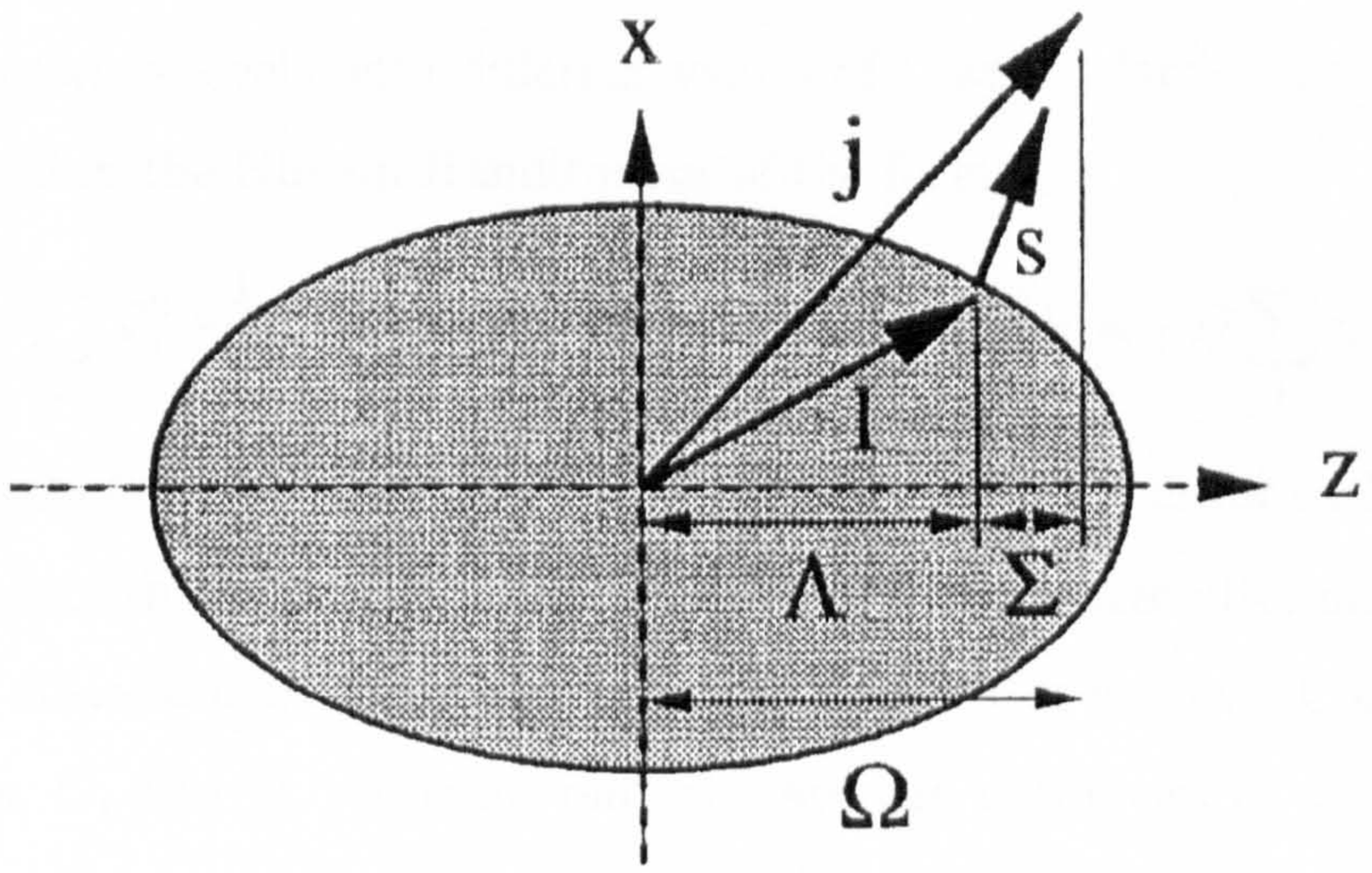

Figure 2.3: Schematic of single-particle coupling to the core, and the Nilsson quantum numbers. Figure taken from Ref [28].

Assumptions of the rotational and reflection invariance of the H_{intr} allow the eigenstates of the H_{intr} to be characterised by the Nilsson quantum numbers (see figure 2.3) as

$$\Omega^{\pi}[N, n_z, \Lambda], \tag{2.14}$$

where z-projection of the total angular momentum of the particle satisfies

$$\Omega = \Lambda \pm \frac{1}{2}. \tag{2.15}$$

The parity satisfies

$$\pi = (-1)^N, \tag{2.16}$$

and the orbital angular momentum projection quantum number, Λ, satisfies,

$$\mid \Lambda \mid = N - n_z, N - n_z - 2, N - n_z - 4, .., \pm 1 \; or \; 0. \tag{2.17}$$

Just as in the spherical shell model where the zeroth-order single-particle Hamilton, H_0, required a spin-orbit term, $C\mathbf{l}\cdot\mathbf{s}$ and $D\mathbf{l}^2$, to reproduce the splitting between levels with different values of l, well deformed nuclei may be expressed in the Nilsson Hamiltonian of the form,

$$H = \frac{\hbar^2}{2M}\sum_i \nabla_i^2 + \frac{1}{2}M\sum_i [w_x^2(x_i^2+y_i^2)+w_z^2 z_i^2] + C\sum_i \mathbf{l}_i\cdot\mathbf{s}_i + D\sum_i \mathbf{l}_i^2. \quad (2.18)$$

The constants C and D are empirical values, and are different for each major shell. The fact that the Nilsson model provides two or three alternatives for the lowest state of a given nucleus indicates the limit of validity. Constants, such as w_0, C, and D, represent only the average properties of the underlying real nucleon–nucleon interactions, so that more detailed examination of experimental data requires the inclusion of residual interactions, such as pairing.

2.4 Pairing Interaction

The total wavefunction from the BCS formalism takes the form [29, 30],

$$\Psi_0^{BCS} = \Pi_\nu U_\nu + V_\nu a_{jm}^+ a_{j\overline{m}}^+ a_{j\overline{m}'} a_{jm'}|0>, \quad (2.19)$$

where the pairing hamiltonian employed is

$$H_{pair} = \Sigma_\nu a_{jm}^+ a_{j\overline{m}}^+ a_{j\overline{m}'} a_{jm'}, \quad (2.20)$$

where $\overline{m}$ refers to the time-reversed orbits of m, and a^+ and a refer to creation and destruction operators for single particles. The resulting two-particle wavefunction in equation 2.19 is a product over all states ν, and U_ν and V_ν are subject to the normalisation conditions

$$U_\nu^2 + V_\nu^2 = 1, \quad (2.21)$$

and

$$2\Sigma_\nu V_\nu^2 = N, \tag{2.22}$$

where U_ν^2 refers to the probability of an orbital ν not being occupied, V_ν^2 refers to the probability that it is occupied, and N is the total number of nucleons. The required wavefunction of equation 2.19 is the one which minimises the total energy under the conditions of equation 2.21 and 2.22. The solution of the hamiltonian in equation 2.20 then yields the probability of an orbit being occupied by a pair of nucleons as [24]

$$V_\nu^2 = \frac{1}{2}\left[1 - \frac{(\epsilon_\nu - \lambda)}{E_\nu}\right], \tag{2.23}$$

where E_ν is the quasi-particle energy, and is

$$E_\nu = \sqrt{(\epsilon_\nu - \lambda)^2 + \Delta^2}, \tag{2.24}$$

where

$$\Delta = G\Sigma_\nu U_\nu V_\nu. \tag{2.25}$$

Here, ϵ_ν represents the single-particle energy, G the pairing strength, λ the chemical potential, and Δ the pairing gap, which is often taken as the odd-even mass difference. According to the equation 2.23, each quasiparticle orbital represents a mixture of Nilsson single-particle orbitals, and the quasi-particle energies, E_ν, are dependent on both ϵ_ν and λ.

However, significant changes to the gap equation of 2.24 have to be made in moderately deformed odd-even nuclei ($40 < \mathrm{N} \approx \mathrm{Z} < 150$) due in part to their low level densities. Such nuclei have only a small number of summations over states ν in equations 2.21 and 2.22, so that the Pauli Principle, which forbids the occupancy of a quasiparticle level already occupied by an odd particle (by a particle pair), and the replacement of the number N in equation 2.22 with $N - 1$ modify the equations 2.22 and 2.25 as

$$2\Sigma_\nu V_\nu^2 = N - 1, \tag{2.26}$$

and

$$\Delta = G\Sigma_{\nu \neq \nu_1} U_\nu V_\nu, \tag{2.27}$$

where the ν_1 represents the quasiparticle level already occupied by the odd particle in the ground state wavefunction, Ψ_0^{BCS}. These changes in Δ and in the U_ν/V_ν are called the *blocking effect*, and may be observed as the reduction of pairing gap Δ and the delay in band-crossing frequencies for odd-even nuclei around mass A $\simeq$ 100.

2.5 Cranked Shell Model

The single-particle description of the Nilsson model, with or without pairing, cannot reproduce the dynamical moment of inertia exhibited by the yrast bands, since it does not incorporate rotation. The cranking model of Inglis [31] introduced waves on the nuclear surface by providing a distortion that depends on spin. Further contributions from Bengtsson and Frauendorf [32] treat the nuclear rotation classically, with a rotation vector superimposed on a major axis (often x-axis in figure 2.3), and describe the cranked hamiltonian h^ω as

$$h^\omega = h_{sp} - \hbar\omega j_x, \tag{2.28}$$

where h_{sp} is the Nilsson hamiltonian, j_x is the total angular momentum projection operator on to the rotation axis, and the term $-\hbar\omega j_x$ contains Coriolis and centrifugal effects which modify the single-particle orbital motion. Also, the pairing interaction is often included with the cranked hamiltonian h^ω,

$$h'_{qp} = h^\omega - \Delta(P^+ + P) - \lambda N, \tag{2.29}$$

where h'_{qp} is the quasiparticle hamiltonian, Δ is the pairing gap, P^+/P are the quasiparticle pair creation/annihilation operators, and N is the particle

number operator, included to keep the total number of particles constant.

The solutions of the h'_{qp} are only approximate due to the use of perturbation theory, as well as the broken invariance of time-reversal symmetry by the $-\hbar\omega j_x$ term. Restoration of this symmetry involves the approximate transformation of the Hamiltonian of equation 2.29 into the intrinsic frame of the nucleus. In particular, the solutions of the h'_{qp} are all related to a reference configuration, so that the resultant relative energies are often taken with respect to the yrast band of an even-even nucleus. Only two symmetries remain good quantum numbers, and they are parity π and signature α. Signature is related to a rotation operator,

$R_x = e^{-i\pi\alpha}$, where π is the rotation about the x-axis and when the nucleus is rotated by $\pi = 180°$, this quantum number implies a selection rule for the angular momentum of a γ-ray transition that is $\Delta I = \alpha$ mod 2. A quasi-particle (1-qp) excitation will have $\alpha = \pm\frac{1}{2}$ and a 2-qp excitation will have a signature which is the sum of all values of α, $\alpha_t = 0$ or 1, where α_t refers to the total signature for an excitation. Using the expression, $I = \alpha_t$ mod 2, $I = \frac{1}{2}, \frac{5}{2}, \frac{9}{2}, \ldots$ for $\alpha = \frac{1}{2}$ and $I = \frac{3}{2}, \frac{7}{2}, \frac{11}{2}, \ldots$ for $\alpha = -\frac{1}{2}$ as $I = \alpha_t + 2n$, where n is an integer.

The eigenvalues of the quasiparticle hamiltonian, h'_{qp}, summed over all occupied states, ν, is the total energy E^ω of the cranking system in the laboratory frame,

$$E^\omega = \sum_\nu e^\omega_\nu + \omega \sum_\nu < \nu^\omega \mid j_x \mid \nu^\omega >, \tag{2.30}$$

and the projection of the total angular momentum onto the rotation axis (x-axis) can be determined by

$$I_x = \sum_\nu < \nu^\omega \mid j_x \mid \nu^\omega > . \tag{2.31}$$

A plot of the single-particle energy against the rotational frequency is known as a Routhian diagram, and the differential of the Routhian e^{ω} is related to the aligned single-particle angular momentum, i_x, by

$$i_x = -\frac{de^{\omega}}{d\omega}. \tag{2.32}$$

Equation 2.30 also allows the theoretical Routhians in the intrinsic frame of a nucleus to be compared to the experimental aligned angular momentum. The experimental Routhians are expressed as

$$E^{\omega}_{expt} = \frac{1}{2}[E(I+1) + E(I-1)] - \omega(I)I_x(I), \tag{2.33}$$

where I_x is the aligned angular momentum

$$I_x \approx [(I+1/2)^2 - K^2]^{1/2}, \tag{2.34}$$

and the K is the projection of the total angular momentum along the symmetry axis. The angular frequency, w, is derived from the experimental γ-ray energies via

$$\omega = \frac{dE(I)}{dI_x(I)} \approx \frac{E(I+1) - E(I-1)}{I_x(I+1) - I_x(I-1)} \approx \frac{E_\gamma}{\sqrt{(I+\frac{3}{2})^2 - K^2} - \sqrt{(I-\frac{1}{2})^2 - K^2}}, \tag{2.35}$$

in which E_γ is taken as the γ-ray transition energy. Furthermore, comparison between the experimental and theoretical quasi-particle Routhians require the contributions of the core to be removed from the energy reference. The experimental Routhian and alignment are thus defined by

$$e^{\omega}_{expt} = E^{\omega}_{expt}(I) - E^{\omega}_{ref}(I), \tag{2.36}$$

and

$$i^{expt}_x(\omega) = I_x(\omega) - I^{ref}_x(\omega). \tag{2.37}$$

The energy reference is often calculated via a variable moment of inertia fit to the low-lying transitions as a function of ω,

$$\Im^{(1)}_{ref}(\omega) = \Im_0 + \omega^2 \Im_1, \tag{2.38}$$

where $\Im_0$ and $\Im_1$ are the Harris parameters [33]. Further, the reference aligned angular momentum can be given by

$$I_x^{ref}(\omega) = \frac{1}{\hbar}(\Im^{(1)}_{ref}(\omega))\omega, \tag{2.39}$$

and the reference energy, E'_g, by

$$E'_g = -\frac{1}{2}\Im_0 w^2 - \frac{1}{4}\Im_1 w^4 - \frac{1}{8}\frac{\hbar^2}{\Im_0}. \tag{2.40}$$

The integration constant $\frac{1}{8}\frac{\hbar^2}{\Im_0}$ is introduced to ensure that the ground state reference energy is zero.

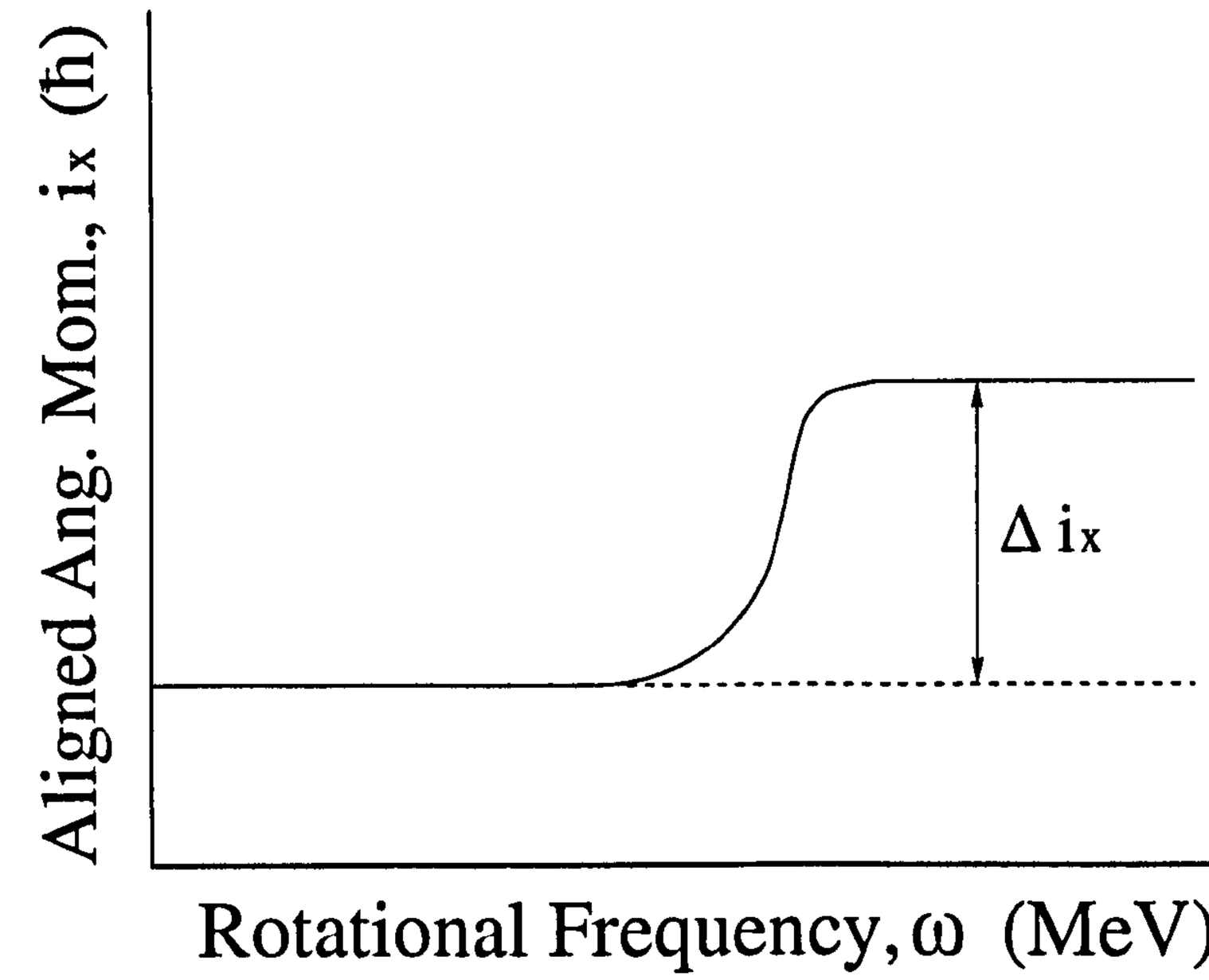

Figure 2.4: Example of a backbending with alignment gain, Δi.

2.6 Nilsson-Strutinsky Model

A global nuclear property, such as the binding energy, usually maintains an irregular variation as a function of the mass A (or Z/N). The Nilsson-Strutinsky method considers the nuclear binding energy of a nucleus to have a shell structural contribution, ΔE_{sh}, superimposed on to a smoothly varying liquid drop part, E_{LD}, both with respect to the nuclear mass;

$$E = \Delta E_{sh} + E_{LD}. \tag{2.41}$$

The total shell model energy, E_{sh}, is further decomposed into a smoothly varying $\widehat{E}_{sh}$ and a fluctuating ΔE_{sh} part,

$$E_{sh} = \sum_i \epsilon_{\nu i} = \widehat{E}_{sh} + \Delta E_{sh}, \tag{2.42}$$

so that the total energy of the nucleus can be expressed as

$$E = E_{LD} + \Delta E_{sh} = E_{LD} + [E_{sh} - \widehat{E}_{sh}], \tag{2.43}$$

where E_{LD} is the macroscopic contribution describing the bulk properties, and

$$\Delta E_{sh} = [E_{sh} - \widehat{E}_{sh}], \tag{2.44}$$

is the microscopic quantal shell correction. With the inclusion of the term ΔE_{sh}, ground state nuclear energies can be determined as a function of deformation parameters and nuclear rotation. Usually, a pairing correction is included in the total Routhian, so that the Routhian may be constructed from an expression

$$E^{\omega}(Z, N, \widehat{\beta}) = E^{\omega}_{macro}(Z, N, \widehat{\beta}) + \Delta E^{\omega}_{shell}(Z, N, \widehat{\beta}) + \Delta E^{\omega}_{pair}(Z, N, \widehat{\beta}), \tag{2.45}$$

where $\widehat{\beta}$ represents all deformation parameters. The shell correction term is calculated using the deformed Nilsson potential at zero rotational frequency

($\omega = 0$), and the pairing term is determined using the self-consistent solution of the BCS equations. The microscopic-macroscopic form of the total Routhians can therefore be constructed as

$$\begin{aligned} E^{\omega}(Z,N,\widehat{\beta}) &= E^{\omega=0}(Z,N,\widehat{\beta}) + [\langle \nu^{\omega} \mid H^{\omega}(Z,N,\widehat{\beta}) \mid \nu^{\omega} \rangle \\ &- \langle \nu^{\omega} \mid H^{\omega=0}(Z,N,\widehat{\beta}) \mid \nu^{\omega} \rangle] \\ &- \frac{1}{2}\omega^2[\Im_{macro}(A,\widehat{\beta}) - \Im_{Strut}(Z,N,\widehat{\beta})], \end{aligned} \tag{2.46}$$

where $E^{\omega=0}$ corresponds to the sum of liquid drop energy, the single-particle shell correction energy, and the pairing energy at zero frequency. The total Routhian is calculated in a lattice of deformation space ($\widehat{\beta} = \beta_2$, β_4, and γ) at a fixed rotational frequency, and then minimised with respect to the shape parameters to obtain the equilibrium deformation. As described in section 2.3 in relation to the deformed harmonic oscillator potential, the shell structure is not unique to spherical nuclei, but also for certain finite deformations of the nuclear potential. Although stable liquid drops are always spherical, the 'Strutinsky averaged energy' of equation 2.46 could therefore possess a minimum at finite values of deformation.

The results are usually displayed as a Total Routhian Surface (TRS) plot, which is a contour map of energy in the $\beta_2 - \gamma$ plane. A typical TRS map is shown in figure 2.5. The triaxiality parameter γ describes the deviation of a nucleus from the axial symmetry, and is defined such that $\gamma = 0°$ and $\gamma = 60°$ correspond to axially symmetric prolate and oblate deformations, respectively. The quadrupole deformation defines the parameter β_2, and at each point in the $\beta_2 - \gamma$ plane, the potential energy has been minimised with respect to the hexadecapole deformation β_4.

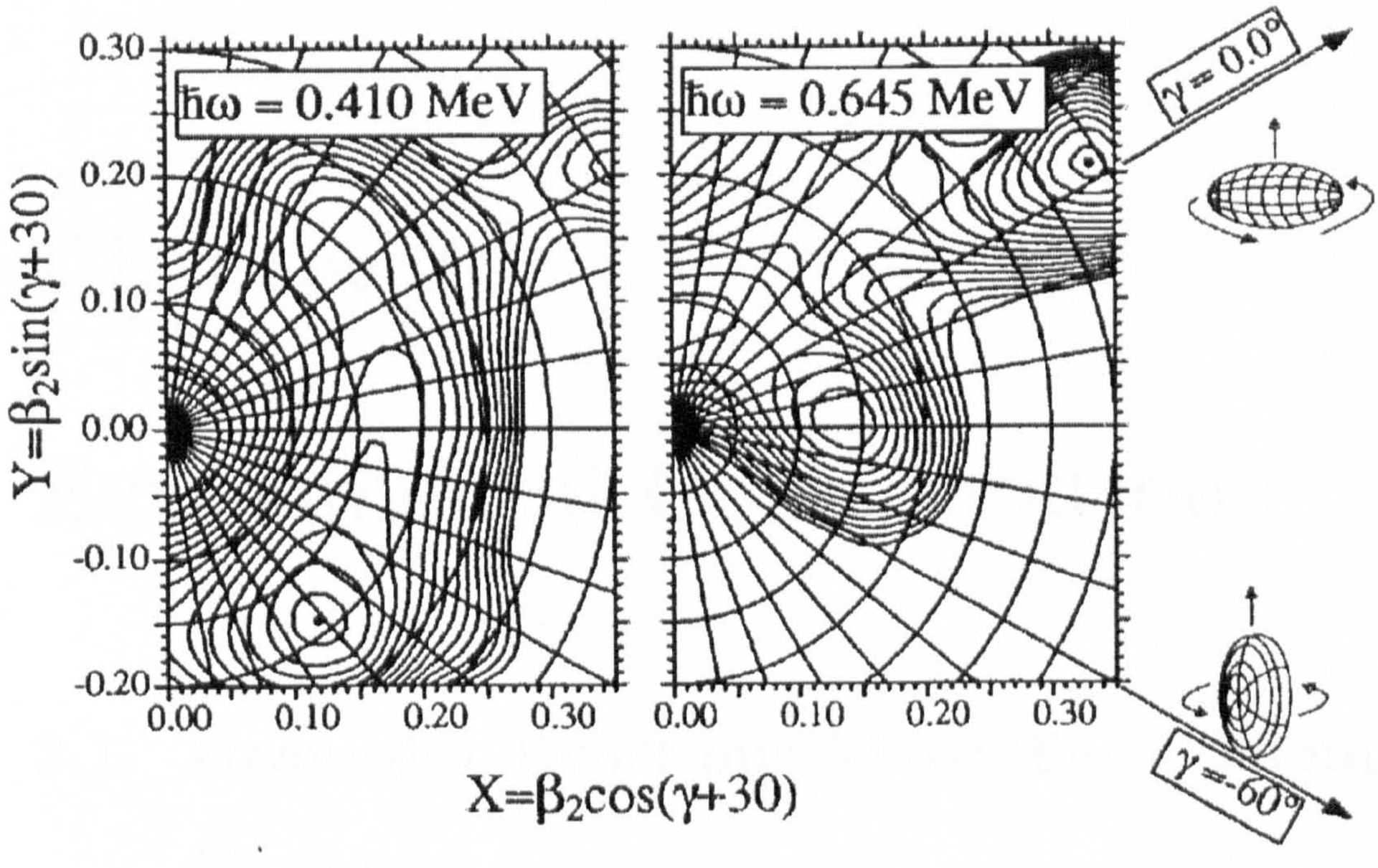

Figure 2.5: Total Routhian Surfaces calculated for parity/signature, $(\pi,\alpha) = (-,-1/2)(\nu,\mathbf{E})$, configuration in $^{133}_{58}Ce_{75}$ at two rotational frequencies of $\hbar\omega =$ 0.410 MeV and 0.645 MeV. $\gamma = 60°$ represents oblate deformation, while $\gamma = 0°$ corresponds to prolate deformation. Figure taken from Ref [28].

Chapter 3

Experimental Considerations

3.1 Heavy-Ion Reactions Above The Coulomb Barrier

Extensive studies into heavy-ion collisions above the Coulomb barrier suggested that the semi-classical approach to the nuclear collisions may be appropriate, as the range of angular momenta leading to the reactions are typically $\Delta l \sim \Delta bp > 1\ \hbar$ [34]. Often, the macroscopic representations of the above-barrier reaction mechanisms include frictional forces in addition to the conservative two-body interaction potential (i.e. Coulomb, centrifugal and nuclear potential), and an outcome of such reactions is determined according to its partial wave. The definition of different reaction mechanisms should then be possible in terms of the final spin distribution, as shown in figure 3.1 and 3.2. Experimentally, dynamical fluctuations, as well as quantum and statistical transfers of angular momenta between a projectile and a target nuclei meant the sharp cutoff approximation in the spin regime often employed for the classification of the various reaction mechanisms cannot be made [35], however.

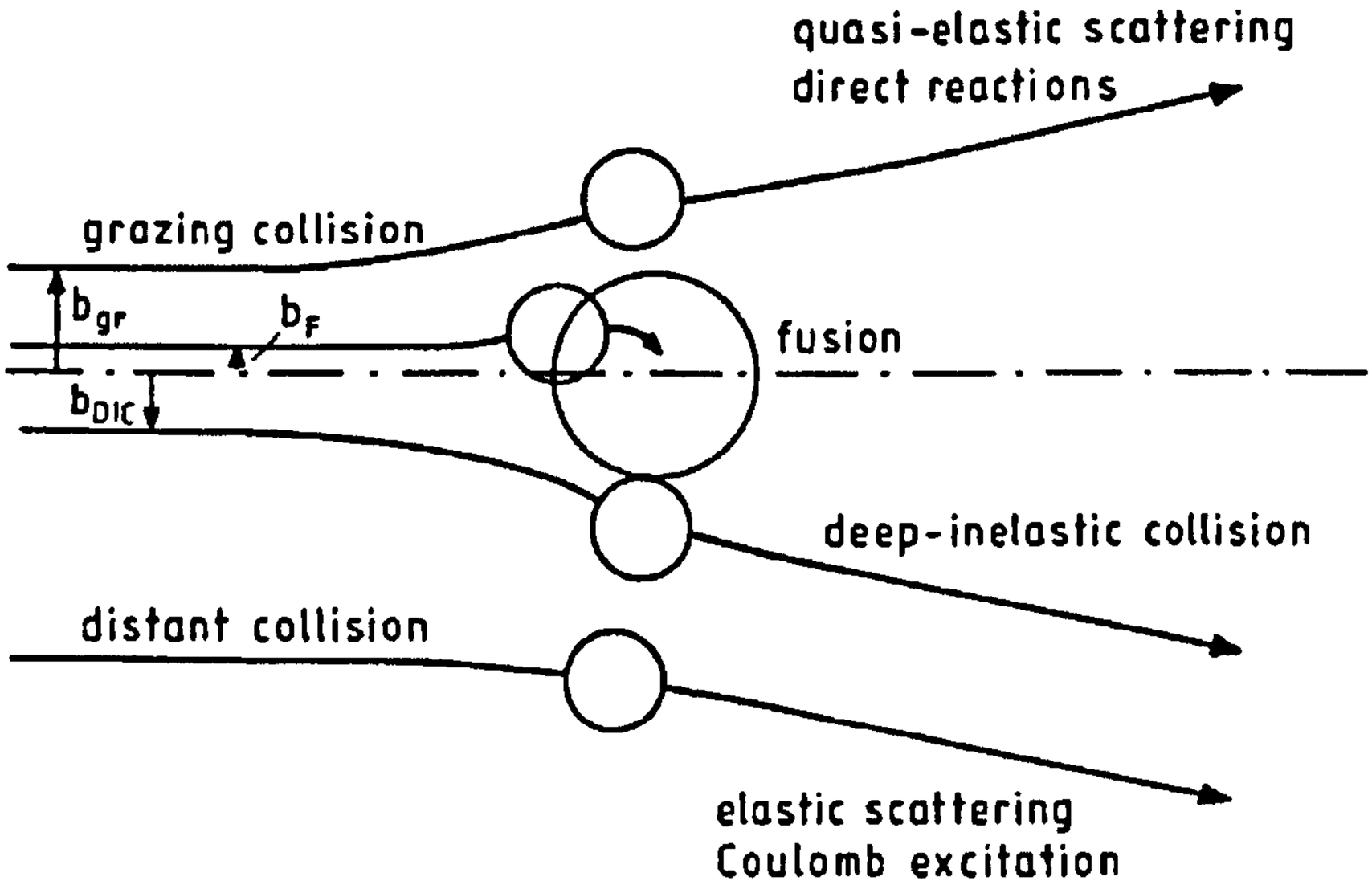

Figure 3.1: Schematics of possible reaction mechanisms above the Coulomb barrier. Figure taken from Ref [35].

For fusion-evaporation reactions, the conditions of smallest of impact parameters and the relative energy greater than the Coulomb barrier for two colliding nuclei result in a large amount of initial kinematic energies and all relative angular momenta to be converted into the excitation energy and the angular momentum of a compound nucleus, respectively. The conservation of energy and mass provide an expression for the excitation energy of the compound nucleus, E_{ex}, as

$$E_{ex} = Q + E_{cm}, \tag{3.1}$$

where the Q-value of the reaction, Q, is

$$Q = M_P + M_T - M_{CN}, \tag{3.2}$$

and the energy of the nucleus in the centre-of-mass, E_{cm}, is

$$E_{cm} = \frac{M_T}{M_P + M_T} E_b. \tag{3.3}$$

Here, the subscript CN refers to the residual nucleus, E_b is the beam energy in the laboratory frame, and $M_{P,T}$ are the nuclear masses of projectile and target nuclei, respectively.

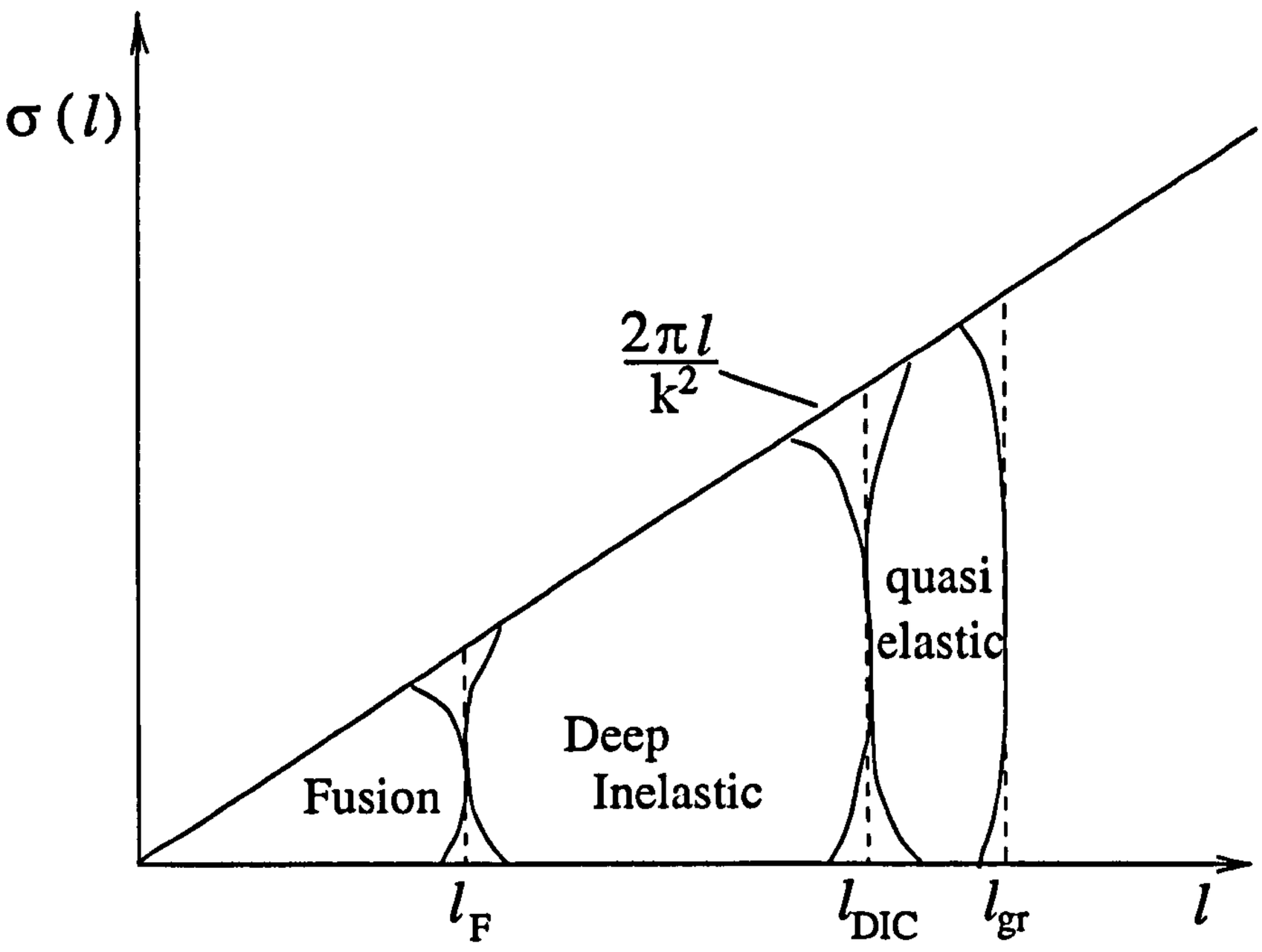

Figure 3.2: The spin distribution of a heavy-ion reaction. The regions for fusion, deep inelastic, and quasi-elastic collisions and the associated maximum angular momentum (l_F, l_{DIC}, and l_{gr}), leading to each type of the reaction are shown.

The resultant high excitation energies are often larger than the nucleon binding energies, and hence lead to the statistical particle emission, each carrying ~5-8 MeV of energy, but typically only ~2 $\hbar$ of angular momentum.

This means that the high angular momentum acquired by the particle-bound reaction residue can only be removed through γ-ray emissions, firstly by statistical γ-rays, followed by the discrete γ-rays decaying along the yrast line. The maximum angular momentum, l_{max}, of the fusion-evaporation reaction can also be defined as [35]

$$l_{max}^2 = \frac{2\mu R^2}{\hbar^2}(E_{cm} - V_c), \tag{3.4}$$

where E_{cm} is the centre-of-mass collision energy and μ is the reduced mass, $\mu = M_P M_T / M_P + M_T$. Here, the V_c refers to the Coulomb barrier between the target and the projectile to be overcome [36], and is given by

$$V_c = 1.44 \frac{Z_P Z_T}{R}, \quad (MeV) \tag{3.5}$$

where R is the radius of the compound nucleus,

$$R = R_P + R_T \approx 1.2(A_P^{\frac{1}{3}} + A_T^{\frac{1}{3}}). \tag{3.6}$$

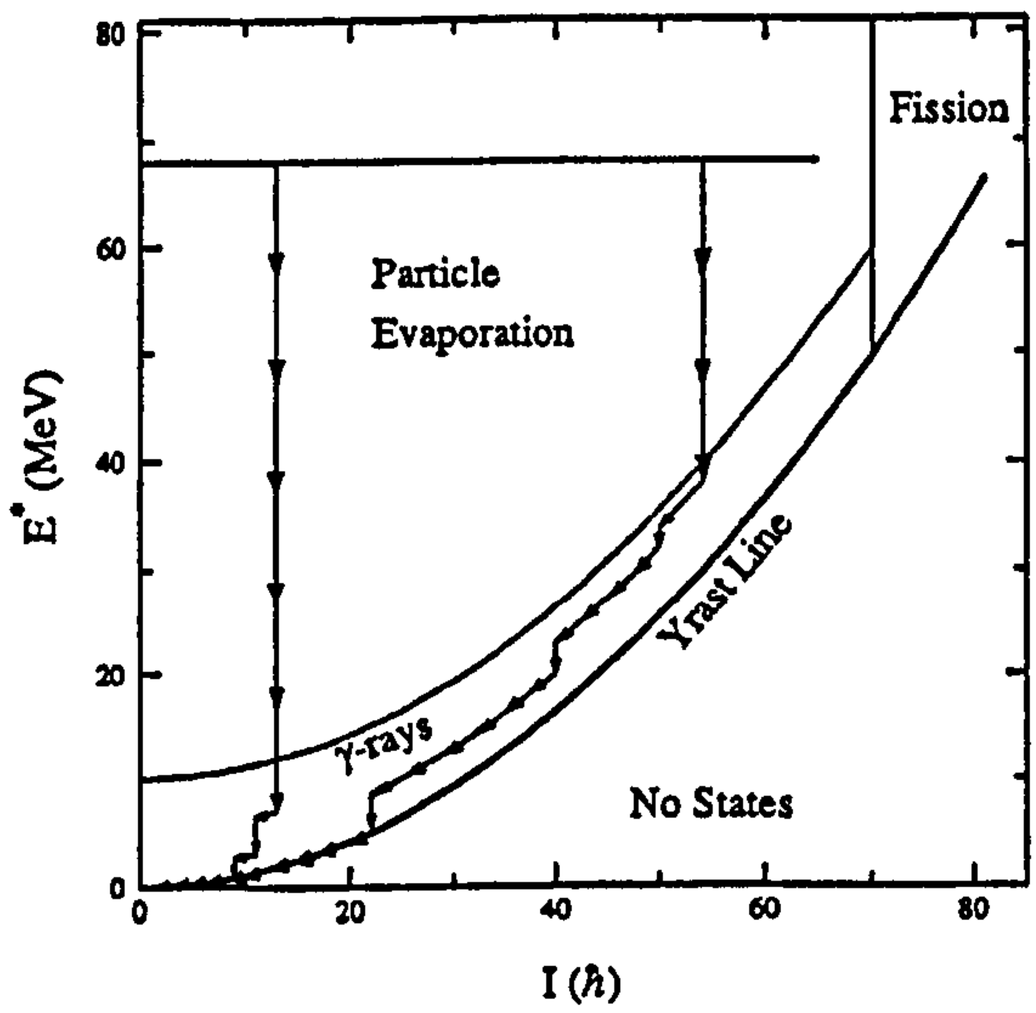

Figure 3.3: Schematic diagram of nuclear decays in the fusion evaporation process.

The highest excitation energies and angular momenta are therefore reached by the fusion-evaporation reactions for a given projectile-target combination above the barrier, and the reaction is most favourably employed for the study of high-spin states in proton-rich nuclei. However, the reaction preferably emits neutrons, so that the high-spin investigations of neutron-rich nuclei often require transfer reactions, such as pick-up and stripping reactions. For binary, heavy-ion reactions ($A_{proj,targ} \geq 60$) slightly above the Coulomb barrier, large angular momenta can be generated in the reaction residues via energy dissipative processes, such as quasi-elastic (QE) and deep inelastic (DIC) reactions. The large cross-section reserved for the transfer processes for these reactions also ensure their suitability for the study of neutron-rich nuclei.

The DIC reaction involves the transfer of massive particles between the two interacting nuclei and is particularly useful in populating neutron-rich nuclei. The most important variables which characterise the DIC reaction mechanism were found to be the N/Z ratio of target-like (TLF) and projectile-like (PLF) fragments, their energy losses and masses, and the relative angular momenta. Assuming the angle of rotation to increase with the interaction time, the previous experimental and theoretical works on binary reactions [37, 38, 39, 40] suggest that the radial kinetic energy equilibrates first, followed by the N/Z ratio, which equilibrates in $\sim 10^{-22}$ seconds. Sharing of angular momentum between the TLF and the PLF completes next, then their masses equilibrate in $\sim 10^{-20}$ seconds. This slow rate of equilibration process for the fragment mass in the DIC reaction results in the appearance of both target-like (TLF) and projectile-like (PLT) fragments. In particular, a large variation in energy loss observed in the reaction led to the development of the 'surface-friction model', in which the equations of

motion are derived from the Lagrange-Rayleigh formalism [41]. According to this model, the attractive nuclear interaction force traps the intermediate, di-nuclear system temporarily, while it rotates and loses energy via friction. The interpretation of such strongly inelastic channels often involves the reaction deflection angle, θ, of the outgoing fragments, and the value of θ is assumed to reflect the interaction time of the di-nuclear system and its l–dependent rotational velocity. At a particular l-window, where the impact parameter b is the parameter of the *grazing trajectory*, whose distance of closest approach is equal to the radius of the target nucleus, the experimentally measurable deflection angle of a reaction fragment can often be defined as the *grazing angle* for that fragment in a given projectile-target combination with beam energy, E_b.

Relations between the deflection angle and the energy loss in the form of a *Wilczyńsky* plot [42] can provide a way to distinguish the different reaction regimes (see section 5.5). Moreover, the surface-friction model allows an estimate of the amount of relative to intrinsic angular momentum transferred onto the reaction fragments to be calculated, in accordance with their observed degree of inelasticity.

3.1.1 Dynamical Model of The Binary Reaction

As assumed in the previous section, the relative motion of two heavy nuclei colliding with a relatively short deBroglie wavelength may be treated in a semi-classical limit, which is experimentally supported by the observation that the emerging fragment masses retain closely the initial mass asymmetry. The relative motion of the system can then be approximated by conservative and dissipative forces, and the equations of motion of a set $\{q_i\}$ of n

coordinates can be determined by the Lagrange-Rayleigh equation:

$$\left(\frac{d}{dt}\frac{\partial}{\partial \dot{q}_i} - \frac{\partial}{\partial q_i}\right)\mathfrak{L} = -\frac{\partial}{\partial \dot{q}_i}\mathfrak{F}, \qquad i = 1, ..., n \tag{3.7}$$

Here, $\mathfrak{L} = \mathfrak{J} - V$ is the Lagrangian, and $\mathfrak{F}$ is the Rayleigh dissipation function, which is related to the rate of energy dissipation, dE/dt, where $E = \mathfrak{J} + V$. The potential energy $V(q_1, ..., q_n)$ is a function of the collective coordinates q_i, whereas the kinetic energy is dependent on the associated velocities $\dot{q}_i$ and the inertia tensor (m_{ij}) according to

$$\mathfrak{J} = \frac{1}{2}\sum_{i,j=1}^{n} m_{ij}\dot{q}_i\dot{q}_j. \tag{3.8}$$

Assuming that the dissipated energy is consumed by velocity-dependent frictional forces, $F_i = -\partial\mathfrak{F}/\partial\dot{q}_i$, the dissipation function is given by

$$\mathfrak{F} = \frac{1}{2}\sum_{i,j=1}^{n} c_{ij}\dot{q}_i\dot{q}_j, \tag{3.9}$$

where (c_{ij}) is the frictional tensor. The inertia and frictional tensors are also taken as functions of the coordinates q_i.

A simple relation of geometries often considered in the above formalism is shown in figure 3.4, containing the scattering of two rigid spherical nuclei induced by central and conservative Coulomb and nuclear interaction potentials V_{coul} and V_n, respectively. Four coordinates are then required to describe a collision: the distance r between the mass centres of projectile and target, their relative orientation angles θ_P and θ_T, respectively, and the orientation θ of the total system.

The Lagrangian can then be expressed as

$$\mathfrak{L} = \frac{1}{2}\mu[\dot{r}^2 + (r\dot{\theta})^2] + \frac{1}{2}\Im_P\dot{\theta}_P^2 + \frac{1}{2}\Im_T\dot{\theta}_T^2 - V_{coul} - V_N. \tag{3.10}$$

In the above equation 3.10,

$$\Im_i = \frac{2}{5}M_iR_i^2, \qquad i = P, T \tag{3.11}$$

where μ denotes the reduced mass of the system and $\Im_i$ the moment of inertia of the projectile and target masses M_P and M_T, respectively. The dissipation function may be represented in terms of a friction coefficient $c_r(r)$ associated

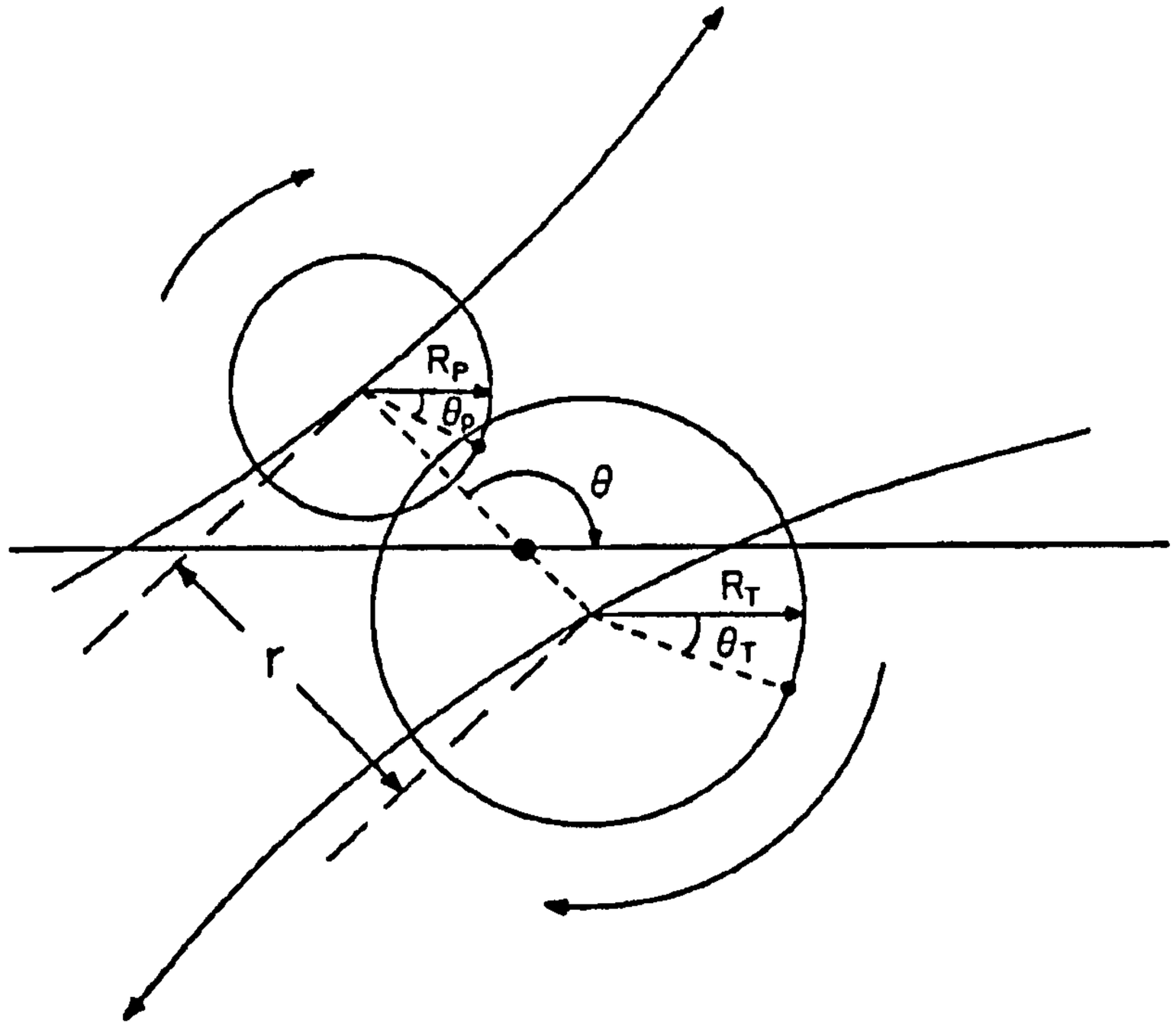

Figure 3.4: Reaction variables for a simple heavy-ion collision involving two spherically rigid fragments. Figure taken from Ref [43].

with the radial motion, and the coefficient $c_t(r)$ describing the slowing-down of the relative sliding motion of the two nuclear surfaces:

$$\mathfrak{F} = \frac{1}{2}\left\{c_r\dot{r}^2 + c_t\left(\frac{r}{R_P+R_T}\right)^2[R_P(\dot{\theta}_P-\dot{\theta})R_T(\dot{\theta}_T-\dot{\theta})]^2\right\}. \qquad (3.12)$$

From the Lagrange-Rayleigh expression of equation 3.7, the equations of motion may be obtained as

$$\mu\ddot{r} - \mu r\dot{\theta}^2 + c_r\dot{r} + \frac{\partial V_{coul}}{\partial r} + \frac{\partial V_N}{\partial r} = 0, \qquad (3.13)$$

$$\mu r^2\ddot{\theta} + \dot{I}_P + \dot{I}_T = 0, \qquad (3.14)$$

$$\dot{I}_i = \frac{d}{dt}\Im_i\dot{\theta}_i = -c_t\left[\frac{r}{R_P + R_T}\right]^2 R_i(\dot{\theta}_i - \dot{\theta}). \quad i = P,T \tag{3.15}$$

Here the terms I_P and I_T are the intrinsic spins of projectile and target, respectively, and $l = \mu r^2\dot{\theta}$ is the orbital angular momentum.

In the above model, dissipation of angular momentum ceases at the 'rolling limit', $R_P(\dot{\theta}_P - \dot{\theta}) = R_T(\dot{\theta} - \dot{\theta}_T)$. Using this relation on the angular velocity and the balance of tangential forces acting on the surfaces of the two nuclear spheres, the final angular momentum in the rolling limit can be described as

$$l_r = \frac{5}{7}l, \tag{3.16}$$

regardless of the masses and radii of the two nuclei. The missing angular momentum $l - l_r$ is said to be transformed into intrinsic spin I_i of the nuclei:

$$I_i = \frac{2}{7}\frac{R_i}{R_P + R_T}l. \quad i = P,T \tag{3.17}$$

In addition to the tangential sliding friction associated with the coefficient c_t, the presence of 'rolling friction' can be introduced [41, 44, 45] to dissipate angular momentum further, until $\dot{\theta}_P{=}\dot{\theta}_T = \dot{\theta}$. In this sticking mode, a dinuclear system rotates rigidly around its centre of mass with final orbital angular momentum l_s and intrinsic spins I_i

$$l_s = \frac{\Im}{\Im + \Im_P + \Im_T}l, \tag{3.18}$$

$$l_i = \frac{\Im_i}{\Im_i + \Im_P + \Im_T}l, \tag{3.19}$$

where $\Im = \mu r^2$ is the moment of inertia for the orbital motion of two nuclei with reduced mass μ, and $\Im_{P,T}$ are the moments of inertia of projectile and target nuclei, respectively.

3.2 HPGe Detectors

Details of nuclear structure can be inferred from the measurement of radiations emitted by nuclei and detected by high-purity germanium (HPGe) detectors. The nature and geometry of such semi-conductor detectors are therefore optimised to match the absorption characteristics of the radiation they are intended to observe. Figure 3.5 illustrates a typical HPGe detector with Compton suppression shields (see later).

The most desirable photon-matter interaction for γ-ray spectroscopy is the photoelectric effect, in which the complete photon absorption within a HPGe detector could result in the ejection of a bound electron with energy E_{e^-}, such that

$$E_{e^-} = E_\gamma - E_b, \tag{3.20}$$

where E_γ is the γ-ray energy, and E_b is the electron binding energy. The average energy needed to create a e^- – hole pair, the so-called W-value, in the HPGe detectors is ~3 eV, which is small enough to provide good energy resolution, but is too small for operation under normal room temperature, and liquid nitrogen cooling of the detectors to 77 K [47] is needed to reduce thermal excitation across valance-conduction band gap.

The cross-section for the photoelectric effect, σ_{photo}, in a typical HPGe detector varies as

$$\sigma_{photo} = \frac{Z^N}{E^{3.5}}, \tag{3.21}$$

where N varies from $3 \sim 5$ and Z is the atomic number of the detector. Thus, the photoelectric absorption is dominant only in a limited γ-ray energy range, as also indicated in figure 3.6 [17]. This fact makes the spectral suppression of other photon-matter interactions in particular the Compton scattering, crucial. Compton-suppression shields (CSSs) are hence commonly employed

with the HPGe detectors, and typically improve the intrinsic peak-to-total (P/T) ratio from ∼25 % to ∼60 % for a 1.3 MeV γ-ray [47].

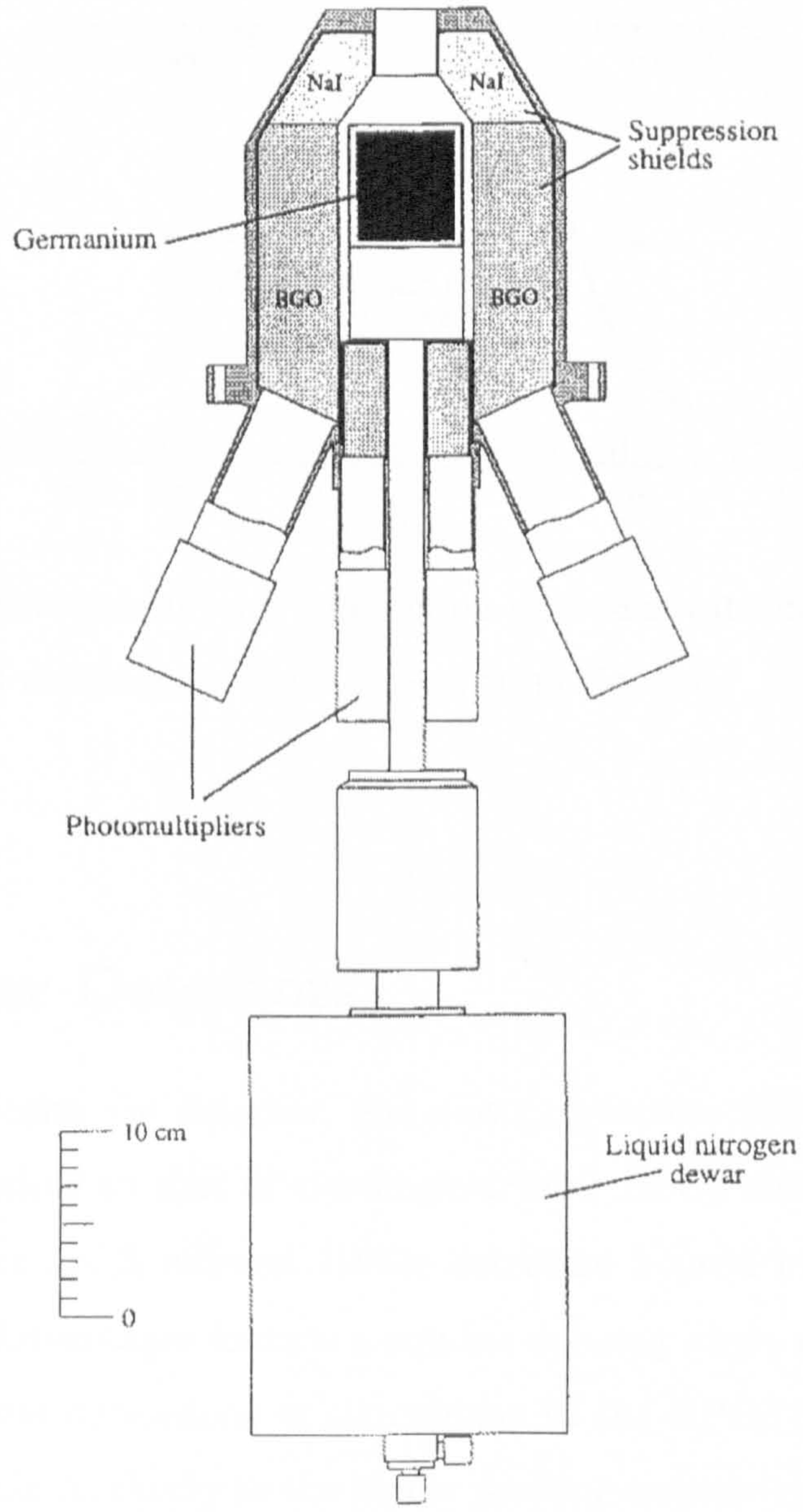

Figure 3.5: A HPGe spectrometer with Compton-suppression shields (CSSs). Figure taken from Ref [48].

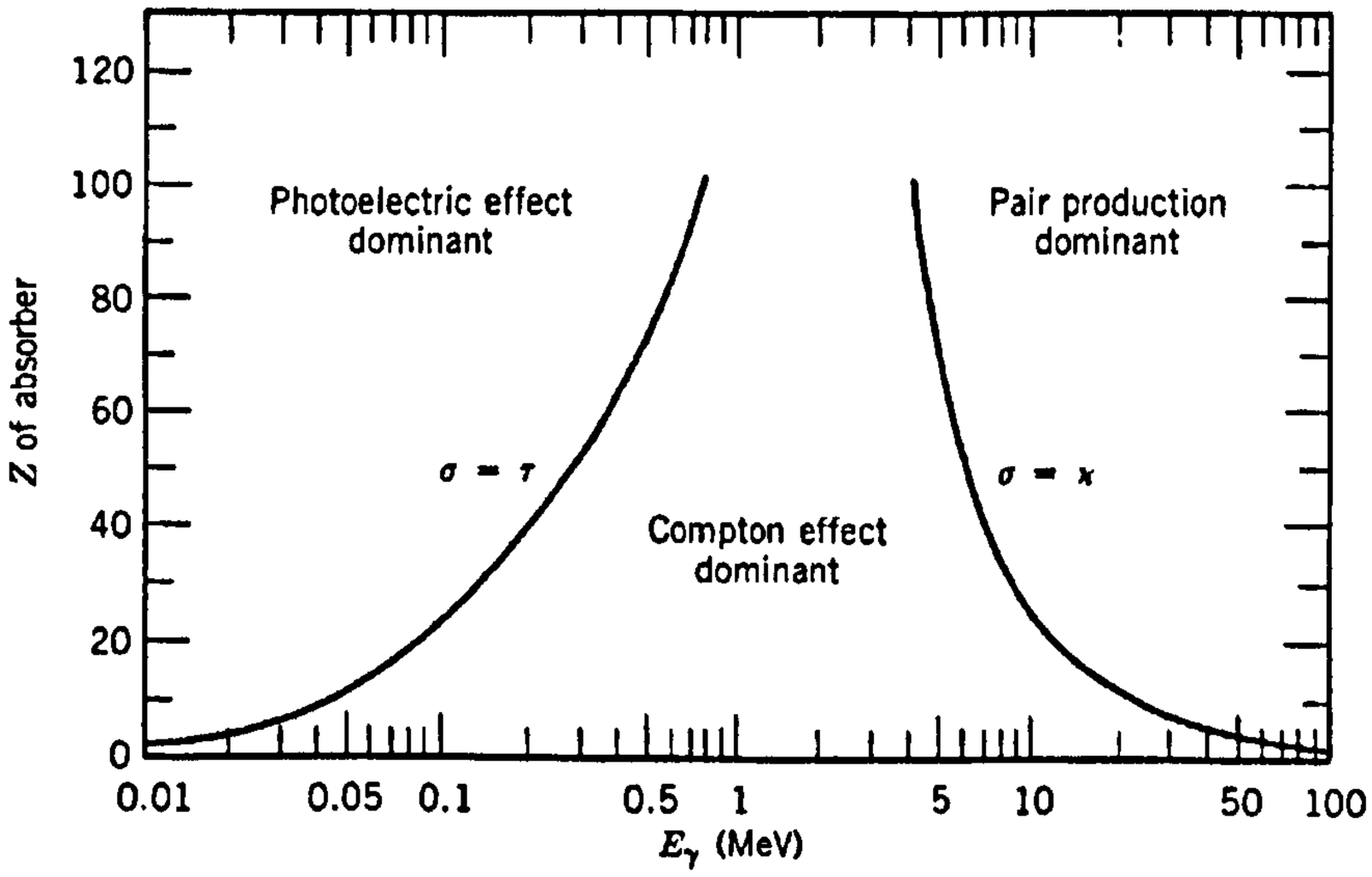

Figure 3.6: The three main γ-ray interaction processes with matter and their energy regions of dominance. Figure taken from Ref [17].

3.3 Clover Detectors

A type of composite Ge detector, the clover detectors (figure 3.7), work in a similar principle to that of the single-crystal HPGe detectors, but are comprised of four 25 % efficient HPGe detectors housed in a single CSS casing [49, 50]. Advantages include a smaller opening angle per crystal and the reduced crystal dimensions in comparison to the HPGe detectors, both of which contribute markedly to the higher position sensitivity and improved time and energy determination. The high Compton scattering probability out of the crystal, as well as the sharing of the electrical noise with the neighbouring crystals reduce the sensitivity of the detector for higher energy γ-rays.

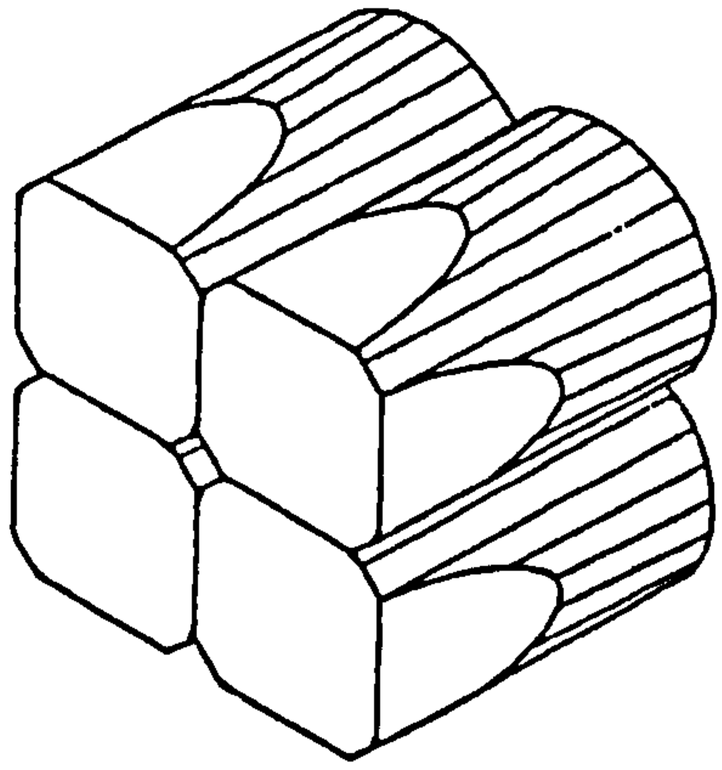

Figure 3.7: Schematic diagram of a clover detector. Figure taken from Ref [51].

Incident γ-rays which Compton scatter through multiple elements of a composite detector experience successive interactions with the detector's atomic electrons. The need for the $add-back$ correction therefore arises due to this partial deposition of γ-ray energy over multiple elements. The most probable Compton scattering through the elements by an angle θ is governed by the Klein-Nishina Formula [17], and is expressed as [47]

$$\frac{d\sigma_{KN}}{d\Omega} = r_0^2 \left[\frac{1}{1+\alpha(1-cos\theta)}\right]^2 \left[\frac{1+cos^2\theta}{2}\right] \left[1+\frac{\alpha^2(1-cos\theta)^2}{(1+cos^2\theta)[1+\alpha(1-cos\theta)]}\right], \tag{3.22}$$

where α is the photon energy in the electron rest energy ($\alpha = E_\gamma/M_e c^2$), and $r_0 = 2.818$ fm. Two polar plots produced using the formula above are shown in figure 3.8.

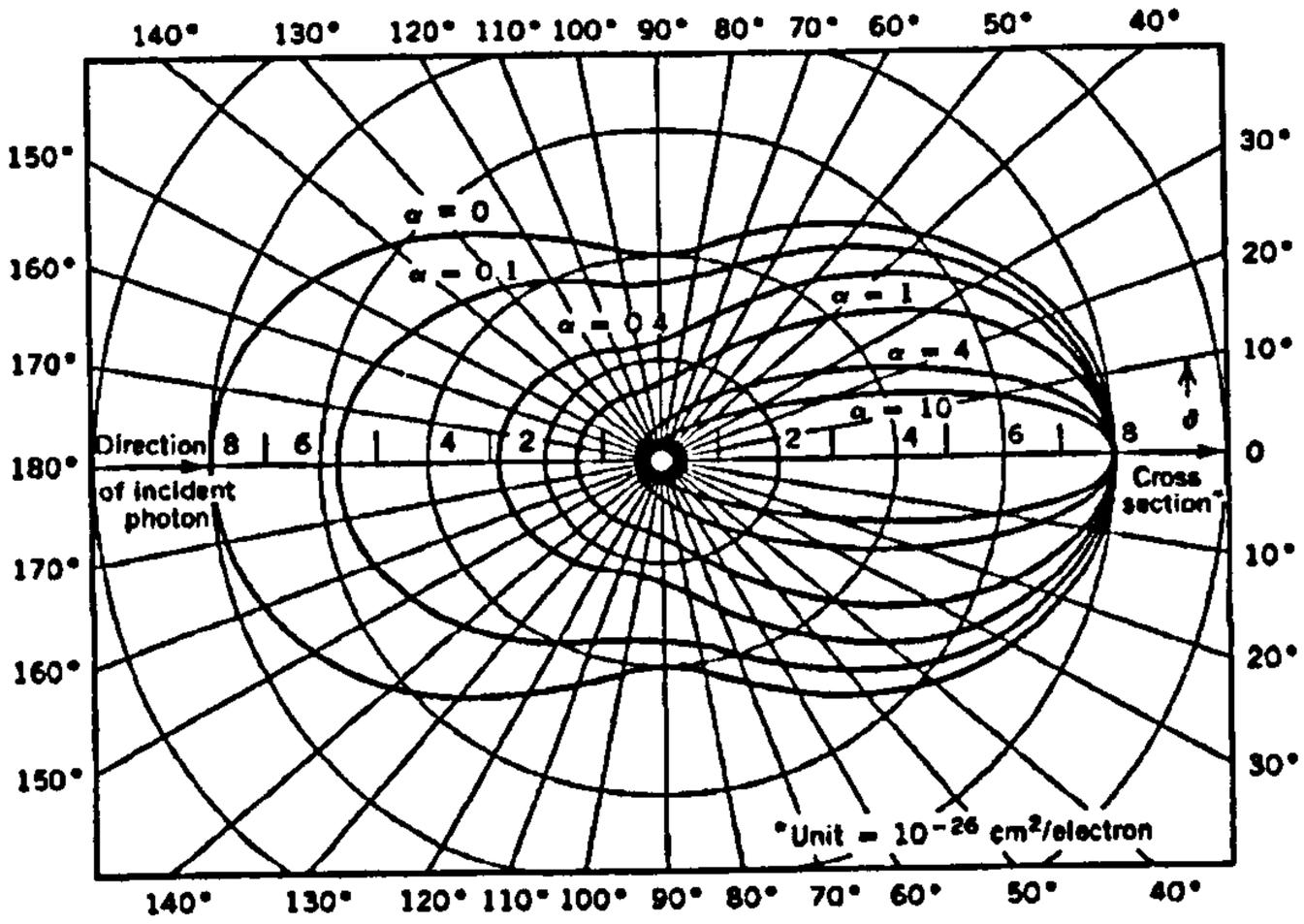

Figure 3.8: Klein-Nishina curve for the Ge detectors. Figure taken from [17].

For a composite detector, the full energy of a γ-ray can be recovered, however, if the individual hits are summed together and corrected for the Doppler effects appropriately. Furthermore, the total photopeak efficiency (ϵw) is enhanced as compared with the photopeak efficiency of a single element detector, $(\epsilon w)_D$, by the add-back contribution $(\epsilon w)_{AB}$. The total photopeak efficiency (ϵw) can therefore be written as the product of $(\epsilon w)_D$ and the add-back factor, F [49], such that

$$(\epsilon w) = (\epsilon w)_D + (\epsilon w)_{AB} = (\epsilon w)_D \times [1 + f] = (\epsilon w)_D \times F, \tag{3.23}$$

where the additional factor 'f' is given by

$$f = \frac{(\epsilon w)_{AB}}{(\epsilon w)_D}, \tag{3.24}$$

and the add-back factor F $= 1 + f$ is larger or equal to one [49].

Once the add-back correction has been performed, the doppler shift correction can be applied. The output energy of $m-$fold scattered events in a

clover detector can be expressed as

$$E_{add} = \frac{1}{1 + \left(\frac{v}{c} \times \cos\theta\right)} \sum_{n=1}^{m} F_{E_n}^{c_n} E_n, \tag{3.25}$$

where m is the multiplicity of the clover event, E_n is the energy of hit n in capsule c_n, $F_{E_n}^{c_n} E_n$ is the gain-matching function for the energy E_n in capsule c_n. Here, the angle θ is often taken to be the mid-point of a clover element, where the energy of the largest proportion was detected in a single scattering event. Taking of angle θ of the largest signal as above can be justified from the Klein-Nishina formula (3.22), since the cross-section of scattering into neighbouring detectors is higher for low-energy photons.

3.4 HPGe Detector Arrays

A single crystal germanium detector has an excellent resolution (typically ~2 keV for a 1.3 MeV γ-ray), but has a poor spectral response when operated alone. By constructing an *array* of the HPGe detectors or the composite detectors, such as the YRASTBALL [52] (see section 3.4.1) and the GAMMASPHERE array [53] (see section 3.4.3), dramatic improvements in the spectral selectivity and the sensitivity, can both be achieved through increased detection efficiency and γ-ray multi-fold coincidence capability. Modern γ-ray studies can now detect reaction channels in a ~few μb range of cross-section and up to ~60 $\hbar$ within a band [54].

The high spin, thin-target γ-ray spectroscopy employing fusion-evaporation and deep inelastic reactions demands a highly efficient and granular HPGe detector array which can minimise the effect of Doppler broadening, from which the γ-rays suffer, when they are emitted from a moving recoil. The amount of Doppler shift in energy for a given γ-ray, E_0, is dependent on the angle θ between the detector to the recoil direction, such that [17]

$$E_s(\theta) = E_0 \frac{\sqrt{1-\beta^2}}{1-\beta cos\theta}, \tag{3.26}$$

Figure 3.9: Schematic of a few closely packed GAMMASPHERE detectors. Figure taken from Ref [55].

where E_s is the shifted γ-ray energy. Since the Doppler shift has an angular dependence, accurate Ge detector angles with respect to a target were required and these can be determined from a known reaction γ-ray energy.

The Doppler effect also leads to the 'Doppler broadening' of spectroscopic peaks. This effect arises due to the finite opening angle $\Delta\theta$ subtended by the Ge crystal with respect to the beam direction, z, and also to the change in the recoil direction within a recoil cone. Approximating equation 3.26 to $E_s \simeq E_0(1 + \beta cos\theta)$ and then by differentiating it gives

$$\Delta E_s \approx E_0 \Delta\beta cos\theta - E_0 \beta sin\Delta\theta. \tag{3.27}$$

Uncertainties in the recoil velocity $\Delta\beta$ are mainly due to the variation in the number and energies of the particles evaporated.

For a Ge detector array, the Doppler broadening effect degrades the resolving power, R, through the worsening energy resolution, ΔE_{γ}^{tot}, as [56]

$$R = \left(\frac{S_{E_\gamma}}{\Delta E_{\gamma}^{tot}} PT \right), \tag{3.28}$$

where S_{E_γ} is the average separation of γ-ray peaks, PT is the peak-to-total ratio, and ΔE_{γ}^{tot} is [56]

$$\Delta E_{\gamma}^{tot} = (\Delta E_{int}^2 + \Delta E_D^2 + \Delta E_R^2 + \Delta E_V^2)^{1/2}. \tag{3.29}$$

Here, ΔE_{int} is the intrinsic resolution of the detector, ΔE_D is the Doppler broadening due to finite detector opening angle, ΔE_R arises due to the recoil kinematics, and ΔE_V is the Doppler broadening resulting from the energy variation of the recoils. In many cases, the dominant effect is the opening half-angle of the detector. Typically, efforts are made to keep this below 6°, so that the degradation in the array resolution may be minimised by having a large granularity. The resulting resolution for an array of the detectors depends on the average of the contributions from the detectors at different angles.

The high fold coincidence utility made possible through highly granular arrays helps to reduce the uncorrected background under a F-dimensional peak of width ΔE_γ as [57]

$$N_b = \left(\frac{\Delta E_\gamma}{S E_\gamma} \right)^F \frac{N_{un}}{M_\gamma^n}, \tag{3.30}$$

where N_b is the number of uncorrelated background counts below the peak, N_{un} is the initial number of uncorrelated background counts before coincidence gating, and M_γ^n is the number of transitions within a cascade under

study. The above relation reveals the effect of the diminishing area of uncorrelated background counts with increasing γ-ray folds, while the area under the peak remains concentrated in a smaller volume of ΔE_γ.

3.4.1 YRASTBALL Germanium Detector Array

The Yale Rochester Array for SpecTroscopy (YRASTBALL) [52], located at the WNSL, Yale University, USA, is designed to accommodate up to 30 Compton suppressed HPGe detectors, including 9 clover detectors. The total photopeak efficiency of the full array is ~3 % [52]. The Ge detectors in the YRASTBALL are mounted in four rings at 160° (5 detectors), 126° (8), 90° (9), and 50° (8) with respect to the beam axis. The detectors mounted on the non-90° rings are ~25 % efficient relative to a standard 7.6 cm × 7.6 cm NaT(Tl) detector each, and surrounded by their own anti-Compton BGO shields. The clover detectors, exclusively mounted in the 90° ring, have a larger efficiency of ~150 % with respect to the standard NaT(Tl) detector, where the total peak efficiency is the sum of four leaf detectors in add-back mode (see section 3.3).

3.4.2 YRASTBALL Electronics

The electronics system used NIM-standard nuclear spectroscopy modules as schematically shown in figure 3.11. The signal from the germanium detectors is split into two, one channel is used to determine the γ-ray energy, the other is for timing purposes. The energy signals from γ events in a germanium crystal were pre-amplified and amplified by a spectroscopy amplifier. The output from the spectroscopy amplifier is then fed to an analogue-to-digital converter (ADC) where it can be processed by the data acquisition system.

The time signals from a germanium crystal were pre-amplified and passed

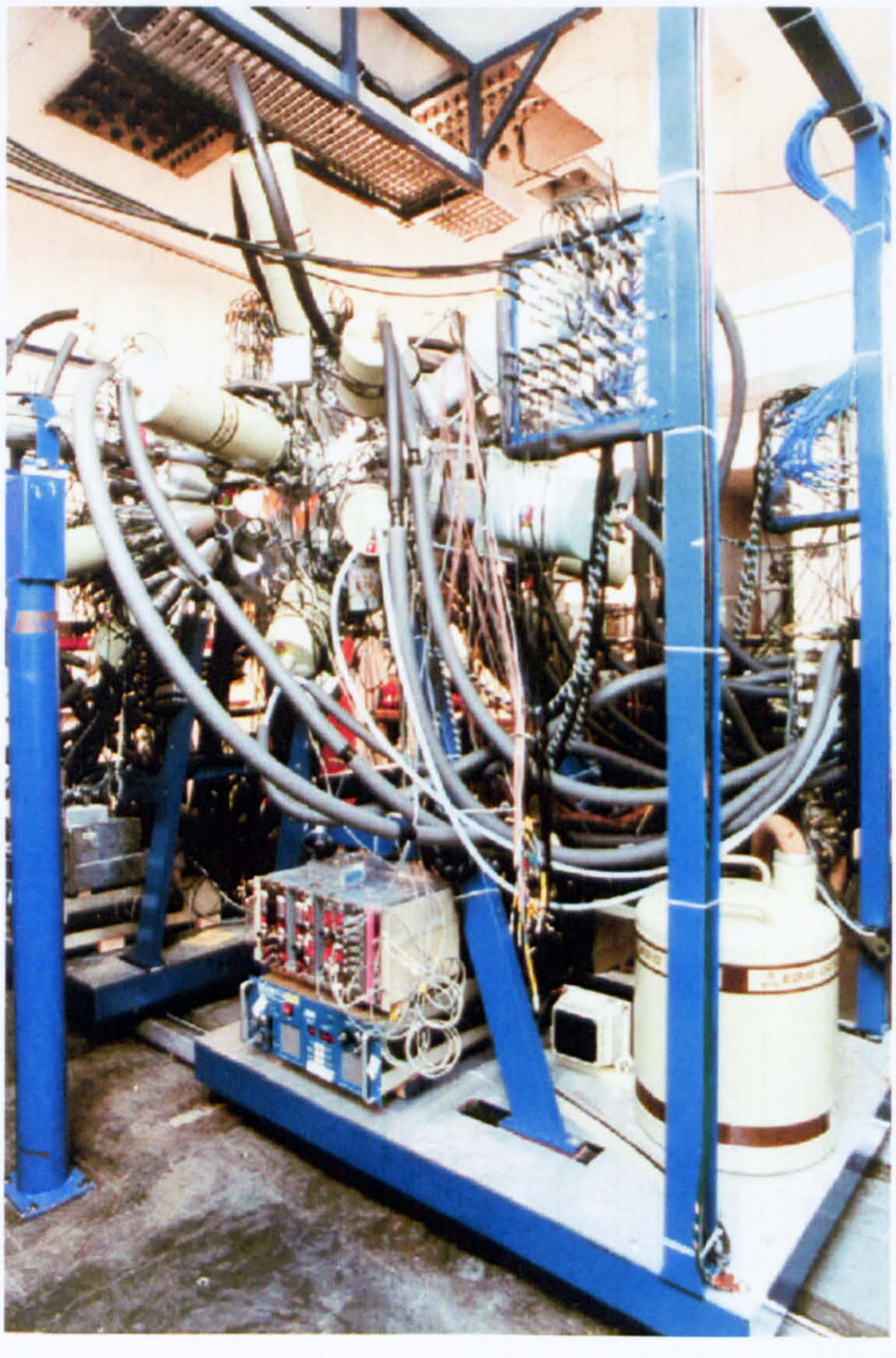

Figure 3.10: Photograph of the YRASTBALL HPGe detector array.

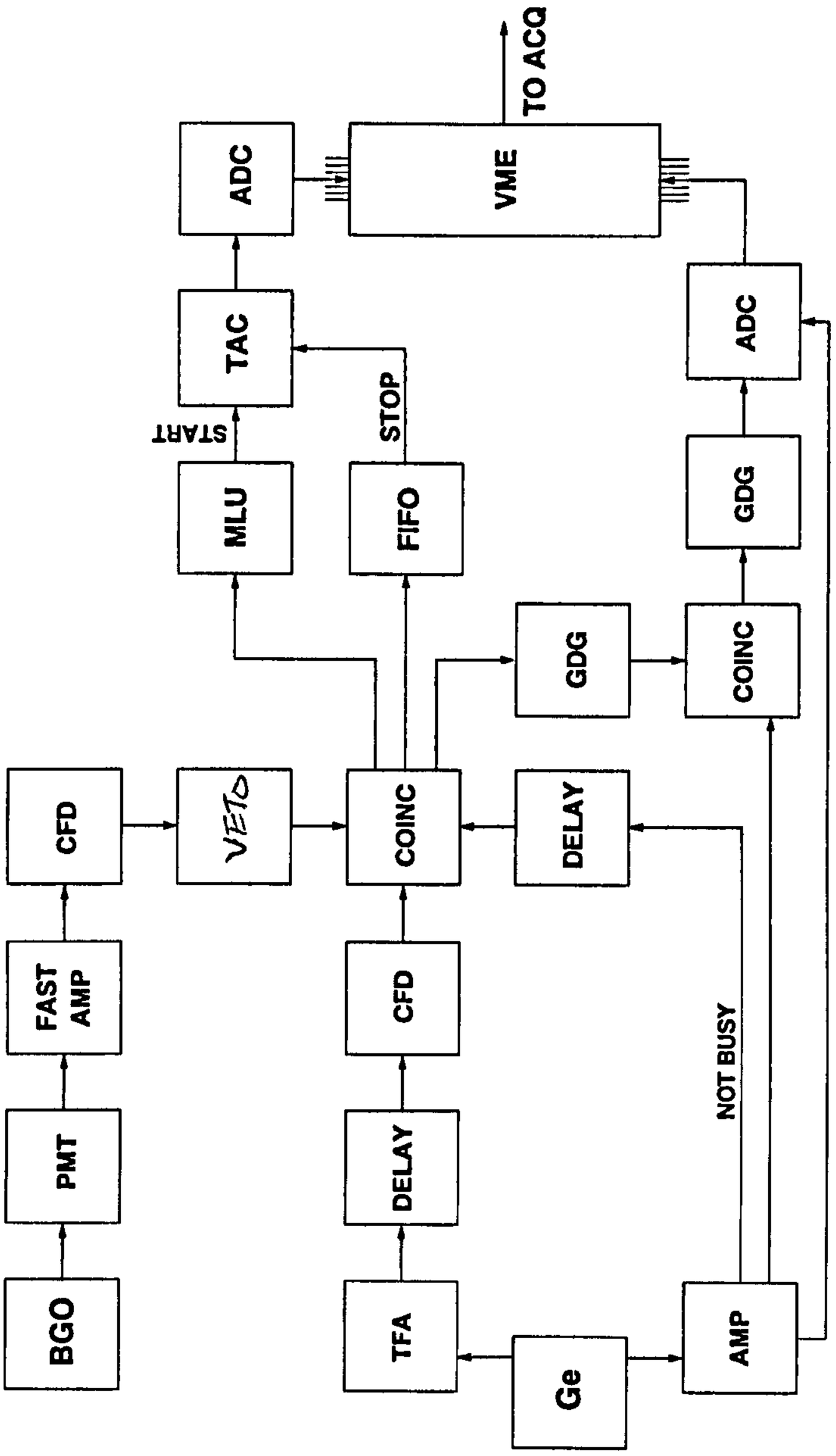

Figure 3.11: Electric circuit diagram of the YRASTBALL.

through a Timing Filter Amplifier (TFA) in order to provide a fast amplified signal for timing purposes. The TFA output was converted into a fast logic pulse using a Constant Fraction Discriminator (CFD). This produced a timing pulse for any signal that exceeded a low level threshold which was set to remove noise. The logic signal from the CFD is then fed to a coincidence unit which has two other inputs. These are an input from the BGO suppression shield which vetos Compton scattered events and a signal from the spectroscopy amplifier which is present when the amplifier is not processing an event ("not-busy"). The not-busy is used to reject "pile-up" events, that is if two γ-rays are detected by an individual germanium crystal in a short space of time (such that the energy of the two γ-rays are summed in the amplifier), then the event is not processed by the system. The coincidence unit only gives an output if both of these signals are present. The output of the coincidence unit is fed to a multiplicity logic unit (MLU) and a fan in/fan out unit (FIFO). The MLU only gives an output logic signal if the number of inputs present, n, is greater than a threshold. In this experiment the threshold was set to n $\geq$ 3 and the output from the MLU was used to start the γ-γ-γ master gate fed from the time-to-amplitude converter (TAC). The FIFO is used to provide a logical OR of all the germanium detectors, and gives a signal that a γ-ray has been detected. The output from the FIFO is then used as a stop signal for the γ-γ-γ TAC . The time-to-amplitude converter records the time difference between the stop and start signals that are fed to it .

The further processing of events is controlled by the data acquisition code. The task of the acquisition code, which runs on a Linux workstation, is to read data from the VME modules, construct events from this data, and save these events to disk and/or transmit them to the online sorting code which runs on the same workstation.

3.4.3 GAMMASPHERE Germanium Detector Array

The full GAMMASPHERE was housed at the Lawrence Berkeley National Laboratory, CA (USA), and was comprised of 110 HPGe detectors in a hexagonal/honeycomb shape. Each detector module is 71 mm in diameter, >80 mm in length, and has a BGO suppression shields plus cylindrical BGO backplugs behind the detector. The detector half opening angle is 7.4° (0.418 % of 4π), which for 110 detector modules yield a total Ge coverage of 46 % of 4π. The Ge detectors are positioned as summarised in Table 3.1.

For the 80 Ge detectors at a θ angle of $\geq 50°$ with respect to the beam axis, a two-fold segmentation can yield an effective detector half opening angle of 3.7°, and can provide a two-fold increase in the resolving power in comparison to the full 110 Ge detector arrangement without this segmentation facility. The full GAMMASPHERE geometry gives a total peak efficiency of 9.4 % and a resolution (FWHM) of ~2.1 keV for a 1.3 MeV γ ray [57].

The signal processing for the Ge detectors are provided by pre-amplifiers which are mounted directly on the detectors and on the BGO phototube bases. They are connected to an interface unit, which also is attached to each Ge/BGO module, and performs monitoring operations. The output signals from the interface are processed at the nearby VXI crates, in which the histogrammers, the event builder, and the data-storage system can be setup to incorporate the data from ancillary detectors, such as the CHICO detector (see section 3.5).

3.5 CHICO Detector Array

The 4π position-sensitive heavy-ion (HI) detector, CHICO [58], is comprised of two hemispherical assemblies of 10 PPACs each, arranged in a truncated

Table 3.1: The THETA angle is the polar angle with respect to the Z axis pointing along the beam. PHI is the azimuthal angle with respect to the coordinate system where the X axis is pointing into the ground and the Z axis is the direction of the beam.

THETA (θ°)	PHI (ϕ°)				
17.3	72.0	144.0	216.0	288.0	360.0
31.7	36.0	108.0	180.0	252.0	324.0
37.4	72.0	144.0	216.0	288.0	360.0
50.1	22.8	49.2	94.8	121.2	166.8
	193.2	238.8	265.2	310.8	337.2
58.3	72.0	144.0	216.0	288.0	360.0
69.8	18.5	53.5	90.5	125.5	162.5
	197.5	234.5	269.5	306.5	341.5
79.2	72.0	144.0	216.0	288.0	360.0
80.7	36.0	108.0	180.0	252.0	324.0
90.0	18.0	54.0	90.0	126.0	162.0
	198.0	234.0	270.0	306.0	342.0
99.3	72.0	144.0	216.0	288.0	360.0
100.8	36.0	108.0	180.0	252.0	324.0
110.2	17.5	54.5	89.5	126.5	161.5
	198.5	233.5	270.5	305.5	342.5
121.7	36.0	108.0	180.0	252.0	324.0
129.9	13.2	58.8	85.2	130.8	157.2
	202.8	229.2	274.8	301.2	346.8
142.6	36.0	108.0	180.0	252.0	324.0
148.3	72.0	144.0	216.0	288.0	360.0
162.7	36.0	108.0	180.0	252.0	324.0

cone, and is positioned coaxially with respect to the beam direction. The housing for the PPACs is a 1.58 mm thick aluminium hemisphere shell 35.6 cm in diameter, and each PPAC is mounted in fixtures epoxied to the inside of the hemisphere. A pressure window made from 0.9 μm (120 μg/cm^2) thick mylar contains the detector grade isobutane gas at 4 Torr from the high vacuum target chamber. All ten PPACs in a single hemisphere share a common gas volume.

The main body of each PPAC is comprised of an anode film with two-fold segmentation glued to a frame above a cathode board using a 3.2 mm thick spacer. The two electrically separated sections of the anode provide ϕ-angular coverages of 9.3° and 18.6°, while 1° wide tracers covered the cathode board. When a charged particle is detected, time signals from the anode and the cathode were carried to an amplifier by a transmission line carrying a 400 V bias voltage. Amplifiers with 500 MHz bandwidth are found to be sufficient to ensure that the rise time of each signal is not profoundly degraded during amplification.

For a pair of projectile-like and target-like fragments produced in a binary reaction, two-body kinematics (see section 5.3) demand the pair to be co-planar in ϕ, so that the geometrical combination of the small and large segments of the PPAC anodes set this resolution to $\Delta\phi \sim \pm 4.7°$ (see figure 3.12). The θ angle is obtained from the two detector signals travelling in the opposite direction along a delay line, the time difference of which determines the location of an event within a PPAC segment.

The CHICO timing signal associated with the anode of each PPAC had a detection rate of ~500 ps and an arbitrary zero offset. The offsets were different for each anode due to the variation in the resistivity of the delay line leading to the TDCs. The largest uncertainty in the time measurement

is known to arise from the varying size of the beam spot [58]. The total angular coverage of the CHICO detector used for the ^{100}Mo + 700 MeV ^{136}Xe study was $20° < \theta < 70°$ and $0° < \phi < 280°$, or ~17 % of 4π. The presence of the detector had a shadowing effect on the GAMMASPHERE, however. Simulations modelling of the shadowing effect of the CHICO detector on the response of the GAMMASPHERE array found this reduction in the peak-to-total ratio to be approximately 7 % down from 58.3 % (without the CHICO detector present) to 51.3 % (with CHICO present) for a 1.33 MeV γ-ray [58].

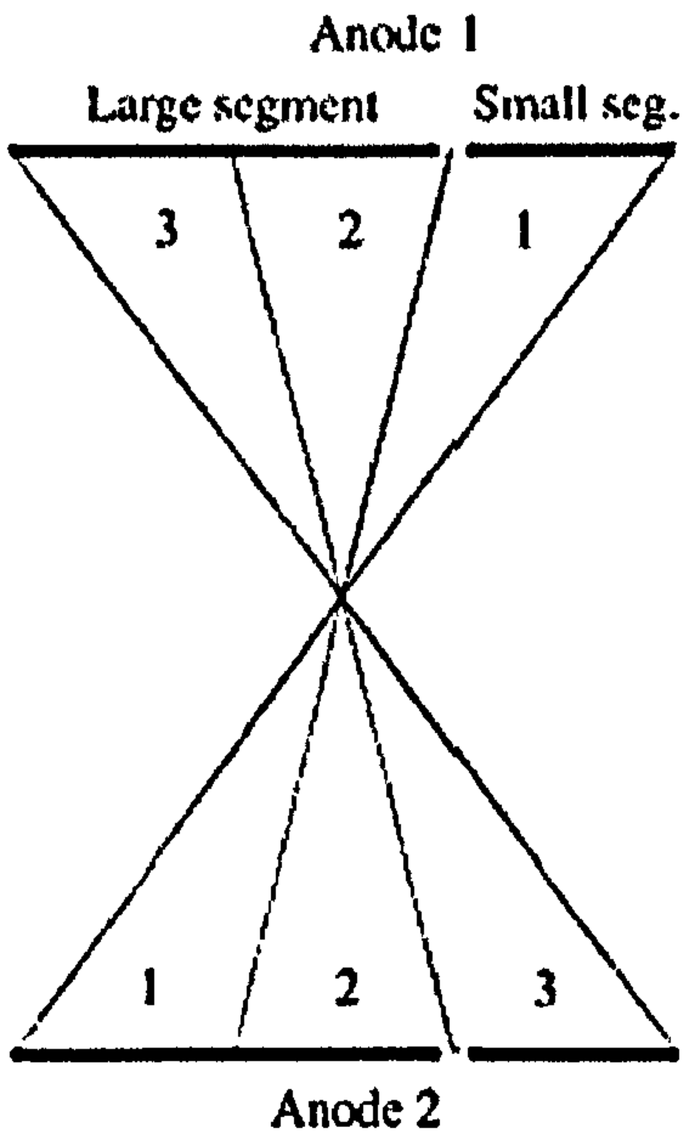

Figure 3.12: Co-planar PPACs arrangement used for the ϕ resolution, as utilised by the CHICO detector. Figure taken from Ref [58].

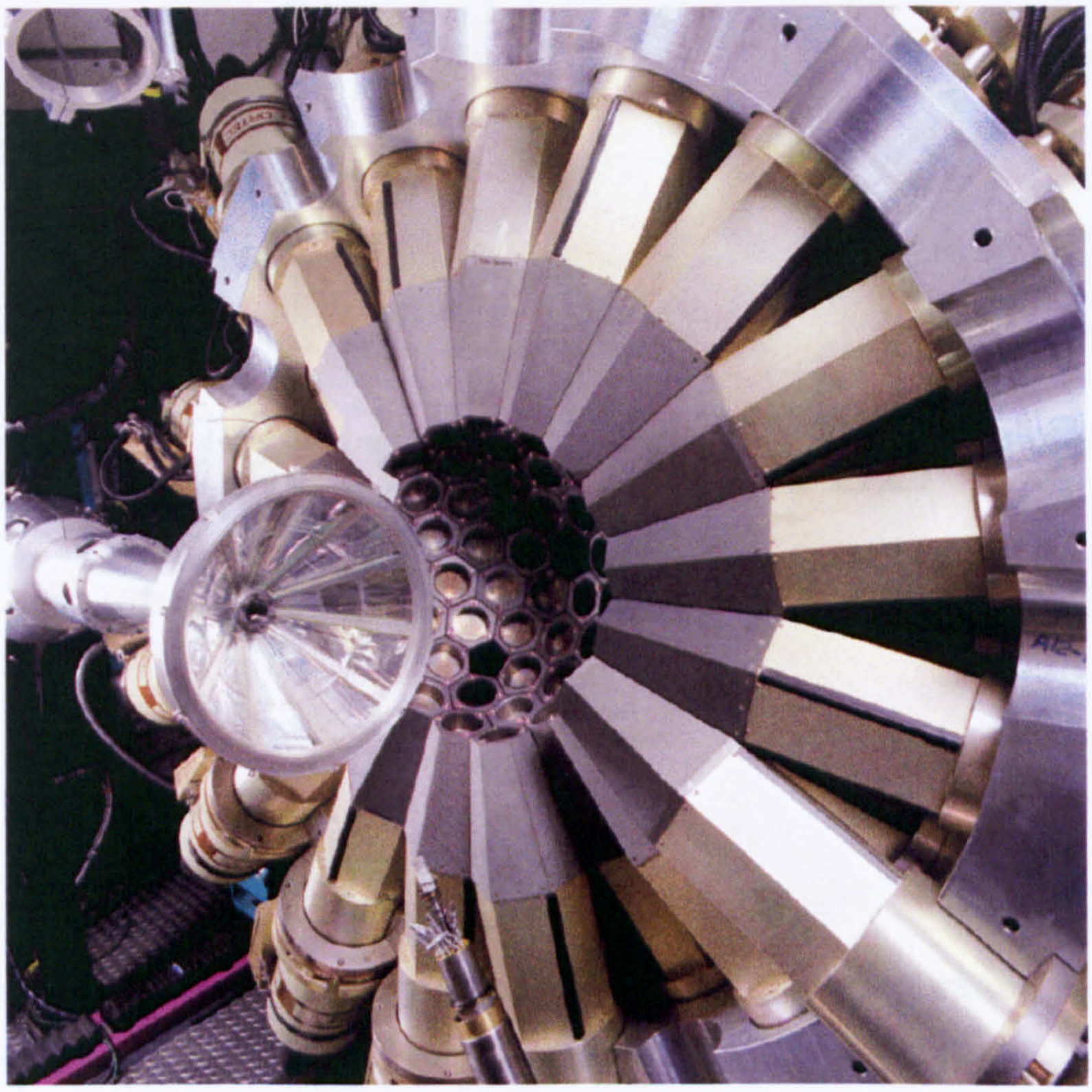

Figure 3.13: Photograph of the CHICO detector with one-half of the GAMMASPHERE HPGe detector array.

Chapter 4

$^{96}_{40}$Zr + $^{9}_{4}$Be YRASTBALL Experiment

4.1 Introduction

The high-spin states were populated using the fusion-evaporation reaction between a ^{96}Zr target and a ^{9}Be beam at 46 MeV. The DC beam was provided by the WNSL Tandem Accelerator at Yale University, CT (USA), and impinged on a target consisting of an isotopically enriched ($\sim$ 85%) metallic zirconium foil of thickness 670 μg/cm^2 mounted on a 5 mg/cm^2 lead backing. The target was placed with the lead backing facing the beam, hence allowing the residual nuclei of interest to recoil into vacuum. A lead collimator, with a 2 cm diameter exit hole, was placed approximately 4 cm behind the target position in order to protect the target chamber from unwanted reactions induced by the beam particles scattered by the target. The beam nuclei with initial energy of 46 MeV were calculated to lose $\sim$2 MeV in the lead support layer, leading to an 'on-target' laboratory energy of approximately 44 MeV. This corresponded to a classical maximum angular momentum transferred

to the compound system of $\sim 22\hbar$.

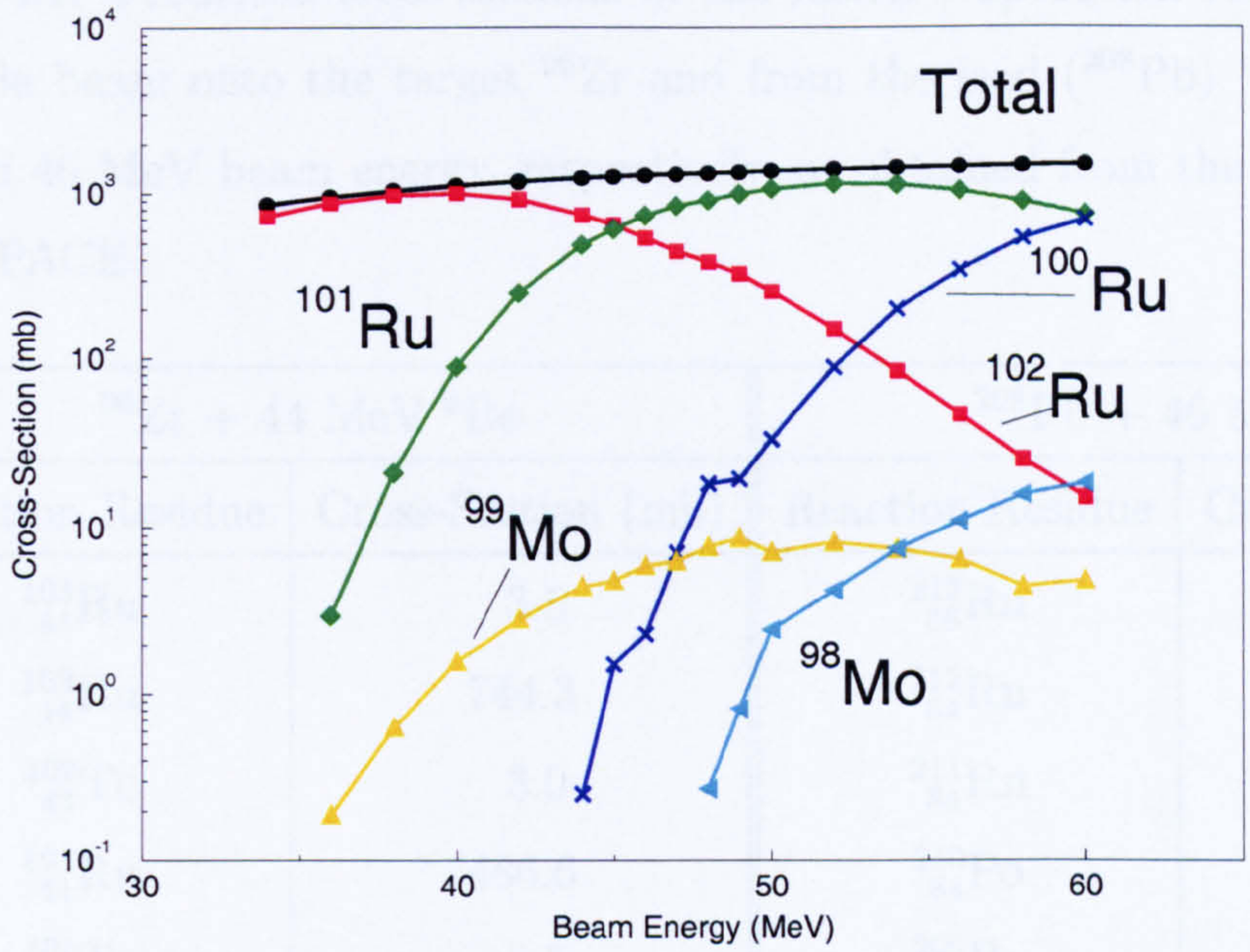

Figure 4.1: Calculated cross-sections for Ru- and Mo-isotopes, as obtained by PACE [59] code. Total cross-section for the compound nucleus formation was also calculated.

The reaction gamma-rays were detected using the YRASTBALL array, which in this experiment comprised of six, four-element clover detectors at 90° to the beam direction, together with five smaller (25%) co-axial germanium detectors at 50°, 126°, and three more at 160°. The acquisition master gate was set such that 'good' events were defined as the detection of at least three gamma rays within 200 ns of each other, and the required γ-ray energy and time were written to magnetic tapes for subsequent off-line analysis. Typical on-target beam currents were between two and four particle nanoamps, and were supplied for the duration of two days. This resulted in master event ($\geq \gamma^3$) rates of between 500 and 1000 Hz, leading to a total of 425×10^6, unfolded γ-γ coincidence events.

Table 4.1: Predicted cross-sections of the fusion-evaporation residues from the ^{9}Be beam onto the target ^{96}Zr and from the lead (^{208}Pb) 'backing' at 44 and 46 MeV beam energy, respectively, as obtained from the calculation code, PACE.

^{96}Zr + 44 MeV ^{9}Be		^{208}Pb + 46 MeV ^{9}Be	
Reaction Residue	Cross-Section (mb)	Reaction Residue	Cross-Section (mb)
$^{103}_{44}$Ru	3.5	$^{213}_{86}$Rn	2.6
$^{102}_{44}$Ru	744.3	$^{212}_{84}$Rn	341.4
$^{102}_{43}$Tc	3.0	$^{211}_{84}$Rn	26.6
$^{101}_{44}$Ru	486.6	$^{210}_{84}$Po	1.3
$^{101}_{43}$Tc	0.5	$^{209}_{84}$Po	8.8
$^{100}_{44}$Ru	0.3	$^{208}_{84}$Po	0.1
$^{100}_{42}$Mo	1.2		
$^{99}_{42}$Mo	4.5		

4.2 Gamma-Ray Corrections

The six clover detectors positioned at 90° with respect to the beam were physically separated into four individual detector units surrounded by anti-Compton shields. Such a composite detector allows the addition of signals from neighbouring detectors, the signals of which arise from the Compton scattered γ-rays, and enables to recover the total absorption events. Thus the total Compton background is reduced and the improved peak-to-total ratio enhances the photopeak efficiency simultaneously.

All germanium detectors were firstly gain-matched, and the add-back correction was made to the clover detectors in the 90° ring. The total relative

efficiency curves were hence obtained for the whole YRASTBALL array with and without the use of this add-back utility, and is shown in figure 4.2. The resultant calibration spectra are also shown in figure 4.3. The improved YRASTBALL efficiency in the add-back operation mode was found to be about 10 % higher in comparison to the operation mode without the add-back facility.

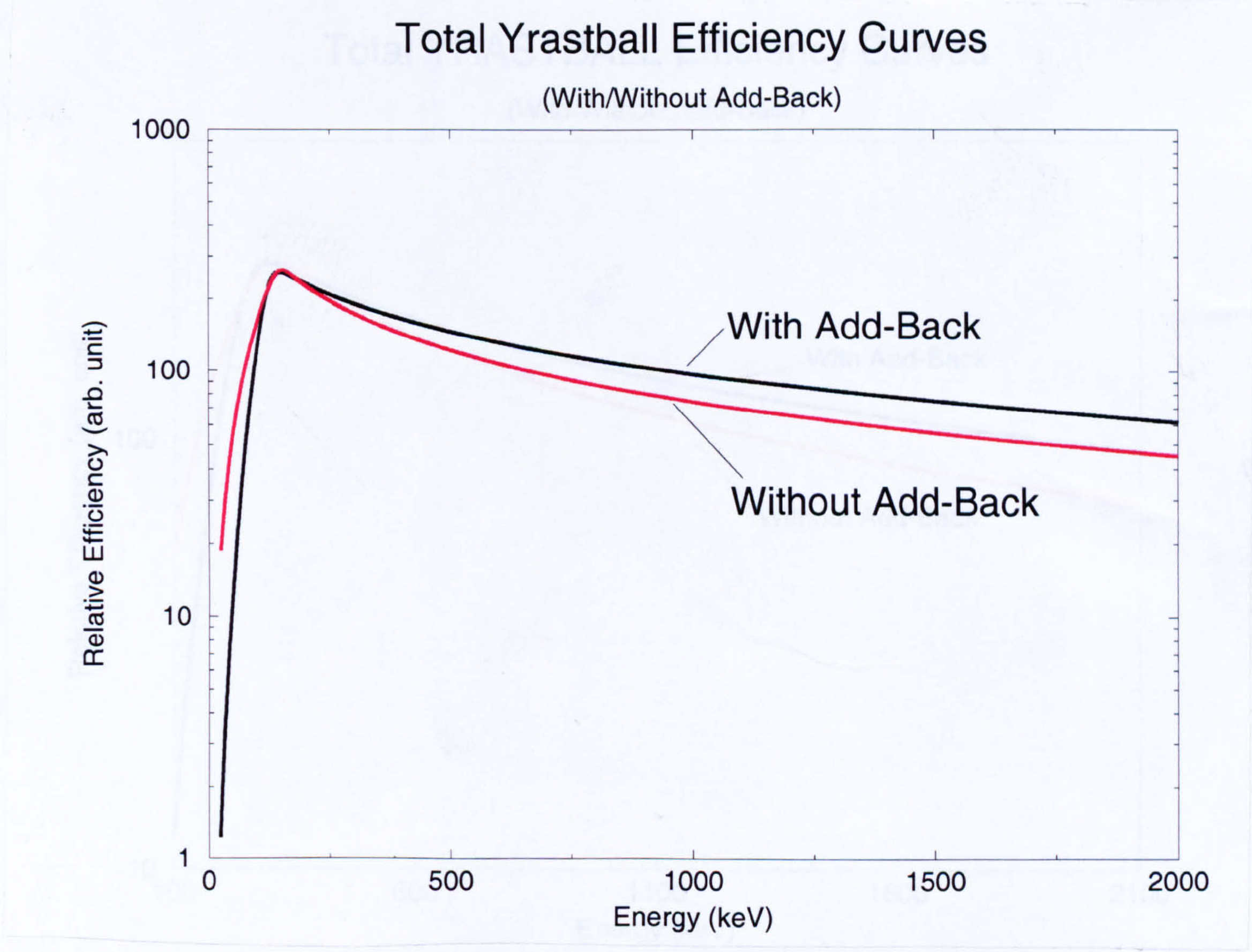

Figure 4.2: Comparison between the γ-ray efficiency curves with and without applying the add-back correction for the YRASTBALL array.

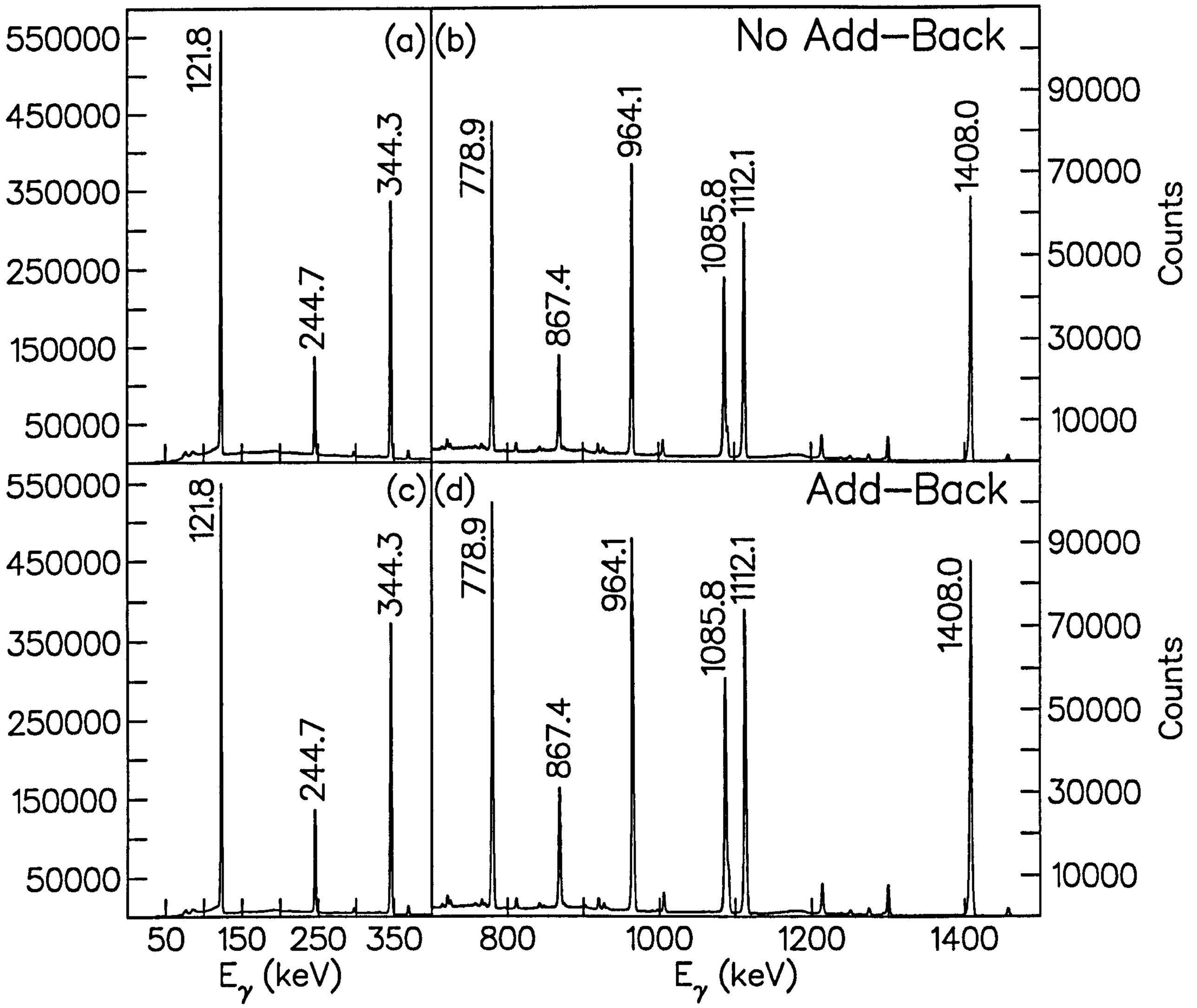

Figure 4.3: ^{152}Eu calibration spectra (a,b) without and (c,d) with the add-back correction, as obtained from the YRASTBALL clover detectors in the 90° ring.

Doppler corrections were subsequently applied to every Ge energy event in the gain-matched and add-back spectra. The velocity, β_{recoil}, of the reaction recoils were then calculated using a known γ-ray transition in ^{101}Ru using the equation 3.26. Figure 4.4 shows γ-ray spectra obtained from the present experiment, and the value of β_{recoil} was found to be $\beta_{recoil} = 0.61$ % of the speed of light. Effects of the Doppler shift are clearly shown, and the energy peaks originating from ^{101}Ru can be seen to move to lower energies for detector angles greater than 90° and increase in the observed energies for the detectors closer to 180°. Conversely for the energy peaks belonging to the stopped recoils (i.e. ^{214}Rn), they are shifted in energy when the Doppler correction was applied. Also, the effect of Doppler broadening can be seen in figure 4.4 as a larger peak width of 3.1 keV (FWHM) for the 664 keV transition associated with the ^{101}Ru, in comparison with the stopped 2.7 keV (FWHM) wide 694 keV peak belonging to ^{214}Rn.

4.3 Spin-Parity Assignments

Utilising the γ-ray coincidence technique, multipolarities of specific transitions can be identified using the DCO method (*Directional Correlation from Oriented states* [60, 61, 62]) on pairs of coincident γ-rays. By placing gamma-ray energy gates on transitions whose multipolarity had been previously established, DCO ratios were extracted in the present experiment from the Ge detector rings at 90° and 160° as

$$R_{DCO} = \frac{\text{I(160°) gated at 90°}}{\text{I(90°) gated at 160°}} \times \varepsilon \tag{4.1}$$

where I is the number of counts in a peak and ε is an efficiency multiplication factor which corrects the experimental value for the detection efficiencies of

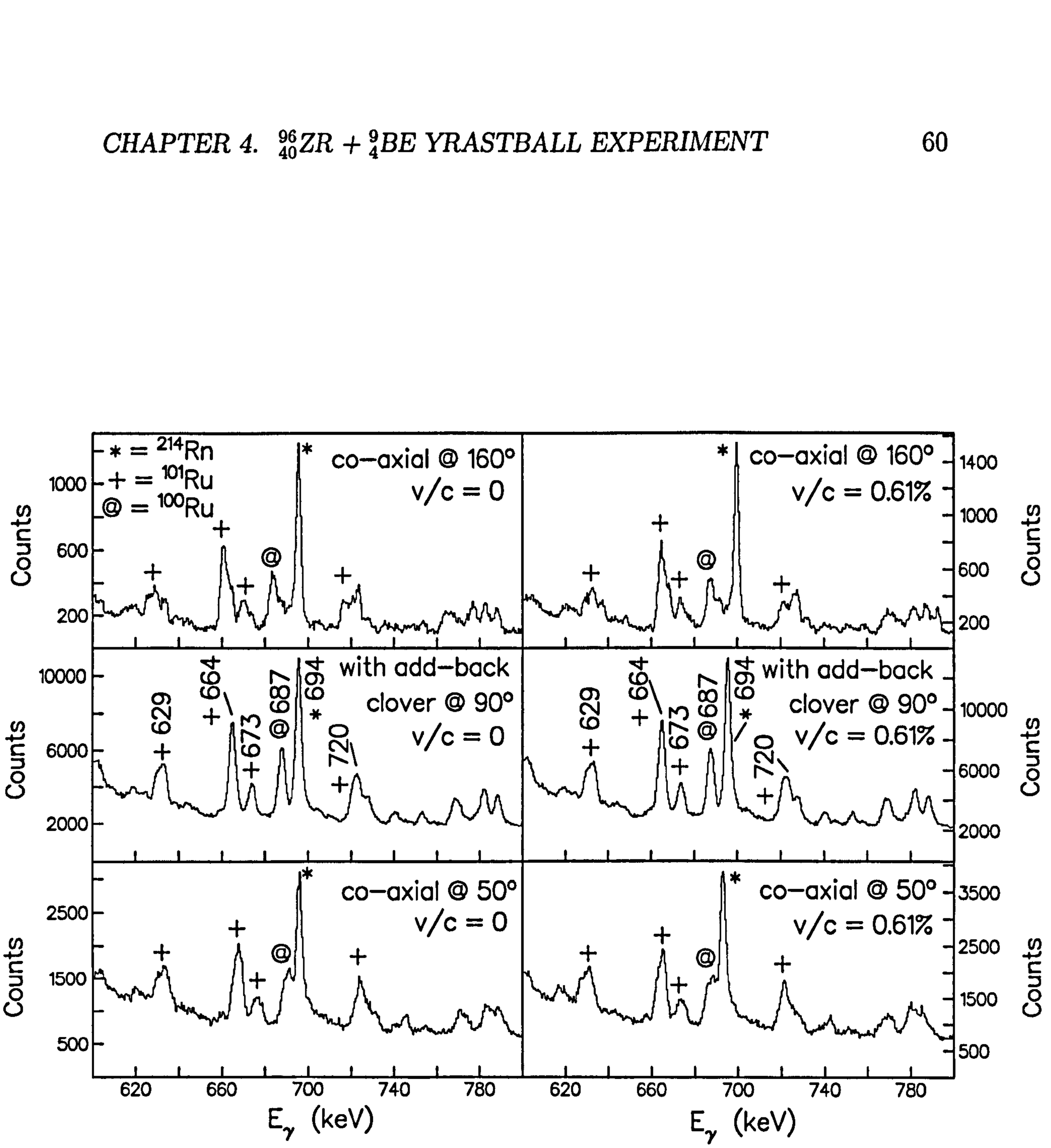

Figure 4.4: Comparison between the Doppler corrected (left) and uncorrected (right) spectra from the YRASTBALL detectors positioned at 50°, 90°, and 160°, as obtained from the current work.

both the gate and the projected transition. This factor is equal to

$$\varepsilon = \frac{\varepsilon_g\,(160°)\ \times\ \varepsilon_p\,(90°)}{\varepsilon_g\,(90°)\ \times\ \varepsilon_p\,(160°)} \tag{4.2}$$

where ε_g is the detection efficiency of the gate and ε_p is the detection efficiency of the projected transition.

The difference in the projected intensity of stretched quadrupole γ-rays (assumed to be of E2 character) and $\Delta I = 1$ transitions, when both are gated by an E2 transition, is clearly illustrated in figures 4.5. Typical values for the DCO ratio of ~1.0 and ~0.6 were found for stretched quadrupole and pure dipole transitions respectively, when gated by a stretched E2 transition. Where possible, the spin/parity assignments given in references [63] and [64] were assumed for the lower-spin members of all the decay schemes obtained in the present study.

The assumption that heavy-ion fusion-evaporation reactions preferentially populate near-yrast states has been applied and thus the spins were found to increase with increasing excitation energy. Figure 4.6 summarises the DCO ratio associated from the YRASTBALL experiment.

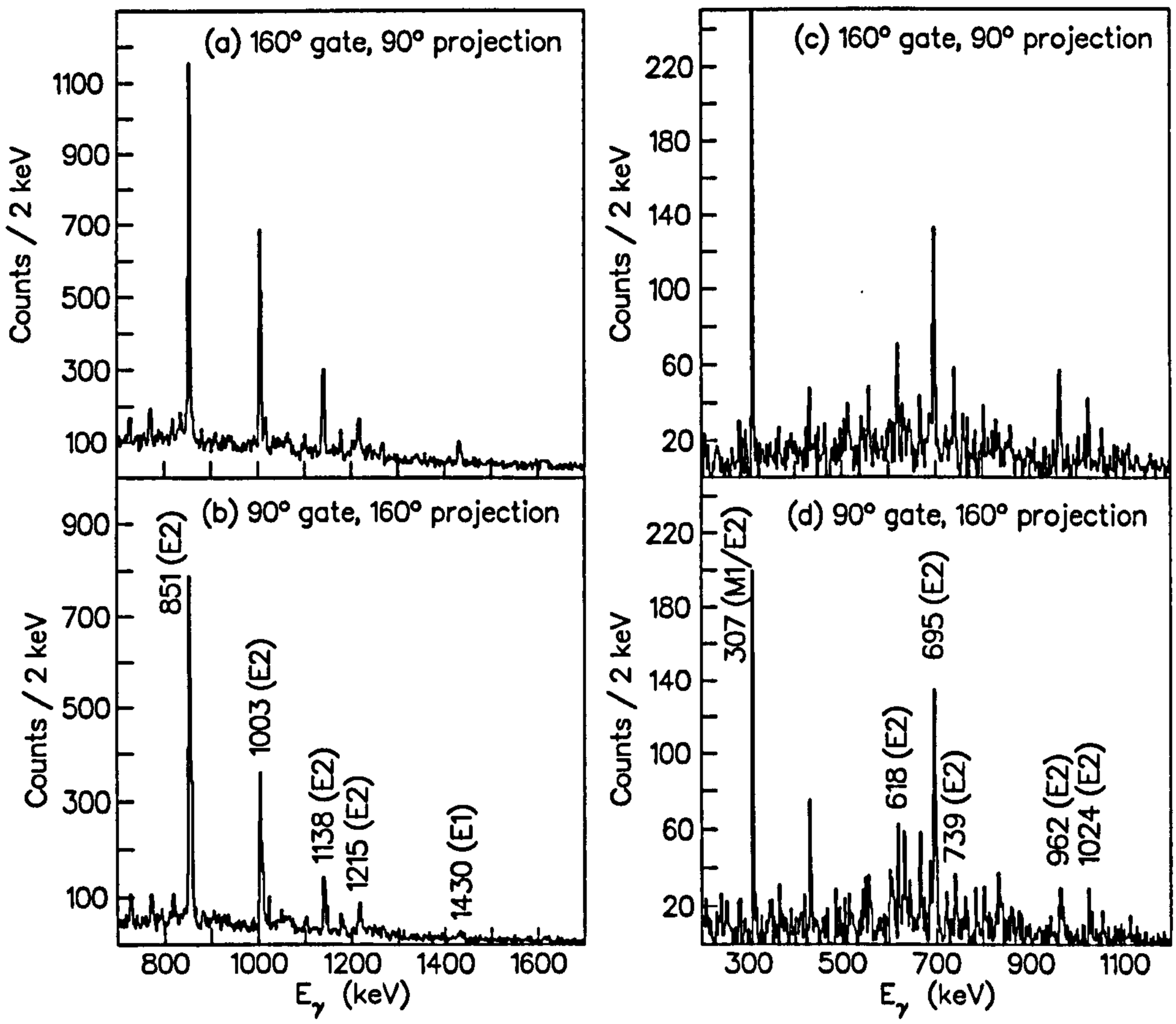

Figure 4.5: Typical sum of single gated spectra obtained for ^{101}Ru for the DCO analysis: (left hand side) Sum of the 431 keV and 664 keV (E2) gates belonging to band 3 from the (90,160) matrix; (right hand side) 861 keV gate in band 2. Note the relative intensities of the projected E2 and dipole (307 keV and 1430 keV) transitions (see Table 4.2 for specific ratio values).

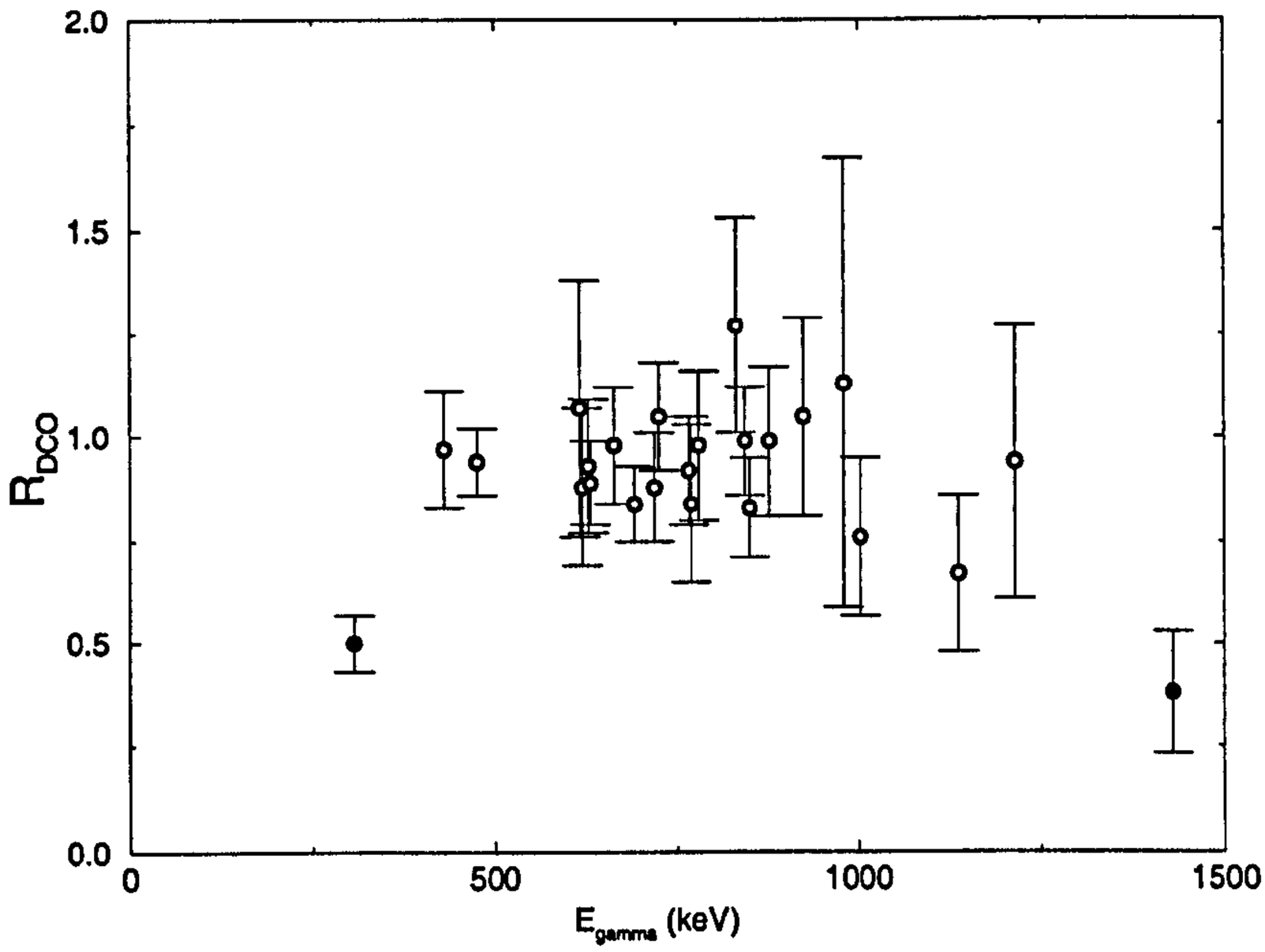

Figure 4.6: Extracted DCO ratio for transitions in ^{99}Mo and ^{101,102}Ru, using stretched E2 gates. The filled data points correspond to the 307 keV and 1430 keV transitions in ^{101}Ru, each of which is assigned as a stretched (ΔI = 1) E1 decay, while the empty points correspond to stretched ΔI = 2 (E2) decays.

Table 4.2: Gamma-ray transitions identified in ^{101}Ru from the current work. The γ-ray intensities (in arbitrary units) were taken from a 2-D fit to the $\gamma - \gamma$ coincidence matrix using the program ESCL8R [73].

E_γ (keV)	I_γ (arb.)	E_i, E_f (keV)	$J_i^\pi \rightarrow J_f^\pi$	R_{DCO}
175.3(3)	46(2)	720,545	$\frac{9}{2}^+, \frac{7}{2}^+$	
221.0(2)	254(10)	528,307	$\frac{11}{2}^-, \frac{7}{2}^+$	
281.0(5)	16(2)	1002,720	$\frac{11}{2}^+, \frac{9}{2}^+$	
307.4(2)	214(20)	307,0	$\frac{7}{2}^+, \frac{5}{2}^+$	0.50(7) [1]
363.0(5)	10(4)	1864,1501	$\frac{15}{2}^+, \frac{13}{2}^+$	
391.8(5)	16(4)	3444,3053	$\frac{23}{2}^+, \frac{21}{2}^+$	
413.7(4)	26(2)	720,307	$\frac{9}{2}^+, \frac{7}{2}^+$	
431.1(2)	586(22)	960,528	$\frac{15}{2}^-, \frac{11}{2}^-$	0.97(14) [2]
459.4(5)	22(2)	4141,3681	$(\frac{27}{2}^+), \frac{25}{2}^+$	
500.6(6)	14(2)	4183,3681	$\frac{27}{2}^+, \frac{25}{2}^+$	
516.4(6)	14(2)	4967,4451	$(\frac{31}{2}^+), \frac{29}{2}^+$	
545.1(4)	85(30)	545,0	$\frac{7}{2}^+, \frac{5}{2}^+$	
556.3(5)	12(4)	3444,2887	$\frac{23}{2}^+, \frac{19}{2}^+$	
571.4(4)	5(2)	5956,5375	$\frac{35}{2}^+, \frac{33}{2}^+$	
618.4(4)	38(4)	3444,2825	$\frac{23}{2}^+, \frac{19}{2}^+$	1.07(31)[1]
628.8(3)	80(4)	3681,3053	$\frac{25}{2}^+, \frac{21}{2}^+$	0.93(16)[3]
664.3(2)	542(16)	1624,960	$\frac{19}{2}^-, \frac{15}{2}^-$	0.98(14)[4]
673.4(3)	82(6)	3053,2379	$\frac{21}{2}^+, \frac{17}{2}^+$	
695.0(4)	186(8)	1002,307	$\frac{11}{2}^+, \frac{7}{2}^+$	
697.0(7)	20(2)	4141,3444	$(\frac{27}{2}^+), \frac{23}{2}^+$	

Table 4.2 (continued....)

E_γ (keV)	I_γ (arb.)	E_i, E_f (keV)	$J_i^\pi \rightarrow J_f^\pi$	R_{DCO}
720.1(3)	115(7)	720,0	$\frac{9}{2}^+, \frac{5}{2}^+$	0.88(13)[3]
739.2(3)	28(4)	4183,3444	$\frac{27}{2}^+, \frac{23}{2}^+$	
769.7(3)	52(6)	4451,3681	$\frac{29}{2}^+, \frac{25}{2}^+$	0.84(19)[3]
781.0(4)	180(6)	1501,720	$\frac{13}{2}^+, \frac{9}{2}^+$	0.98(18)[5]
815.8(8)	22(4)	3291,2475	$(\frac{27}{2}^+), \frac{23}{2}^-$	
826.6(7)	26(4)	4967,4141	$(\frac{31}{2}^+, \frac{27}{2}^+)$	
851.3(3)	310(10)	2475,1624	$\frac{23}{2}^-, \frac{19}{2}^-$	0.83(12)[2]
861.2(4)	88(6)	1864,1002	$\frac{15}{2}^+, \frac{11}{2}^+$	
878.0(3)	86(8)	2379,1501	$\frac{17}{2}^+, \frac{13}{2}^+$	0.99(18)[3]
923.7(5)	30(6)	5375,4451	$\frac{33}{2}^+, \frac{29}{2}^+$	1.05(24)[3]
961.7(4)	42(4)	2825,1864	$\frac{19}{2}^+, \frac{15}{2}^+$	
968.6(8)	10(2)	3443,2474	$\frac{23}{2}^+, \frac{23}{2}^-$	
979.0(8)	14(2)	5946,4967	$(\frac{35}{2}^+, \frac{31}{2}^+)$	
1003.1(3)	146(6)	3478,2475	$\frac{27}{2}^-, \frac{31}{2}^-$	0.76(19)[2]
1023.7(4)	16(2)	2887,1864	$\frac{19}{2}^+, \frac{15}{2}^+$	
1050.4(5)	16(2)	5233,4183	$(\frac{31}{2}^+, \frac{27}{2}^+$	
1094.2(5)	18(2)	6469,5375	$\frac{37}{2}^+, \frac{33}{2}^+$	
1130.4(8)	8(2)	7077,5946	$(\frac{39}{2}^+, \frac{35}{2}^+)$	
1138.2(3)	66(4)	4616,3478	$\frac{31}{2}^-, \frac{27}{2}^-$	0.67(19)[1]

Table 4.2 (continued....)

E_γ (keV)	I_γ (arb.)	E_i, E_f (keV)	$J_i^\pi \rightarrow J_f^\pi$	R_{DCO}
1181.0(1.0)	10(2)	3656,2475		
1206.2(8)	14(4)	3681,2474	$\frac{25}{2}^+, \frac{23}{2}^-$	
1209.8(6)	6(2)	7679,6469	$\frac{41}{2}^+, \frac{37}{2}^+$	
1214.7(3)	28(2)	5831,4616	$\frac{35}{2}^-, \frac{31}{2}^-$	0.94(33)[4]
1239.0(1.0)	14(2)	3714,2474		
1241.4(1.0)	3(1)	8318,7077	$(\frac{43}{2}^+, \frac{39}{2}^+)$	
1264.5(5)	8(2)	7096,5831	$\frac{39}{2}^-, \frac{35}{2}^-$	
1286.4(1.2)	4(1)	5903,4616	$(\frac{35}{2}, \frac{33}{2}), \frac{31}{2}^-$	
1323.5(7)	2(1)	9002,7679	$\frac{45}{2}^+, \frac{41}{2}^+$	
1337.0(7)	4(2)	8433,7096	$\frac{43}{2}^-, \frac{39}{2}^-$	
1393.7(8)	1(0.5)	9826,8433	$\frac{47}{2}^-, \frac{43}{2}^-$	
1429.6(6)	22(2)	3053,1624	$\frac{21}{2}^+, \frac{19}{2}^-$	0.38(15)[1]
1613.0(1.5)	10(4)	3237,1624	$(\frac{23}{2}, \frac{21}{2}), \frac{19}{2}^-$	
1786.9(1.5)	4(2)	5265,3478	$(\frac{29}{2}, \frac{27}{2}), \frac{27}{2}^-$	
1896.4(1.5)	2(1)	5375,3478	$(\frac{31}{2}, \frac{29}{2}), \frac{27}{2}^-$	

[1]861 keV gate.

[2]664 keV gate.

[3]673 keV gate.

[4]431 keV gate.

[5]878 keV gate.

Table 4.3: Gamma-ray transitions identified in ^{102}Ru from the current work. The γ-ray intensities (in arbitrary units) were taken from a 2-D fit to the $\gamma - \gamma$ coincidence matrix using the program ESCL8R [73].

E_γ (keV)	I_γ (arb.)	E_i, E_f (keV)	$J_i^\pi \rightarrow J_f^\pi$	R_{DCO}
227.4	53(6)	2294,2067	8^+,6^+	0.94(8)[1]
292.5	7(4)	2943,2650	8^-,6^-	
333.6	4(2)	2705,2371	7^-,5^-	
430.2	25(6)	3135,2705	9^-,7^-	
476.2	—	475,0	2^+,0^+	
597.2	14(4)	3540,2943	10^-,8^-	
620.7	24(4)	4053,3432	12^+,10^+	0.88(19)[2]
631.8	100(13)	1107,475	4^+,2^+	0.89(10)[2]
727.7	25(4)	3432,2705	10^+,8^+	1.05(13)[2]
752.6	15(3)	4805,4053	14^+,12^+	
767.9	44(6)	1874,1107	6^+,4^+	0.92(13)[2]
775.0	8(3)	2650,1874	6^-,6^+	
830.4	24(4)	2705,1874	7^-,6^+	
831.6	28(7)	2705,1874	8^+,6^+	1.27(26)[2]
891.2	9(3)	3596,2705	10^+,8^+	
915.6	10(2)	5721,4805	16^+,14^+	
960.0	19(5)	2067,1107	6^+,4^+	
1065.3	11(3)	6784,5721	18^+,16^+	
1208.2	4(2)	7989,6784	20^+,18^+	
1264.0	5(2)	2371,1107	5^-,4^+	

[1]767 keV gate.

[2]476 keV gate.

Table 4.4: Gamma-ray transitions identified in ^{98}Mo from the current work. The γ-ray intensities (in arbitrary units) were taken from a 2-D fit to the $\gamma - \gamma$ coincidence matrix using the program ESCL8R [73].

E_γ (keV)	I_γ (arb.)	E_i, E_f (keV)	$J_i^\pi \rightarrow J_f^\pi$
241.8	2(1)	3098,2856	7^-,8^+
385.3	15(3)	3659,3274	9^-,8^+
417.5	5(2)	3274,2856	8^+,8^+
476.1	13(3)	3098,2622	7^-,5^-
511.1	37(5)	2856,2345	8^+,6^+
561.4	15(3)	3659,3098	9^-,7^-
722.7	100(9)	1511,788	4^+,2^+
753.3	16(3)	3098,2345	7^-,6^+
768.2	22(3)	4427,3659	11^-,9^-
787.4	—	788,0	2^+,0^+
802.9	9(2)	3659,2856	9^-,8^+
834.2	66(6)	2345,1511	6^+,4^+
878.0	17(3)	4152,3274	10^+,8^+
928.4	19(3)	3274,2345	8^+,6^+
1112.0	10(3)	2622,1511	5^-,4^+

Table 4.5: Gamma-ray transitions identified in ^{99}Mo from the current work. The γ-ray intensities (in arbitrary units) were taken from a 2-D fit to the $\gamma - \gamma$ coincidence matrix using the program ESCL8R [73].

E_γ (keV)	I_γ (arb.)	E_i, E_f (keV)	$J_i^\pi \rightarrow J_f^\pi$	R_{DCO}
449.2	—	689,236	$\frac{11}{2}^-$, $\frac{7}{2}^+$	
481.8	—	1166,684	$\frac{15}{2}$, $\frac{11}{2}^-$	0.84(9)[1]
693.0	100(41)	1859,1166	$\frac{19}{2}$, $\frac{15}{2}^-$	0.99(13)[1]
845.4	74(22)	2704,1859	$\frac{23}{2}$, $\frac{19}{2}^-$	1.13(54)[1]
978.6	19(10)	3684,4743	$\frac{27}{2}$, $\frac{23}{2}^-$	
1059.1	6(3)	4743,3684	$(\frac{31}{2}, \frac{27}{2}^-)$	

[1]482 keV gate.

4.4 Decay Scheme of ^{101}Ru

4.4.1 The ground state and the $d_{5/2}$ band

The $\frac{5}{2}^+$ assignment of the ground state is well established from the β decay of ^{101}Tc [65], and has a configuration based on the spherical shell model neutron states $(g_{7/2})^6(d_{5/2})^1$. This state is populated by transitions de-exciting the band 1 (see figure 4.7). These transitions are clearly seen from the double-γ coincidence analysis (see figure 4.8), and similar bands have also been observed in the other odd-A Ru and Pd isotopes [66, 67]. The level at 545 keV directly feeds the ground state, and has been tenatively assigned $\frac{7}{2}^+$ [66], primarily based on the E1 nature of this transition, as determined from the angular

distribution analysis. New, high-spin states have been found at 4451 keV, 5375 keV, 6469 keV, 7679 keV and at 9002 keV from the present γ^3 analysis. The systematics of these levels within the band and the enhanced E2 nature of those transitions, as obtained from the angular distribution study (see section 5.2), confirms their assignment to be $(\frac{29}{2}^+)$, $(\frac{33}{2}^+)$, $(\frac{37}{2}^+)$, $(\frac{41}{2}^+)$, and $(\frac{45}{2}^+)$, respectively.

The positive-parity band, built on the $\frac{5}{2}^+$ ground state (band 1 in figure 4.7) was reported by Klamra et al. [64] up to a spin of $(\frac{21}{2}^+)$. This band is extended fully through the first alignment up to spin $\frac{45}{2}^+$. The ordering of the lower lying band members in the current work also differs from that reported by Klamra et al. [64] in that the 673 keV, $\frac{17}{2}^+ \rightarrow \frac{13}{2}^+$ transition reported in reference [64] is replaced by one at 878 keV in the current work. The revised ordering places the 673 and 628 keV transitions reported by Klamra et al. above the 878 keV transition. (Note that this change in ordering has significant consequences when extracting the alignment properties of his band, see below.) The identification of the 1430 keV, stretched dipole $(\frac{21}{2}^+ \rightarrow \frac{19}{2}^-)$ and 1207 keV, $\frac{25}{2}^+ \rightarrow \frac{23}{2}^-$ transitions which link this positive parity band with the negative parity structure provide confirmation of the new ordering.

4.4.2 The 307 keV state and the $g_{7/2}$ band

The $\frac{7}{2}^+$ assignment of this state is also well established [65]. It has a possible configuration admixture of $(g_{7/2})^5(d_{5/2})^2$, as indicated by the intense β branch observed to this level from the $\frac{9}{2}^+$ ground state of ^{101}Tc. From the $\gamma\gamma$ and γ^3 coincidence analysis, previously unseen levels are found at 4141 keV, 4967 keV, 5946 keV, 7077 keV, and 8318 keV (see figure 4.7). They are again assigned from the coincidence work and angular distribution study as $(\frac{27}{2}^+)$,

$(\frac{31}{2}^+)$, $(\frac{35}{2}^+)$, $(\frac{39}{2}^+)$, and $(\frac{43}{2}^+)$. Further, γ^3 study of this band led to many new interband transitions being observed.

In the $\gamma\gamma$ analysis, a 1024 keV line was found to be in coincidence with the 307 keV transition and the first two cascade transitions in the $g_{7/2}$ band. Due to the doublet nature of this transition with a decay in ^{100}Ru [67], no previous assignment to this level has been made. However, using the γ^3 analysis, it was possible to tentatively assign this level at 2887 keV as $(\frac{19}{2}^+)$. It was also found to be in coincidence with transitions in the band 4 of figure 4.7.

Klamra *et. al.* also observed the band built on the $\frac{7}{2}^+$ state at 307 keV (band 2 in figure 4.7) up to a tentative spin of $\frac{23}{2}^+$. In the current work this is extended through the first backbend, up to spin/parity of $(\frac{43}{2}^+)$. The decays between this structure and the negative parity band are also established via the observation of the weak 1206 and 969 keV transitions. The decoupled rotational band built on the $\frac{11}{2}^-$ isomeric bandhead which was observed by Klamra *et. al.* up to spin $\frac{35}{2}^-$, is extended to a spin of $(\frac{47}{2}^-)$ (band 3 in figure 4.7).

4.4.3 The 528 keV and the $h_{11/2}$ band

The relatively intense 220 keV transition, in coincidence with the 307 keV ground state transition, establishes a level at 528 keV, which is known to have a spin-parity of $\frac{11}{2}^-$, and is built on a decoupled $\nu h_{11/2}$ orbital [66]. This state lies below the lowest $\frac{9}{2}^+$ state, and is consequently isomeric with a half-life of 17 μs [66, 68]. This band is by far the most strongly populated ^{101}Ru band, and extends up to the spin-parity of $(\frac{47}{2}^-)$. The 1430 keV transition was observed between the yrast $\frac{21}{2}^+$ level and $\frac{19}{2}^-$ $(h_{11/2})$ state. A number of new transitions are also observed to feed the $h_{11/2}$ band, without having further coincidence relations with any other observed transitions.

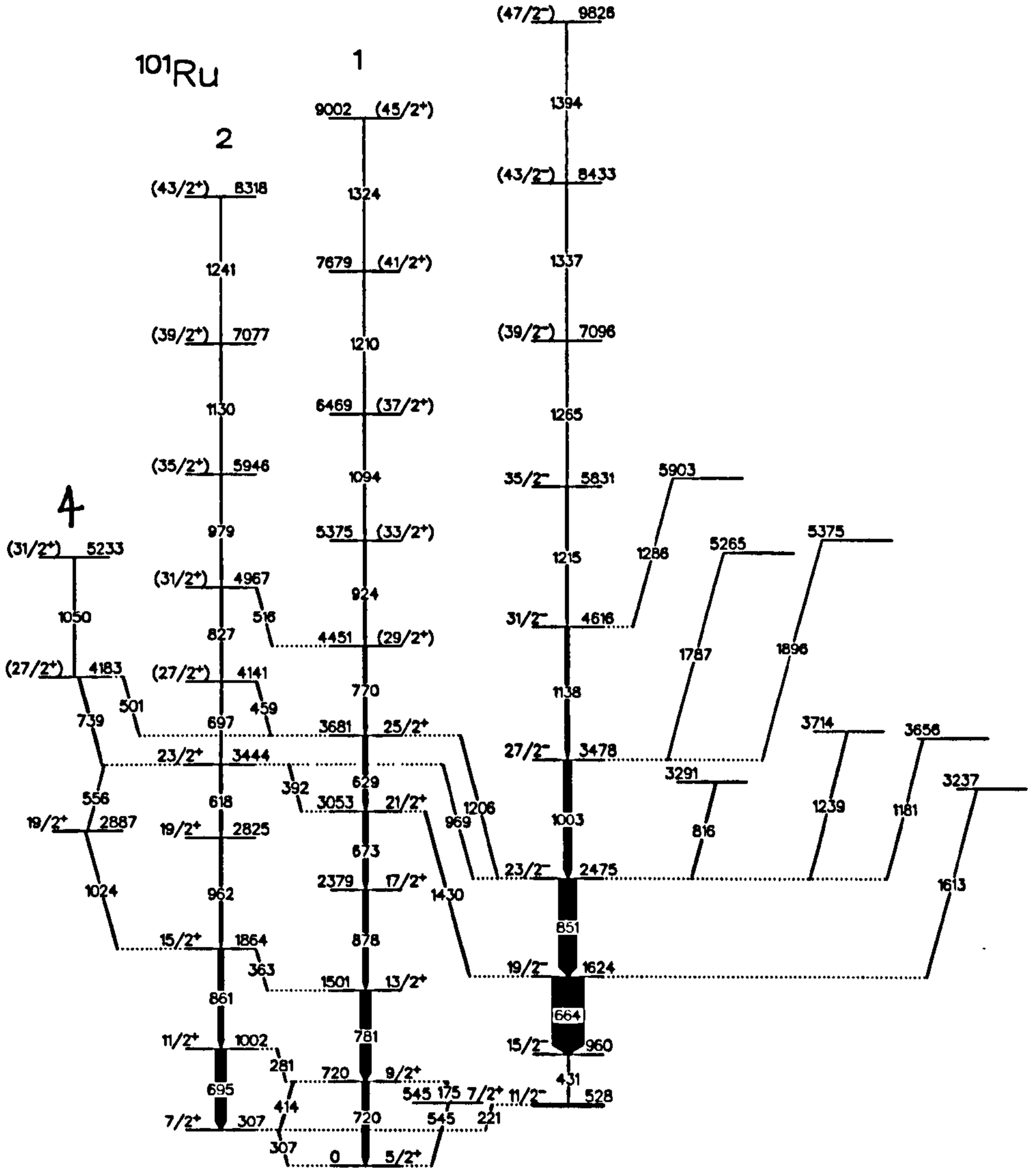

Figure 4.7: Decay scheme of ^{101}Ru, as obtained from the present study.

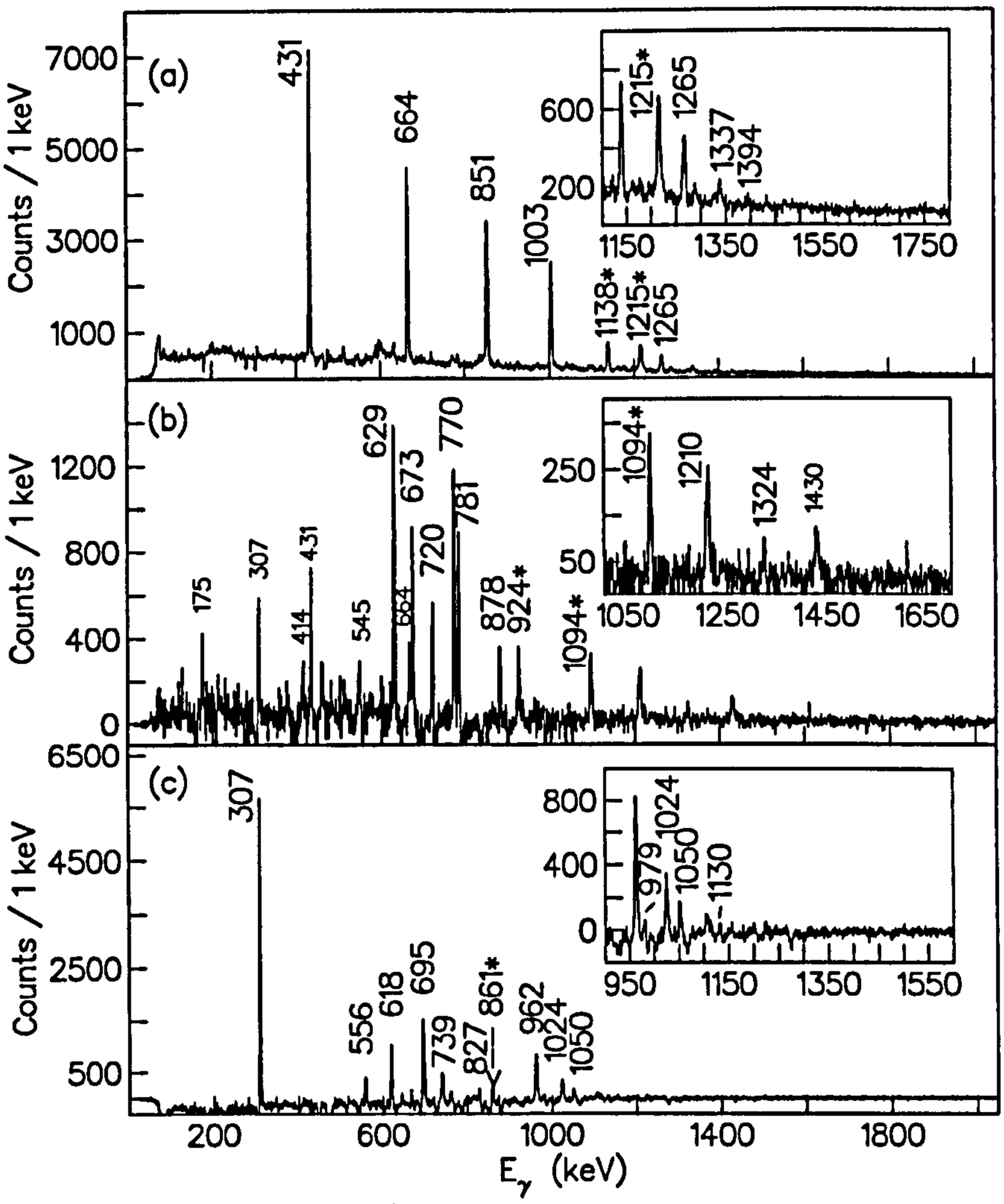

Figure 4.8: Summed Single γ-ray gated spectra highlighting the (a) $\frac{11}{2}^-$ band, (b) the $\frac{5}{2}^+$ band, and (c) the $\frac{7}{2}^+$ band in ^{101}Ru. The gating transitions are marked with asterisks. Band members are shown in large font with links to other structures in ^{101}Ru and are highlighted with the smaller sized labels. The insets correspond to expanded regions of the main figures.

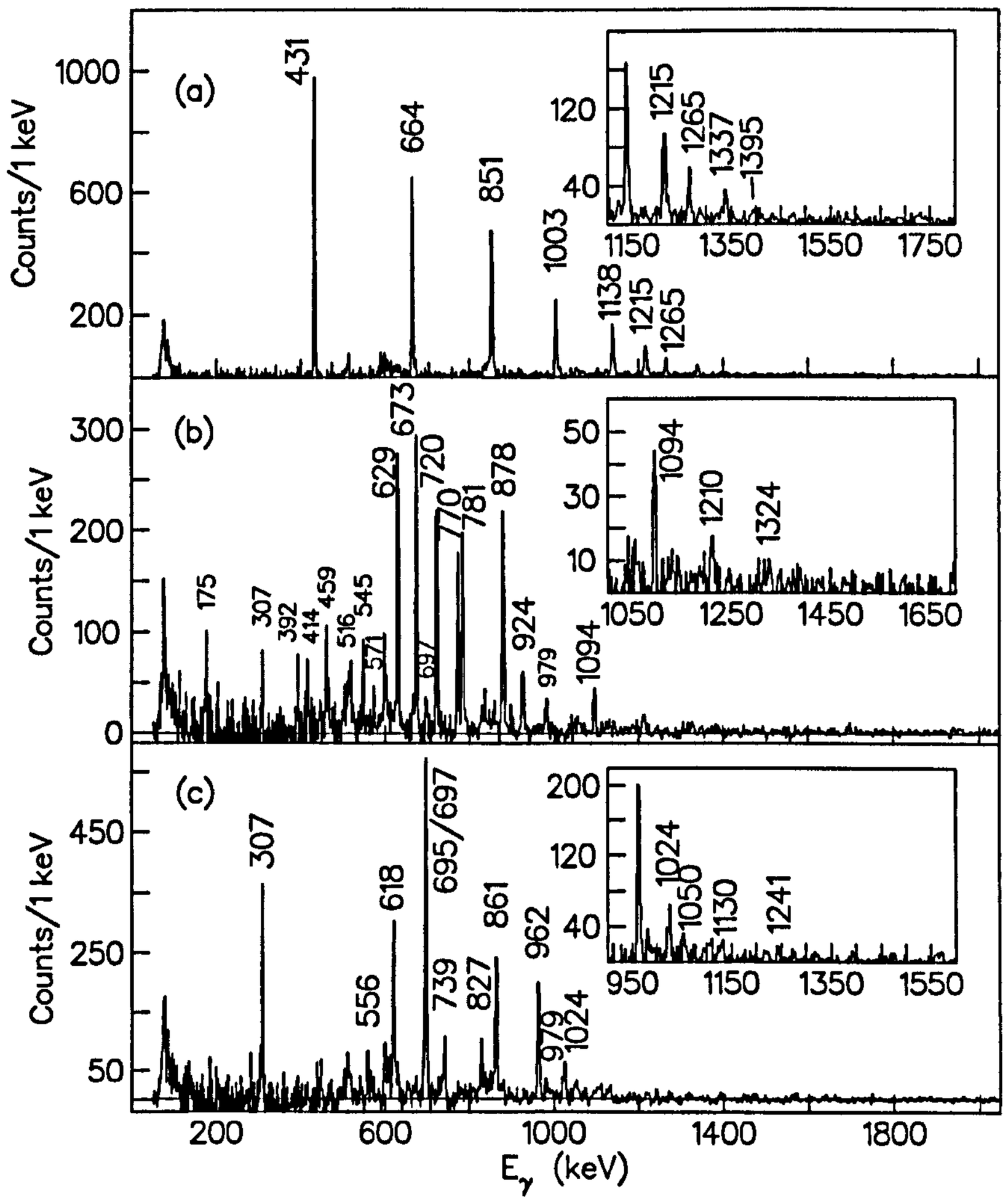

Figure 4.9: Summed double-ray gated spectra highlighting the (a) $\frac{11}{2}^-$ band, (b) the $\frac{5}{2}^+$ band, and (c) the $\frac{7}{2}^+$ band. Band members are shown in large font with links to other structures in ^{101}Ru and are highlighted with the smaller sized labels. The insets correspond to expanded regions of the main figures.

4.5 Decay Scheme of ^{102}Ru

Previously reported members of the yrast states have been identified up to $J^\pi = 16^+$ at 5725 keV [69]. Two additional transitions of 1065 keV and 1208 keV were also found in coincidence with the known yrast cascade, and are shown in a spectrum in figure 4.14. The ordering of these new transitions was tentatively made as shown in the decay scheme (figure 4.10), and is based on their measured intensity. Unambiguous spin-parity assignment for this yrast band have been performed by anisotropy measurement up to 14^+ [69], but were not possible for the new 1065 keV and 1208 keV transitions due to poor statistics. Usual stretched E2 systematics for the intra-band transitions were assumed for those 1065 and 1208 keV γ-rays, and they were tentatively assigned as $18^+ \rightarrow 16^+$ and $20^+ \rightarrow 18^+$, respectively (figure 4.10).

Negative parity bands were known up to 9^- at 3135 keV and 10^- at 3540 keV, and the placement of intra-band members of 293, 334, 430, and 597 keV transitions, as well as the inter-band 775, 830, and 1264 keV transitions observed by Dejbakhsh and Bouttchenko [69] are confirmed by the present coincidence analysis. An additional transition of 891 keV which decays out from the $J^\pi = (10^+)$ level at 3598 keV was also found without in coincidence with any other transitions.

4.6 Decay Scheme of ^{98,99}Mo

The yrast band transitions observed in ^{98}Mo (summarised in Table 4.4) confirm the previously established yrast levels up to 4150 keV ($J^\pi = 10^+$) [70] (see also figure 4.12). Known negative parity levels of $J^\pi = 5^-$, 7^-, 9^-, and 11^- at 2622, 3098, 3659, and 4427 keV, respectively, were also identified from the γ^3 coincidence relations [70]. In addition, the 8^+ state at 2856 keV, which

decays by a 512 keV transition to the 6^+ yrast state at 2344 keV, was found in the present study, and was found to be fed by 416 and 803 keV transitions from the yrast 8^+ and (9^-) states at 3272 and 3659 keV, respectively. Inter-band transitions of 242, 387, 754, and 1112 keV were also identified in the present coincidence study, as shown in the decay scheme of figure 4.11.

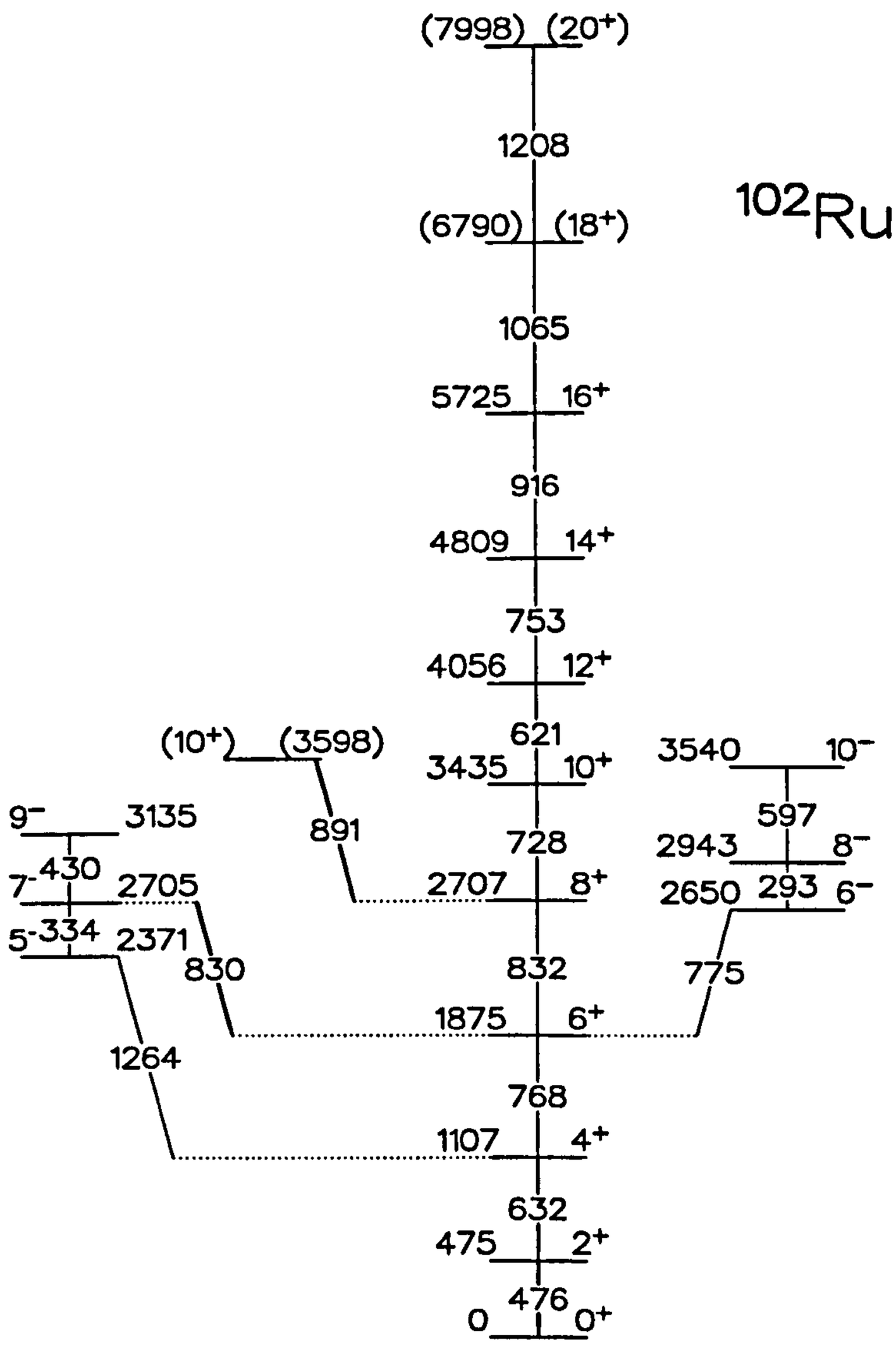

Figure 4.10: Partial decay scheme of ^{102}Ru deduced from the present study.

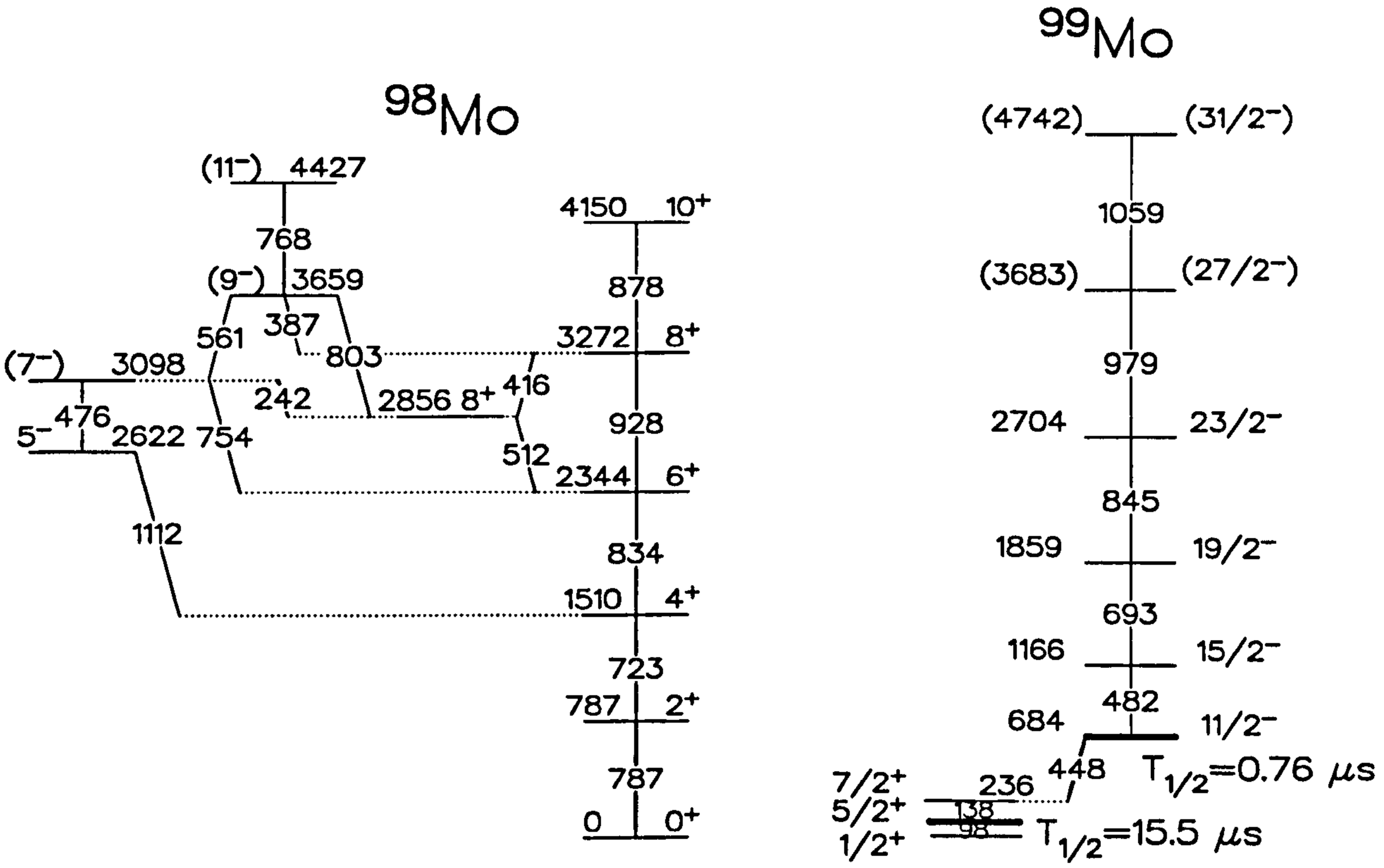

Figure 4.11: Partial decay schemes of ^{98}Mo and ^{99}Mo deduced from the current work.

A cascade of 482, 693, 845, 979, 1059 keV transitions belonging to ^{99}Mo were all found to be in coincidence, and form a band built on a bandhead of known spin-parity, $\frac{11}{2}^-$ state [71, 72], populated in the current study via the α2n evaporation channel. This band has been extended by two transitions (979 and 1059 keV) from the present study up to 4742 keV, and was identified in the triple-γ coincidence spectrum of figure 4.13. The spin-parity assignment for this cascade was confirmed by the systematics of the enhanced E2 nature of these transitions (figure 4.6) and represents the continuation of

the $\nu h_{\frac{11}{2}}$ decoupled structure, as observed in other N = 57 isotones in this mass region.

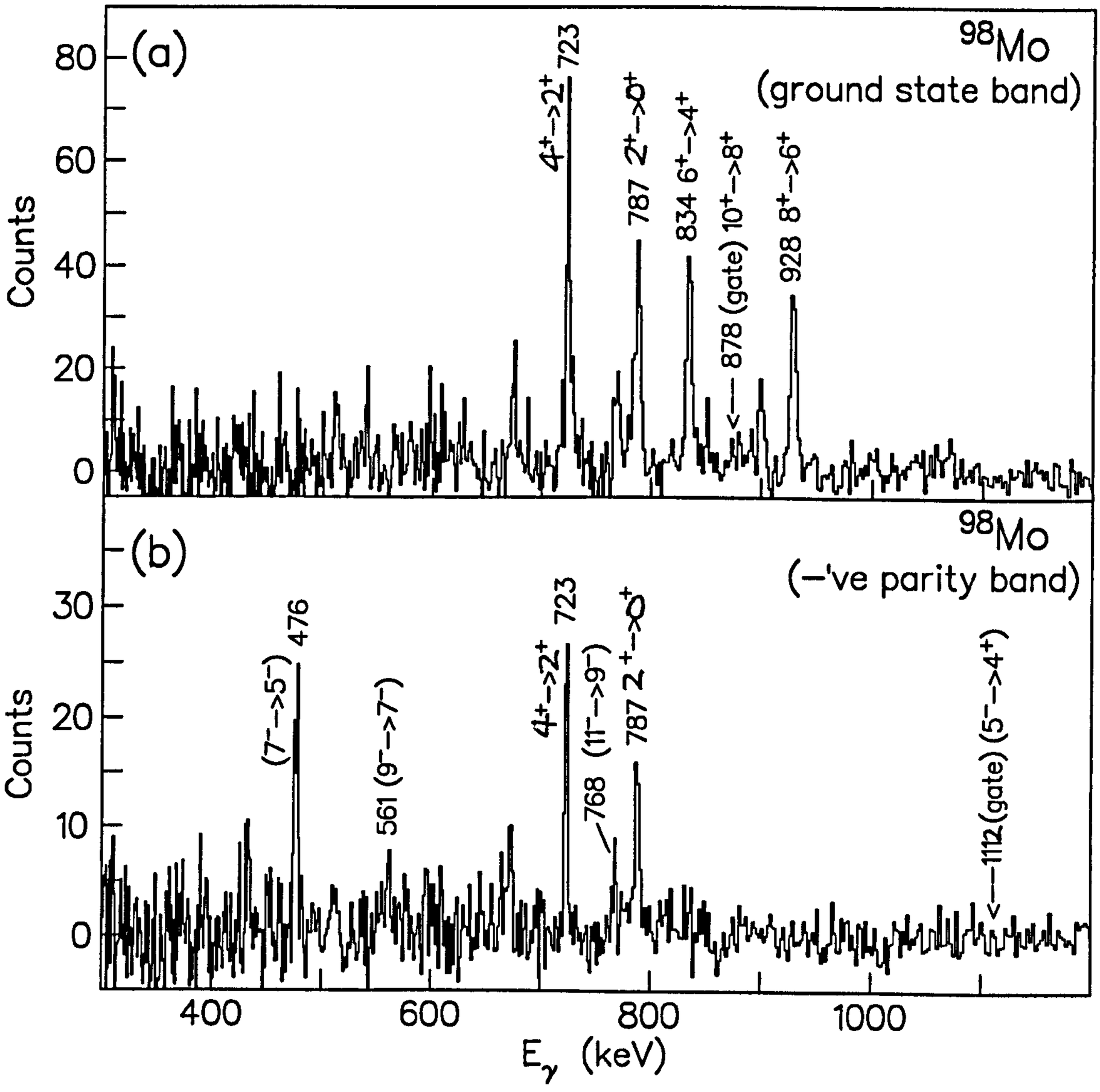

Figure 4.12: Spectra of the sum of single γ-ray gates in the positive parity and $\nu h_{11/2}$ bands in ^{98}Mo.

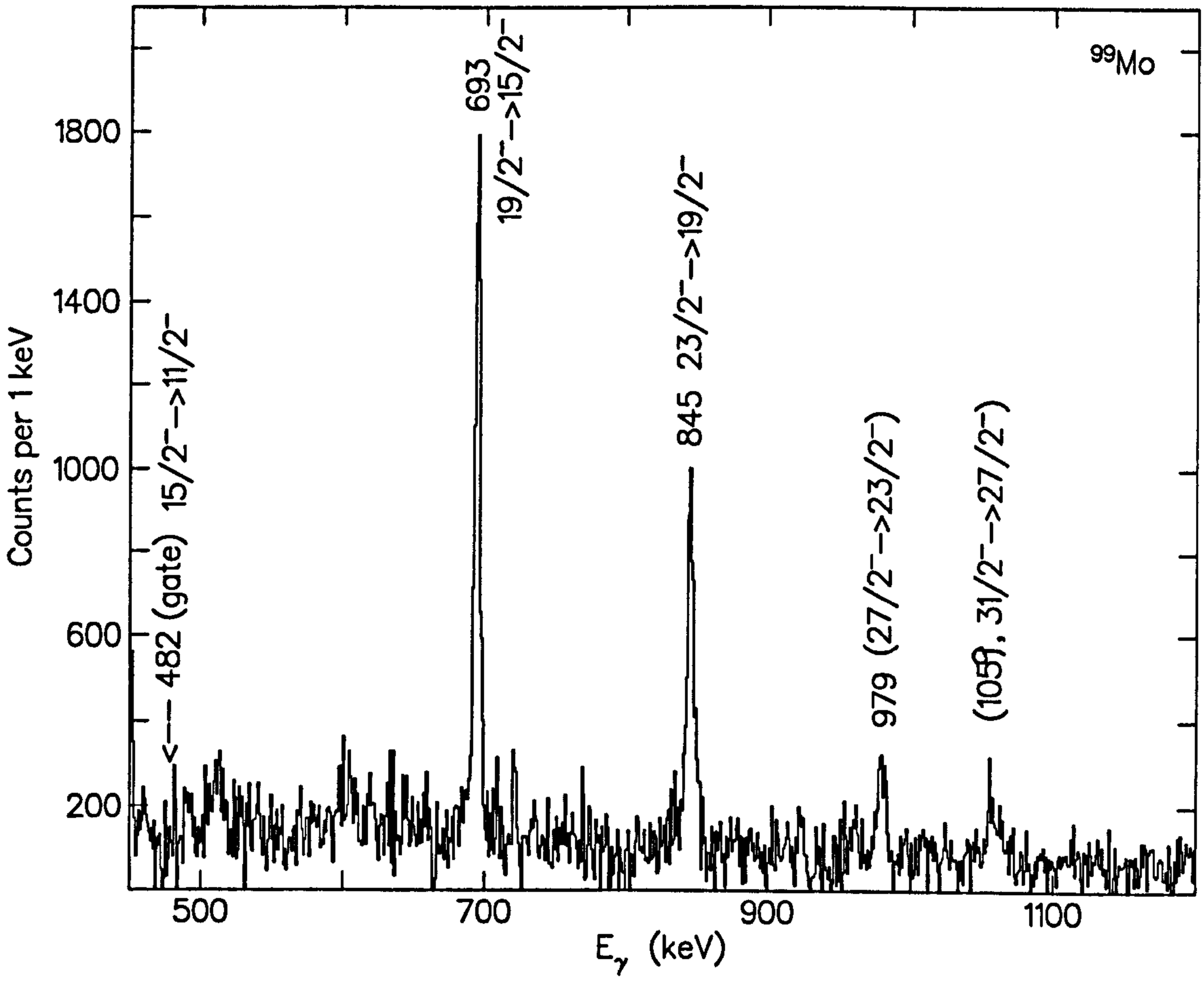

Figure 4.13: $\gamma\gamma$ coincidence spectrum gated on the 482 keV, $\frac{15}{2}^- \rightarrow \frac{11}{2}^-$ member of the $\nu h_{11/2}$ band in ^{99}Mo.

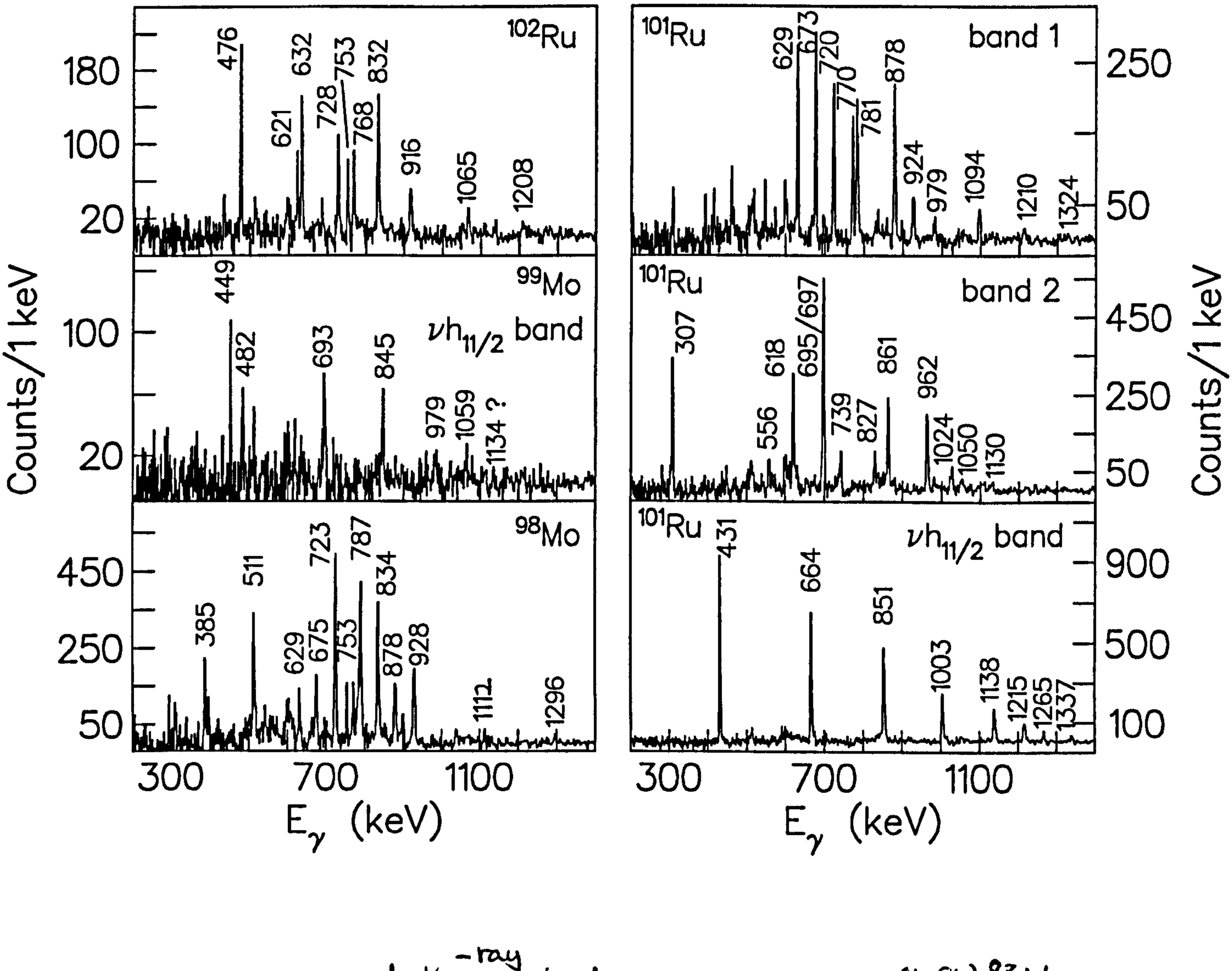

Figure 4.14: Sum of double-γ-ray gated spectra belonging to (left) ^{98}Mo, $\nu h_{11/2}$ band in ^{99}Mo and the ground state band in ^{102}Ru, and (right) $\nu h_{11/2}$ band, band 2 and band 1 in ^{101}Ru, as shown in figure 4.7.

Chapter 5

$^{100}_{42}$Mo + 700 MeV $^{136}_{54}$Xe Experiment

5.1 Introduction

Excited states in A $\simeq$ 100 $_{42}$Mo-isotopes were populated in a binary reaction using an enriched, self-supporting ^{100}Mo target and a ^{136}Xe beam at 700 MeV. The pulsed beam of 15.27 MHz in frequency and between ~1-2 pnA in intensity was provided by the 88-inch cyclotron accelerator at Lawrence Berkeley National Laboratory, USA, and bombarded the 420 μg/cm^2 target. For the present experiment, the one hundred and two HPGe detectors were employed in the GAMMASPHERE array, and was used for γ-ray detection in coincidence with the reaction fragments, which in return were detected utilising the position-sensitive and fast counting CHICO detector. The CHICO detector performed angular and time-of-flight measurements of the fragments on an event-by-event basis to reconstruct the reaction kinematics. The β_{recoil} values were subsequently obtained assuming two-body kinematics, and the measured γ-ray energies were Doppler corrected to yield their

true energies. Simultaneous and complete isotopic identification of target-like and projectile-like fragments (TLFs and PLFs, respectively) was then possible through the triple-γ coincidence relations. The identification of high-spin states in $_{42}$Mo-isotopes required the cleanest separation between different possible reaction mechanisms (e.g. quasi-elastic (QE) and deep inelastic (DIC) reactions) in a large phase space, together with the use of high channel selectivity as offered by the heavy-ion (HI)-γ^3 coincidence technique.

Events fulfilling the hardware coincidence condition of two CHICO events and at least three prompt γ-rays within a 50 ns time window were registered. The Ge detector time window remained opened for 1 μs following the master trigger condition, which enabled the identification of isomers in half-lives between a few hundred nanosecond to microsecond range. A typical trigger gate rate during the experiment was $\sim$3 kHz. The total data set containing both the TLF and PLF scattering angles and their time-of-flight difference (ΔTOF), in addition to the γ-ray energies and the coincident time, were recorded. In total, 9.9×10^8 unfolded HI-HI-γ^3 (or higher γ) events were collected in a four day run for subsequent offline analysis. The data were sorted into both RADWARE and ANA cube formats, and analysed using the GF3 and LEVIT8R [73], and ANA [74] software packages, respectively.

5.2 Detector Calibrations and Corrections

5.2.1 The GAMMASPHERE Array

In the present ^{100}Mo + 700 MeV ^{136}Xe experiment, 102 HPGe detectors were employed and arranged in 17 rings at angles in θ of 17.3°, 31.7°, 37.4°, 50.1°, 58.3°, 69.8°, 79.2°, 80.7° and 90.0° with forward-backward symmetry. For those detectors at the angles greater than 50°, two-fold electric segmentation

was applied, reducing their opening half-angles from 7.4° to 3.7°. The gain of each HPGe detector was set to 0.3 keV/channel, providing 2.7 MeV range with 8192 channel ADCs. The full range of the TDCs for the HPGe detectors was 8192 channels on a ~1 μs scale, which allowed up to ~0.12 ns/channel resolution. Prior to the experiment, absolute energies of the Ge detectors and the relative efficiency of the whole GAMMASPHERE array were determined using the ^{152}Eu and ^{133}Ba calibration sources (see figure 5.1).

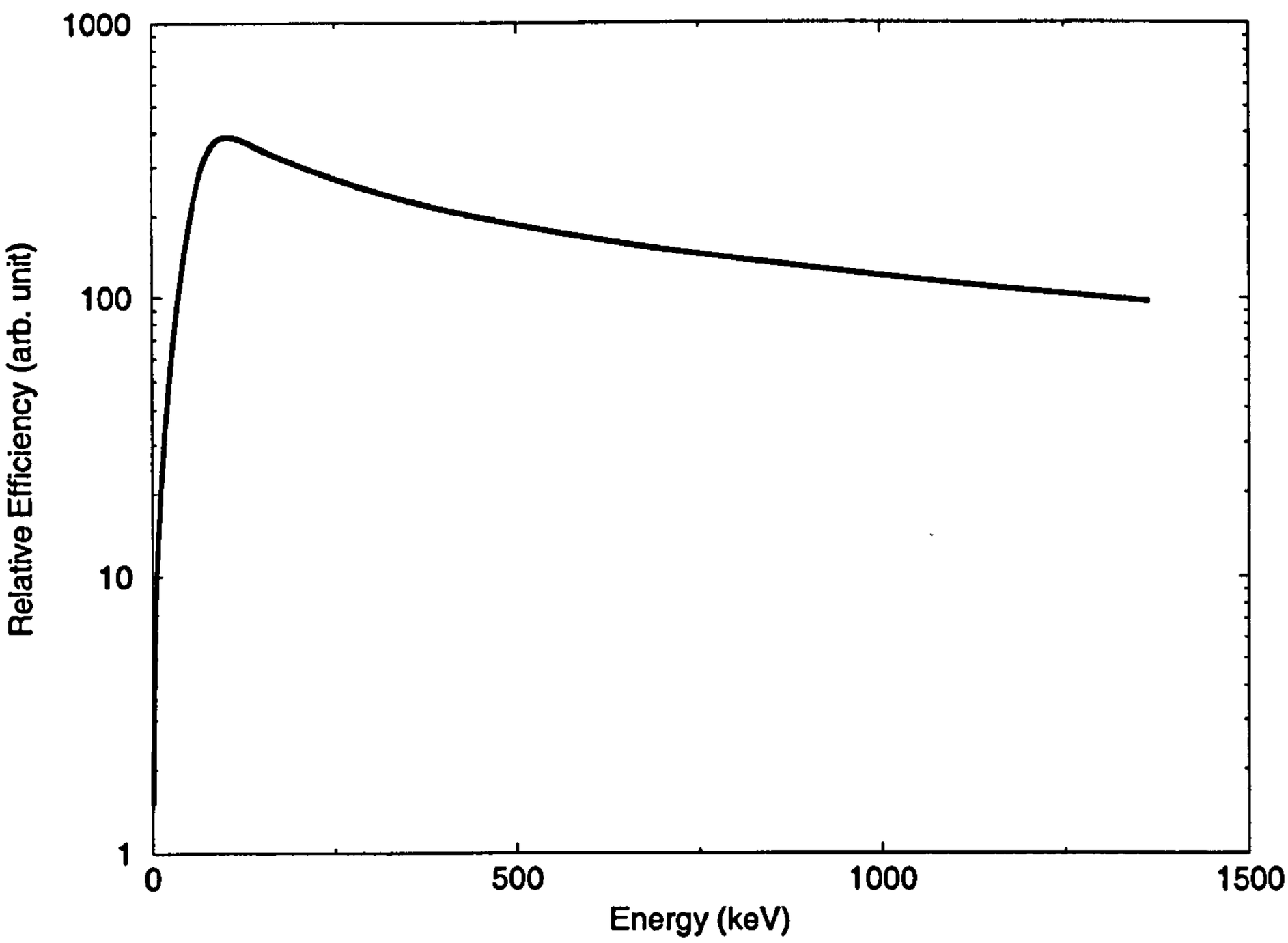

Figure 5.1: Relative HPGe array efficiency curve for the CHICO plus GAMMASPHERE array with 102 HPGe detectors. Both ^{133}Ba and ^{152}Eu calibration sources were used to obtain the curve.

The total γ-ray energy projection was subsequently produced (see figure 5.2), and illustrates a few strong transitions populated by isomeric dec-

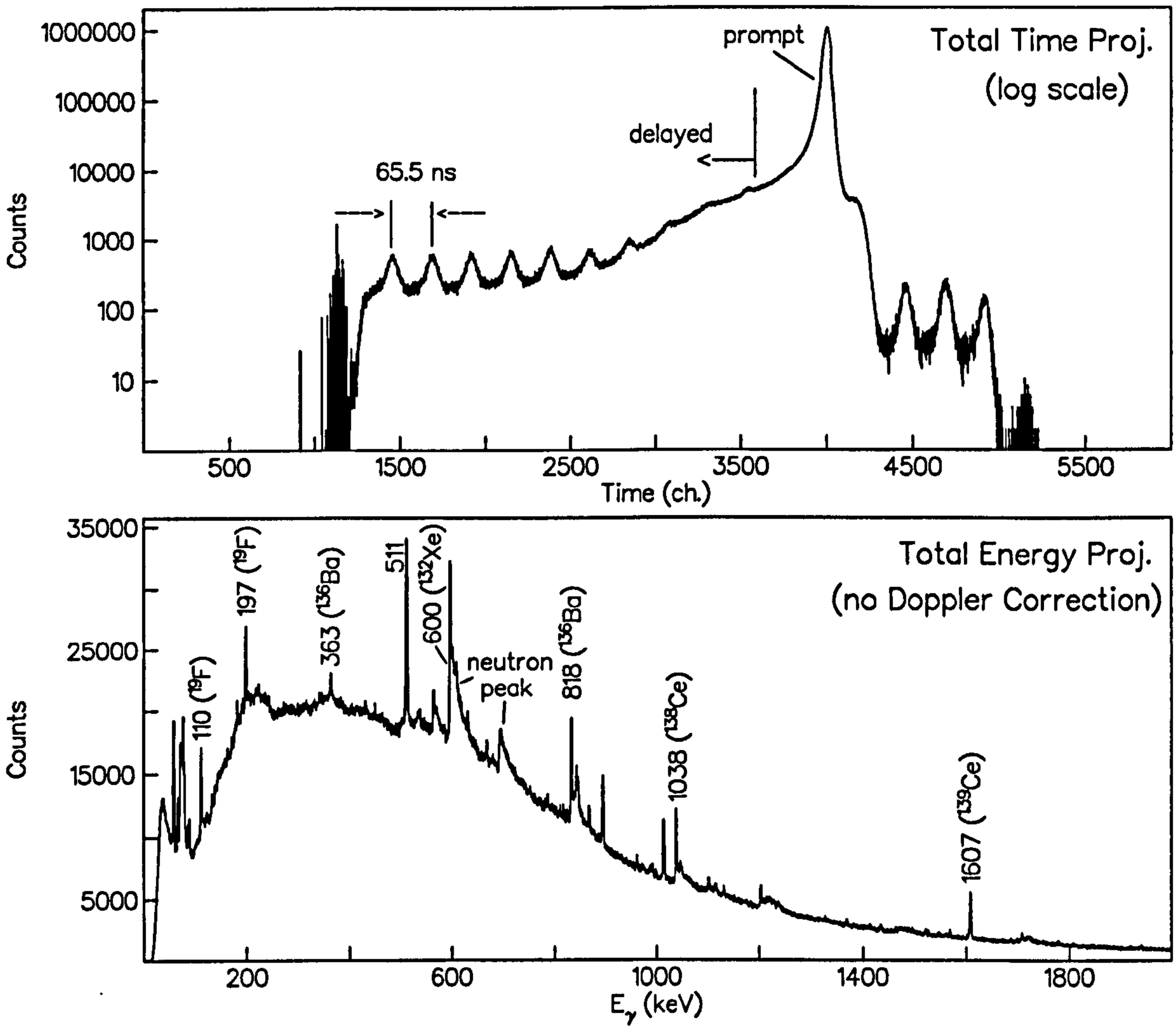

Figure 5.2: Total γ-ray time (top) and energy (bottom) sum projections.

ays of $^{136}_{56}$Ba, $^{138}_{58}$Ce, $^{139}_{58}$Ce. In the same figure, the total Ge time spectrum in logarithmic scale analysed using the ANA software shows a prompt peak on a background that includes several crests, differences in time of which correspond to the 15.27 MHz beam pulses. Around 230 channels between the two neighbouring crests then provided the software time calibration of 0.28 ns/channel. In addition, a total fold distribution (see later) was produced and is shown in figure 5.3. Peaks labelled in the figure illustrate the mode

average of each event type . The total fold distribution refers to the event-by-event summation of both suppressed and unsuppressed Ge fold spectra.

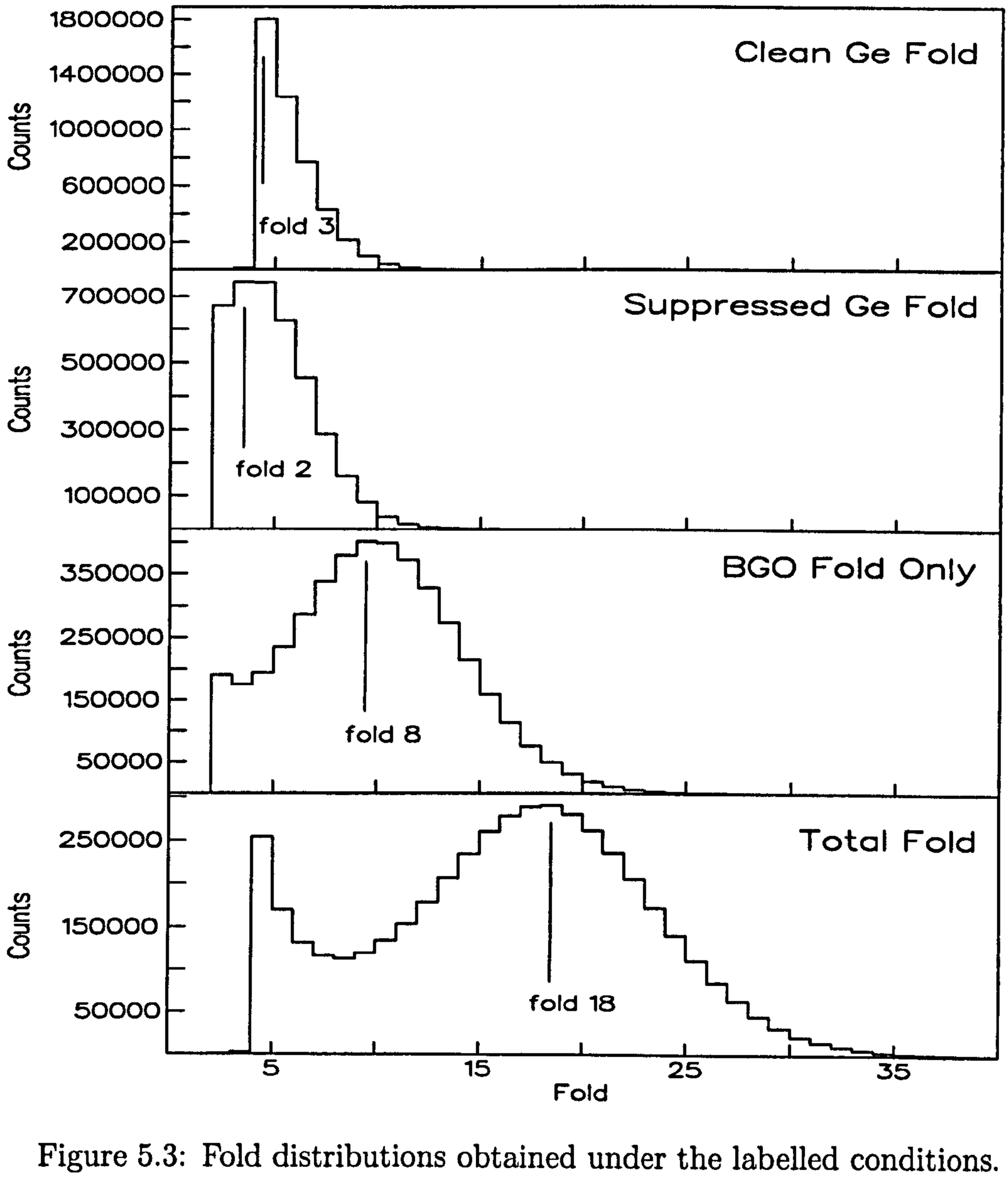

Figure 5.3: Fold distributions obtained under the labelled conditions.

5.2.2 The CHICO Detector

In the present experiment utilising inverse kinematics, a total of 10 PPACs were arranged in five co-planar pairs to be placed in the forward hemisphere (see section 3.5). For genuine heavy-ion events with a particle multiplicity of two, the θ position was calibrated using two intrinsic limits, provided by (i) sharp cut-off in detection efficiency at 20° due to the presence of a collimator, and (ii) a dip in counts at 60° representing a shadow effect from a support rib in the pressure window (see figure 5.4). For time calibrations, arbitrary zero offsets from each of the PPAC detectors (see section 3.5) were evaluated by incrementing the individual PPAC anode spectra and applying appropriate offsets, such that all the software corrected anode spectra peak at the same channel number. Figure 5.4 shows the time difference spectrum obtained with the correct offsets applied to all CHICO anodes, and by subtracting the TDC values associated with the two coincident anode signals. The FWHM of the time coincident peak is ~100 channels and the level of background corresponding to the random coincidences is negligible.

5.3 Kinematic Reconstruction

The first step in analysing the high-spin states populated in the reaction fragments, which were detected in a large phase space, was to assign them with the correct fragment type, i.e. PLF or TLF. For a binary reaction, they can be separated kinematically if both fragments were detected simultaneously in time and in scattering angle, as shown in figure 5.5. The fragments of interest were subsequently selected by placing appropriate loci in this 'particle identification spectrum' (figure 5.5). Once the differentiation between TLFs and PLFs were made, their momenta could be defined from their scattered

angular positions, assuming two-body kinematics [58],

$$P_{1,2} = \frac{P_0 \sin\theta_{2,1}}{\sin(\theta_1 + \theta_2)}, \tag{5.1}$$

where $P_{1,2}$ are the respective momenta of the two coincident fragments, P_0 is the momentum of the beam, $\theta_{2,1}$ is the angle of each of the two fragments with respect to the beam direction.

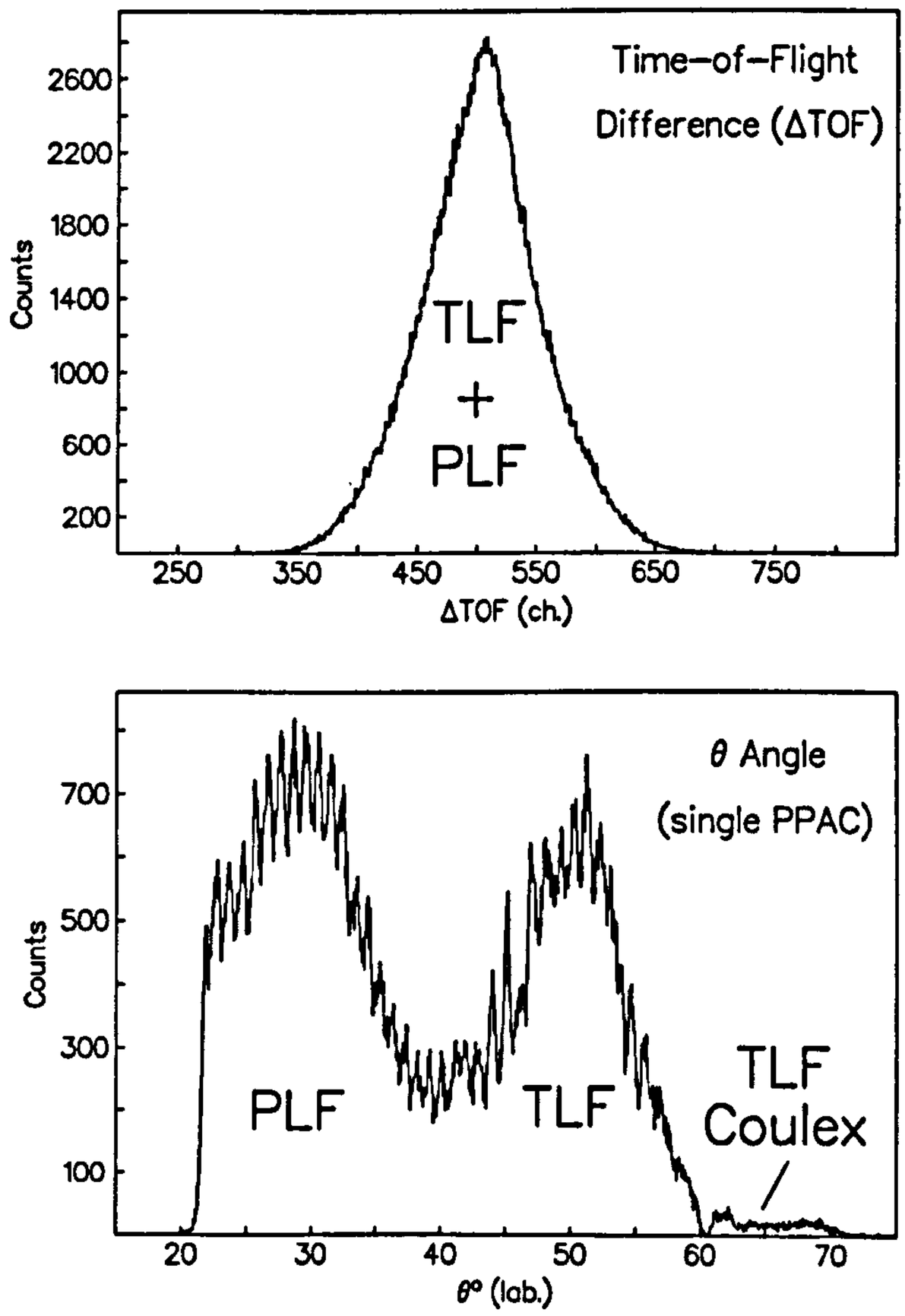

Figure 5.4: One dimensional plots of (top) time-of-flight difference (ΔTOF) between the TLFs and the PLFs, and (bottom) their scattering θ angles in laboratory frame. Each 'spike' in the measured angles represents the θ_{lab} = 1° detection resolution of the CHICO detector.

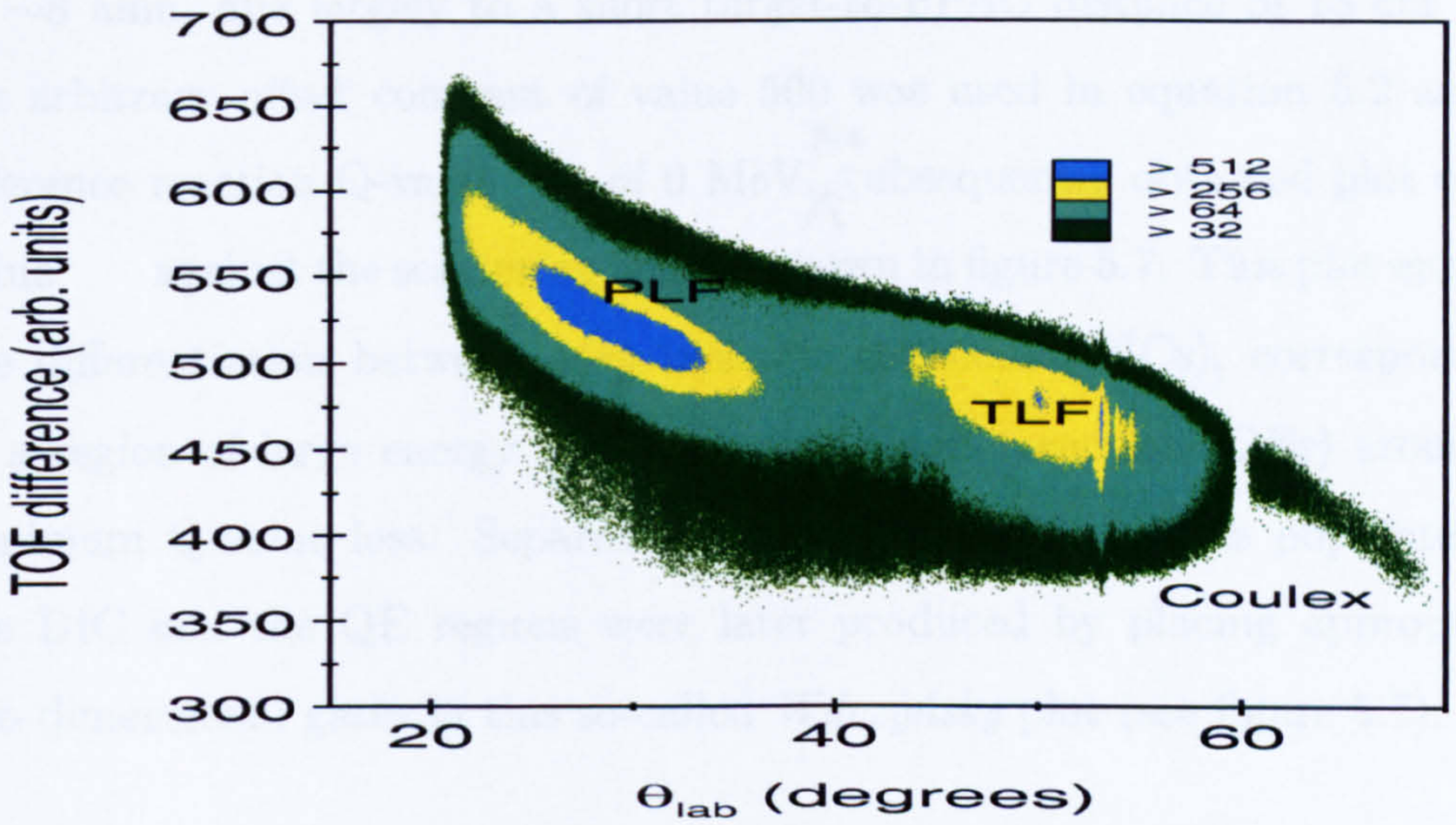

Figure 5.5: Two-dimensional particle identification spectrum, plotting time-of-flight difference between the two fragments as a function of their respective scattering angles.

The collinearity of the two-body kinematics was ascertained by placing additional two-dimensional gates in a θ_{PLF} against θ_{TLF} plot of figure 5.6. Measurement of the azimuthal angle was also required to satisfy the co-planar condition of the PLF-TLF binary pair.

From the assumption of the conservation of reaction mass, the Q-value of the reaction can be determined as [58],

$$Q = \frac{P_0^2}{A_{beam}} - \left(\frac{P_1^2}{A_{PLF}} + \frac{P_2^2}{A_{TLF}} \right) + 500, \tag{5.2}$$

where A_{beam} is the mass of ^{136}Xe beam in amu, and the terms $A_{PLF/TLF}$ refer to the masses of the PLFs and TLFs, respectively. In this analysis, these

masses were taken to be that of the beam and the target, since the masses of the PLF and the TLF fragments can only be determined approximately to ~8 amu, due largely to a short target-to-PPAC distance of 13 cm [58]. An arbitrary offset constant of value 500 was used in equation 5.2 as the reference reaction Q-value of 0 MeV. Subsequently obtained plot of Q-value against the scattering angle is shown in figure 5.7. This plot enables the differentiation between deep inelastic collisions (DICs), corresponding to a region of large energy loss, and quasi-elastic reaction (QEs) around a minimum Q-value loss. Separate γ^3 cubes for the fragments populated in the DIC and the QE regions were later produced by placing appropriate two-dimensional gates in this so-called *Wilczyńsky* plot (see figure 5.7).

5.4 Kinematic Correction

In the present binary reaction, heavy-ion and γ-ray coincidence techniques were employed to help reducing the energy resolution (ΔE_γ^{tot} term in equation 3.29) of the GAMMASPHERE array, as well as in obtaining a higher P/T ratio from the increased resolving power of the array. Angles and velocity vectors involved in the kinematic correction procedures are illustrated in figure 5.8. The relative velocity vectors of the target-like (A) and the projectile-like (B^*) fragments with respect to the beam axis are denoted by the dotted lines.

Evaluation of a velocity vector for a reaction fragment was performed from the angular position (θ,ϕ) assignment and by estimating its magnitude in the limit of Rutherford scattering [17] (see also figure 5.9). Measured γ-ray energies were then kinematically corrected using the standard Doppler formula of equation 3.26. The cosine of angle between a fragment and the

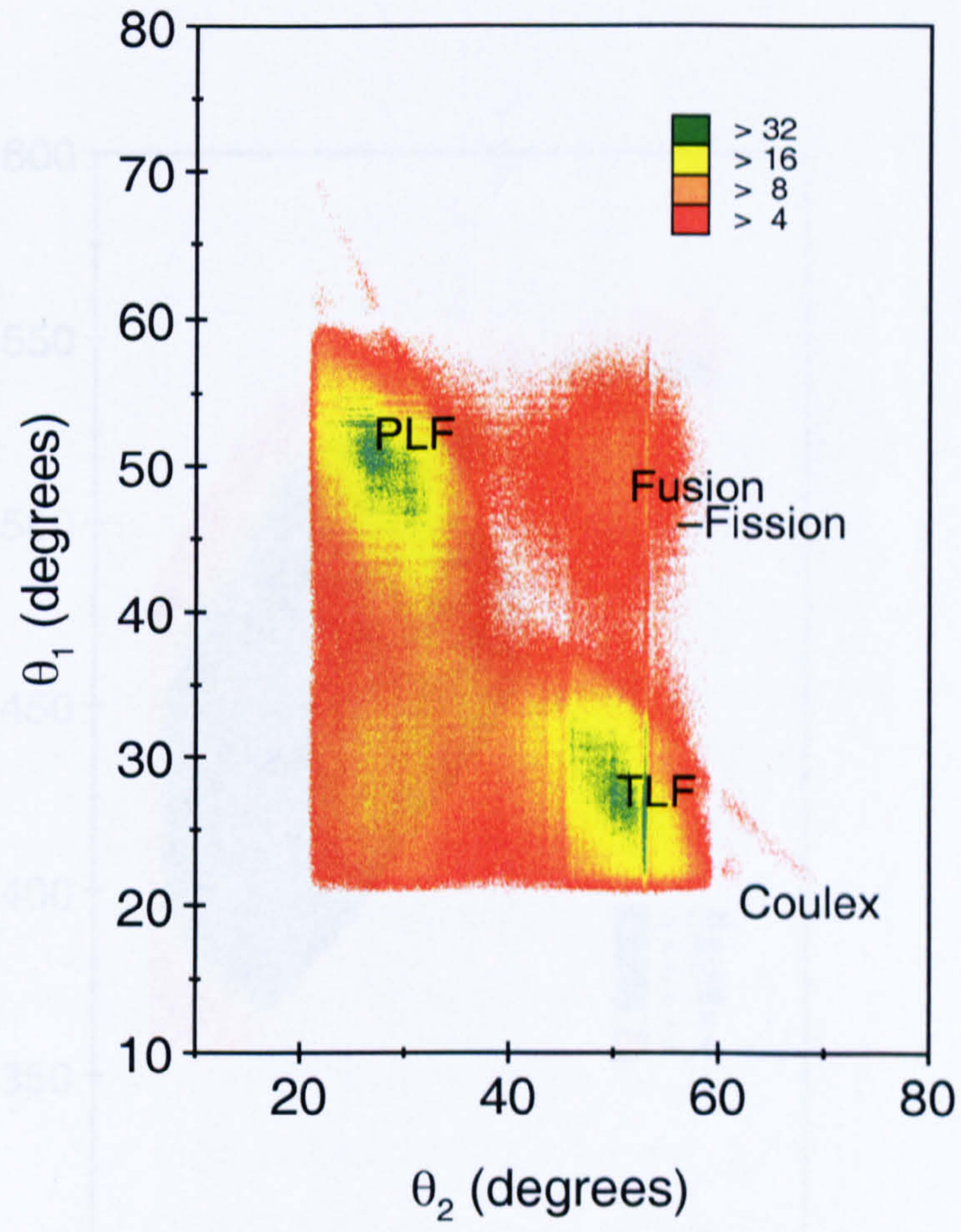

Figure 5.6: A θ_1 against θ_2 plot of measured scattering angles belonging to the PLFs and the TLFs. Label TLF/PLF indicates particle 2.

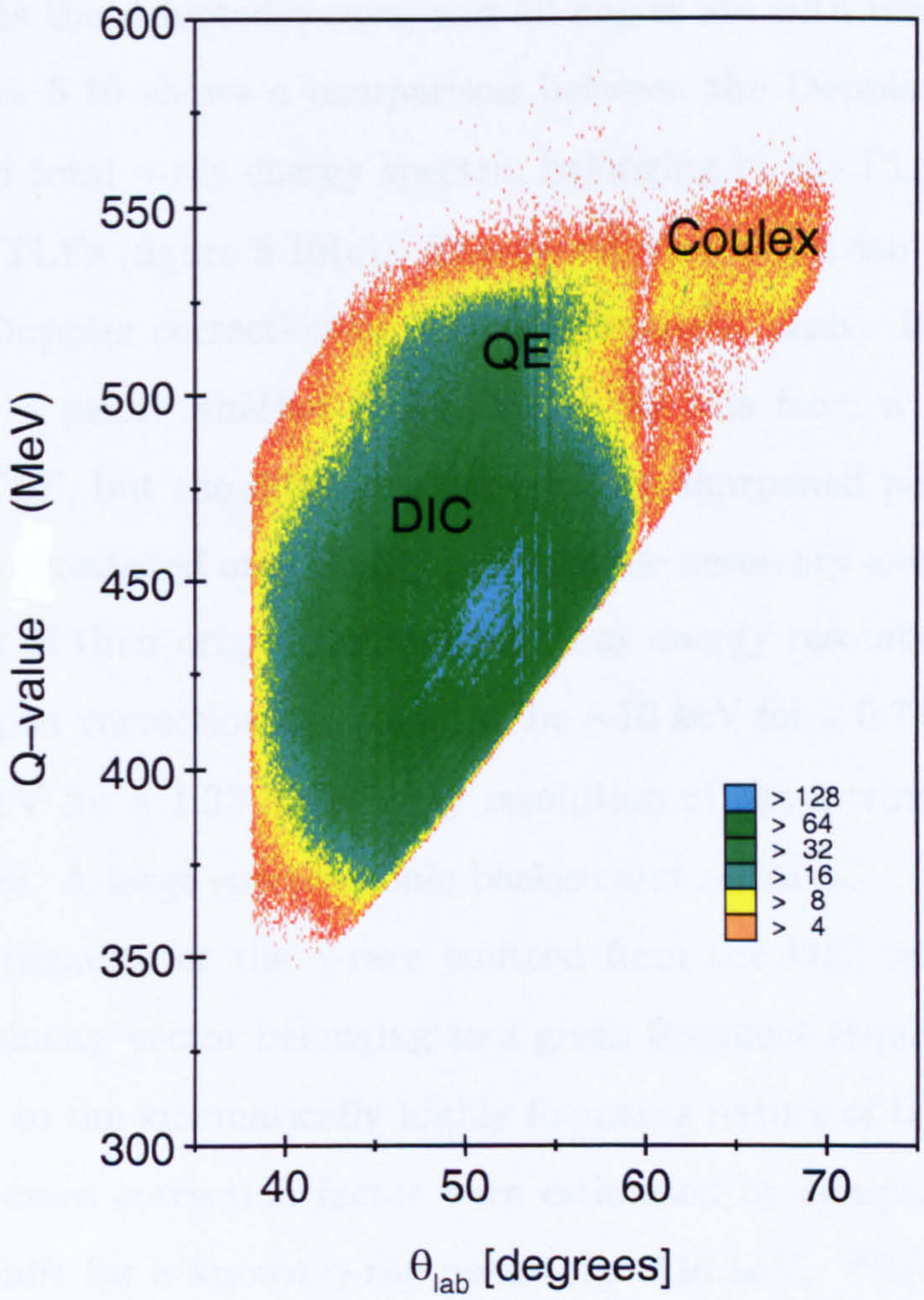

Figure 5.7: Experimental Wilczyńsky plot of Q-value against scattering angles for the TLFs populated in the present reaction. Note that the value 500 MeV was taken as the reference Q-value of 0 MeV.

coincident γ-rays can be calculated as

$$\cos\theta = \sin\theta_f \sin\theta_\gamma(\sin\phi_f \sin\phi_\gamma + \cos\phi_f \cos\phi_\gamma) + \cos\theta_f \cos\theta_\gamma, \qquad (5.3)$$

where the subscript f refers to a target-like or a projectile-like fragment and γ represents the detected γ-rays, and all angles are with respect to the beam.

Figure 5.10 shows a comparison between the Doppler uncorrected and corrected total γ-ray energy spectra, belonging to the PLFs (figure 5.10(b)) and the TLFs (figure 5.10(c)). Sharpened γ-ray lines can be seen to recover by the Doppler correction on an event-by-event basis. It was not possible to know a priori whether a detected γ-ray was from a heavier PLF or a lighter TLF, but the difference between the sharpened peaks in the spectra from the broadened ones clearly provides the necessary assignment about the fragment of their origin. Subsequent γ-ray energy resolution (FWHM) after the Doppler correction was found to be ~10 keV for a 0.711 MeV, compared to ~2 keV for a 1.33 MeV γ-ray resolution of the intrinsic HPGe detector resolution. A large spectroscopic background remains.

Additionally for the γ-rays emitted from the DIC reaction, the magnitude of the velocity vector belonging to a given fragment required further correction due to the kinematically highly focussing nature of the reaction. Values for this extra correction factor were estimated by comparing the measured energy shift for a known γ-ray peak (e.g. 536 keV, ^{100}Mo) at a given fragment scattering angle, θ_{lab}^{DIC}, and calculating the true recoil velocity using the Doppler equation 3.26. A linear dependence of the correction factor was assumed over the whole DIC scattering angle, although no further correction was applied to those fragments populated in the QE and Coulex channels. The resultant high-spin, γ^3 coincidence spectra obtained for all the even-even TLF nuclei populated in the current experiment are shown in figure 5.12, 5.14, 5.16 (DIC) and in 5.18, 5.20, and 5.22 (QE), together with the

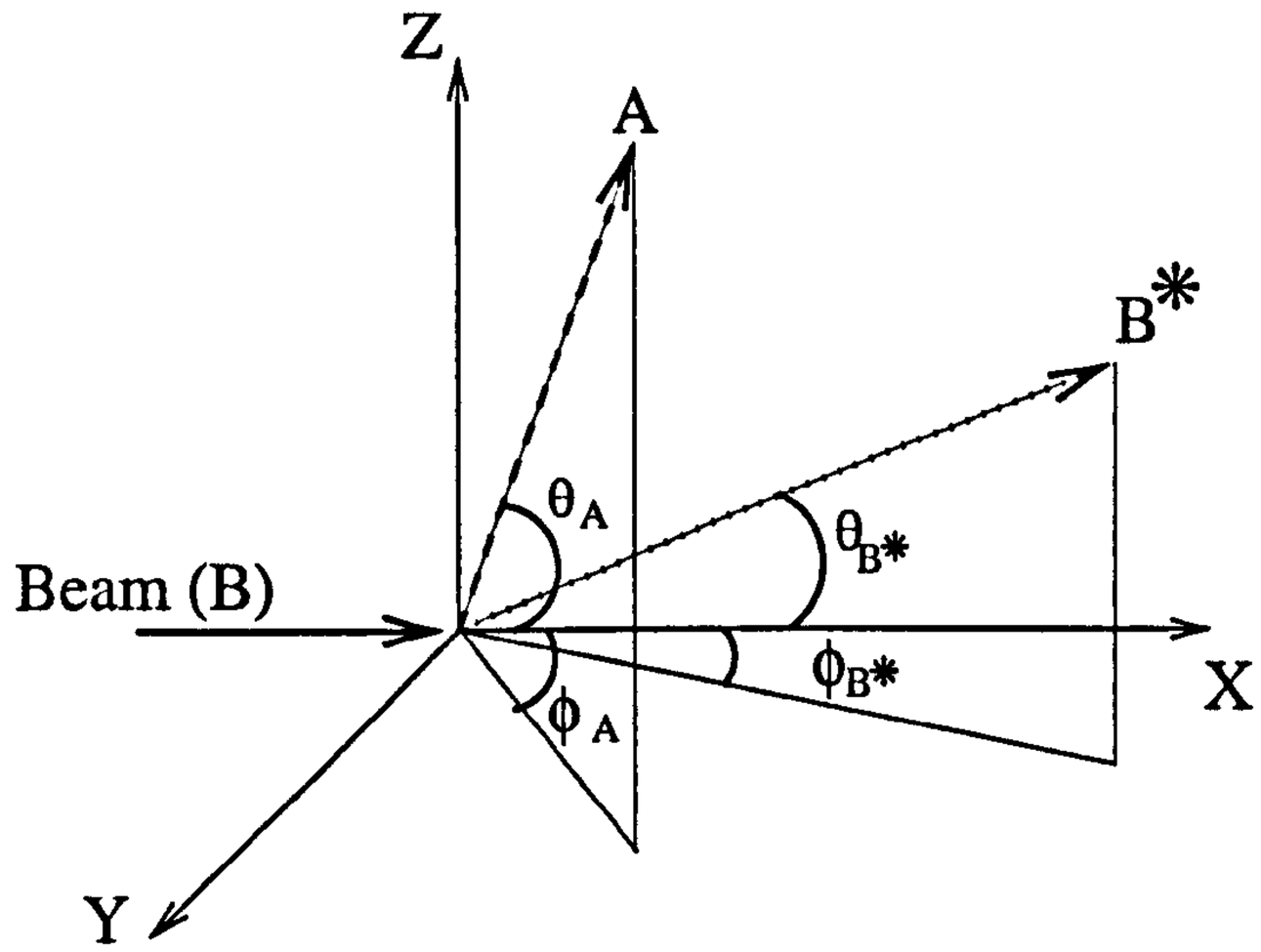

Figure 5.8: Definitions of velocity vectors and angles involved in the kinematic correction analysis.

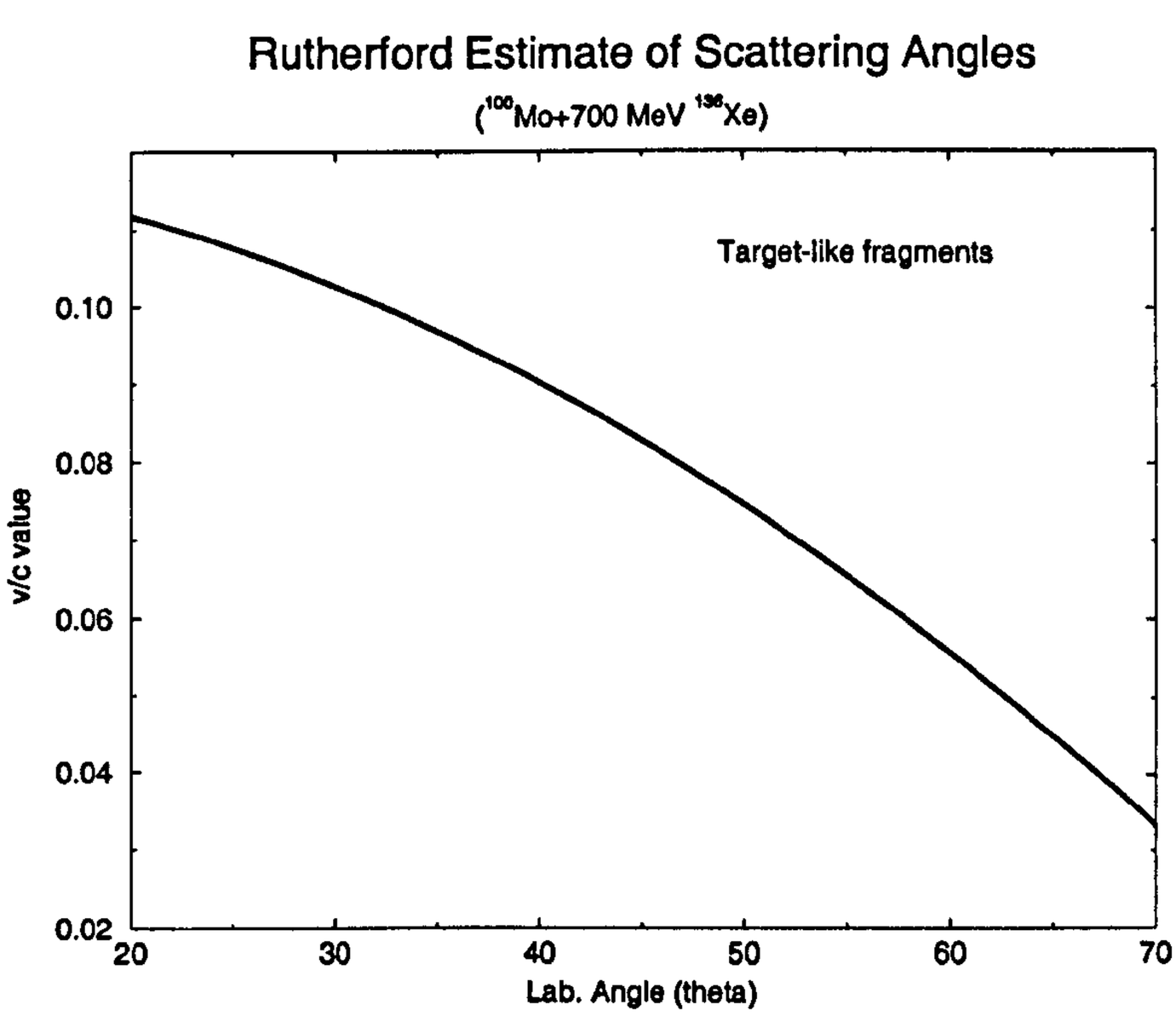

Figure 5.9: The Rutherford scattering estimate was used to calculate the v/c value of the target-like fragments over all detected scattering angles.

partial decay schemes for their yrast structures (figure 5.11, 5.13, 5.15, 5.17, 5.19, 5.21). In general, higher spin states were observed in the DIC-gated spectra as expected, although for the decay schemes of Mo-isotopes (figure 5.38, 5.41, 5.45, 5.48, and 5.15) suggests the QE channel to populate a greater number of low-lying states (see section 5.7).

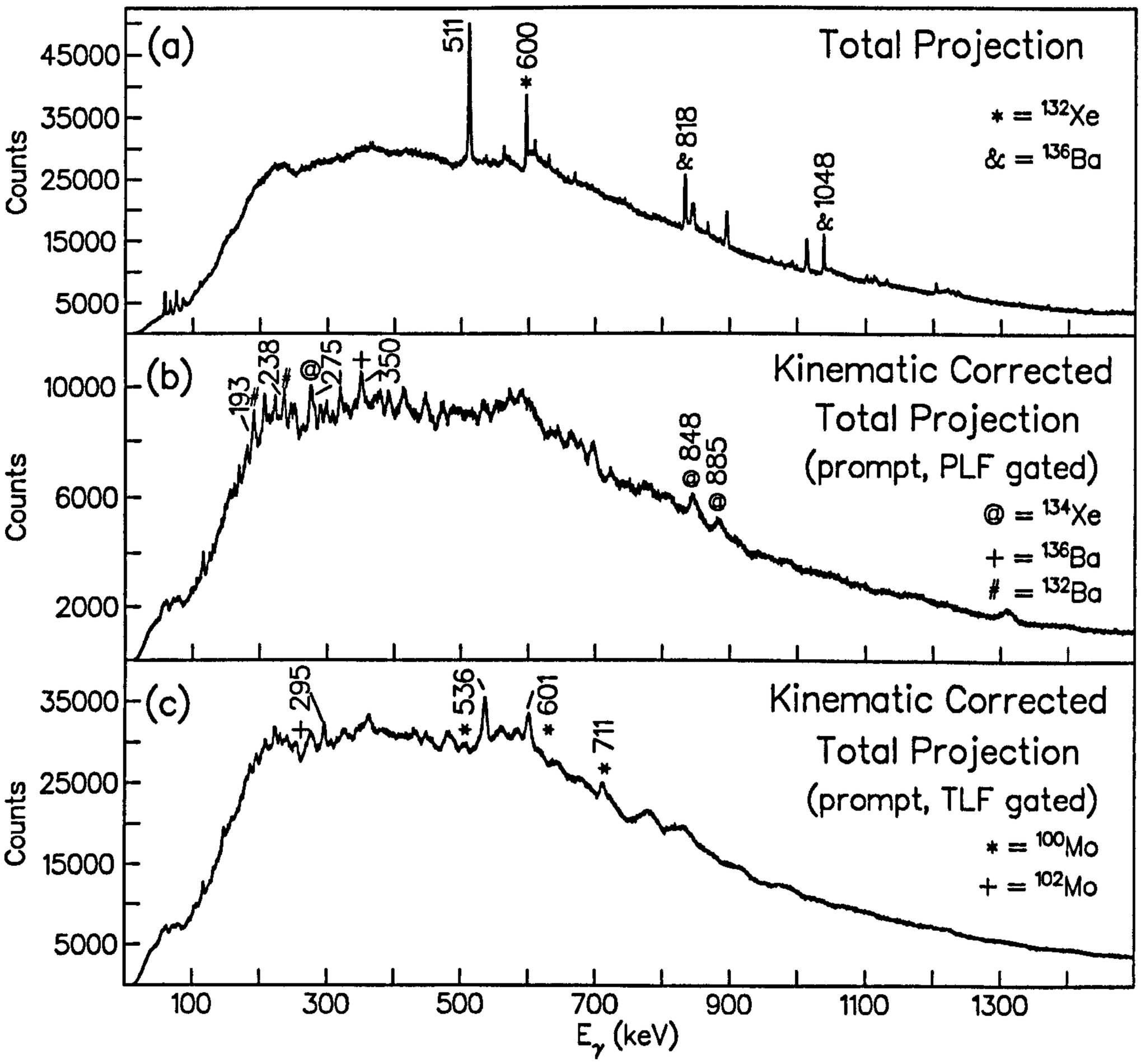

Figure 5.10: Projected prompt γ-ray spectra of (a) total reaction projection, (b) Doppler corrected spectrum for the projectile-like fragments, and (c) Doppler corrected spectrum for the target-like fragments.

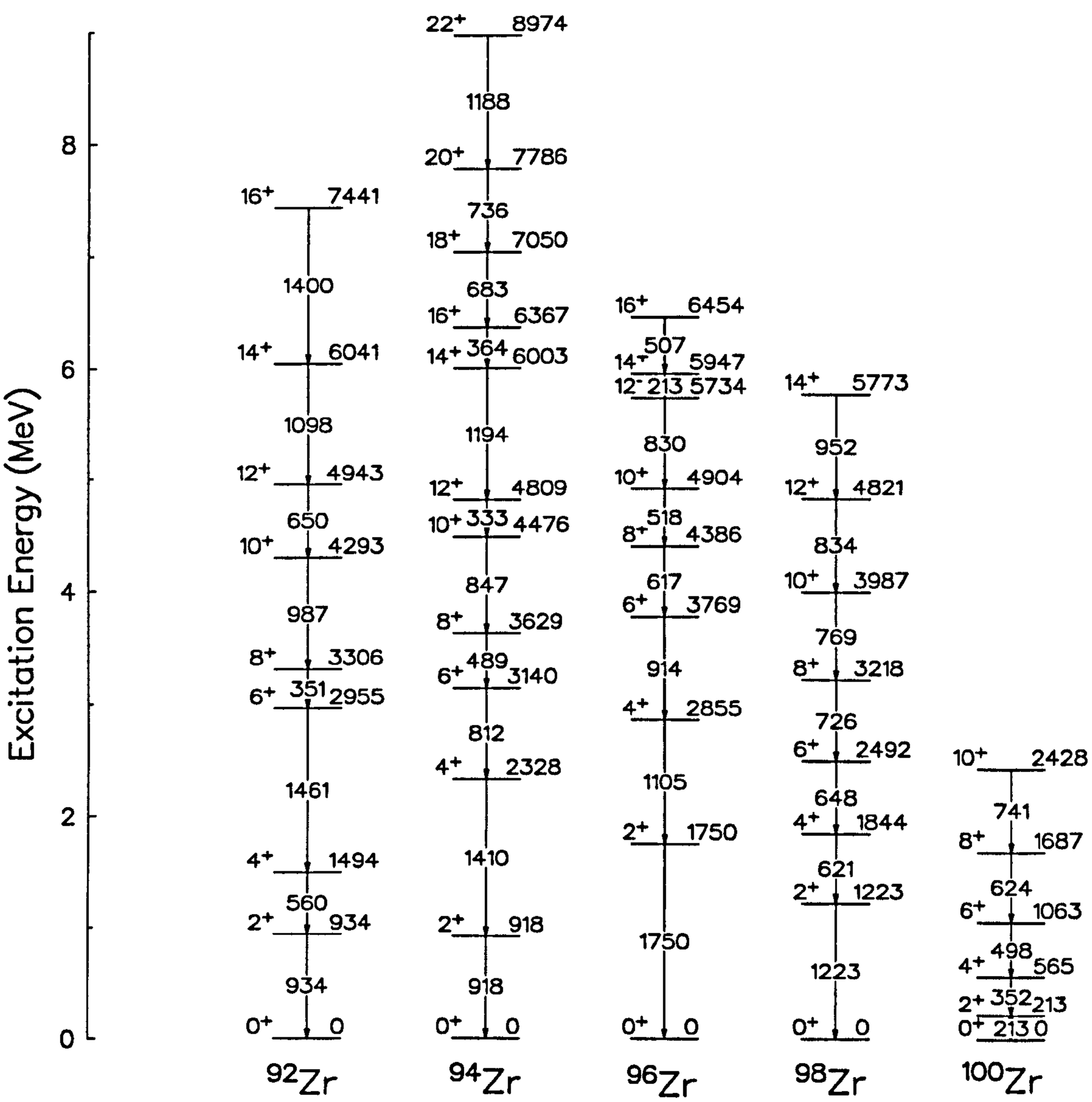

Figure 5.11: Partial decay schemes for the yrast band states of $_{40}$Zr isotopes populated in the DIC reaction [75, 76].

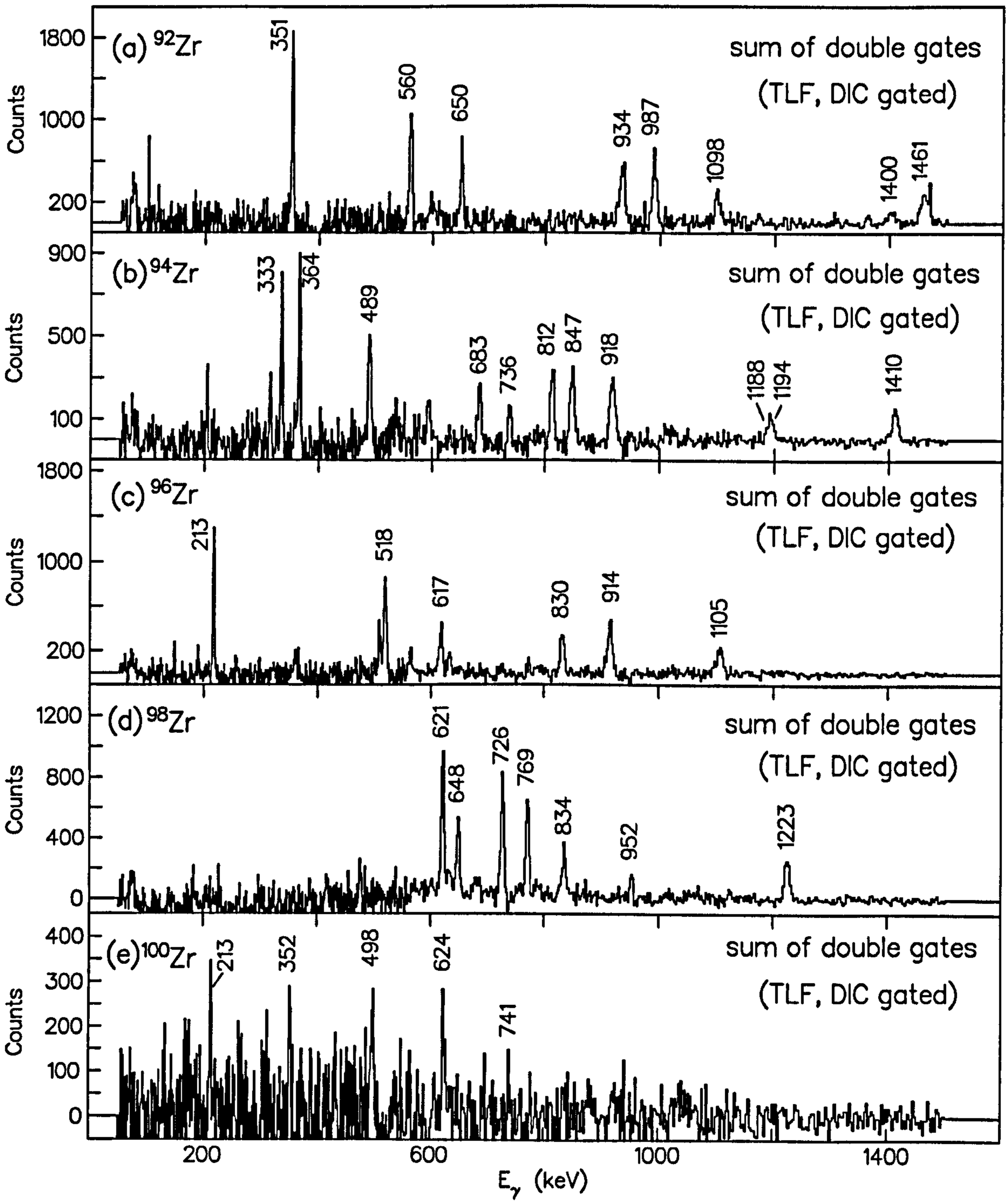

Figure 5.12: DIC-gated spectra of the sum of double γ–ray gates observed in the yrast states in $_{40}$Zr isotopes.

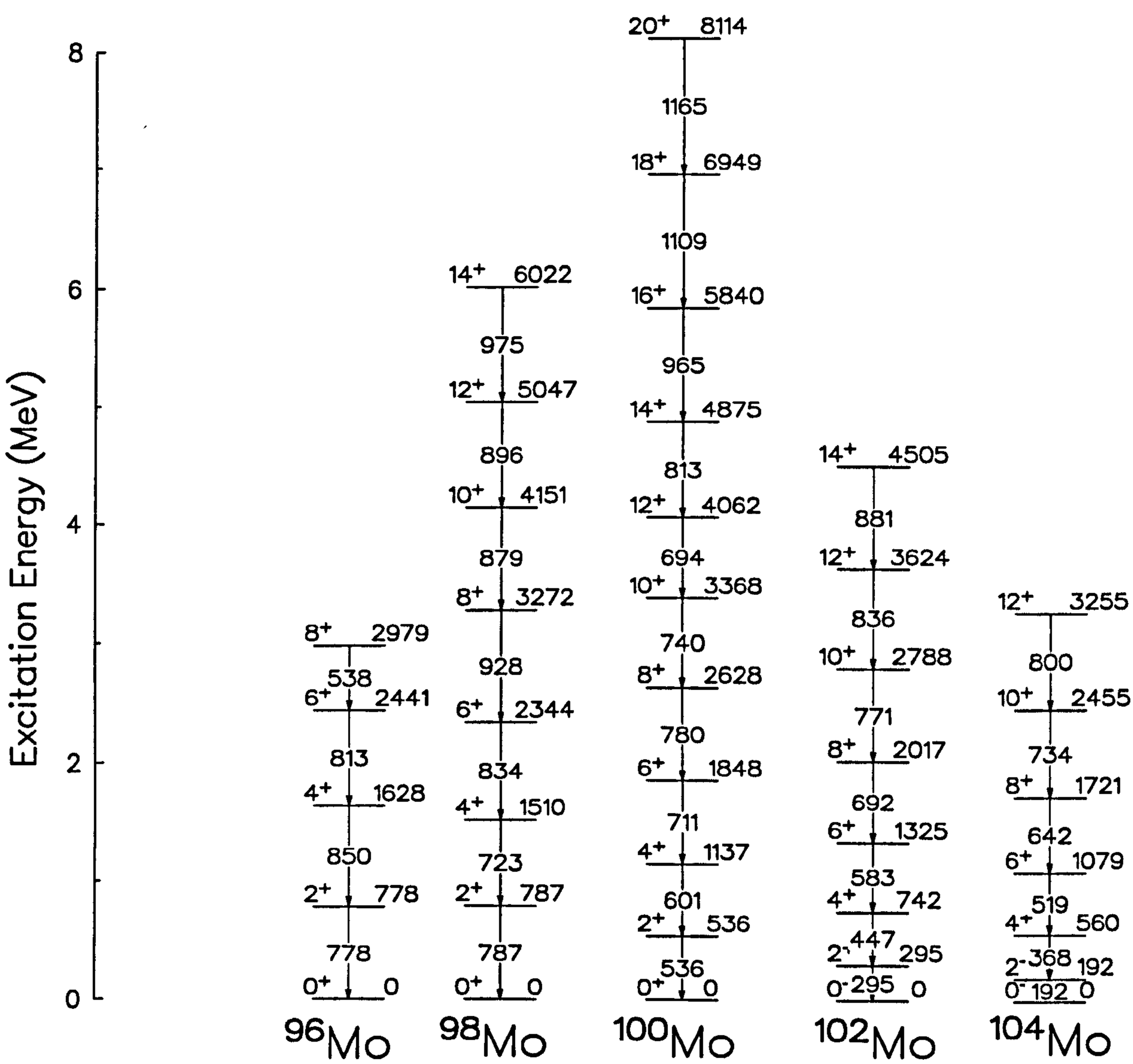

Figure 5.13: Partial decay schemes for the yrast band states of $_{42}$Mo isotopes populated in the DIC reaction [77, 78, 79, 81].

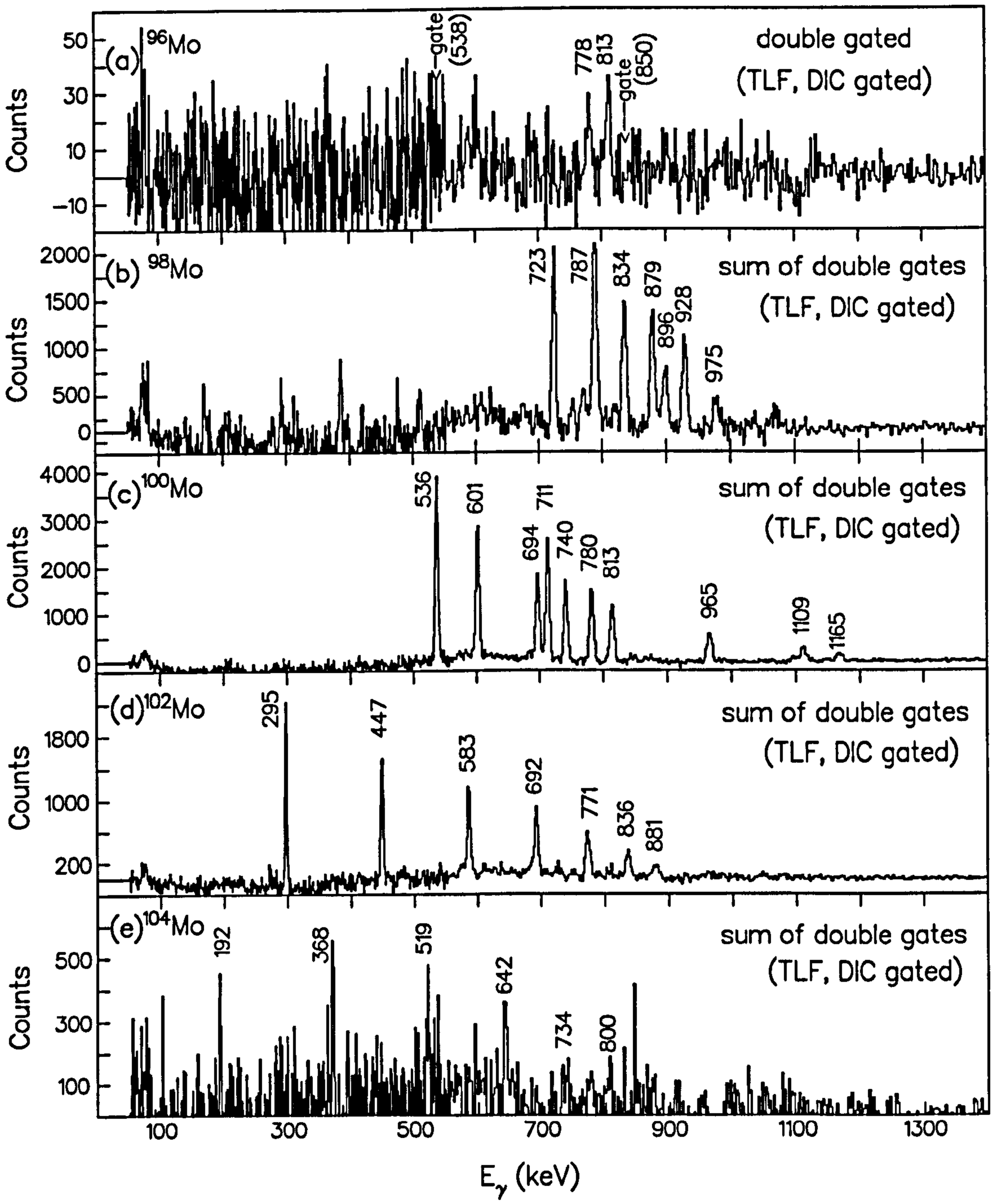

Figure 5.14: DIC-gated spectra of the sum of double γ−ray gates observed in the yrast states in $_{42}$Mo isotopes.

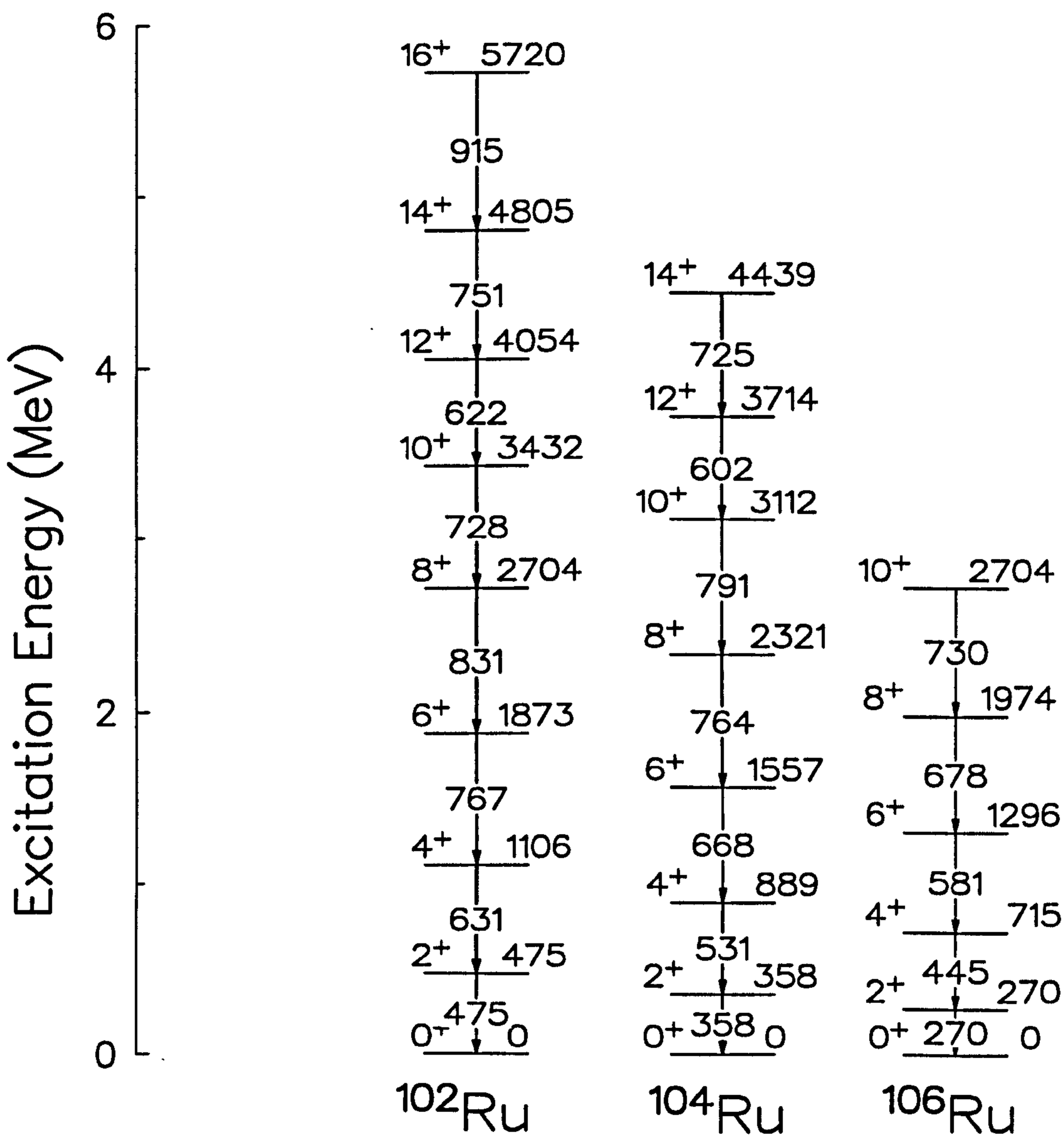

Figure 5.15: Partial decay schemes for the yrast band states of $_{44}$Ru isotopes populated in the DIC reaction [69, 79, 83].

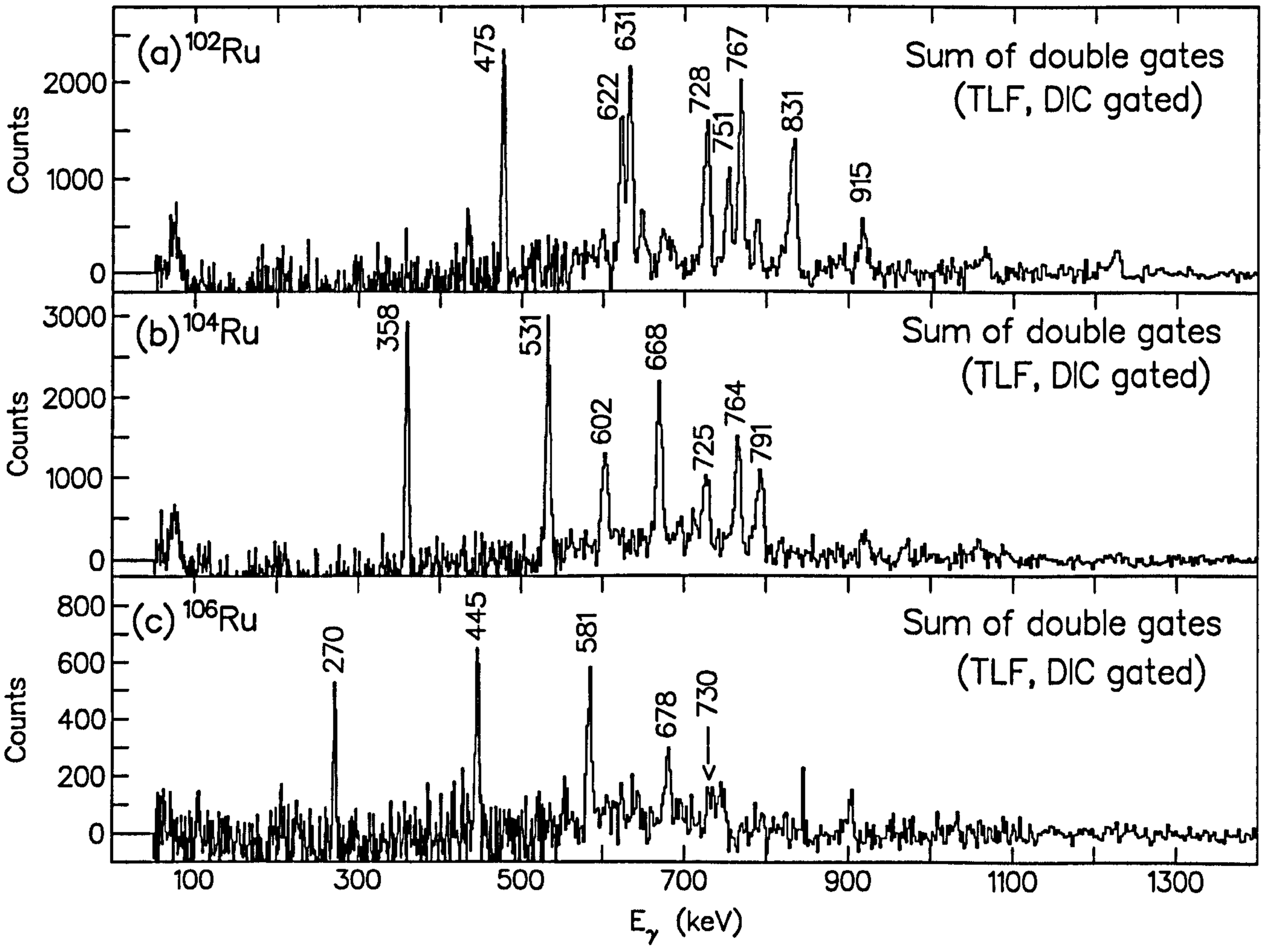

Figure 5.16: DIC-gated spectra of the sum of double γ−ray gates observed in the yrast states in $_{44}$Ru isotopes.

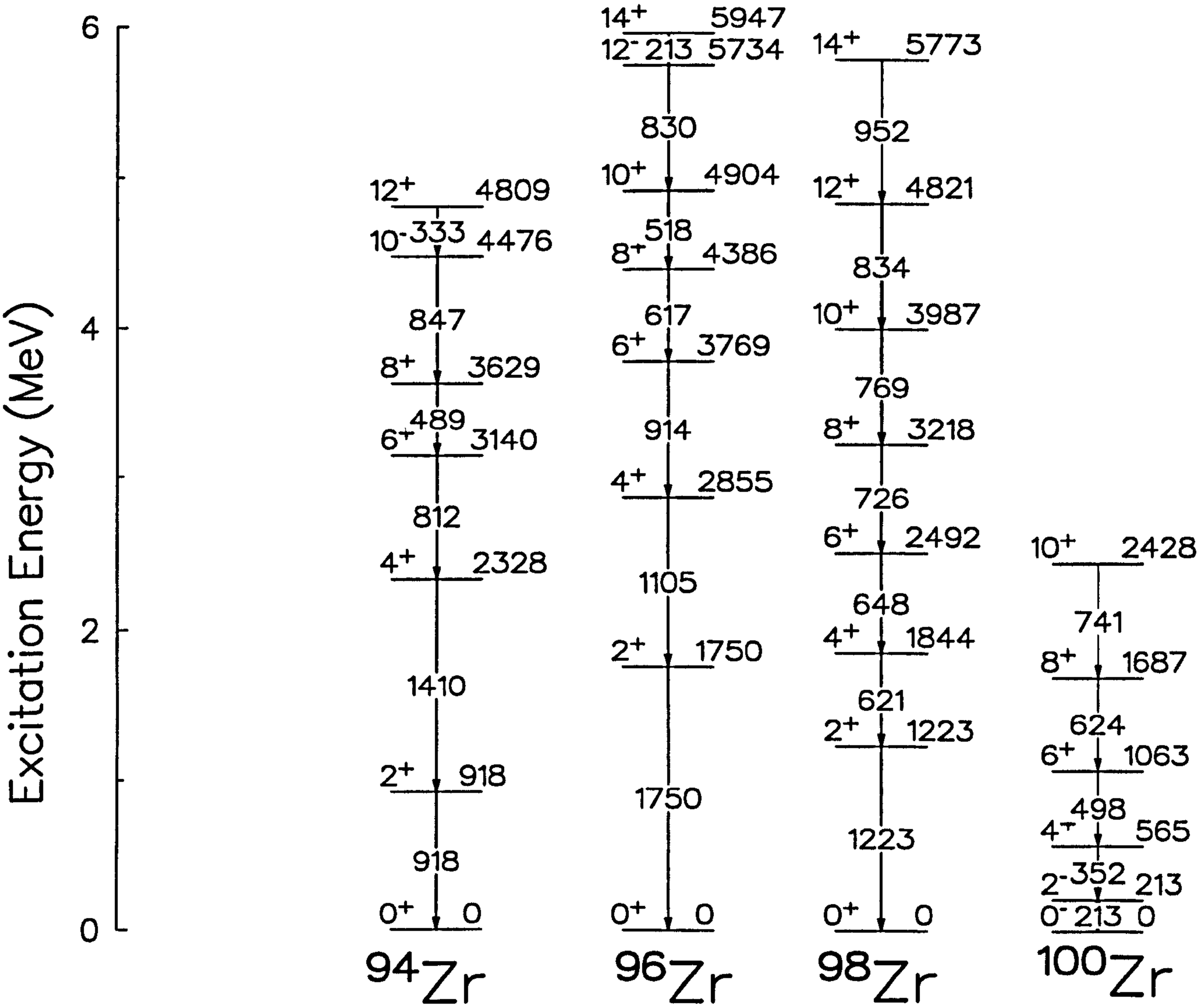

Figure 5.17: Partial decay schemes for the yrast band states of $_{40}$Zr isotopes populated in the QE reaction [75, 76].

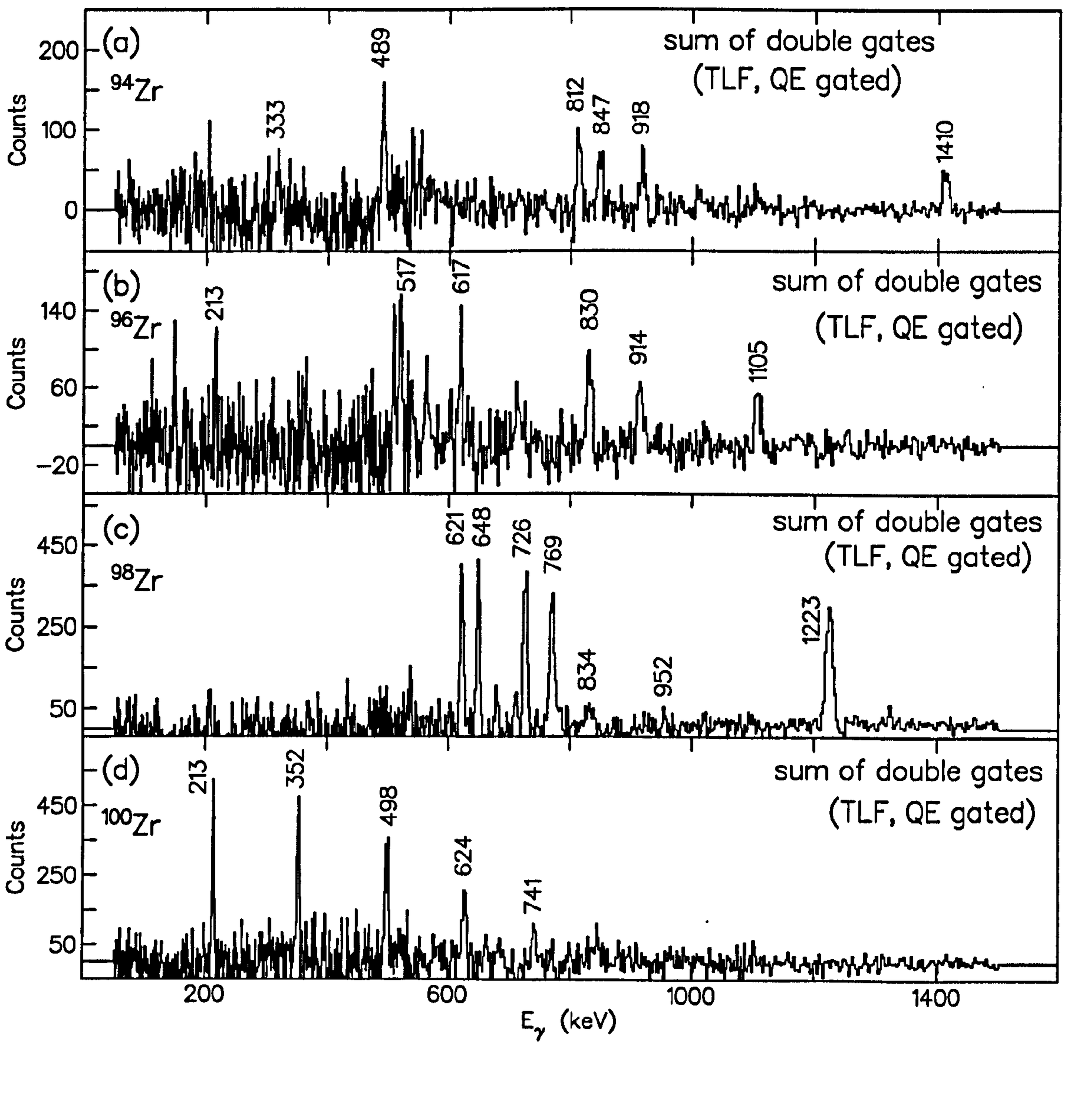

Figure 5.18: QE-gated spectra of the sum of double γ−ray gates observed in the yrast states in $_{40}$Zr isotopes.

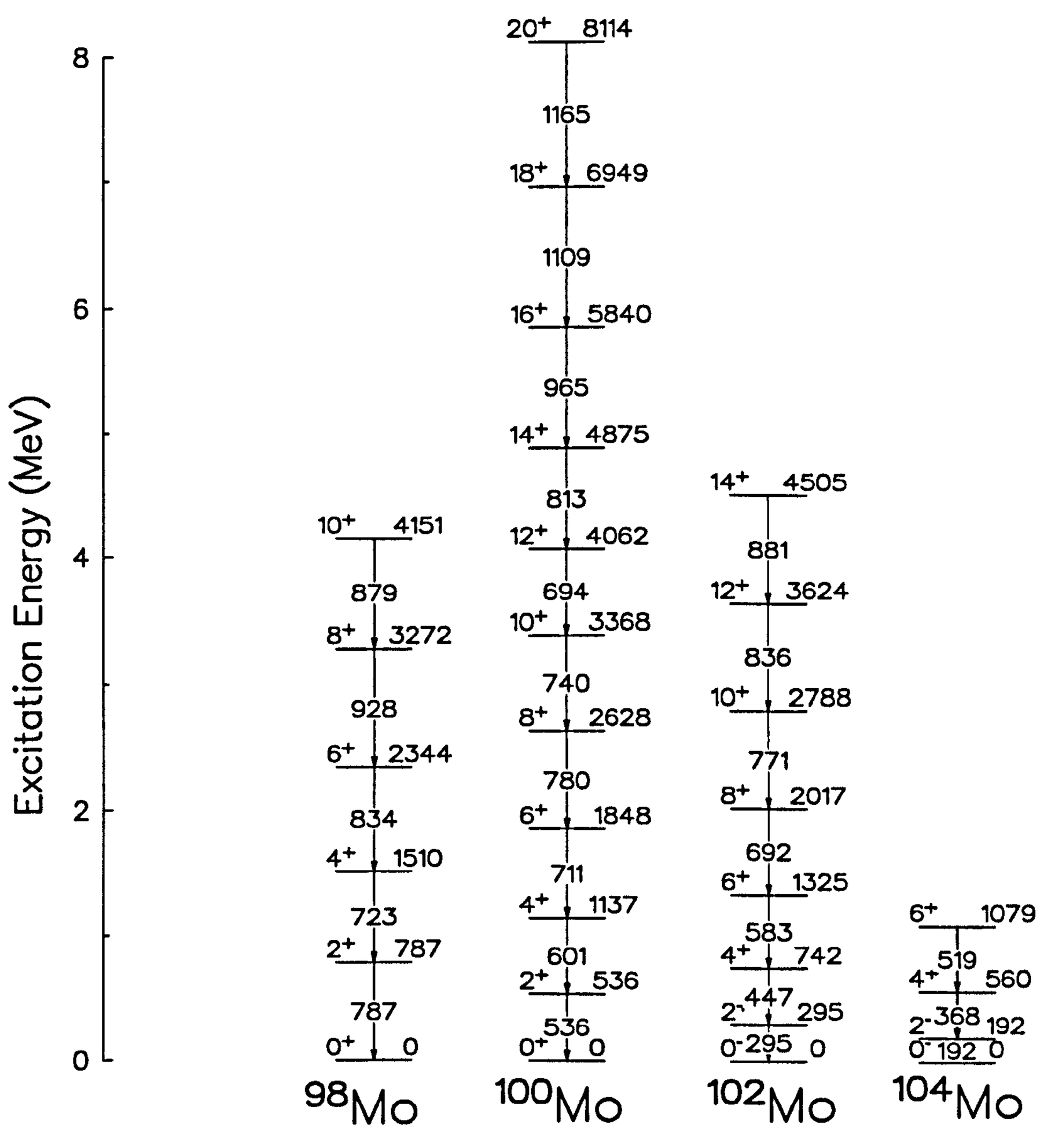

Figure 5.19: Partial decay schemes for the yrast band states of $_{42}$Mo isotopes populated in the QE reaction [77, 78, 79, 81].

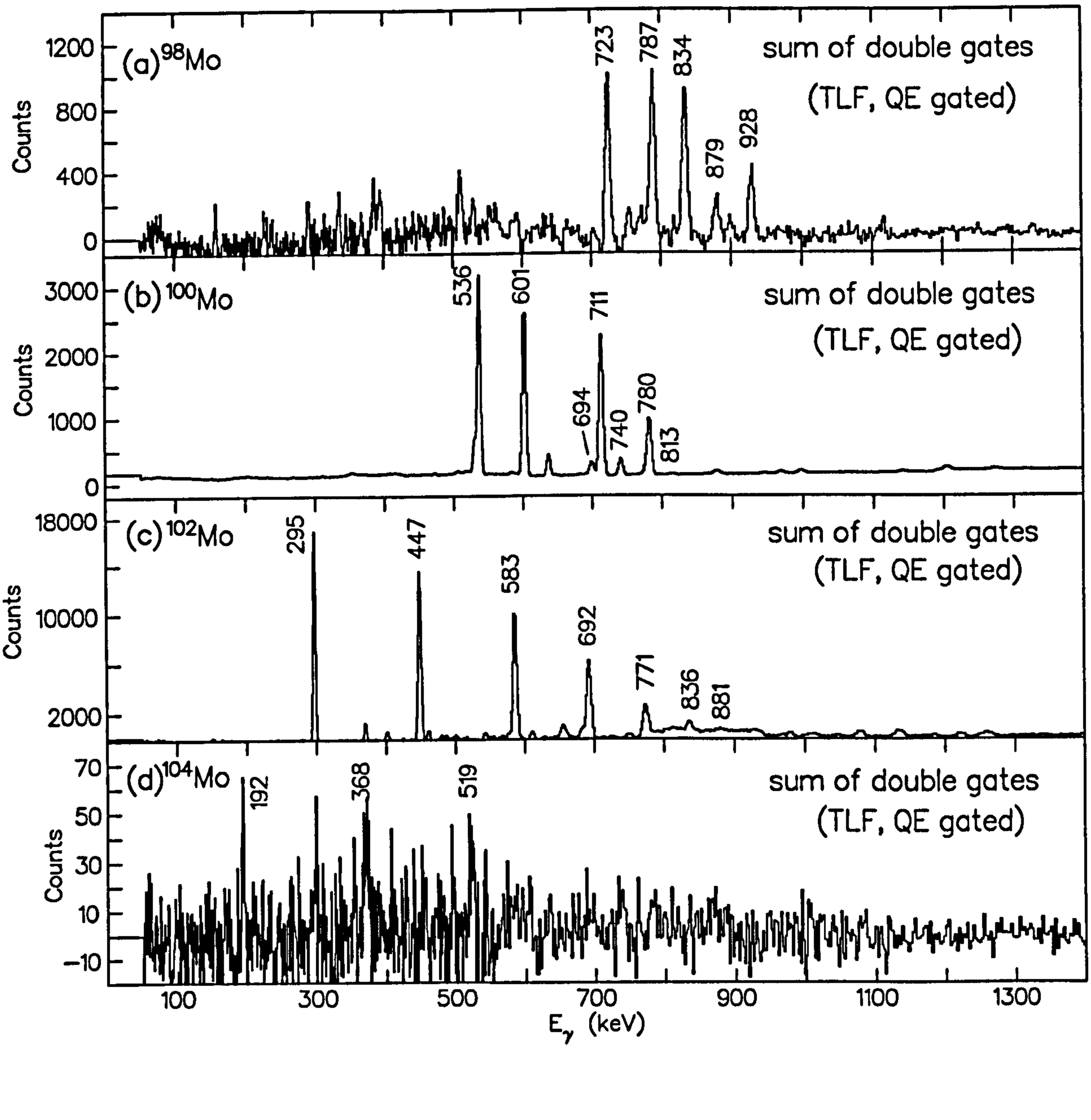

Figure 5.20: QE-gated spectra of the sum of double γ−ray gates observed in the yrast states in $_{42}$Mo isotopes.

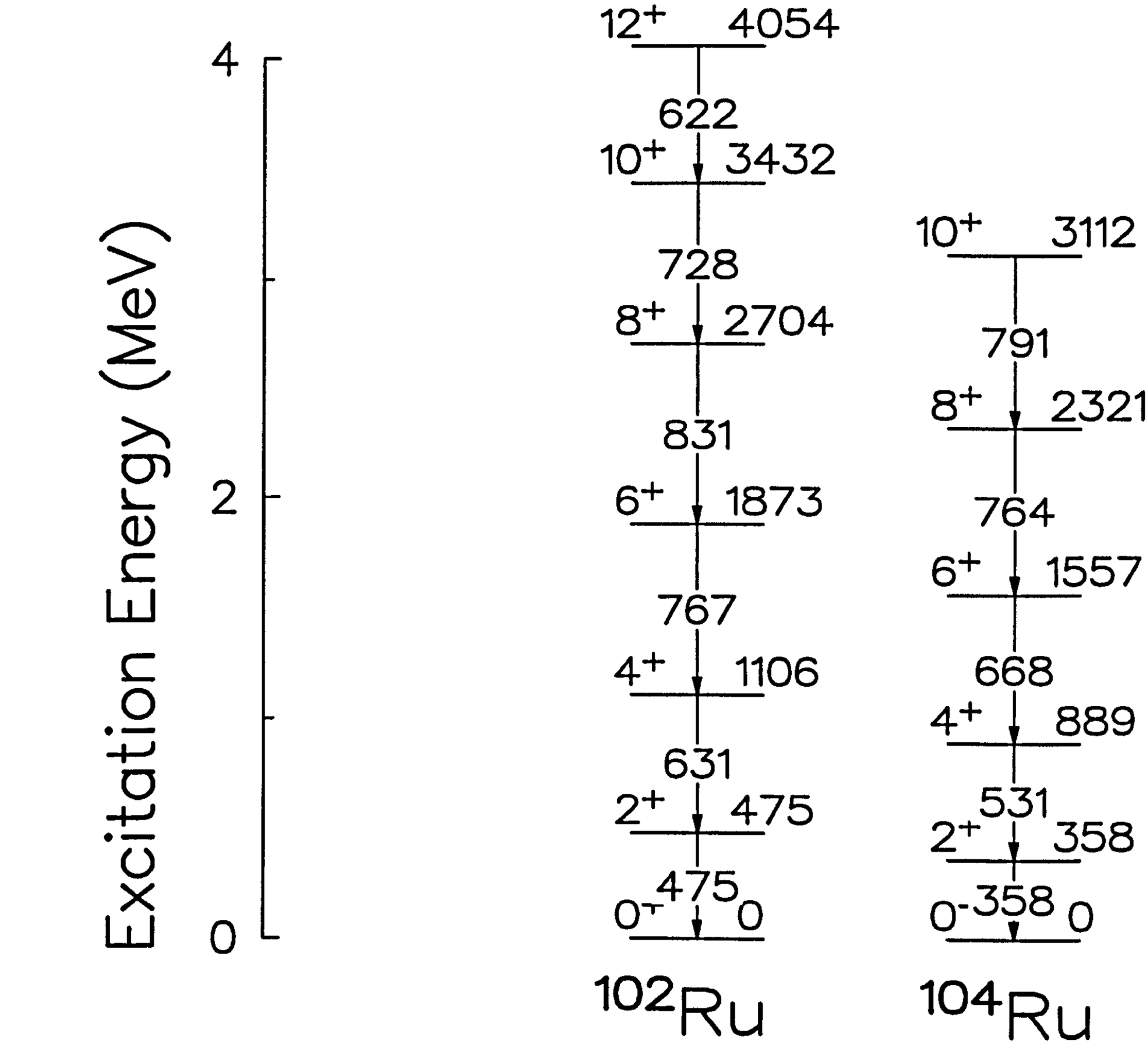

Figure 5.21: Partial decay schemes for the yrast band states of $_{44}$Ru isotopes populated in the QE reaction [69, 79, 83].

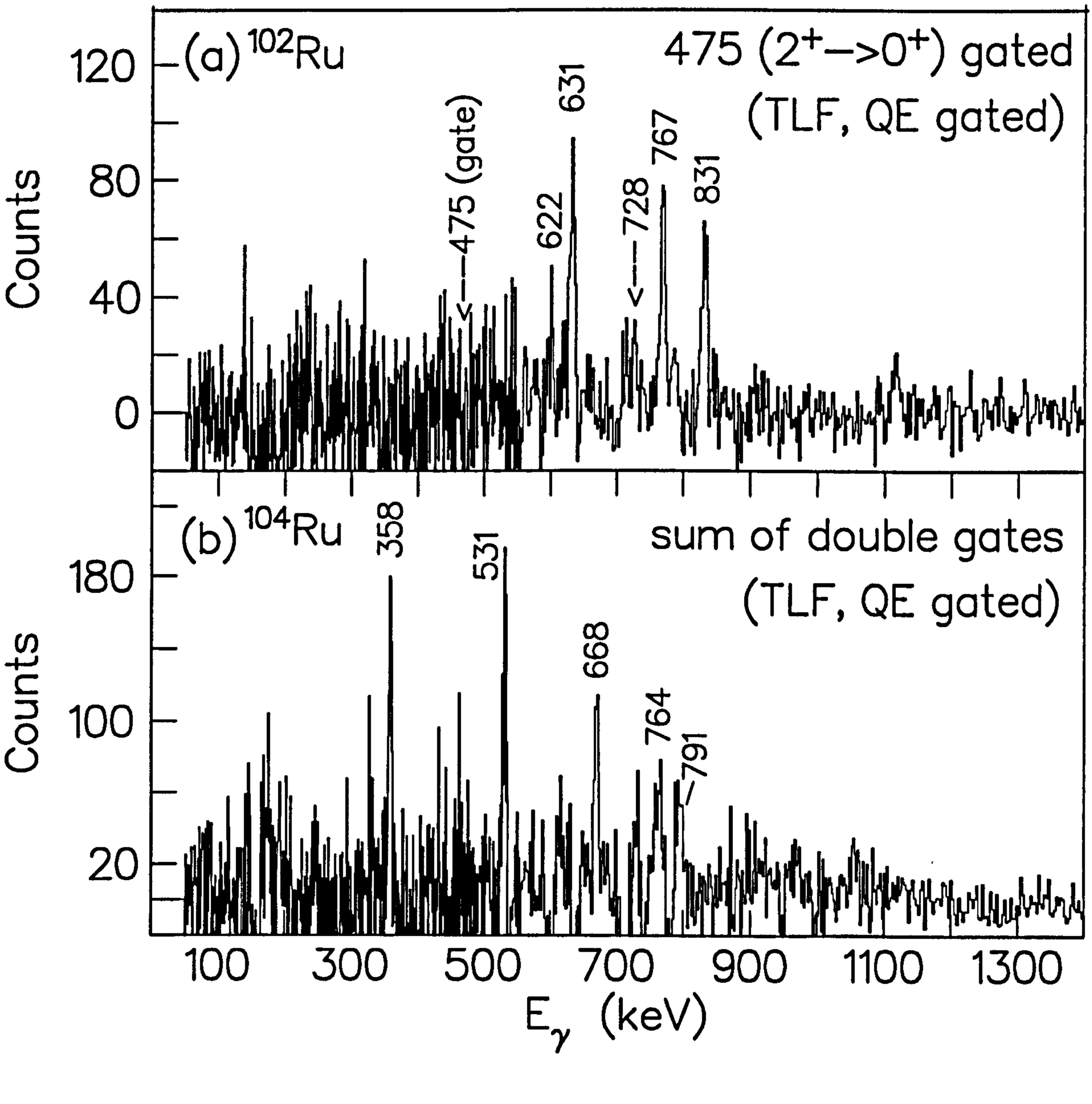

Figure 5.22: QE-gated spectra of the sum of double γ—ray gates observed in the yrast states in $_{44}$Ru isotopes.

5.5 Spin Generation in Binary Reactions

In accordance with the assumptions of the surface-friction model, the total amount of the relative to intrinsic angular momentum transferred in a binary reaction can be presumed to reflect the amount of energy dissipated in the reaction via frictional forces. The γ-ray fold, M_γ, defined as the sum of the number of Compton suppressed and unsuppressed Ge events plus the BGO-only events, can be utilised as a measure of the maximum angular momentum induced in the reaction fragments, neglecting the spins carried away by the evaporated particles.

In the present experiment using the ^{100}Mo + 700 MeV ^{136}Xe binary reaction, a typical fold distribution may be decomposed into a region about a small value of fold, called the quasi-elastic (QE) regime, and a larger value of fold, called the deep inelastic (DIC) regime (figure 5.23). As the fold distribution specifically gated on a 536 keV (^{100}Mo, $2^+_1 \rightarrow 0^+_1$) transition illustrates, different reaction mechanisms may contribute to populate a particular spin state of a given exit channel. The proportion of each reaction mechanism giving rise to the spin of the state is then assumed to reflect the minimum amount of energy loss required to populate the same spin for the same exit channel. Utilising the recoil-γ coincidence, the QE and DIC reactions defined in figure 5.23 were projected onto the Wilczyńsky plots shown in figure 5.24, which seem to provide some support to this assumption. It is worth noting, however, that a strict distinction between the quasi-elastic (QE) and deep inelastic (DIC) regimes could not be made experimentally, and that there were always some tails in the QE or DIC regimes that extended into the other regime within a given fold distribution. This gradual change in the reaction mechanisms when working in the spin regime is usually explained as a manifestation of the diffusiveness associated with the heavy-ion reaction.

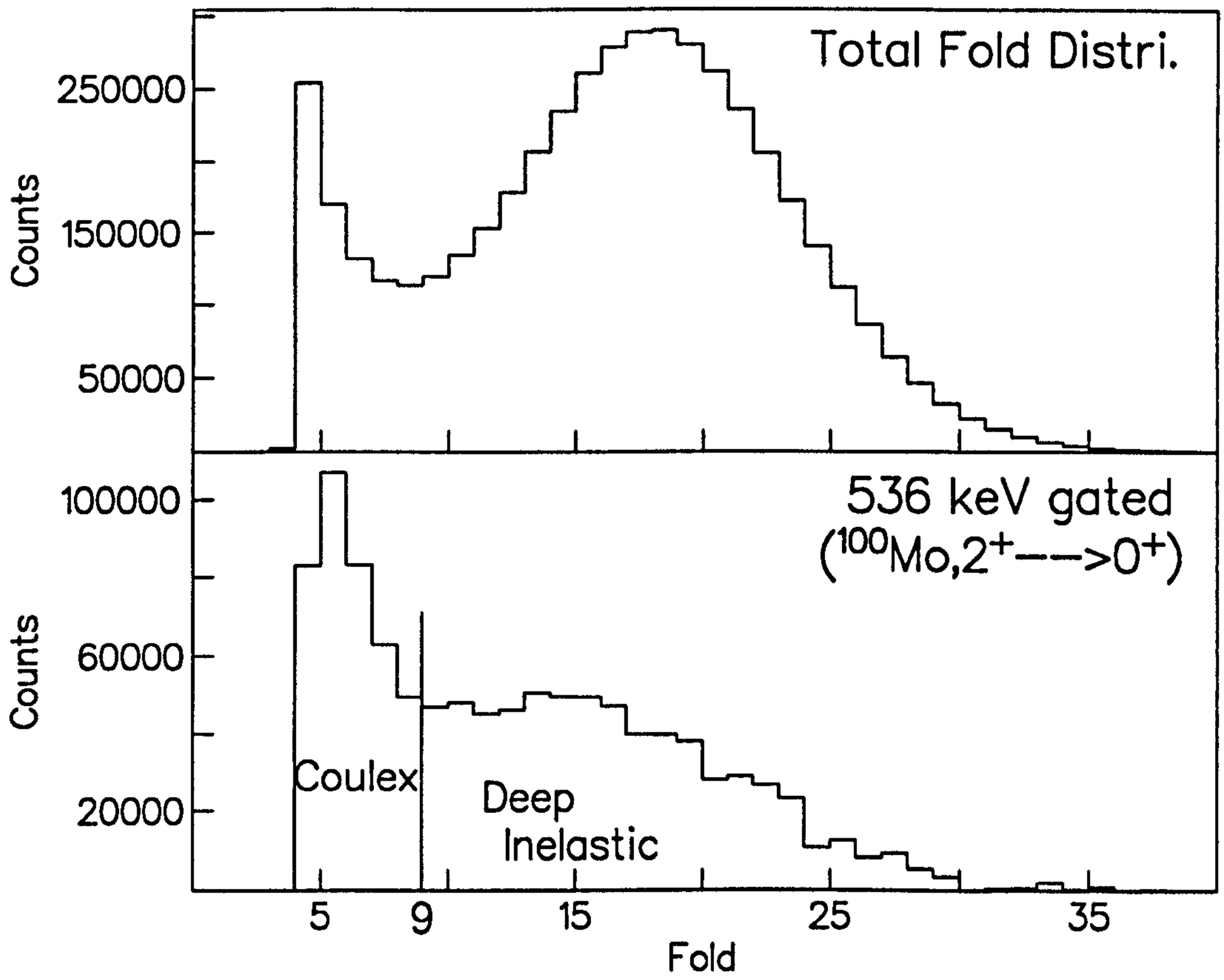

Figure 5.23: Fold distribution spectra obtained from the current experiment in associa tion with (top) the total reaction and (bottom) 536 keV ($2_1^+ \rightarrow 0_1^+$, ^{100}Mo) transition. In the bottom figure, the value of fold less/greater than 9 was defined as Coulex/DIC.

Additionally, different fold distributions obtained by gating on selected, discrete yrast transitions in ^{100}Mo nucleus are shown in figure 5.25. For lower-lying states up to 8^+, a spin state in the beam or target nucleus can be accessed via both quasi-elastic and deep inelastic reactions, although the increasingly important deep inelastic reaction contribution to the population of higher spin states is obvious. At a spin of 10^+ in ^{100}Mo, however, a

sudden change in the underlying population mechanisms seems to suggest that the 10^+ spin state can only be accessed via the DIC process. This particular change at 10^+ coincides with a structural change, namely the band-crossing in the ^{100}Mo nucleus. Thus, the DIC reaction characteristic of high inelasticity seems to be a pre-requisite to access any high spin states involving a high degree of nuclear rearrangement within the reaction fragments. Such a dominantly dissipative character of the DIC reaction mechanisms seems to

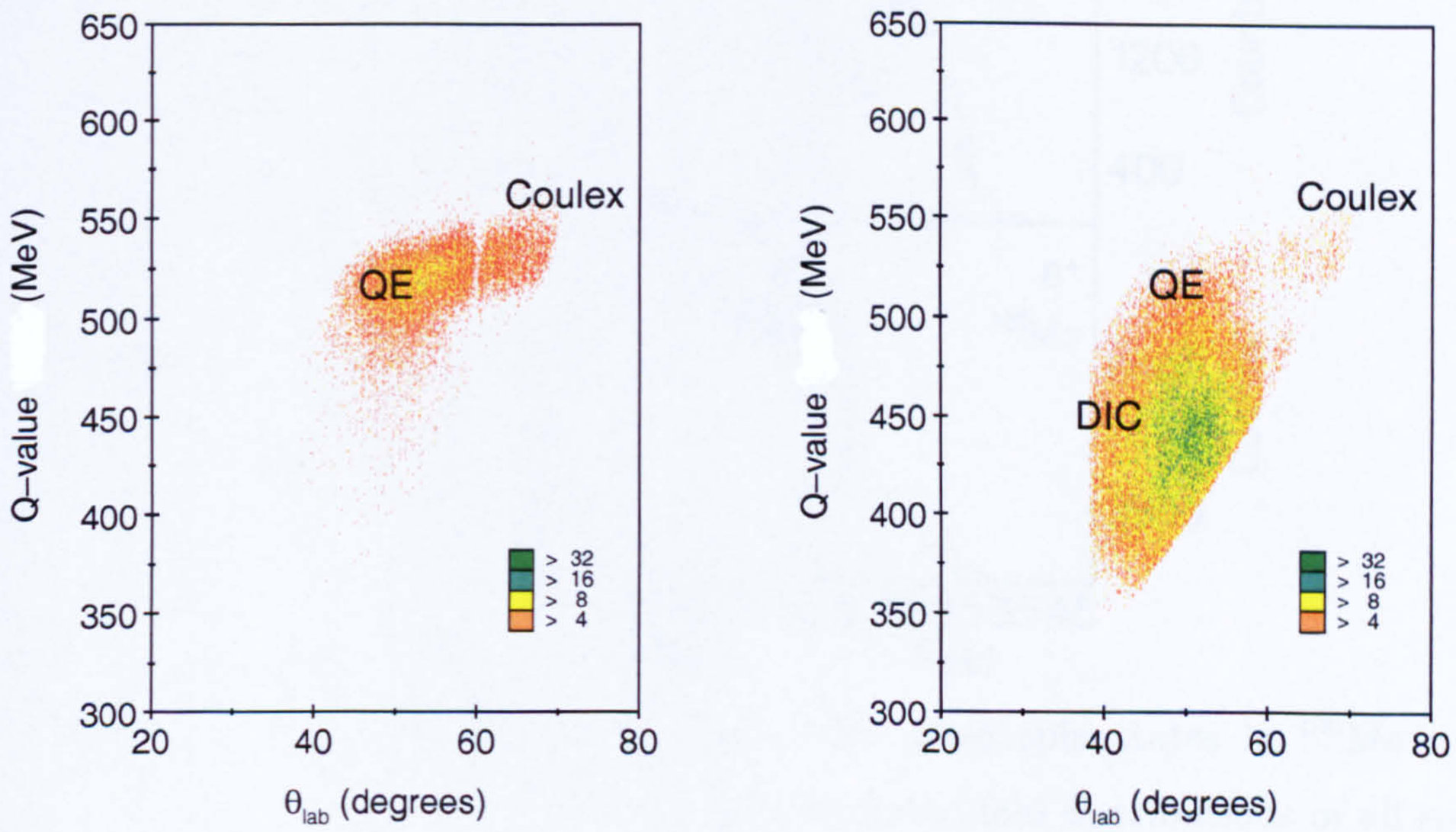

Figure 5.24: Wilczyńsky plots produced by gated on the (left) Coulex and (right) DIC regimes, as defined in the fold distribution belonging to 536 keV ($2_1^+ \rightarrow 0_1^+$) transition in ^{100}Mo (see figure 5.23).

suggest a possible relationship between the initial relative spin and progressive interaction time leading to fusion (a limit of complete thermal and mass equilibrium), indicated by the friction-driven kinetic energy damping.

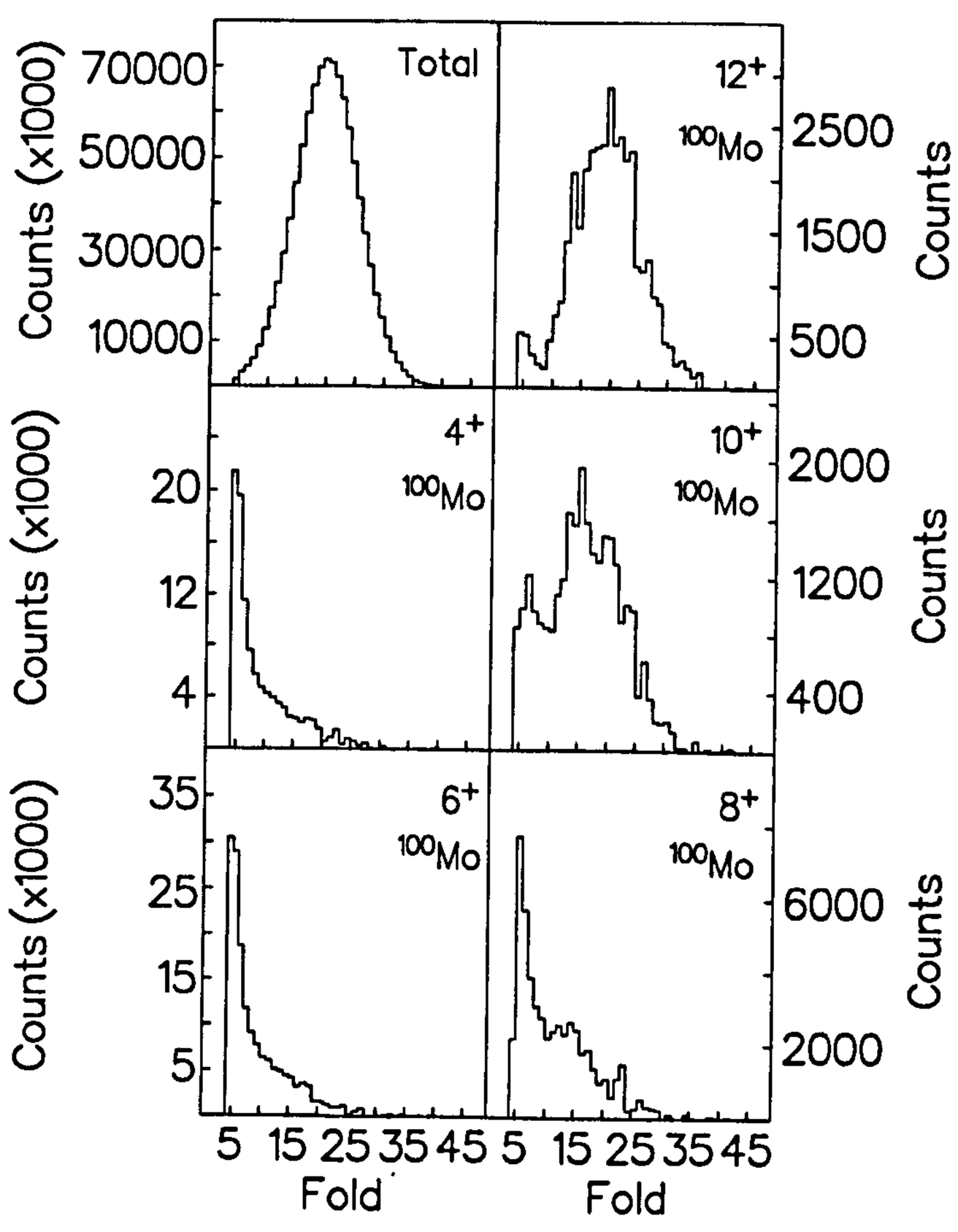

Figure 5.25 Fold distribution spectra for given spin states in ^{100}Mo exit channels. Double γ-ray gated fold distributions of all spin states up to the quoted spin were added to produce the spectra.

Utilising the partial wave approximation of the heavy-ion reactions, the observed scattering angles may be correlated to the length of the interaction time between the two colliding nuclei [89, 90, 91, 92]. Care has to be taken

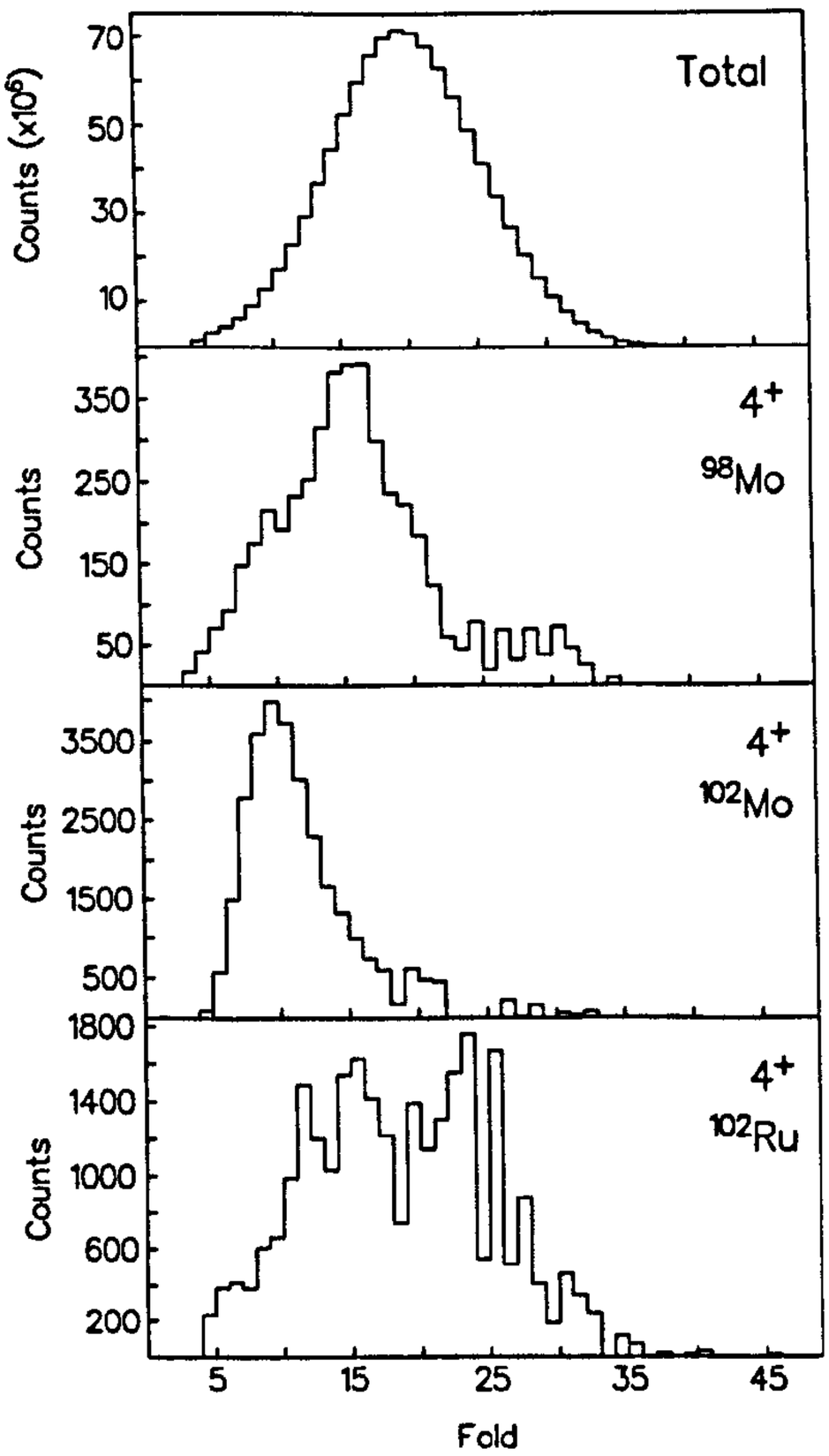

Figure 5.25: Fold distribution spectra for given spin states in ^{98}Mo, ^{102}Mo and ^{102}Ru exit channels. Double γ-ray gated fold distributions of all spin states up to the quoted spin were added to produce the spectra.

for the interpretation of such angular distribution data for the heavy-ion reaction well above the Coulomb barrier, since a large number of open channels and recoil effects present under such conditions may contribute significantly to disturb the average and gross properties of the reaction. Figure 5.26 ((a) and (b)) illustrates the general trends observed between the angular distributions of different TLFs, gated on a specific kinematic energy loss in the present experiment. The average patterns emerging from this figure suggest relatively significant and noticeable changes in the average deflection angle with increasing Q-value loss. Together with the observation of narrowing width in scattering angle distribution with the increasing Q-value loss (which is characteristic of the nuclear rainbow effect leading to kinematic focussing), the measured Q-value loss is likely to be dynamical in origin, and is not quantum or statistical fluctuations. Therefore, it seems clear from the general angular distributions that the deflection angles are dependent on the energy loss, but not on the atomic number, Z, of the reaction fragments. Despite the small distribution of spread in Z observed in this particular experiment, this finding seems to indicate the primary role of the energy loss (inelasticity) as an indicator of the progress of the reaction, *i.e.* interaction time. Therefore, on average, the energy loss may be interpreted to increase with increasing interaction time which, in turn, increases with decreasing initial relative angular momentum. The progressive dissipation of kinetic energy of relative motion during a collision forms the basis for dynamical reaction models employing frictional forces, for which the present data seem to provide independent support.

However, the assumption of strict correlations between the intrinsic angular momentum manifested by the fold distribution and the reaction interaction time represented by the total energy loss may be premature. The

correlation observed from this experiment is illustrated in figure 5.27, which plots the average reaction fold (recoil gated) against the observed Q-value loss, and shows that, with increasing energy loss, the average fold, and presumably the total fragment spin, initially increases. However, for energy losses in excess of ~50 MeV, the average fold starts to saturate and forms a plateau of ~75 MeV wide. This finding seems to invalidate any simple stick-

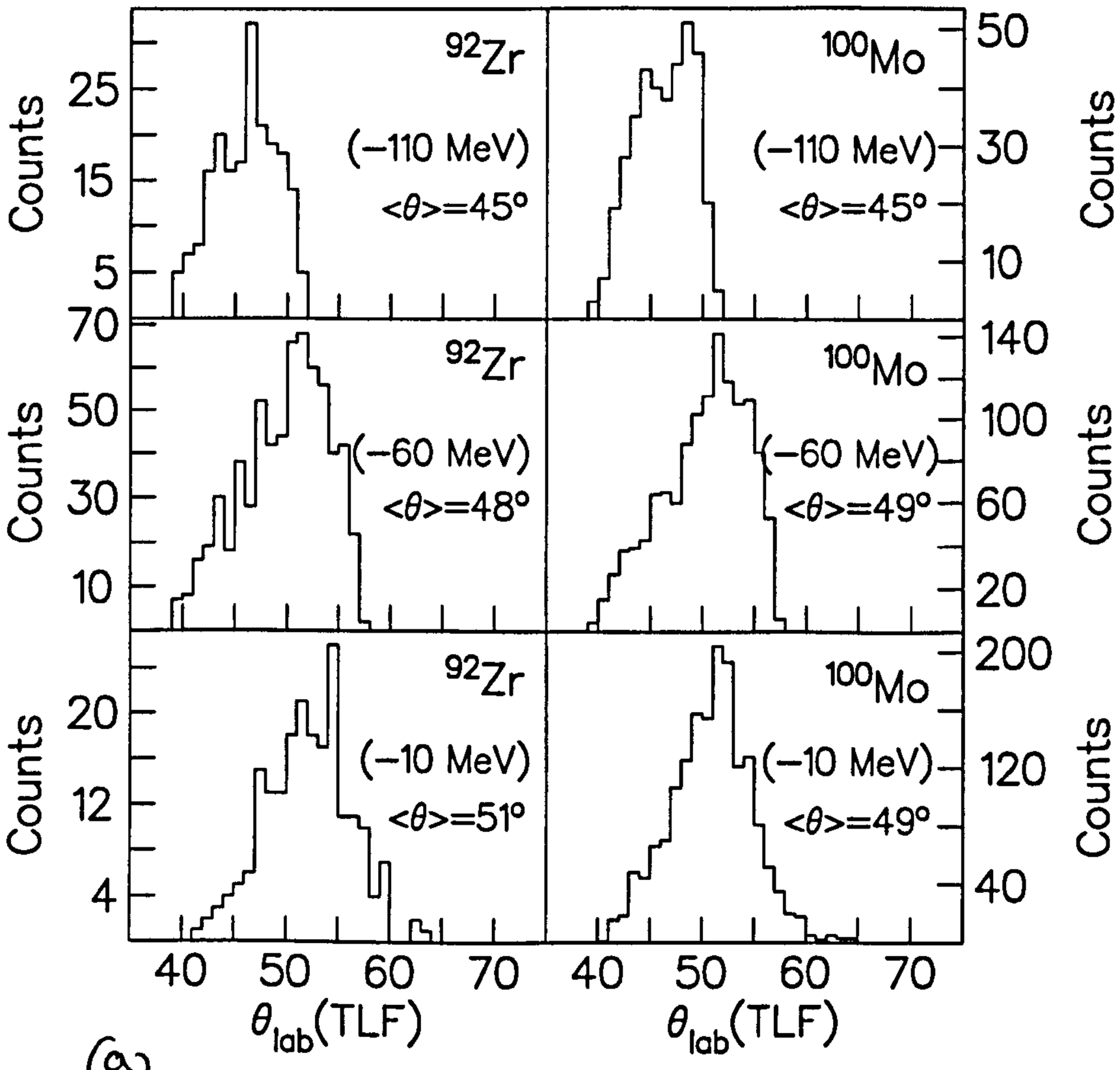

Figure 5.26: TLF scattering angles gated on specific exit channels. All exit channels were identified by gating on the $4^+ \rightarrow 2^+$ and the $2^+ \rightarrow 0^+$ γ-ray transitions (see also figures 5.11 to 5.22), and the quoted numbers in brackets are Q-value (Q-value of 0 MeV is shown as 500 in Figure 5.7).

ing or rolling limit of the surface-friction model, in which the final fragment spin is always proportional to the initial spin, I, although the constants of proportionality for the model depend on the final fragment masses (see

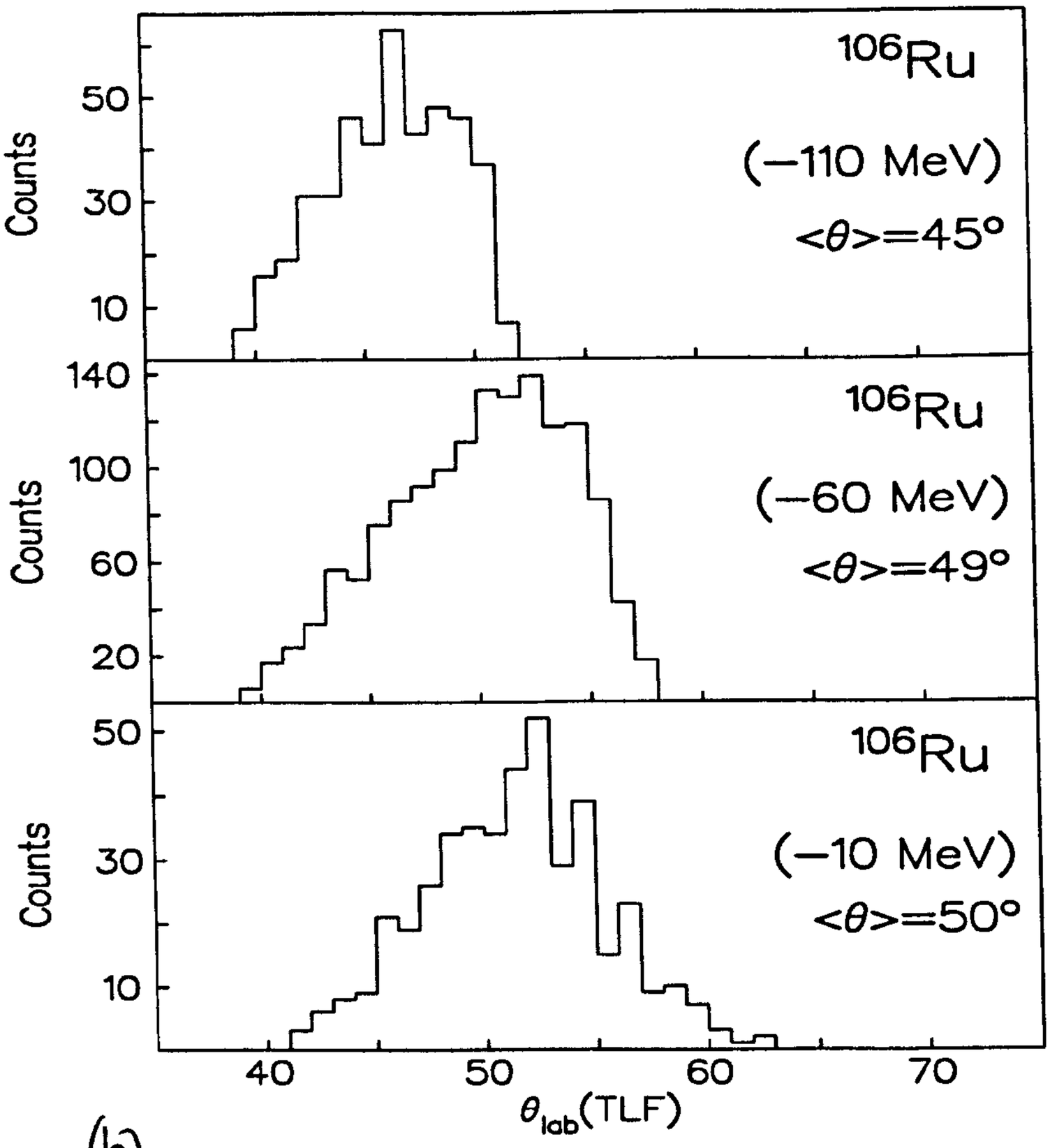

Figure 5.26 (b) TLF scattering angles gated on ^{106}Ru exit channels. All exit channels were identified by gating on the $4^+ \rightarrow 2^+$ and the $2^+ \rightarrow 0^+$ γ-ray transitions (see also figures 5.11 to 5.22), and the quoted numbers in brackets are Q-value (Q-value of 0 MeV is shown as 500 in Figure 5.7).

equations 3.17-3.19). The likely explanation for the discrepancy found above may result from the assumption that the dissipation forces, acting on the tangential motion, are always strong enough to drive a heavy-ion colliding system to a situation of rolling or sticking limit, regardless of the initial orbital angular momentum.

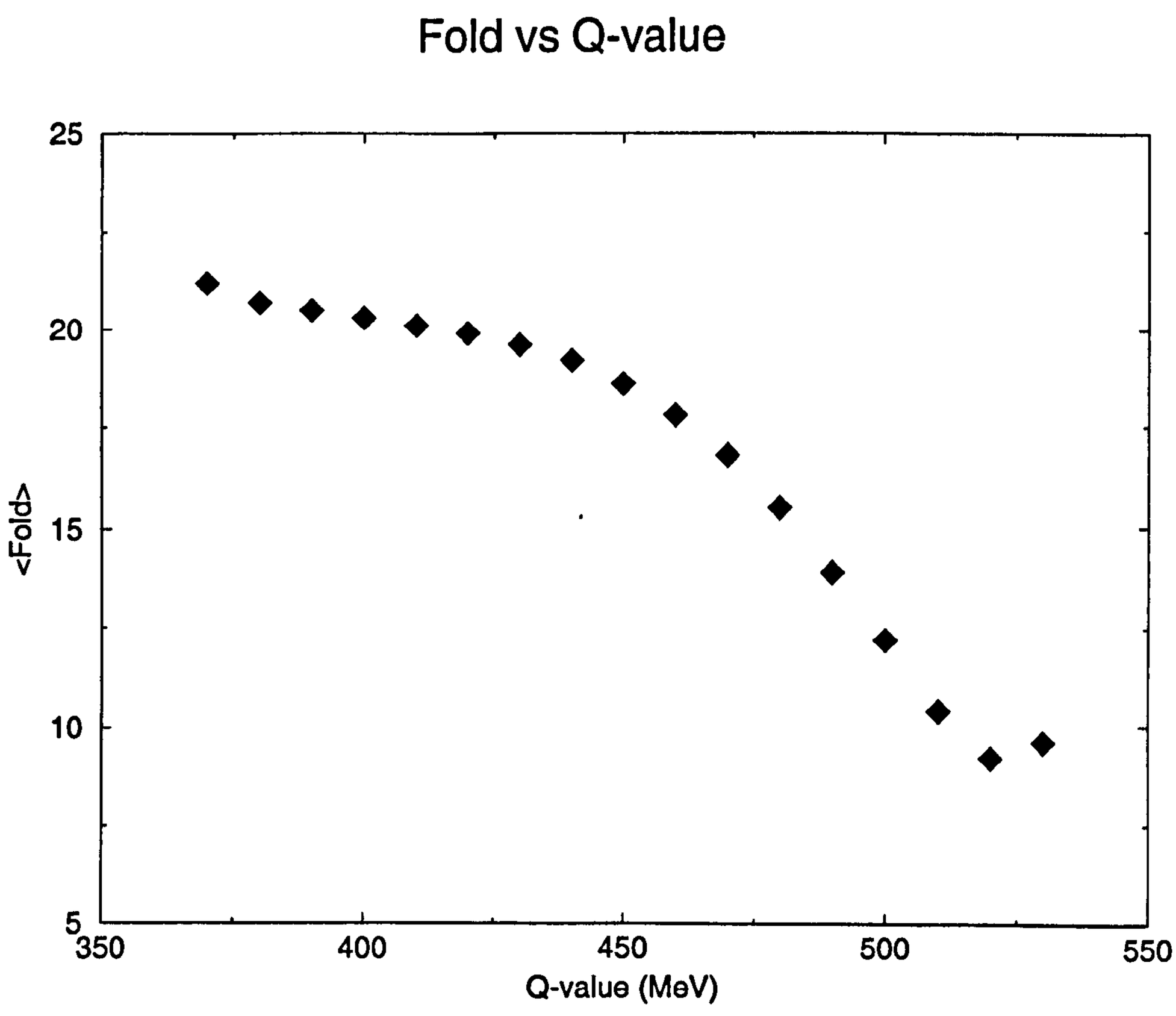

Figure 5.27: Plot of average fold against Q-value, gated on the recoils. Note that 500 MeV is taken as the reference Q-value of 0 MeV in a reaction.

5.6 Isomer Tagging and Lifetime Measurements

Utilising the (heavy-ion)−(γ-ray) coincidence measurement, the highest observed spin states in the neutron-rich nuclei were identified by selecting specific exit channels populated via the deep inelastic reaction. The tagging method employed in the present work additionally required the presence of isomeric states that decay by delayed γ-ray emission. Such isomeric states in the A $\simeq$ 100 mass region often involve the unique parity $h_{11/2}$ orbit, and have already been identified in Mo-isotopes around mass 100. The selectivity offered by the isomer tagging technique is most useful in distinguishing prompt 'above isomer' transitions from the competing and often overwhelming number of other γ-ray decay channels.

This analysis was performed using a recoil-gated prompt γ, delayed γ, and time-difference cube, which was sorted using the ANA software package [74]. In the present analysis, 'prompt' was defined as a ~25 ns wide region about the prompt peak in figure 5.2 and the 'delayed' was determined as greater than 100 ns *difference* in the value of TAC associated with the prompt and the delayed γ-rays.

By correlating prompt and delayed γ-rays across an isomeric state, the high spin structure that feeds the isomer can be observed. As an example, γ-ray gates set on 138 and 448 keV transitions on the delayed axis of the (prompt)−(delayed)−(time difference) cube produced a spectrum of known prompt γ-rays belonging to ^{99}Mo that lie above the isomer, as shown in figure 5.28(c). Note that once the prompt transitions have been established above an isomer, the level scheme of a nucleus can be constructed solely using the statistically superior, prompt γ^3 cubes to examine the coincidences.

Time correlations between the prompt and the delayed γ-ray transitions allowed the lifetimes of isomers to be determined. Those isomers with lifetimes in the accessible time window were subsequently studied (figure 5.32–5.37) and compared with the published values (values marked with an

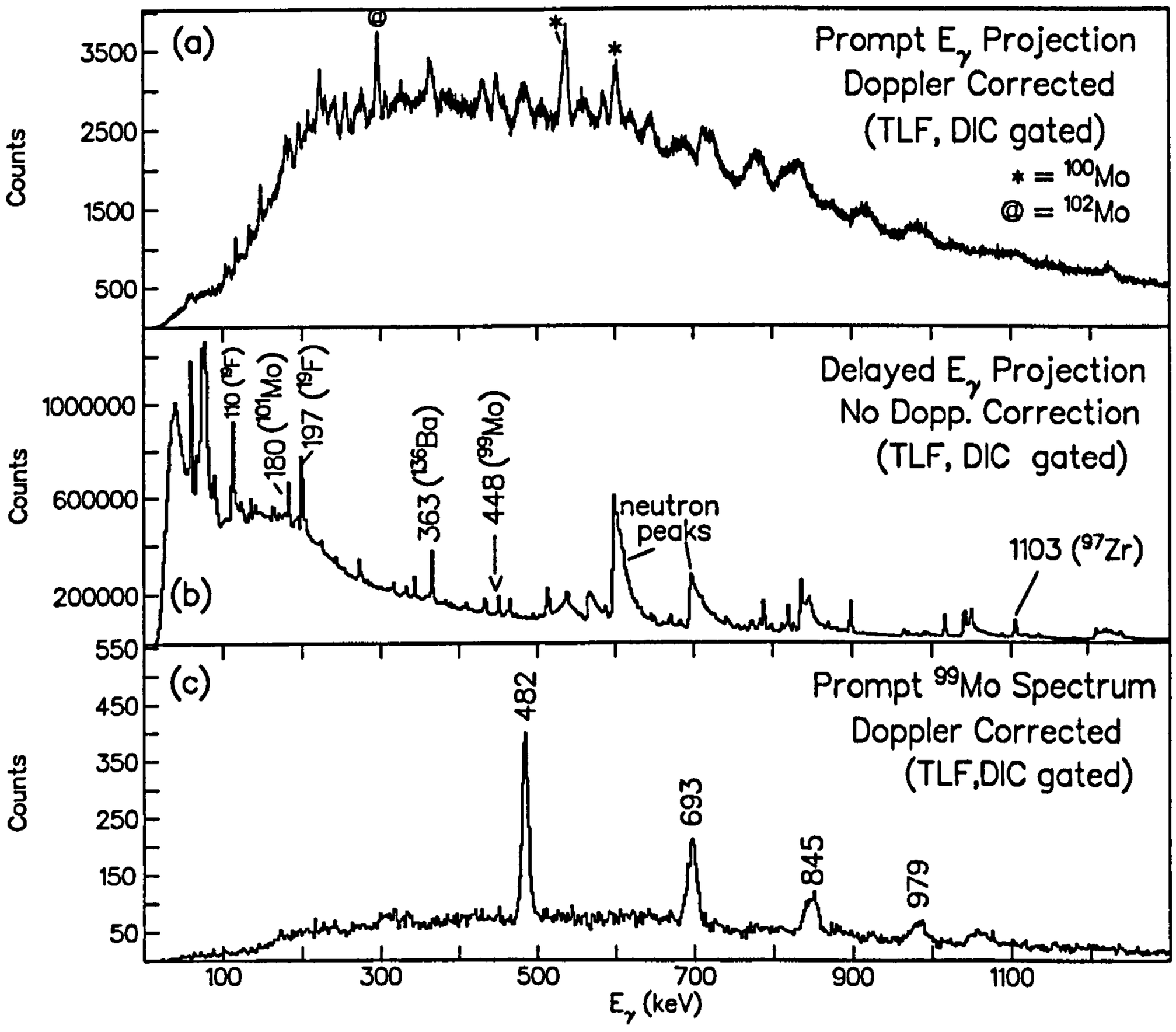

Figure 5.28: Doppler (a) corrected and (b) uncorrected total projection spectrum for the TLFs, and (c) spectrum of above-isomer, prompt γ-ray transitions gated by the known 138 and 448 keV delayed γ-rays belonging to ^{99}Mo.

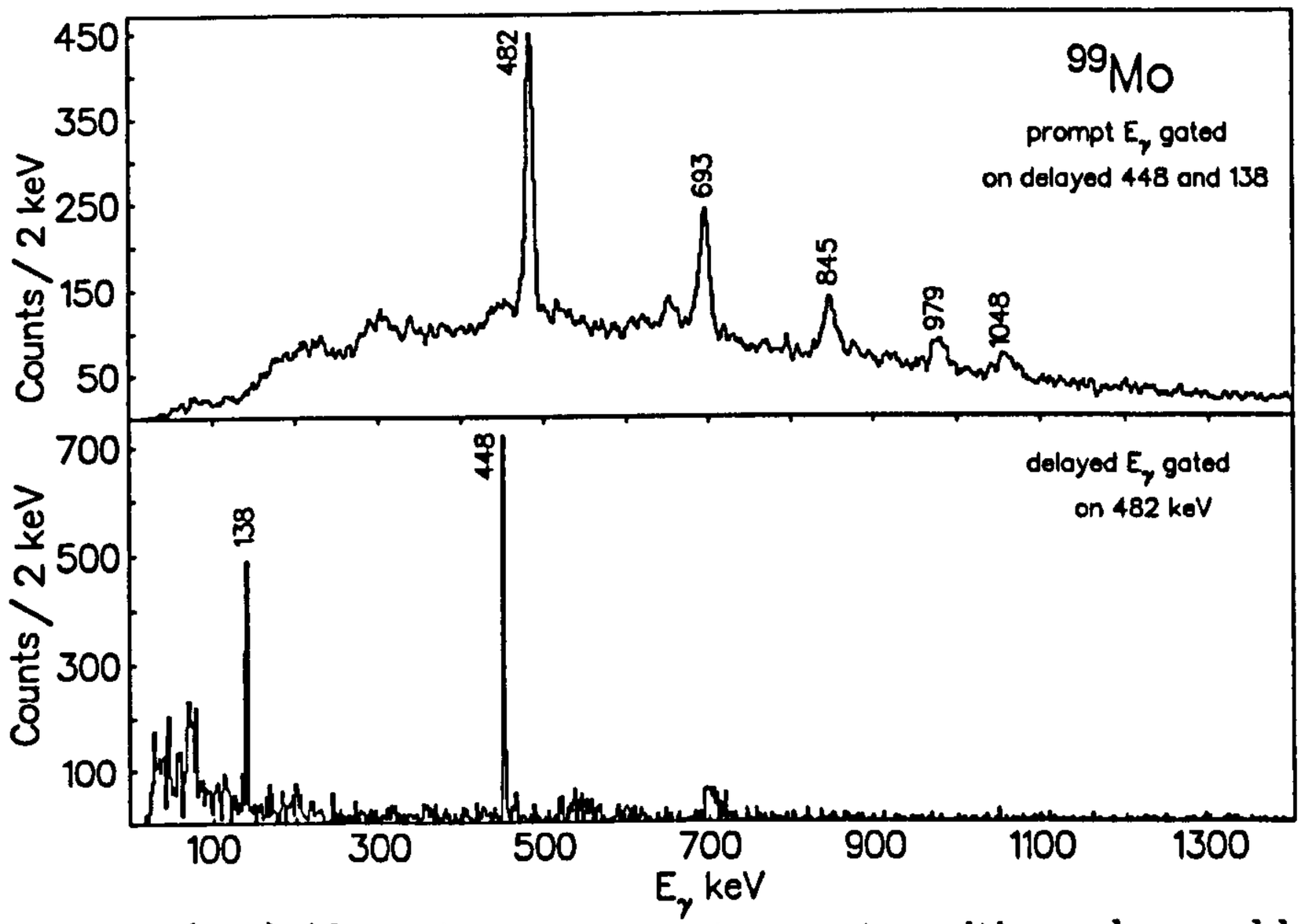

Figure 5.29: (top) Above-isomer prompt γ-ray transitions observed by gating on known 138 and 448 keV delayed γ-rays belonging to ^{99}Mo. (bottom) Below-isomer delayed transitions gated by the prompt 482 keV above-isomer transition, belonging to ^{99}Mo.

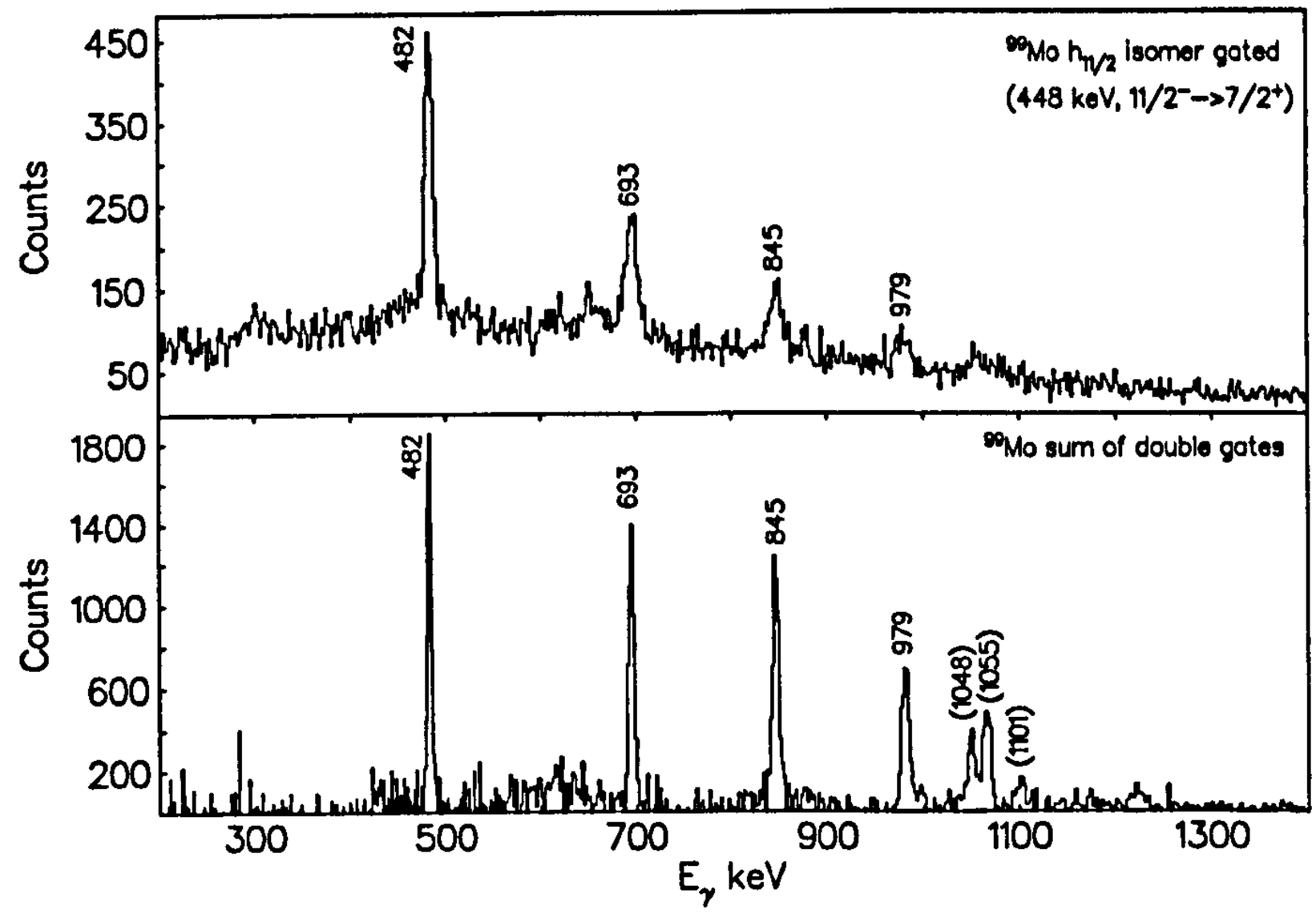

Figure 5.30: Prompt transitions above the $h_{11/2}$ isomer in ^{99}Mo, as obtained from the isomer tagging technique and the γ^3 coincidence analysis.

asterisk in figure 5.32–5.37). The projected time difference spectrum produced after subtracting TAC values of delayed from prompt γ-ray transitions plotted in a linear–logarithmic scale (as x- and y-axis) fits the usual linear decay line (see e.g. figure 5.33). Errors in the lifetime measurements were evaluated after a least squares fit to the data was performed, and the present study gives consistent results (see Table 5.1). In addition to the known isomers listed in Table 5.1, a lifetime measurement on a previously unreported, $h_{11/2}$ isomer in ^{101}Mo was made, and its half-life was determined using a known below-isomer transition of 180 keV [82] and the newly established above-isomer transitions of 429 and 615 keV. From the present study, the half-life of this isomer was established as 105(8) ns, and the projected prompt spectrum of above-isomer transitions were observed for the first time. The rotational character of the prompt transitions similar to other $h_{11/2}$ decoupled bands in the neighbouring Mo-isotopes is obvious.

Table 5.1: Example of evaluated isomeric lifetimes from the ^{100}Mo + 700 MeV ^{136}Xe experiment. They were also compared with the published values. Superscripts on the published values are the reference numbers.

Nucleus	Isomeric Half-life (ns)	
	Present Work	Published Values
^{138}Ba	734(212)	800(100)[82,83]
^{136}Ba	85(5)	91(2)[78]
^{136}Xe	881(613)	2950(100)[84]
^{101}Mo	105(8)	
^{99}Mo	639(130)	760(60)[85]
^{97}Zr	114(14)	106(7)[86]

⊛ For the lifetime measurement of ^{136}Xe, however, a large difference in the estimated and published value for its isomer was due to relatively small measurement time-window, in comparison to its 2950(100) ns, used in the present study.

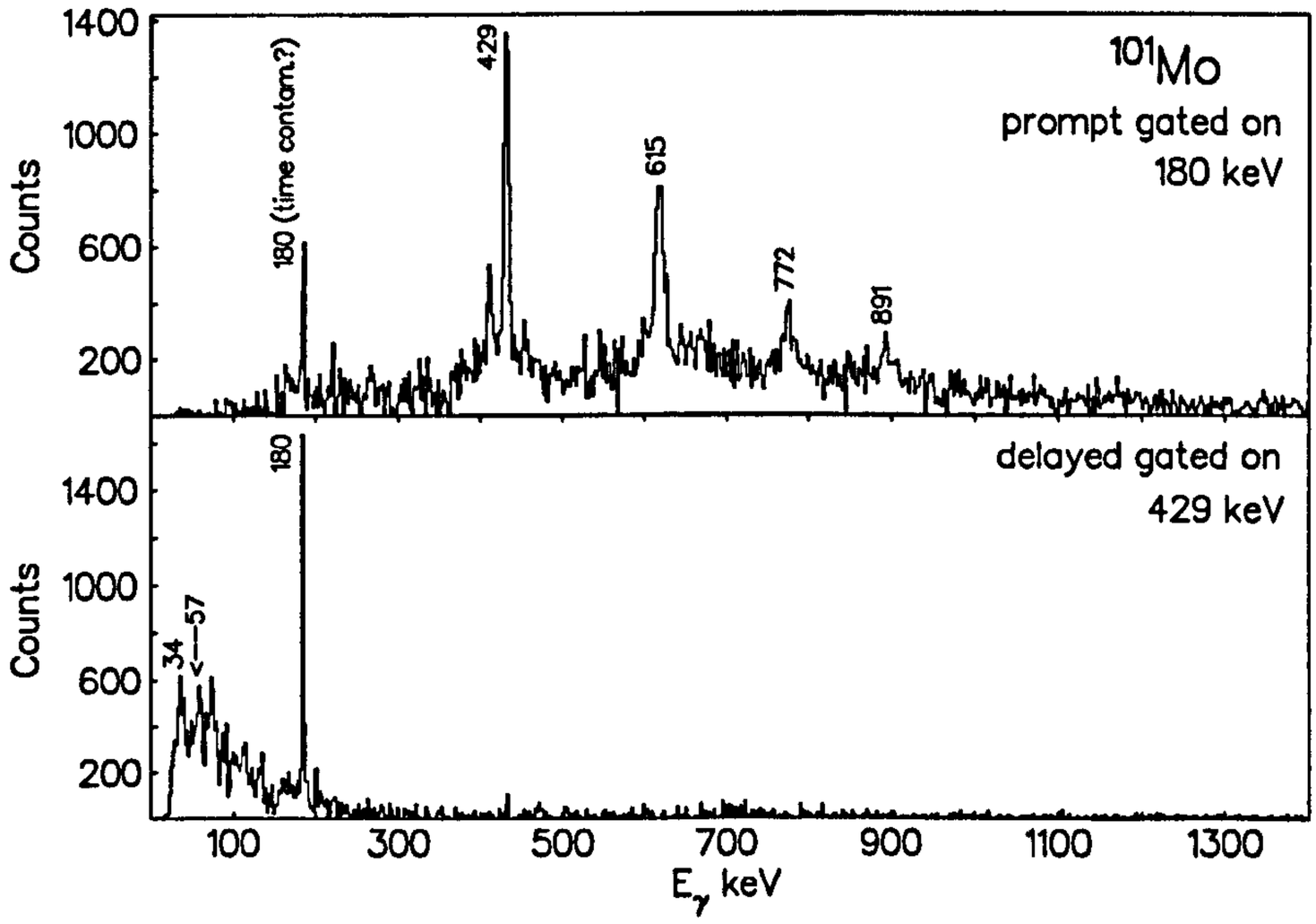

Figure 5.31: Spectrum showing above-isomer, prompt γ-ray transitions gated by a known 180 keV delayed γ-ray belonging to ^{101}Mo.

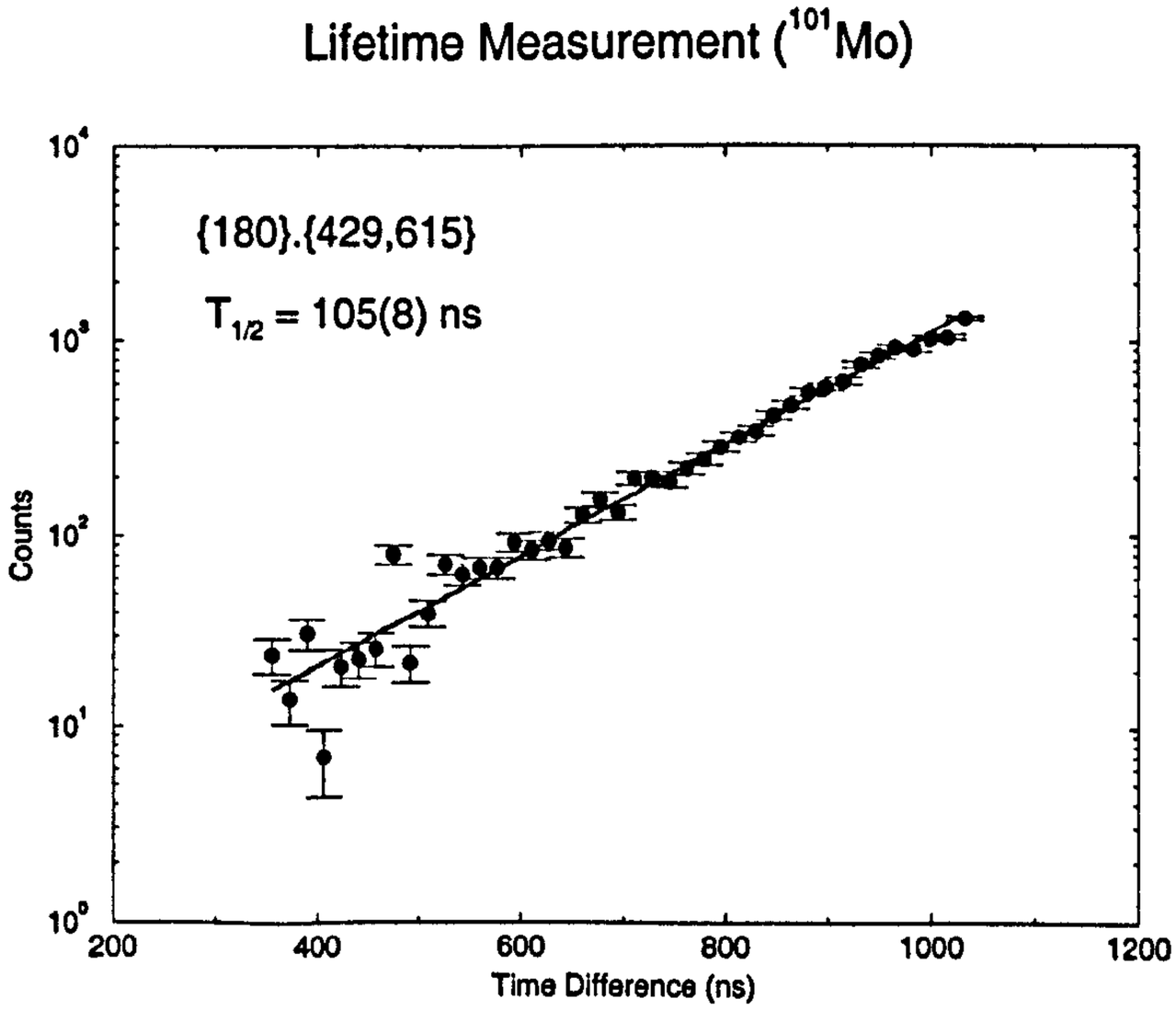

Figure 5.32: Lifetime decay curve obtained by gating on both the prompt (429&615 keV) and delayed γ-rays found in ^{101}Mo.
(180 keV)

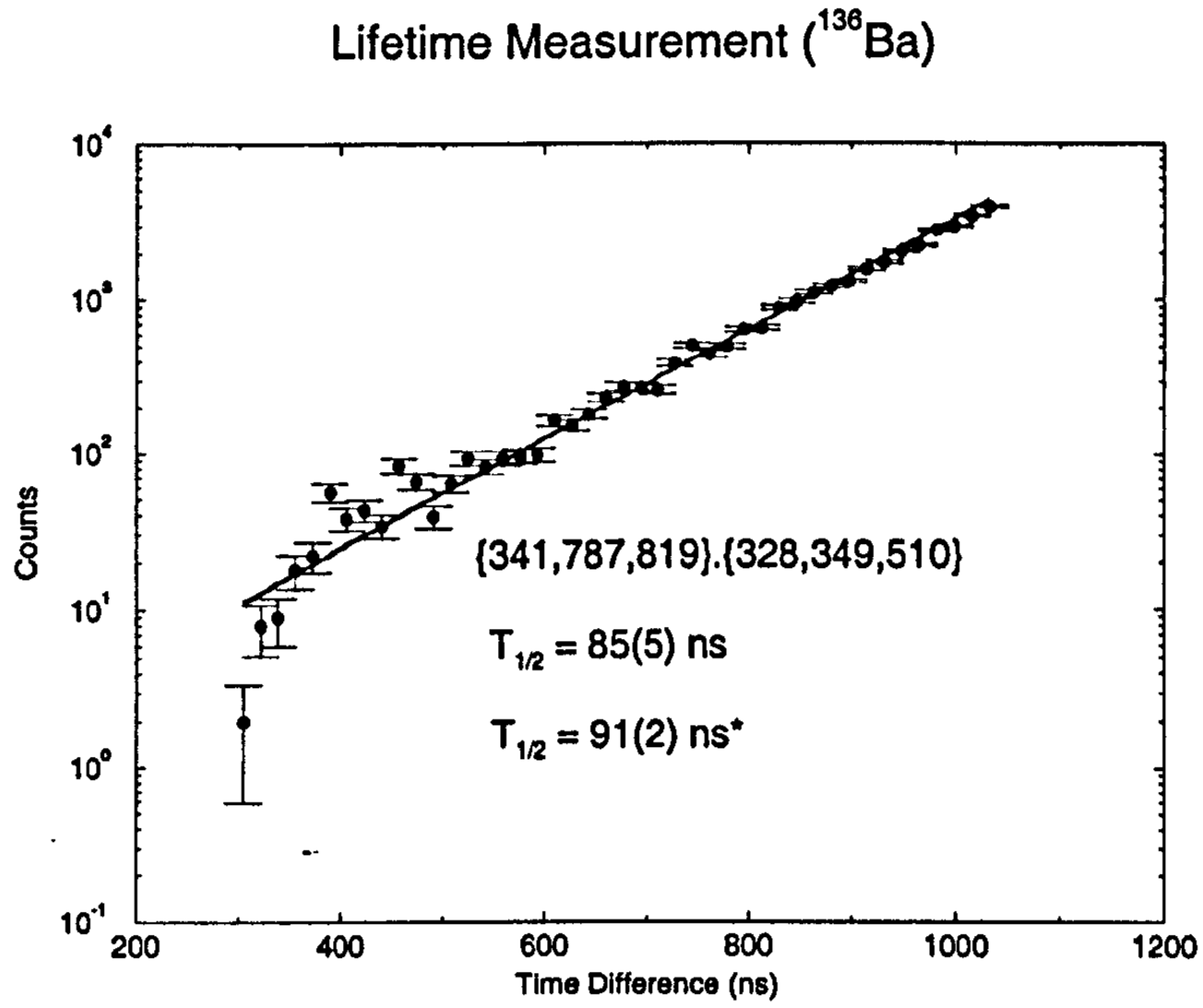

Figure 5.33: Lifetime decay curve obtained by gating on both the prompt and delayed γ-rays found in ^{136}Ba [80].

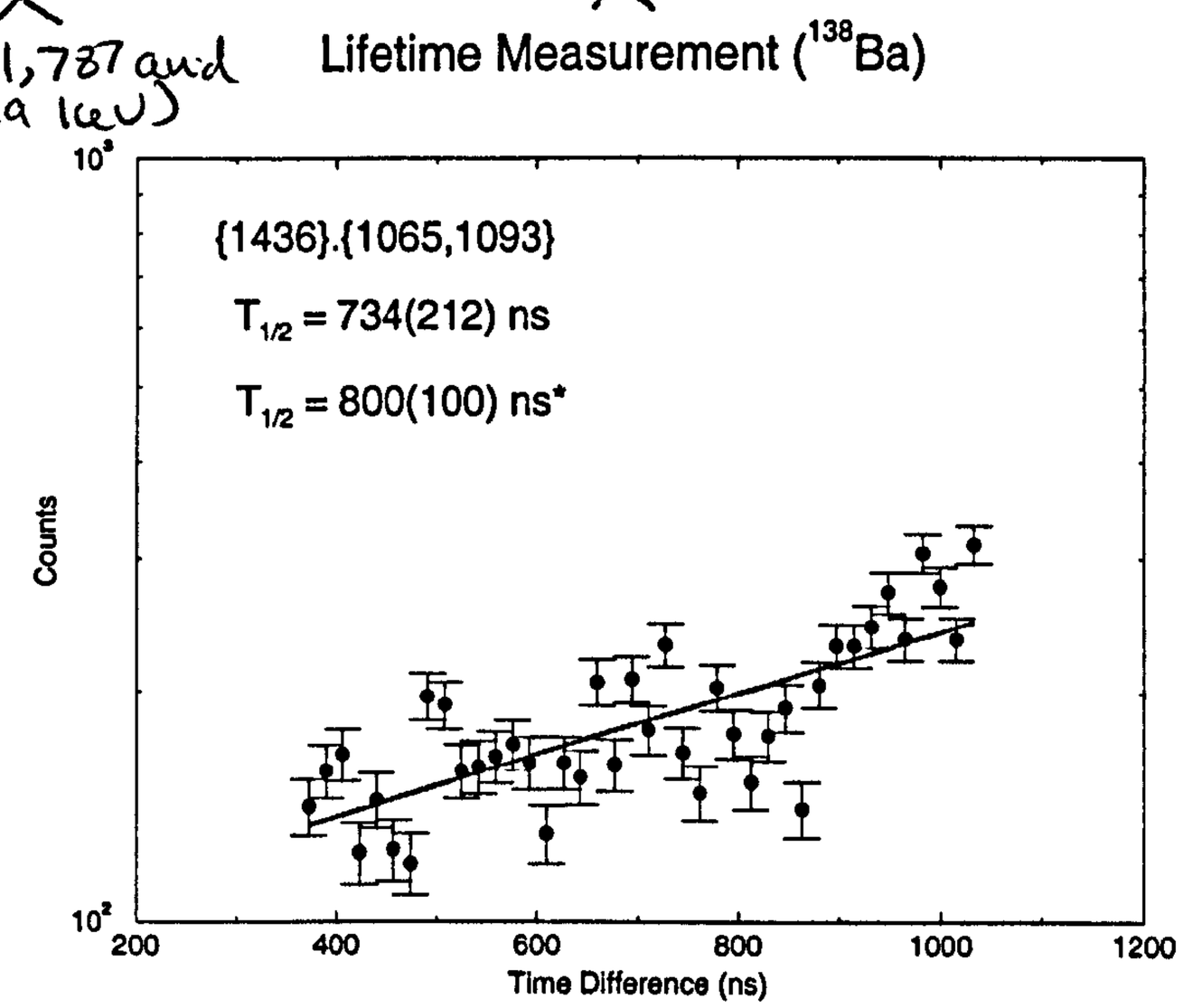

Figure 5.34: Lifetime decay curve obtained by gating on both the prompt and delayed γ-rays found in ^{138}Ba [84, 85].

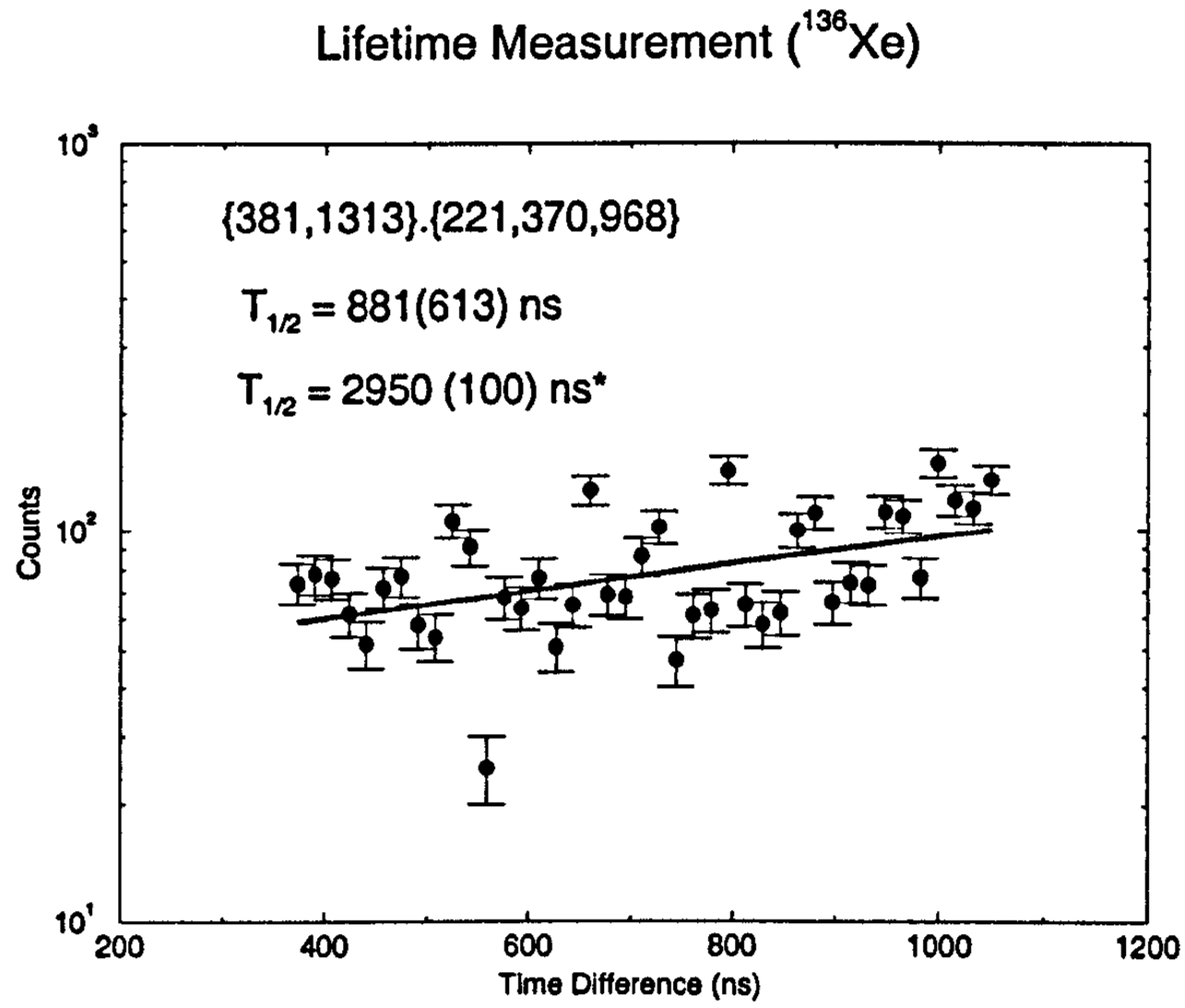

Figure 5.35: Lifetime decay curve obtained by gating on both the prompt (221, 370 and 963 keV) and delayed γ-rays found in ^{136}Xe [86]. Published value for the lifetime is marked with an asterisk [84]. (381 and 1313 keV)

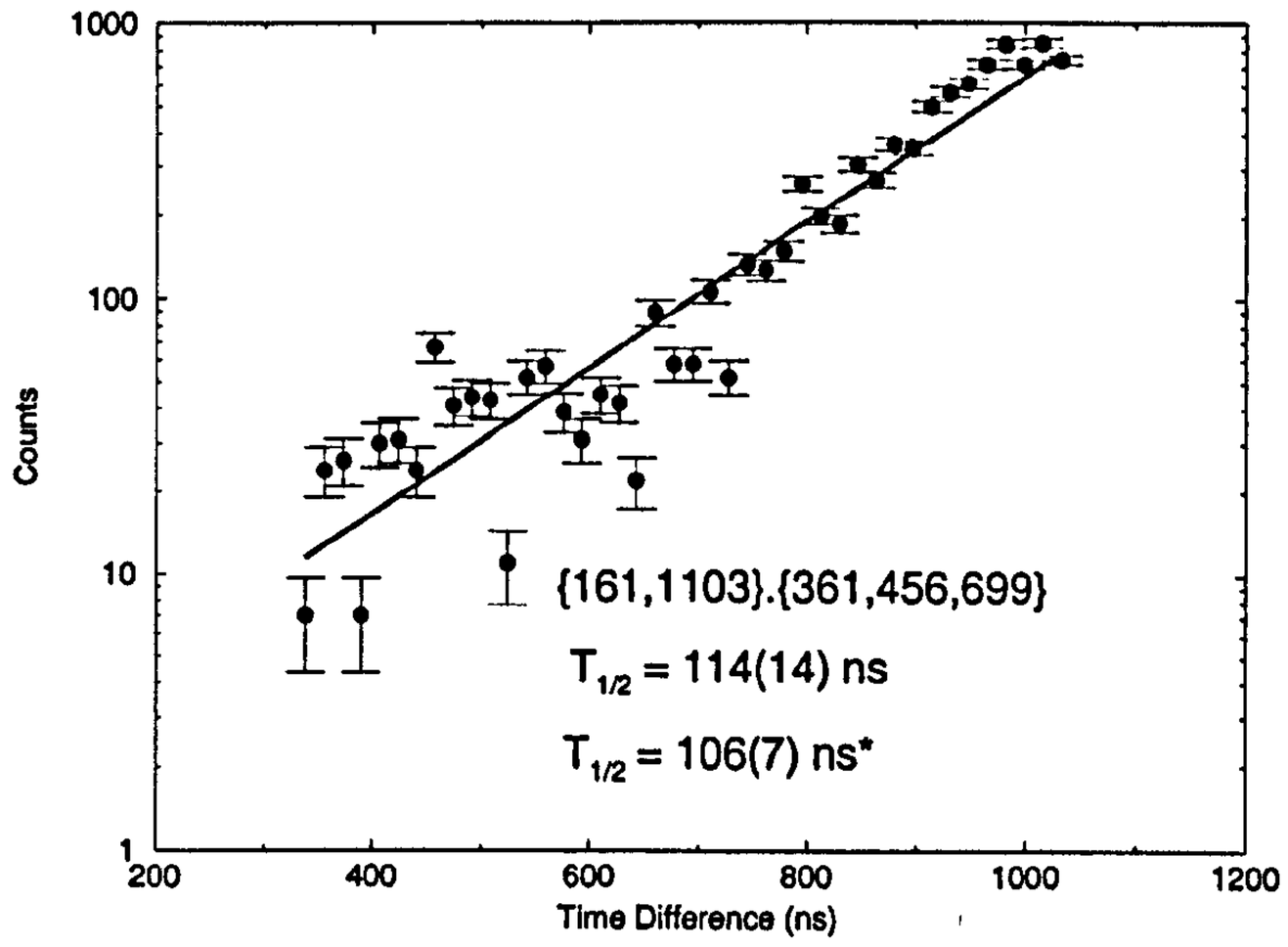

Figure 5.36: Lifetime decay curve obtained by gating on both the prompt (361, 456 and 699 keV) and delayed γ-rays found in ^{97}Zr [88]. Published value for the lifetime is marked with an asterisk [86]. (161 and 1103 keV)

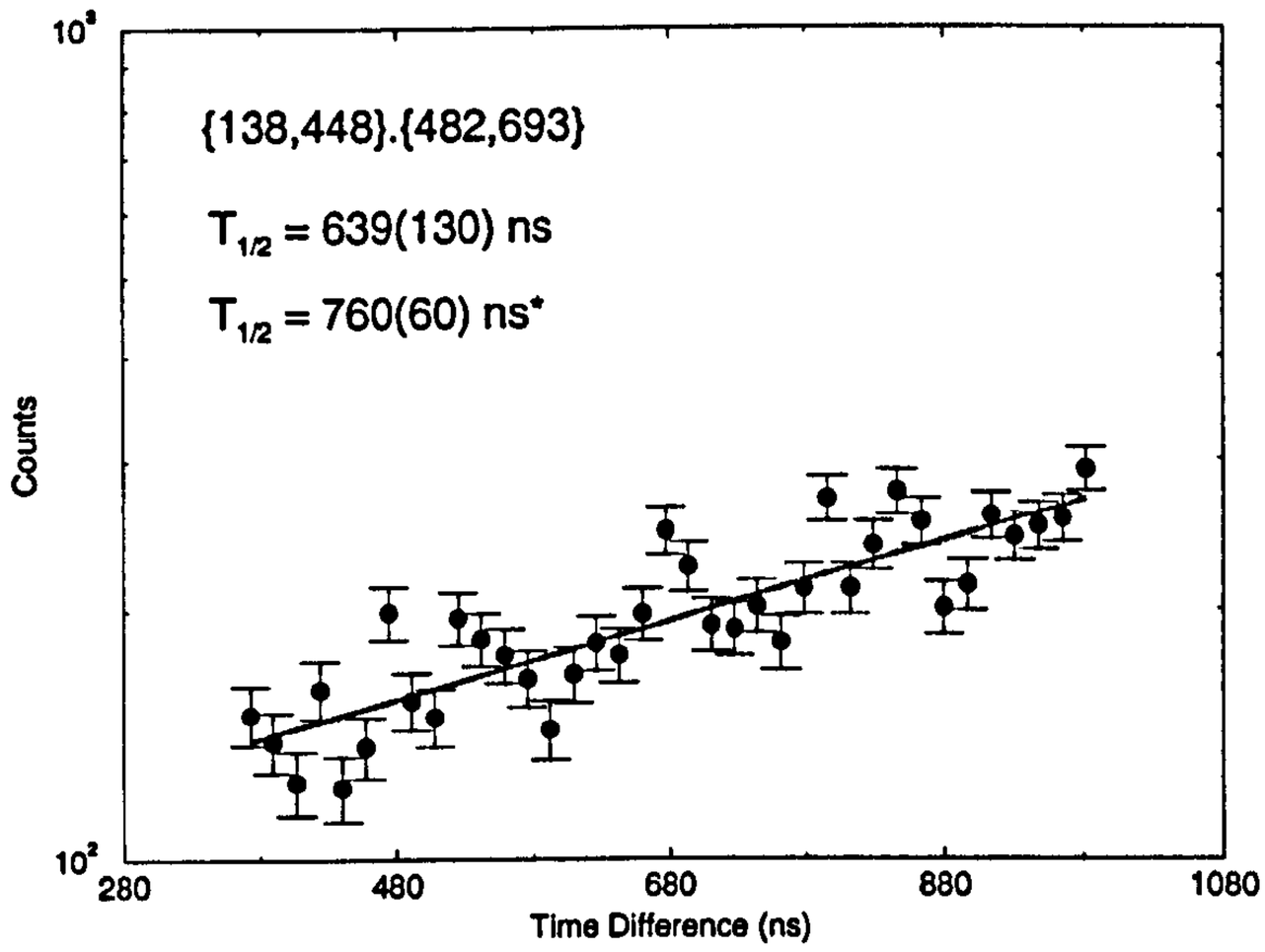

Figure 5.37: Lifetime decay curve obtained by gating on both the prompt (482 and 643 keV) and delayed γ-rays found in ^{99}Mo [87]. The publish value for the lifetime is marked with a asterisk [85]. (138 and 448 keV)

5.7 ^{98}Mo Decay Scheme

The yrast band of ^{98}Mo has previously been established up to the $J^\pi = 10^+$ at 4151 keV by Barrette *et. al.* [78] and Zieliñska *et. al.* [93]. In the present experiment, two new transitions of 896 and 975 keV were found to be populated in the DIC reaction, and in coincidence with the lower-lying members of the yrast band (figure 5.14). The negative parity band already discussed in section 4.6 was also identified in the present experiment. The 2620 keV state is assigned as 5^- and is consistent with the observation that the 2620 keV state decays out to a known 3^- state at 2017 keV [94, 95], and that it is fed by the (7^-) state at 3095 keV. For a band built on a (9^-) state, their level spacings above the 3658 keV state are similar to those of the

collective 2_1^+ and 4_1^+ states, and thus the 4426, 5244, and 6134 keV states are assigned as (11^-), (13^-), and (15^-), which arise from rotational states based on the maximally aligned $(h_{11/2} \otimes g_{7/2})$ configuration. The assignment of (9^-) for the 3658 keV state can be almost confirmed by the further observation of 385 and 563 keV decays to the 8^+ and the (7^-) states, respectively. Two more transitions of 673 and 768 keV previously reported in Ref. [70] were also observed in the current work.

A fusion-evaporation study by Lederer *et. al.* [70] identified the 394 and 663 keV transitions which feed the 6^+ yrast state at 2345 keV. From this decay pattern, Lederer *et. al.* tentatively assigned the 2739 keV state to have a spin of $(6^\pm)$, $(7^\pm)$, or $(8^\pm)$ $\hbar$. The observation of the yrast 8^+ state at 3273 keV and a strongly populated (7^-) member of the band at 3095 keV seem to rule out the assignment of 8^+ and 7^- for the 2739 keV state. If this 2739 keV state were 8^+, it would be yrast and one might expect it to have a stronger intensity and an additional decay out to the 6^+ member of the yrast cascade. The most likely spin-parity assignment for the 2739 keV state is thus $(6^\pm)$ or (7^+), but if the state were (6^+), the additional levels at 4192 and 4995 keV found above the 3401 keV state makes the 4955 keV state (12^+) and yrast, thus preferring the assignment of (6^-) or (7^+) for the 2739 keV state.

The singular decay out from the 2583 keV state to the yrast 4^+ state at 1511 keV suggests the previously unreported 2583 keV and 2874 keV states to be either (5^+) or (7^+). The 2855 keV state previously identified by Lederer *et. al.* is confirmed in the present study, and has been tentatively assigned as (8^+).

Transitions observed from the quasi-elastic reaction regime in the Wilczyński plot of figure 5.7 are observed to populate rather low-lying and non-yrast states, in comparison with those populated through the deep inelastic

regime of the same figure. For ^{98}Mo, known low-lying states identified by Flynn *et. al.* [96] have been observed in the decay scheme of figure 5.38. New transitions of 1120, 1250, 1287, and 1344 keV have been identified to feed the yrast band without being in coincidence with any other known states. Previously reported negative parity states at 2017, 2620, 3095 keV have also been identified, and the (9^-), 3658 keV state was observed to decay with a noticeable strength to the (7^-), 3095 keV state.

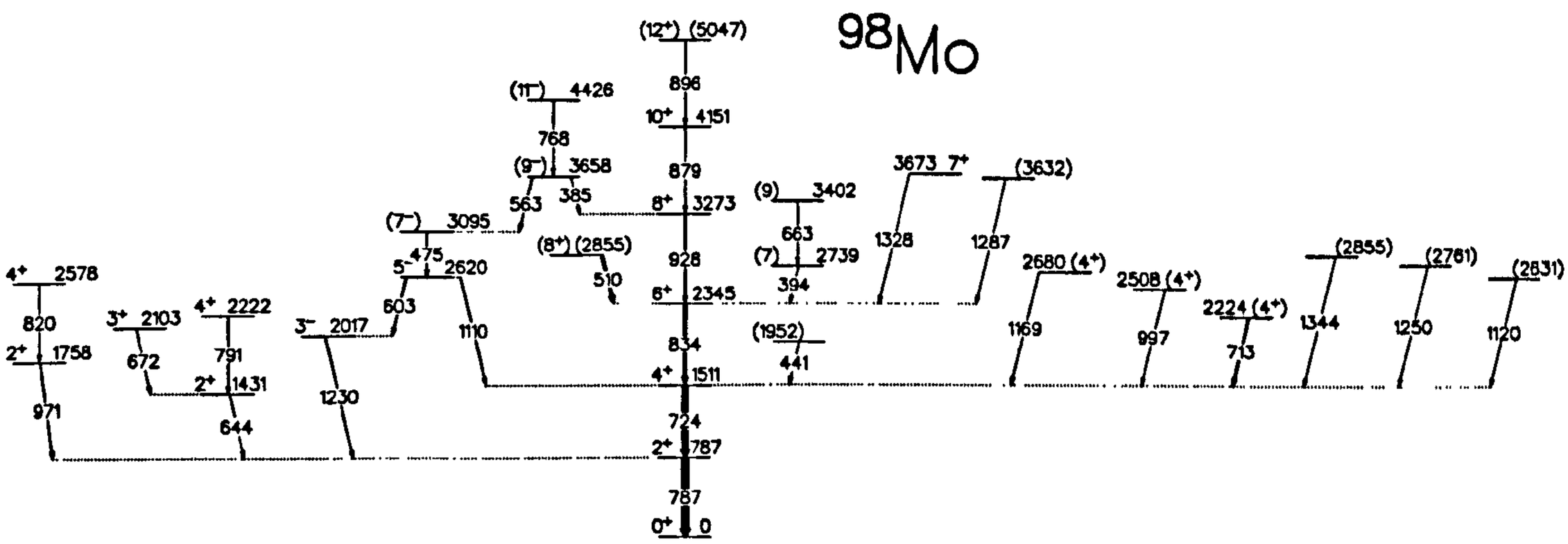

Figure 5.38: Decay scheme of ^{98}Mo as populated in the quasi-elastic reaction.

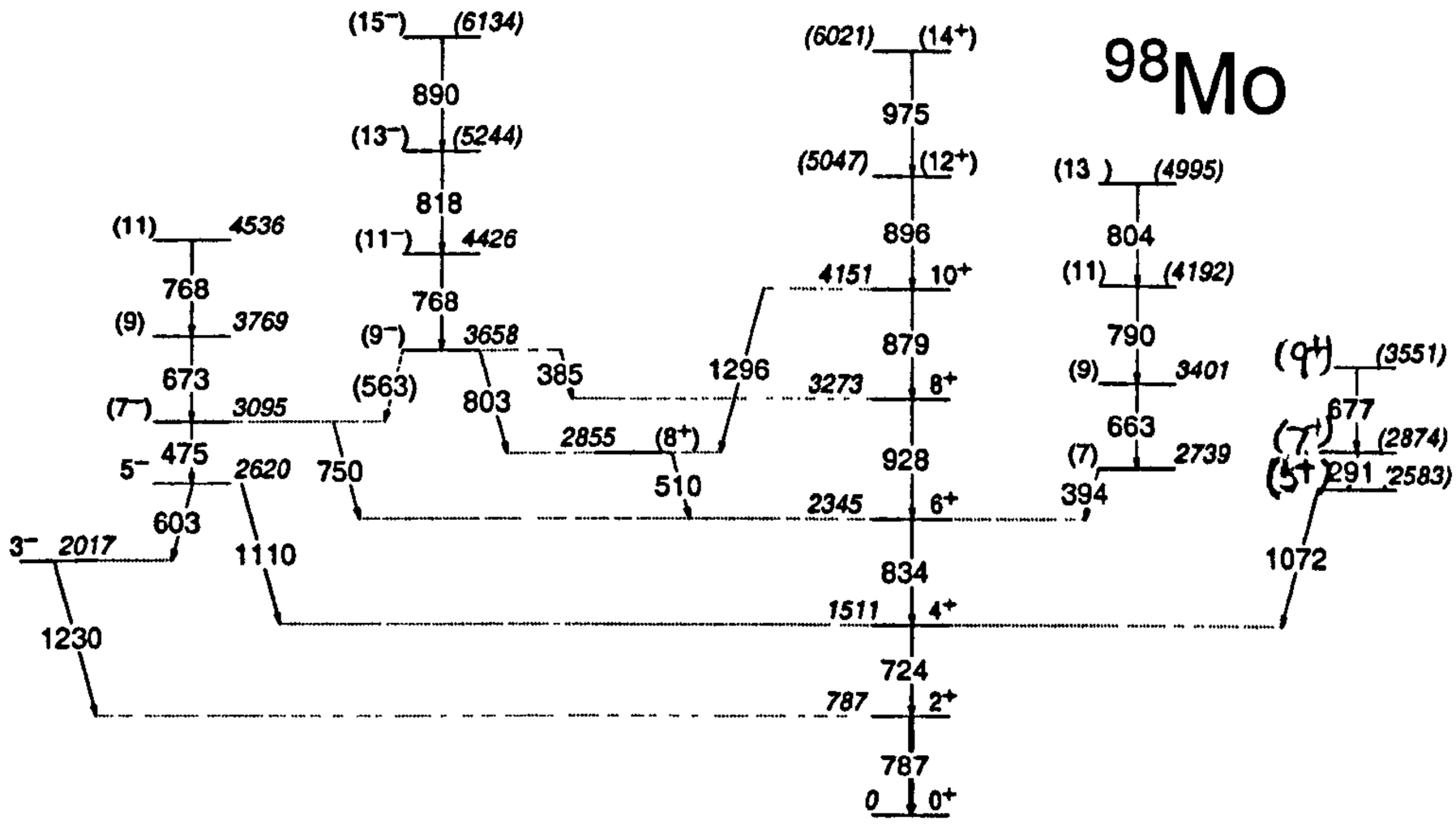

Figure 5.39: Decay scheme of ^{98}Mo as populated in the DIC reaction.

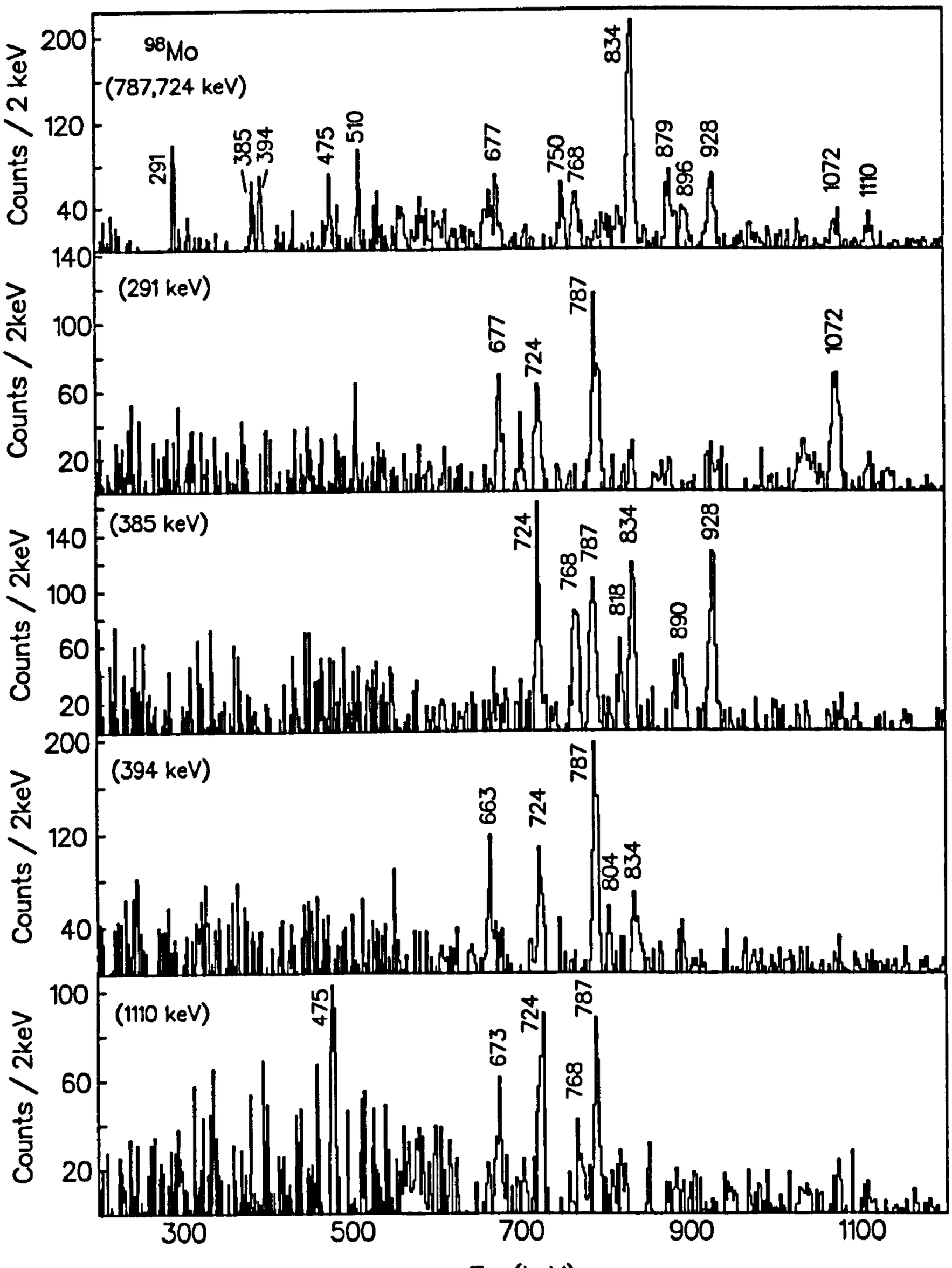

Figure 5.40: Sum of double γ–ray gated spectra, showing the yrast band of ^{98}Mo and the side bands, as populated in the DIC reaction. Gamma-ray energy in brackets is the gating transition in ^{98}Mo used with $2^+_1 - 0^+_1$, 787 keV transition.

Table 5.2: Gamma-ray transitions of ^{98}Mo populated via the quasi-elastic reaction. The γ-ray intensities (in arbitrary units) were taken from a 2-D fit to the $\gamma - \gamma$ coincidence matrix using the program ESCL8R.

E_γ (keV)	I_γ (arb.)	E_i, E_f (keV)	$J_i^\pi \rightarrow J_f^\pi$
385.3	32(11)	3658,3273	$(9), 8^+$
394.0	38(39)	2739,2345	$(7), 6^+$
441.4	12(3)	1952,1511	
475.2	112(18)	3097,2620	$(7^-), (5^-)$
510.1	107(17)	2856,2345	$(4^+), 6^+$
563.3	63(19)	3658,3095	$(9^-), (7^-)$
603.1	55(12)	2620,2017	$5^-, 3^-$
644.0	16(4)	1431,787	$2^+, 2^+$
663.2	36(15)	3401,2739	$(9), (7)$
672.0	56(27)	2103,1431	$3^+, 2^+$
713.4	258(44)	2224,1511	$4^+, (4^+)$
723.7	1000(52)	1511,787	$4^+, 2^+$
768.7	51(20)	4426,3658	$(11^-), (9^-)$
787.2	—	787,0	$2^+, 0^+$
791.0	15(7)	2222,1431	$4^+, 2^+$
820.1	76(21)	2578,1758	$4^+, 2^+$
834.4	506(31)	2345,1511	$6^+, 4^+$
878.5	70(15)	4151,3273	$(10^+), 8^+$
895.9	32(12)	5047,4151	$(12^+), (10^+)$
928.4	150(18)	3273,2345	$8^+, 6^+$
971.0	109(30)	1758,787	$2^+, 2^+$

Table 5.2: Gamma-ray transitions of ^{98}Mo populated via the quasi-elastic reaction (continued...).

E_γ (keV)	I_γ (arb.)	E_i, E_f (keV)	$J_i^\pi \rightarrow J_f^\pi$
997.4	26(20)	2508,1511	$(4^+), 4^+$
1109.9	120(17)	2620,1511	$5^-, 4^+$
1120.4	33(17)	2631,1511	
1169.4	39(15)	2680,1511	$(4^+), 4^+$
1230.0	78(30)	2017,787	$3^-, 2^+$
1250.4	2(1)	2401,1511	
1287.0	2(5)	3632,2345	
1328.0	4(4)	3673,2345	$7^+, 6^+$
1344.4	18(16)	2855,1511	

Table 5.3: Gamma-ray transitions of ^{98}Mo populated via the deep inelastic reaction. The γ-ray intensities (in arbitrary units) were taken from a 2-D fit to the $\gamma - \gamma$ coincidence matrix using the program ESCL8R.

E_γ (keV)	I_γ (arb.)	E_i, E_f (keV)	$J_i^\pi \rightarrow J_f^\pi$
291.4	15(3)	2874, 2583	(7), (5)
385.0	4(1)	3658,3273	(9), 8^+
393.7	2(1)	2739,2345	(7), (6)
474.9	31(4)	3095,2620	$(7^-), (5^-)$
510.0	21(4)	2855,2345	
603.5	11(1)	2620,2017	$5^-, 3^-$
662.8	8(1)	3401,2739,	$9^+, 7^+$
673.1	11(1)	2103,1431	$3^+, 2^+$
677.2	11(1)	3551, 2874	(9), (7)
723.6	100(5)	1511,787	$4^+, 2^+$
750.0	15(2)	3095,2345	
767.7	20(3)	4426,3658	(11), (9)
768.2	20(2)	4536,3769	(11), (9)
787.0	—	787,0	$2^+, 0^+$
790.3	13(3)	4192,3401	(11), (9)
803.1	5(1)	4995,4192	(13), (11)
818.3	8(1)	5244,4426	(13), (11)
834.4	62(3)	2345,1511	$6^+, 4^+$
878.5	25(2)	4151,3273	$(10^+), 8^+$
890.1	6(1)	6134,5244	(15), (13)
895.9	13(2)	5047,4151	$(12^+), (10^+)$
928.0	33(2)	3273,2345	$8^+, 6^+$

Table 5.3: Gamma-ray transitions of ^{98}Mo populated via the deep inelastic reaction (continued...).

E_γ (keV)	I_γ (arb.)	E_i, E_f (keV)	$J_i^\pi \rightarrow J_f^\pi$
1072.2	17(4)	2583,1511	$(5^+), 4^+$
1109.9	20(2)	2620,1511	$5^-, 4^+$
1230.0	6(2)	2017,787	$3^-, 2^+$

5.8 ^{100}Mo Decay Scheme

The yrast band in this nucleus has been previously known up to the $J^\pi = 14^+$ state at 4876 keV [79]. This band in the present work has been extended by three transitions up to 8115 keV, all of which were found to be in coincidence with the well known lower-lying members of this band (figure 5.14). Tentative spin assignments for the 2845 and 3301 keV states as (7^-) and (9^-), respectively [79], are in agreement with the present observation of two inter-band transitions of 503 and 371 keV, linking the proposed (5^-) state at 2342 keV and (7^-), which to and at 2930 keV. The observation of the blocking effect manifested by the negative-parity band also supports this assignment (see Section 6.2).

A previously unknown band built on a 2200 keV level was also identified in the current work (figure 5.42). (Negative-parity side-bands from the coupling of the $h_{11/2}$ and the $d_{5/2}/g_{7/2}$ orbital are commonly observed features of the yrast states in this mass region [97].)

A new single γ-ray transition of 1146 keV to the yrast 6^+ state at 1848 keV was also identified in the current work.

Previous work on the low-spin states in ^{100}Mo including the β^- decay of ^{100}Nb [98], two-neutron transfer through the (t,p) reaction [99], and Coulomb excitation [100], as well as the medium-spin studies by Hook *et. al.* [101] using the ^{96}Zr(^{7}Li,$p2n$)^{100}Mo reaction and by Durell *et. al.* [102] using a spontaneous fission. Many states previously unreported were populated via the present quasi-elastic reaction. Levels at 2546 and 3339 keV have been added to the known 4^+ state at 1771 keV, and were tentatively assigned as (6^+) and (8^+), respectively. The 2310 and 3085 keV states were also tentatively assigned as (5^+) and (7^+), respectively, from their decay systematics.

Additionally, new transitions of 352, 502, 681, and 761 keV were identified, and were found to feed the known 3^+ state at 1607 keV. Previously unknown singular transitions decaying from 2102, 2652, 2870, 3017, 3094, 3900, and 4055 keV levels have also been established.

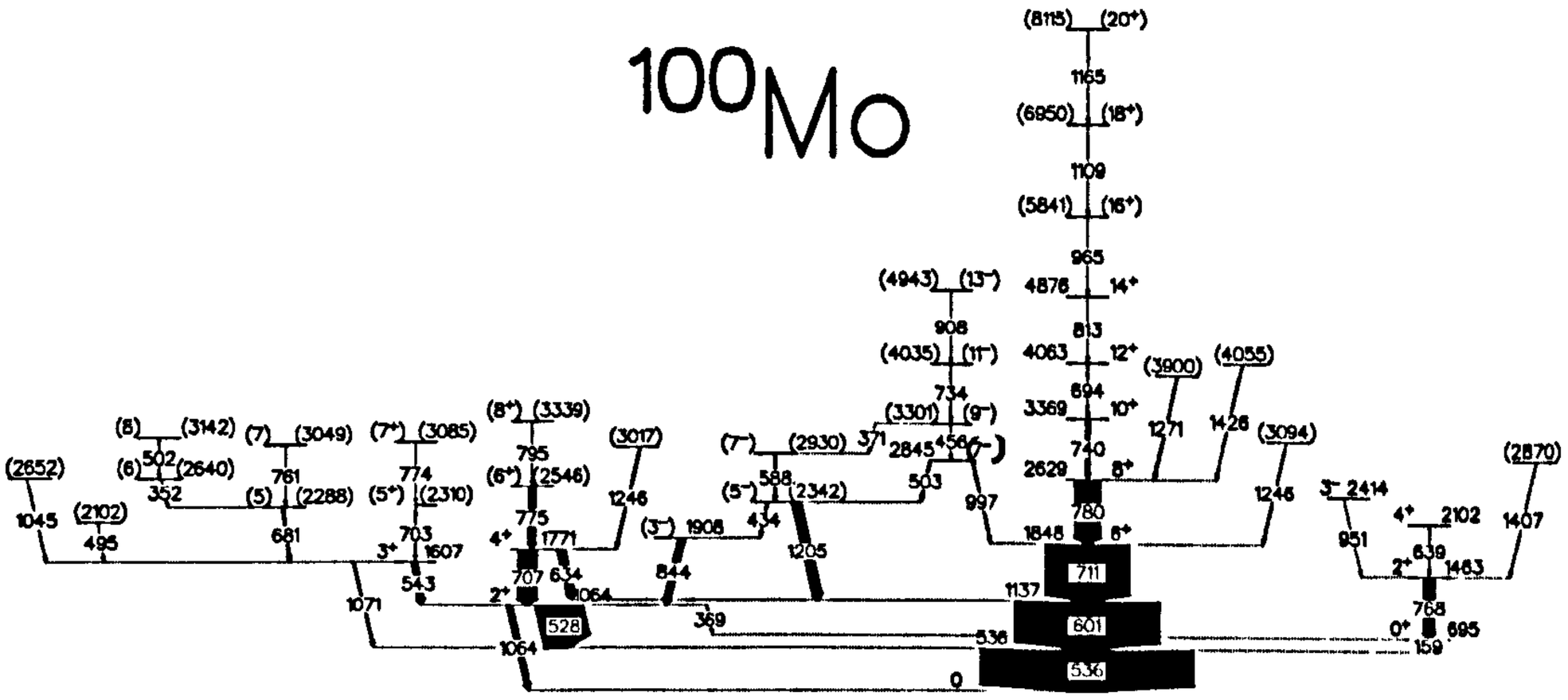

Figure 5.41: Decay scheme of ^{100}Mo as populated in the quasi-elastic reaction.

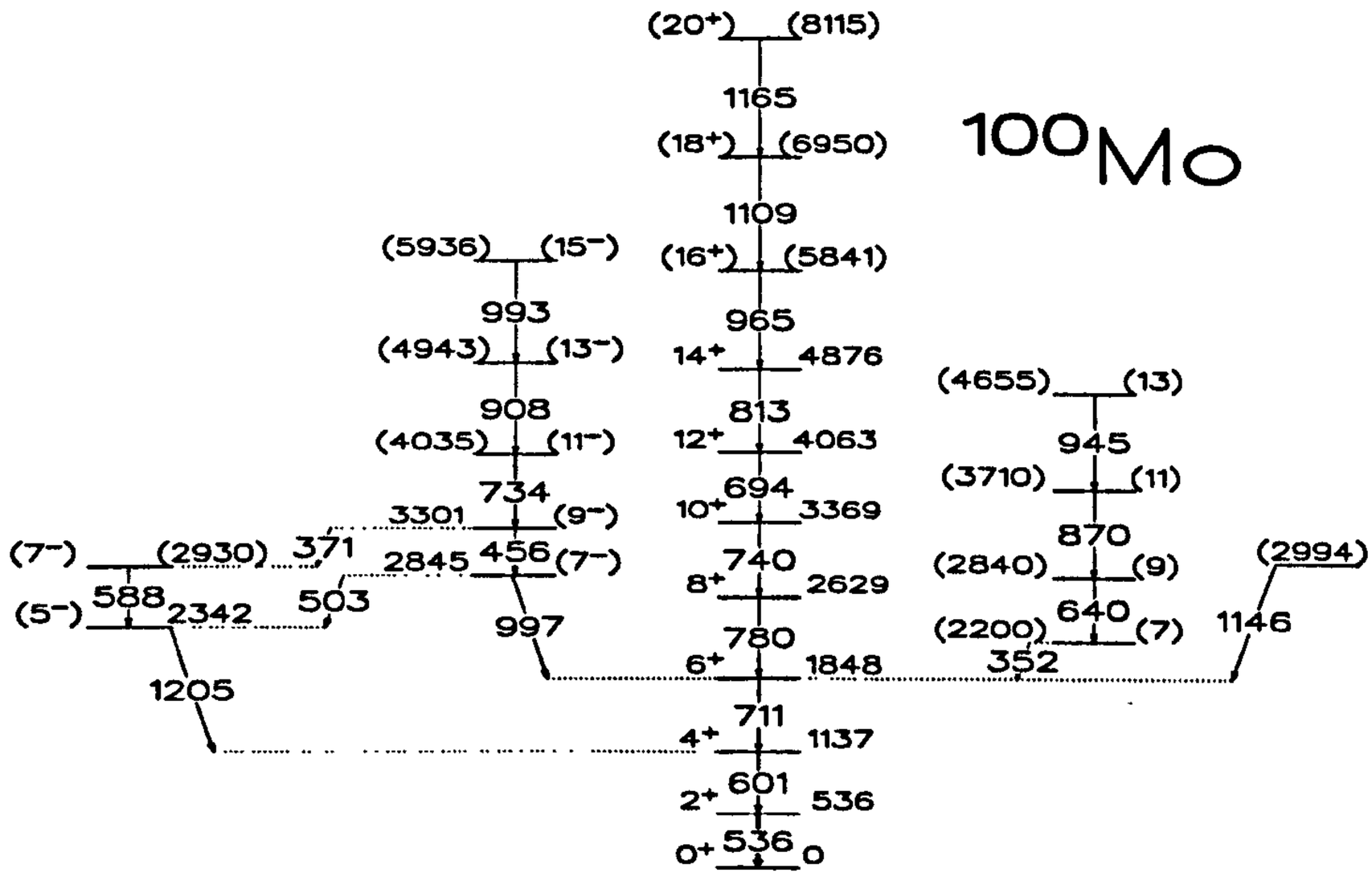

Figure 5.42: Decay scheme of ^{100}Mo as populated in the DIC reaction.

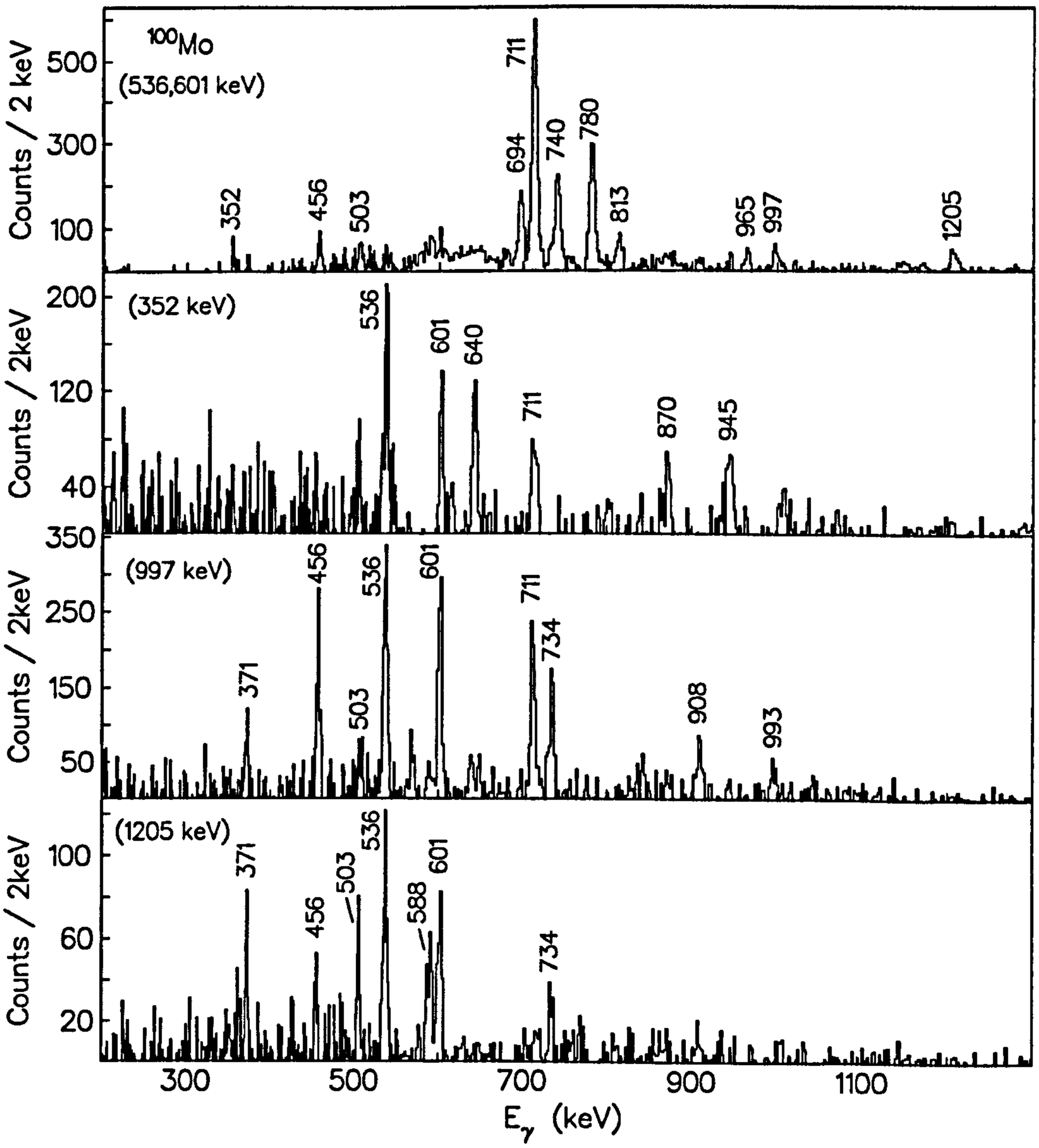

Figure 5.43: Sum of double γ–ray gated spectra, showing the yrast band of ^{100}Mo and the side bands, as populated in the DIC reaction. Gamma-ray energy in brackets is the gating transition in ^{100}Mo used with $2^+_1 - 0^+_1$, 536 keV transition.

Table 5.4: Gamma-ray transitions of ^{100}Mo populated via the quasi-elastic reaction. The γ-ray intensities (in arbitrary units) were taken from a 2-D fit to the $\gamma - \gamma$ coincidence matrix using the program ESCL8R.

E_γ (keV)	I_γ (arb.)	E_i, E_f (keV)	$J_i^\pi \rightarrow J_f^\pi$
159.5	81(3)	695,536	$0^+, 2^+$
352.1	3(1)	2640,2288	(6), (5)
369.4	12(1)	1064,695	$2^+, 0^+$
371.2	6(1)	3301,2930	$(9^-), (7^-)$
434.3	16(1)	2342,1908	$(5^-), (3^-)$
455.7	4(1)	3301,2845	$(9^-), (7^-)$
495.0	1(1)	2102,1607	
502.1	4(1)	3142,2640	(8), (6)
503.3	15(1)	2845,2342	$7^-, (5^-)$
528.5	337(11)	1064,536	$2^+, 2^+$
536.3	—	536,0	$2^+, 0^+$
543.0	53(2)	1607,1064	$3^+, 2^+$
588.2	11(1)	2930,2342	$(7^-), (5^-)$
601.0	1000(30)	1137,536	$4^+, 2^+$
633.9	65(3)	1771,1064	$4^+, 2^+$
638.6	14(2)	2102,1463	$4^+, 2^+$
681.4	14(1)	2288,1607	$(5), 3^+$
693.7	7(1)	4063,3369	$12^+, 10^+$
703.2	10(1)	2310,1607	$(5^+), 3^+$
707.1	148(5)	1771,1067	$4^+, 2^+$
711.2	588(18)	1848,1137	$6^+, 4^+$
734.3	3(1)	4035,3301	$(11^-), (9^-)$
740.0	31(1)	3369,2629	$10^+, 8^+$

Table 5.4: Gamma-ray transitions of ^{100}Mo populated via the quasi-elastic reaction (continued...).

E_γ (keV)	I_γ (arb.)	E_i, E_f (keV)	$J_i^\pi \rightarrow J_f^\pi$
760.8	2(1)	3049,2288	(7), (5)
768.1	48(6)	1463,695	$2^+, 0^+$
774.3	1(1)	3085,2310	$(7^+), (5^+)$
775.0	58(2)	2546,1771	$(6^+), 4^+$
780.4	182(6)	2629,1848	$8^+, 6^+$
794.7	3(1)	3339,2546	$(8^+), (6^+)$
813.3	1(1)	4876,4063	$14^+, 12^+$
844.0	54(2)	1908,1064	$(3^-), 2^+$
908.1	15(4)	4941,4034	$(13^-), (11^-)$
951.2	1(1)	2414,1463	$3^-, 2^+$
965.2	1(1)	5841,4876	$(16^+), 14^+$
997.4	11(1)	2845,1848	$(7^-), 6^+$
1045.3	4(1)	2652,1607	
1064.0	41(3)	1064,0	$2^+, 0^+$
1071.5	11(2)	1607,536	$3^+, 2^+$
1109.4	1(1)	6950,5841	$(18^+), (16^+)$
1165.3	1(1)	8115,6950	$(20^+), (18^+)$
1205.1	71(3)	2341,1137	$(5^-), 4^+$
1245.7	6(1)	3094,2629	
1246.0	11(1)	3017,1771	
1271.5	11(1)	3900,2629	
1407.0	4(1)	2870,1463	
1426.5	7(1)	4055,2629	

Table 5.5: Gamma-ray transitions of ^{100}Mo populated via the deep inelastic reaction. The γ-ray intensities (in arbitrary units) were taken from a 2-D fit to the $\gamma - \gamma$ coincidence matrix using the program ESCL8R.

E_γ (keV)	I_γ (arb.)	E_i, E_f (keV)	$J_i^\pi \rightarrow J_f^\pi$
351.7	10(2)	2200,1848	$(7), 6^+$
371.1	4(1)	3301,2930	$(9^-), (7^-)$
456.3	86(8)	3301,2845	$(9^-), (7^-)$
503.2	6(1)	2845,2342	$7^-, (5^-)$
536.4	—	536,0	$2^+, 0^+$
588.0	9(1)	2930,2342	$(7^-), (5^-)$
601.1	100(18)	1137,536	$4^+, 2^+$
639.8	7(2)	2840,2200	(9),(7)
694.4	25(1)	4063,3369	$12^+, 10^+$
711.2	74(3)	1848,1137	$6^+, 4^+$
734.4	11(1)	4035,3301	$(11^-), (9^-)$
740.0	31(2)	3369,2629	$10^+, 8^+$
780.3	47(4)	2629,1848	$8^+, 6^+$
813.1	19(6)	4876,4063	$14^+, 12^+$
870.2	5(2)	3710,2840	(11), (9)
907.9	6(1)	4943,4035	$(13^-), (11^-)$
945.4	3(1)	4655,3710	(13), (11)
965.0	9(1)	5841,4876	$(16^+), 14^+$
992.6	4(1)	5936,4943	$(15^-), (13^-)$
997.0	12(1)	2845,1848	$(7^-), 6^+$
1109.0	4(1)	6950,5841	$(18^+), (16^+)$
1145.7	4(1)	2994,1848	
1165.0	3(1)	8115,6950	$(20^+), (18^+)$
1204.9	10(1)	2341,1137	$(5^-), 4^+$

5.9 ^{102}Mo Decay Scheme

The yrast sequence of ^{102}Mo has been studied in the ^{234}Cm fission reaction [81] and is known up to 12^+, 3626 keV [81]. A new level has been established at 4507 keV from the present experiment. Another previously unreported level at 1142 keV was found and its only decay to the yrast state at 742 keV suggests it to be $I^\pi = (5^\pm)$ or (6^-) . Two more transitions of 459 and 747 keV were also found to decay into the 1142 keV state (figures 5.45 and 5.46). Newly identified 461 keV and 607 keV transitions were found in coincidence with each other, which ultimately decay to the yrast 6^+ state at 1327 keV. The observation of the 1788 keV state which decays to the 1327 keV level suggests it to be (7^-) . Furthermore, 368, 540, and 1132 keV transitions were also found to be in coincidence, and they decay to 6^+ yrast state at 1327 keV. The only decay to the 1327 keV state from the 2459 keV state suggests it to be either $(7^\pm)$ or $(8^\pm)$, but the assignment of 8^+ for the 2459 keV state may be ruled out, as the 3367 keV state found above the 2459 keV state would then becomes yrast at 12 $\hbar$ (assuming stretched E2 character for the 368 and 540 keV transitions). Moreover, the presence of a strongly populated (7^-) state at 2548 keV in figure 5.44 probably rules out the assignment of 7^- for the 2459 keV state as well. Singularly decaying transitions of 626, 651, and 679 keV were also found in coincidence with the well established yrast states, but were observed without in coincidence with any other known states.

From the quasi-elastic reaction in the present experiment, new transitions have been established, adding to the previously reported decay schemes from β decay studies [103], (t, p) reaction [104, 105, 106] and cold transfer reaction ^{100}Mo(^{18}O, ^{16}O)^{102}Mo [107]. In addition, a new 610 keV transition has been observed to feed a known 4^+ state at 1396 keV, and the 2006 keV level has

been tentatively assigned as (6^+). Four new states at 2147, 2548, 3009, and 3617 keV have also been added above a known 3^- state at 1747 keV, and tentatively assigned as (5^-), (7^-), (9^-), and (11^-) , respectively.

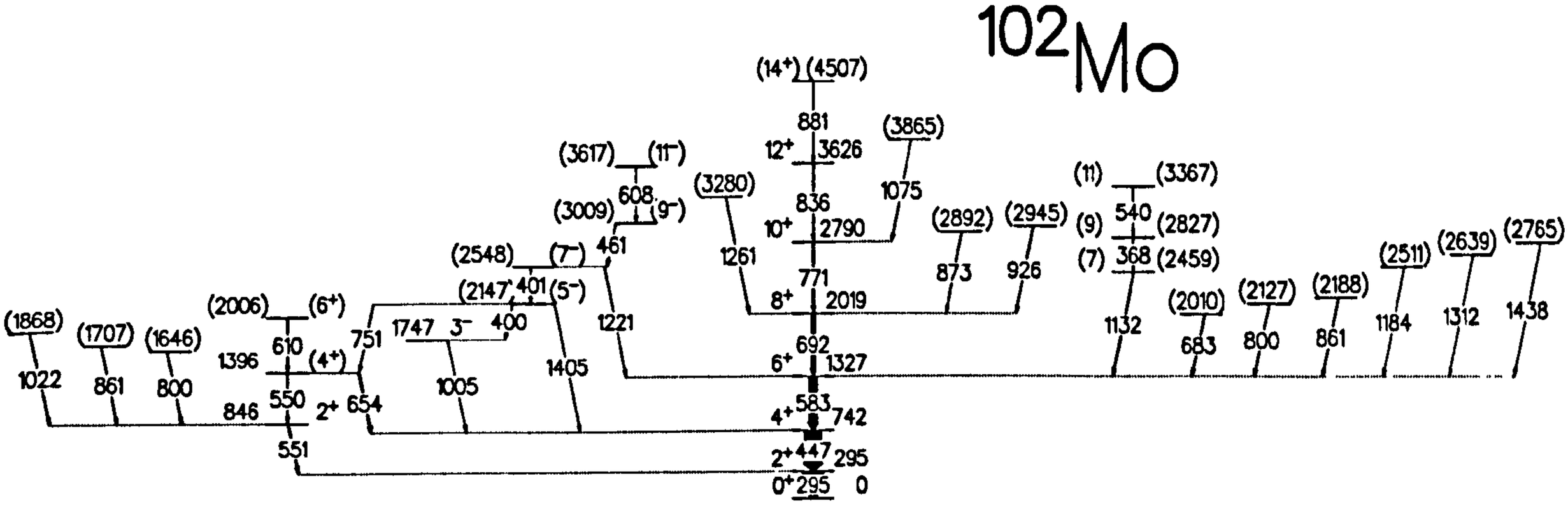

Figure 5.44: Decay scheme of ^{102}Mo as populated in the quasi-elastic reaction.

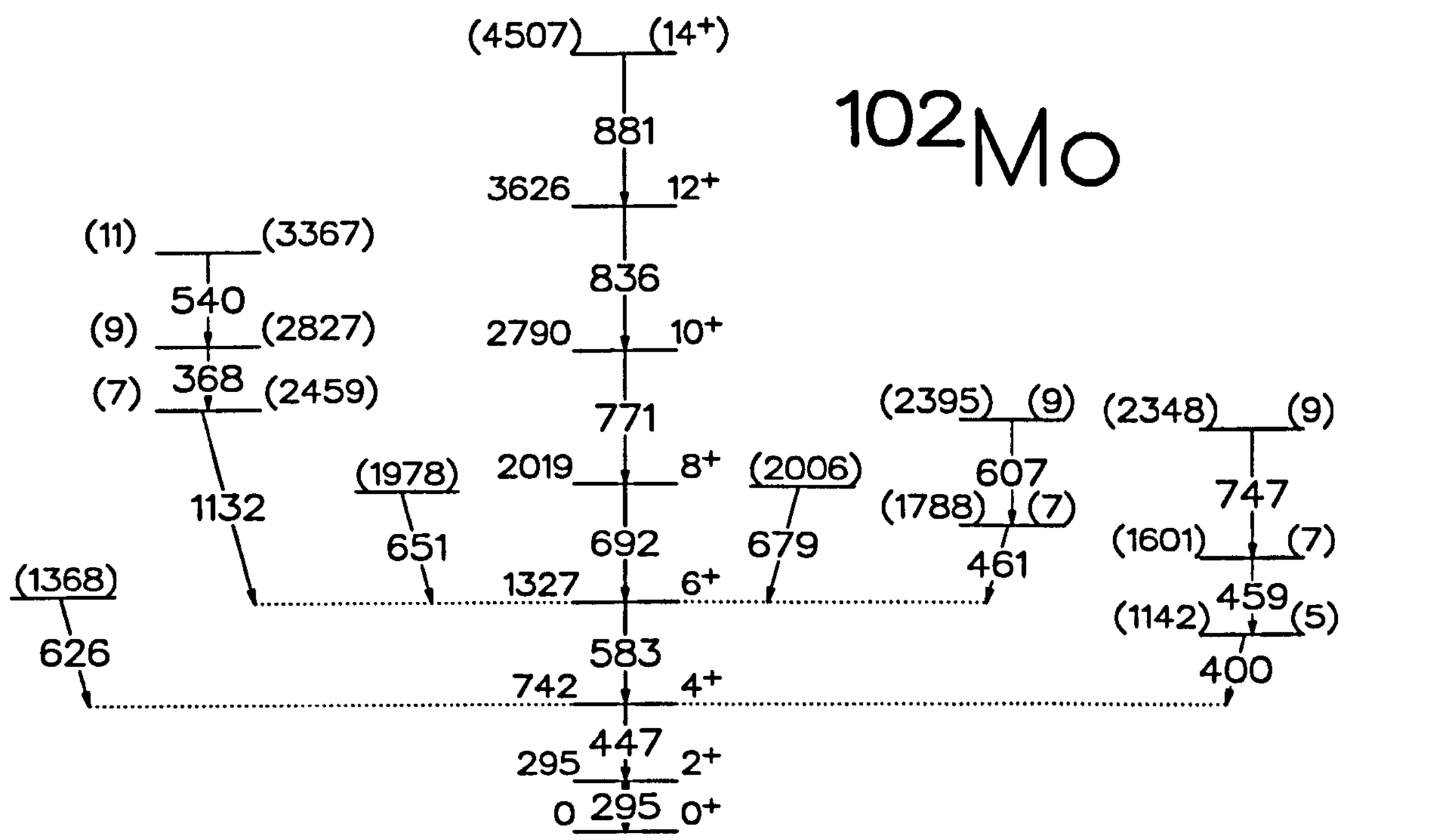

Figure 5.45: Decay scheme of ^{102}Mo as populated in the DIC reaction.

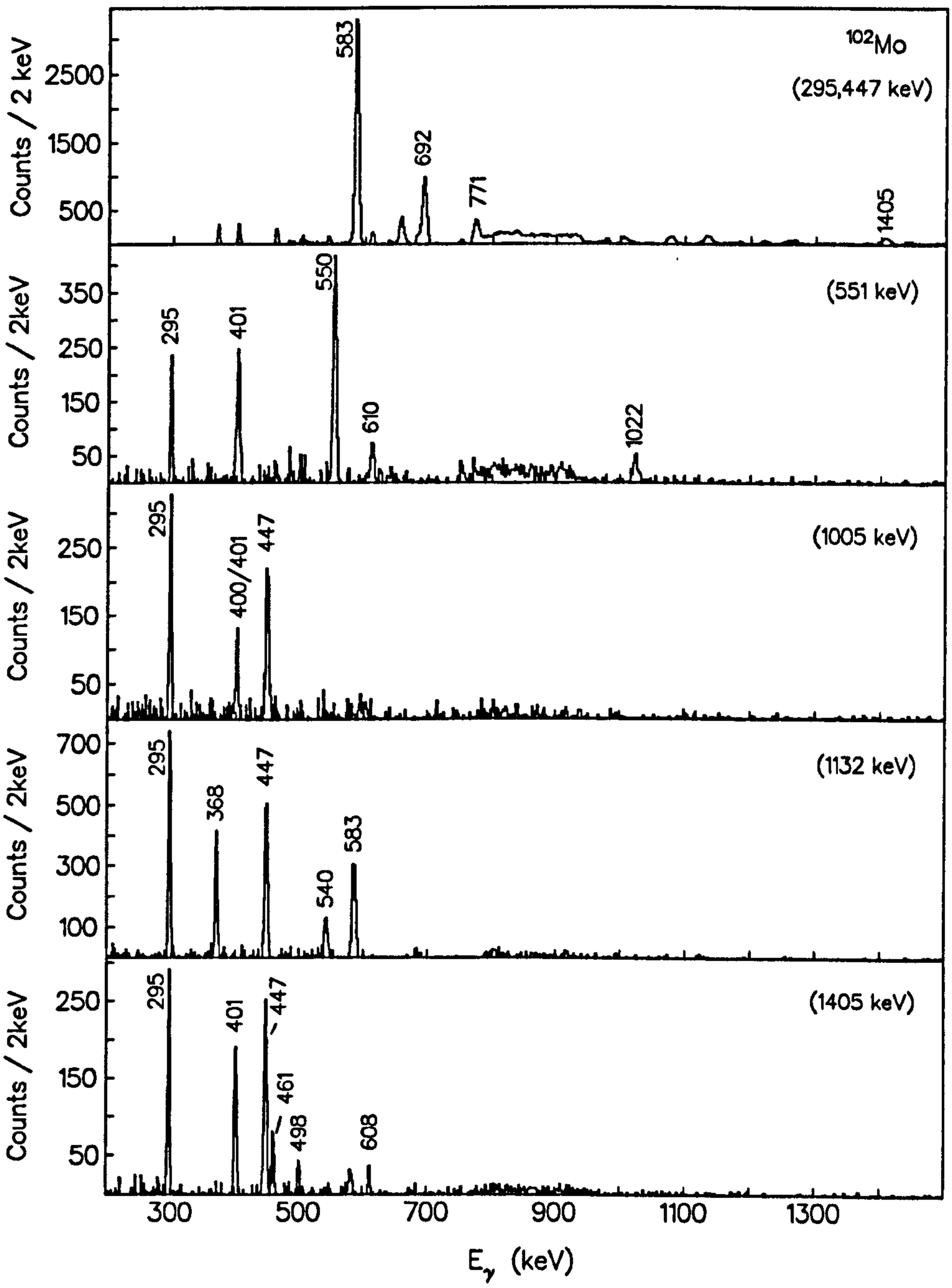

Figure 5.46: Sum of double γ–ray gated spectra, showing the yrast band of ^{102}Mo and the side bands, as populated in the DIC reaction. The γ-ray energies in brackets are the gating transitions in ^{102}Mo used with $2^+_1 - 0^+_1$, 295 keV transition.

Table 5.6: Gamma-ray transitions of ^{102}Mo populated via the quasi-elastic reaction. The γ-ray intensities (in arbitrary units) were taken from a 2-D fit to the $\gamma - \gamma$ coincidence matrix using the program ESCL8R.

E_γ (keV)	I_γ, (arb.)	E_i, E_f (keV)	$J_i^\pi \rightarrow J_f^\pi$
295.0	—	295,0	$2^+, 0^+$
368.3	31(3)	2827,2459	(9),(7)
400.1	7(2)	2147,1747	$(5^-), (3^-)$
401.4	55(3)	2548,2147	$(7^-), (5^-)$
446.9	1000(31)	742,295	$4^+, 2^+$
461.0	28(3)	3009,2548	$(9^-), (7^-)$
539.7	20(3)	3367,2827	$(11^-), (9^-)$
550.3	38(3)	1396,846	$(4^+), 2^+$
551.1	70(7)	846,295	$2^+, 2^+$
583.0	542(17)	1327,742	$6^+, 4^+$
607.6	14(3)	3617,3009	$(11^-), (9^-)$
610.0	45(5)	2006,1396	$(6^+), 4^+$
654.1	67(5)	1396,742	$4^+, 4^+$
683.0	53(5)	2010,1327	
691.7	227(8)	2019,1327	
751.0	24(3)	2147,1396	$(5^-), (4^+)$
771.2	83(5)	2790,2019	$10^+, 8^+$
800.4	36(4)	1646, 846	
800.0	14(4)	2127,1327	
835.5	50(3)	3622,2790	$12^+, 10^+$
860.9	37(4)	2188,1327	
861.2	11(4)	1707, 846	
873.4	23(3)	2892,2019	
881.3	17(3)	4500,3622	$14^+, 12^+$

Table 5.6: Gamma-ray transitions of ^{102}Mo populated via the quasi-elastic reaction (continued...).

E_γ (keV)	I_γ (arb.)	E_i, E_f (keV)	$J_i^\pi \rightarrow J_f^\pi$
926.4	34(3)	2945,2019	
1005.1	21(4)	1747,742	$(3^-), 4^+$
1021.6	10(3)	1868,846	
1075.4	21(2)	3865,2790	
1131.8	50(3)	2459,1327	
1183.7	5(3)	2511,1327	
1221.3	29(3)	2548,1327	
1261.4	17(3)	3280,2019	
1312.2	2(1)	2639,1327	
1405.1	49(3)	2147,742	$(5^-), 4^+$
1437.5	11(2)	2765,1327	

Table 5.7: Gamma-ray transitions of ^{102}Mo populated via the deep inelastic reaction. The γ-ray intensities (in arbitrary units) were taken from a 2-D fit to the $\gamma - \gamma$ coincidence matrix using the program ESCL8R.

E_γ (keV)	I_γ (arb.)	E_i, E_f (keV)	$J_i^\pi \rightarrow J_f^\pi$
295.2	—	295,0	$2^+, 0^+$
368.4	6(2)	2827,2459	(9), (7)
400.1	12(3)	1142,742	(5), 4^+
446.9	100(4)	742,295	$4^+, 2^+$
460.5	10(2)	1788,1327	$6^+, 6^+$
459.1	8(3)	1601,1142	(7),(5)
461.0	4(1)	1788,1327	(7), 6^+
540.2	4(1)	3367,2827	(11), (9)
583.0	79(5)	1327,742	$6^+, 4^+$
607.0	14(3)	2395,1788	(9),(7)
626.1	6(3)	1368,742	
651.0	9(3)	1978,1327	
679.0	19(3)	2006,1327	
691.7	40(4)	2019,1327	$8^+, 6^+$
747.0	3(1)	2348,1601	(9),(7)
771.0	25(3)	2790,2019	$10^+, 8^+$
835.6	18(4)	3625,2790	$12^+, 10^+$
880.8	9(3)	4506,3625	$14^+, 12^+$
1132.3	6(3)	2459,1327	(7), 6^+

5.10 ^{99}Mo Decay Scheme and $h_{11/2}$ band

The low-lying levels in ^{99}Mo below the $\frac{11}{2}^-$ isomer are well established from ^{99}Nb decay studies [108, 109, 110], (d,p) [72], and (d,t) [111, 112] reactions. A stretched E2 cascade of 693 keV and 482 keV γ-rays was first observed above the $\frac{11}{2}^-$ level at 684 keV by Dubuc *et. al.* [113], and later extended up to $\frac{23}{2}^-$ level from the deep inelastic ^{110}Pd + 395 MeV ^{86}Kr reaction[79]. The positive band built on the $T_{1/2} = 15.5$ μs isomer at 98 keV was extended by three transitions up to $(\frac{29}{2}^+)$ from the present triple-γ coincidence study, and is shown in figure 5.49. The usual assumption of stretched E2 systematics for the transitions forming a rotational cascade has been made.

The present study employed the isomer tagging technique to measure the half-life of the $h_{11/2}$ state at 684 keV, and found the half-life to be 639(130) ns (see figure 5.37). This compares with the published value of 0.76(0.06) μs [82]. Previously known transitions of 482, 693, and 845 keV were observed above the isomeric state [79]. Additionally, γ^3 coincidence relations from the present experiment found four more prompt transitions of 980, 1050, 1063, and 1102 keV. Many singularly decaying transitions were also observed in the quasi-elastic channel to feed the $\frac{19}{2}^-$ state at 1859 keV and the $\frac{13}{2}^+$ state at 1679 keV, as well as a 129 keV transition which decays to the $\frac{23}{2}^+$ state at 2704 keV (figure 5.47).

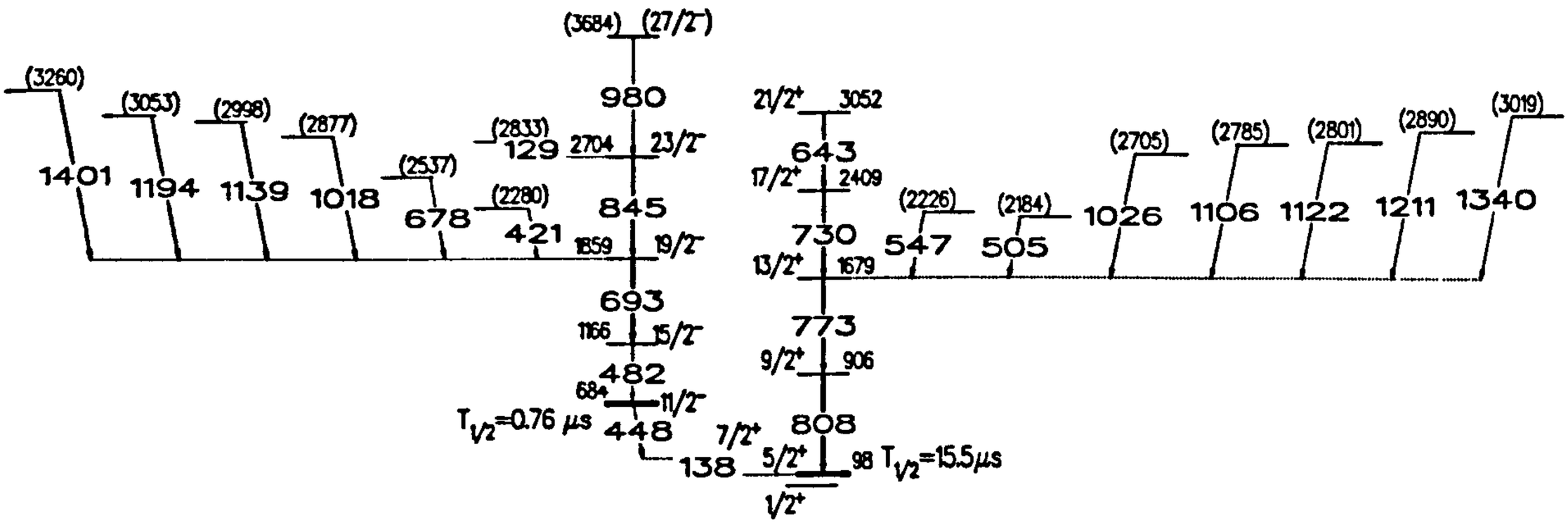

Figure 5.47: Decay scheme of ^{99}Mo deduced from the quasi-elastic gated γ^3 coincidence relations.

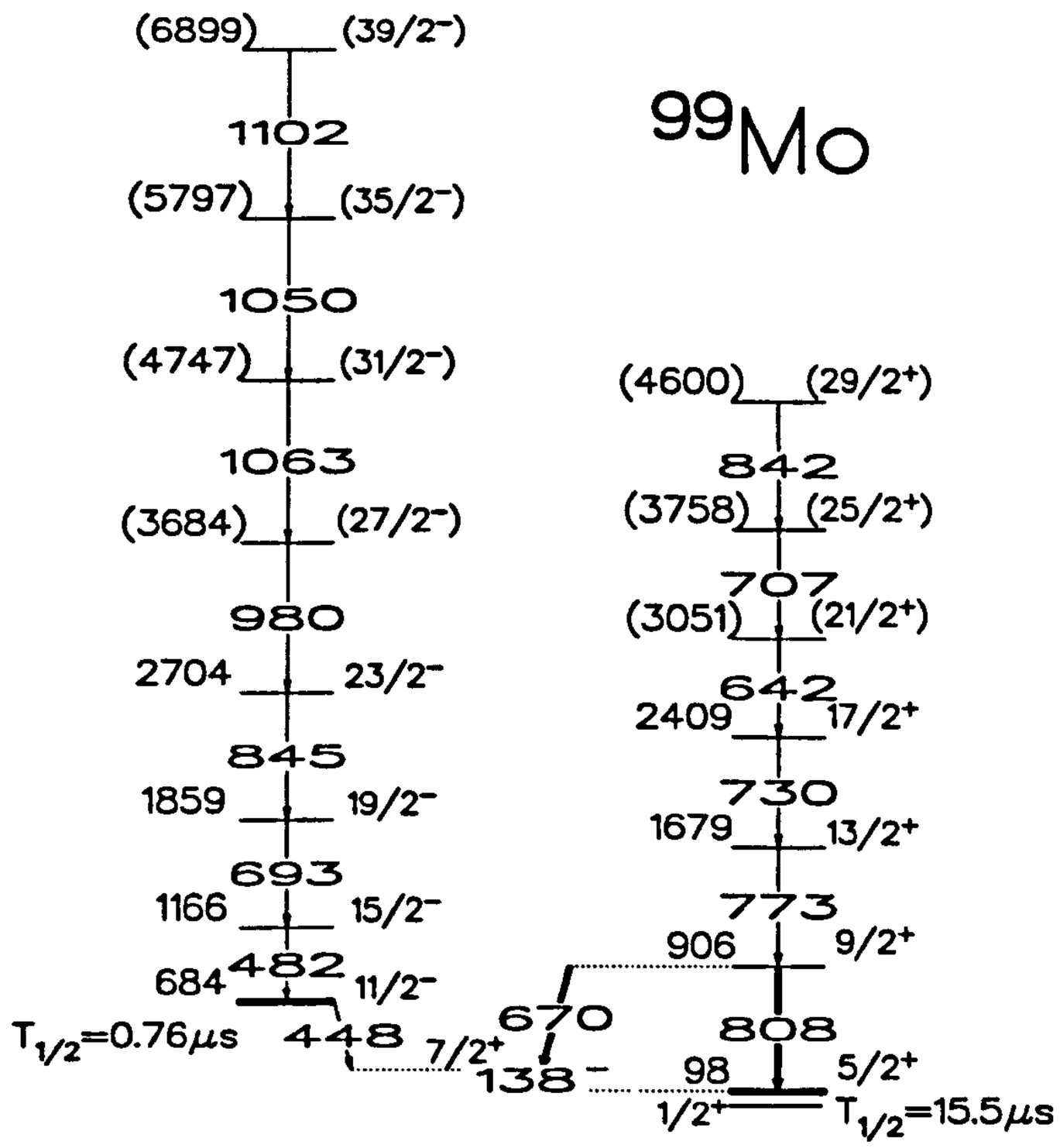

Figure 5.48: Decay scheme of ^{99}Mo deduced from the deep inelastic gated γ^3 coincidence relations.

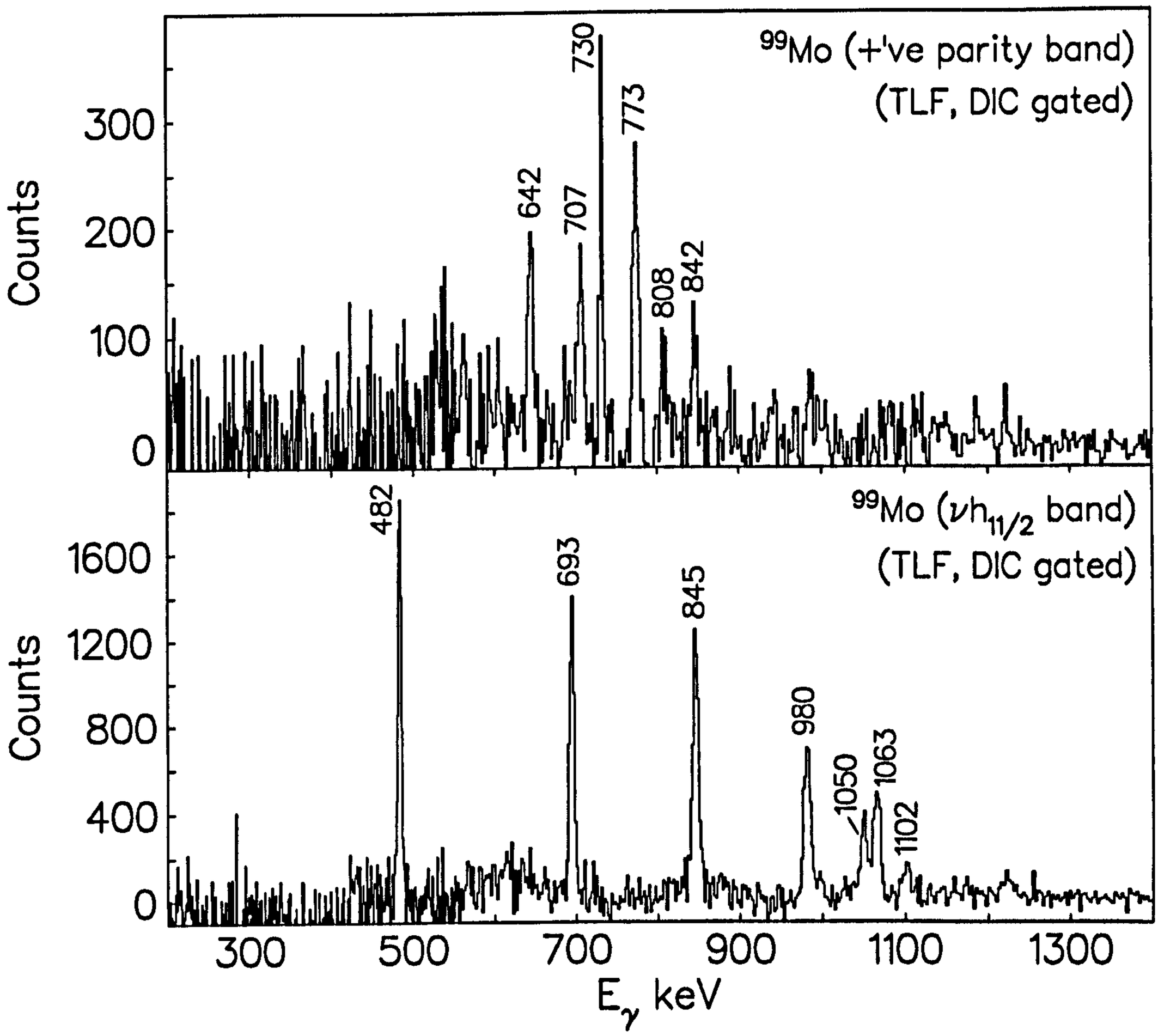

Figure 5.49: Sum of double γ-ray gated spectra for the prompt transitions above the (top) $d_{5/2}$ and (bottom) $h_{11/2}$ isomers in ^{99}Mo, as obtained from the recoil and DIC reaction gated γ^3 coincidence analysis.

Table 5.8: Gamma-ray transitions of ^{99}Mo populated via the quasi-elastic reaction. The γ-ray intensities (in arbitrary units) were taken from a 2-D fit to the $\gamma - \gamma$ coincidence matrix using the program ESCL8R.

E_γ (keV)	I_γ (arb.)	E_i, E_f (keV)	$J_i^\pi \rightarrow J_f^\pi$
420.8	10(6)	2280,1859	$(\frac{17}{2}^-), \frac{19}{2}^-$
482.1	537(29)	1166,684	$\frac{15}{2}^-, \frac{19}{2}^-$
505.4	43(19)	2184,1679	$(\frac{15}{2}^+), \frac{13}{2}^+$
547.2	11(6)	2226,1679	$(\frac{13}{2}^+), \frac{13}{2}^+$
642.6	176(21)	3052,2409	$\frac{21}{2}^+, \frac{17}{2}^+$
678.2	19(5)	2537,1859	$\frac{21}{2}^+, \frac{17}{2}^+$
692.8	654(27)	1859,1166	$\frac{19}{2}^-, \frac{15}{2}^-$
730.3	220(24)	2409,1679	$\frac{17}{2}^+, \frac{13}{2}^+$
773.1	346(37)	1679,906	$\frac{13}{2}^+, \frac{9}{2}^+$
808.0	463(27)	906,98	$\frac{9}{2}^+, \frac{5}{2}^+$
845.2	230(17)	2704,1859	$\frac{23}{2}^-, \frac{19}{2}^-$
979.7	329(31)	3683,2704	$\frac{27}{2}^-, \frac{23}{2}^-$
1018.2	4(2)	2877,1859	$(\frac{19}{2}^-), \frac{19}{2}^-$
1025.6	16(10)	2705,1679	$(\frac{13}{2}^+), \frac{13}{2}^+$
1065.5	28(9)	4750,3684	$(\frac{31}{2}^-), \frac{27}{2}^-$
1106.0	7(2)	2785,1679	$(\frac{15}{2}^+), \frac{13}{2}^+$
1122.1	35(15)	2801,1679	$(\frac{17}{2}^+), \frac{13}{2}^+$
1139.4	74(12)	2998,1859	$(\frac{21}{2}^-), \frac{19}{2}^-$
1194.3	4(1)	3053,1859	$(\frac{23}{2}^-), \frac{19}{2}^-$
1211.0	13(7)	2890,1679	$(\frac{23}{2}^-), \frac{19}{2}^-$
1339.5	2(1)	3019,1679	$(\frac{23}{2}^-), \frac{19}{2}^-$
1401.3	9(6)	3260,1859	$(\frac{21}{2}^-), \frac{19}{2}^-$

Table 5.9: Gamma-ray transitions of ^{99}Mo populated via the deep inelastic reaction. The γ-ray intensities (in arbitrary units) were taken from a 2-D fit to the $\gamma - \gamma$ coincidence matrix using the program ESCL8R.

E_γ (keV)	I_γ (arb.)	E_i, E_f (keV)	$J_i^\pi \rightarrow J_f^\pi$
482.0	4(1)	1166,684	$\frac{15}{2}^-, \frac{19}{2}^-$
642.3	76(9)	3052,2409	$\frac{21}{2}^+, \frac{17}{2}^+$
670.1	4(2)	906, 138	$\frac{21}{2}^+, \frac{17}{2}^+$
692.9	76(5)	1859,1166	$\frac{19}{2}^-, \frac{15}{2}^-$
707.0	49(7)	3758,3051	$(\frac{25}{2}^+), (\frac{21}{2}^+)$
730.3	78(10)	2409,1679	$\frac{17}{2}^+, \frac{13}{2}^+$
773.0	100(14)	1679,906	$\frac{13}{2}^+, \frac{9}{2}^+$
808.1	—	906,98	$\frac{9}{2}^+, \frac{5}{2}^+$
842.0	40(5)	4600,3758	$(\frac{29}{2}^+), (\frac{25}{2}^+)$
845.1	59(2)	2704,1859	$\frac{23}{2}^-, \frac{19}{2}^-$
980.0	38(3)	3684,2704	$\frac{27}{2}^-, \frac{23}{2}^-$
1048.2	15(2)	4734,3684	$\frac{31}{2}^-, \frac{27}{2}^-$
1063.5	24(3)	5797,4734	$(\frac{35}{2}^-), \frac{31}{2}^-$
1102.0	11(2)	6899,5797	$(\frac{39}{2}^-), (\frac{35}{2}^-)$

5.11 ^{101}Mo Decay Scheme and $h_{11/2}$ band

The low-lying structure of ^{101}Mo has been studied by thermal neutron capture [114], (d,p) [115] reaction and sub-Coulomb barrier stripping reaction [116]. The $l = 5$, $h_{11/2}$, nature of the 273 keV level was tentatively assigned from γ-ray angular distribution measurements [117], although no rotational band in ^{101}Mo has been observed prior to the current work. The previously unknown half-life of the $h_{11/2}$ bandhead was measured in the present study using the decay tagging technique, resulting in the observation of a decay curve shown in figure 5.32. A weighted least squares fit to the straight line in the figure yielded a half-life for this isomer of 105(8) ns.

A rotational cascade comprising of γ-ray transitions at 429, 615, 772, 891, 982, and 1071 keV has been observed above the $h_{11/2}$ isomer (figure 5.31), and is observed to have characteristics consistent with a decoupled $h_{11/2}$ band observed in other odd-N Mo-isotopes in this mass region. Once the prompt transitions above the isomer were confirmed, triple γ-ray coincidence analysis identified an additional transition of 1071 keV, and the level at 5033 keV was tentatively assigned as $(\frac{35}{2}^-)$, assuming the stretched E2 systematics for the transitions forming a collective rotational cascade. Singularly decaying transitions of 926, 1189, and 1370 keV were also observed in coincidence with the $(\frac{19}{2}^-)$ level of the decoupled band (figure 5.50).

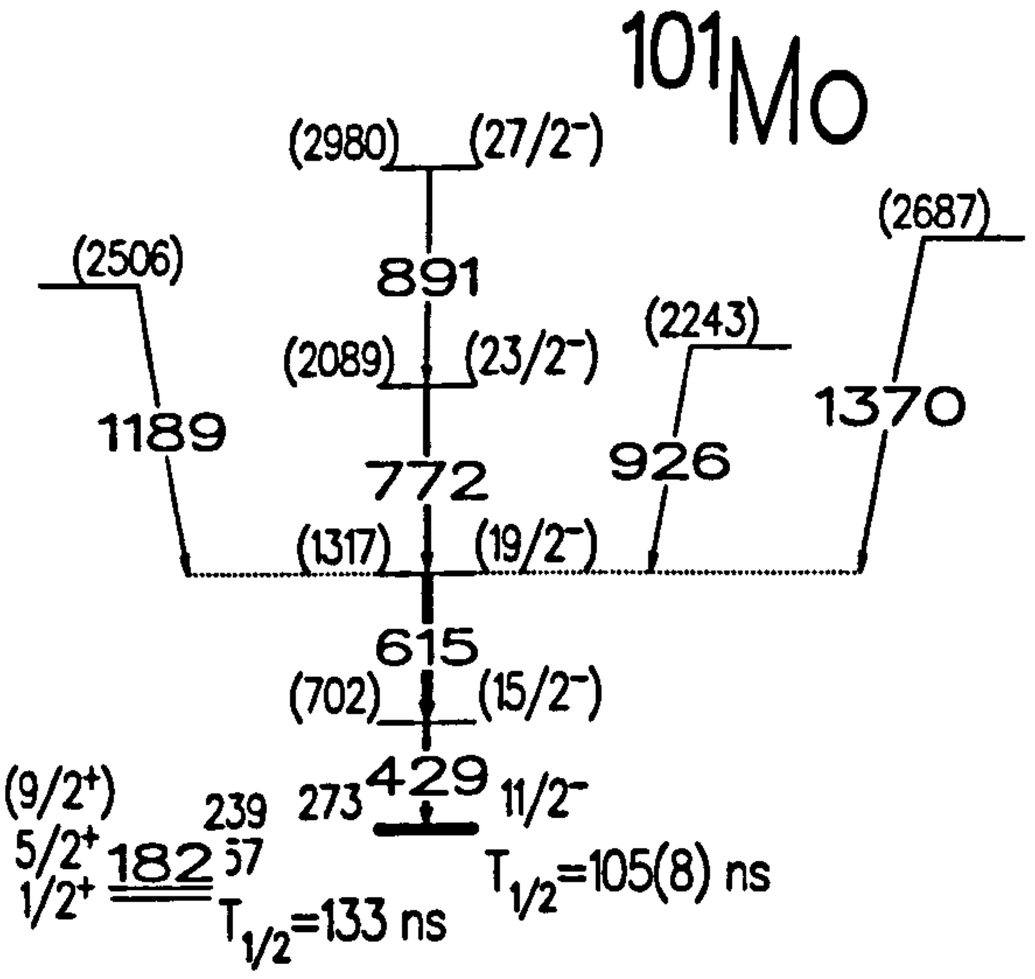

Figure 5.50: Decay Scheme for ^{101}Mo deduced from the quasi-elastic gated γ^3 coincidence relations, and the $h_{11/2}$ isomer lifetime deduced from the current work.

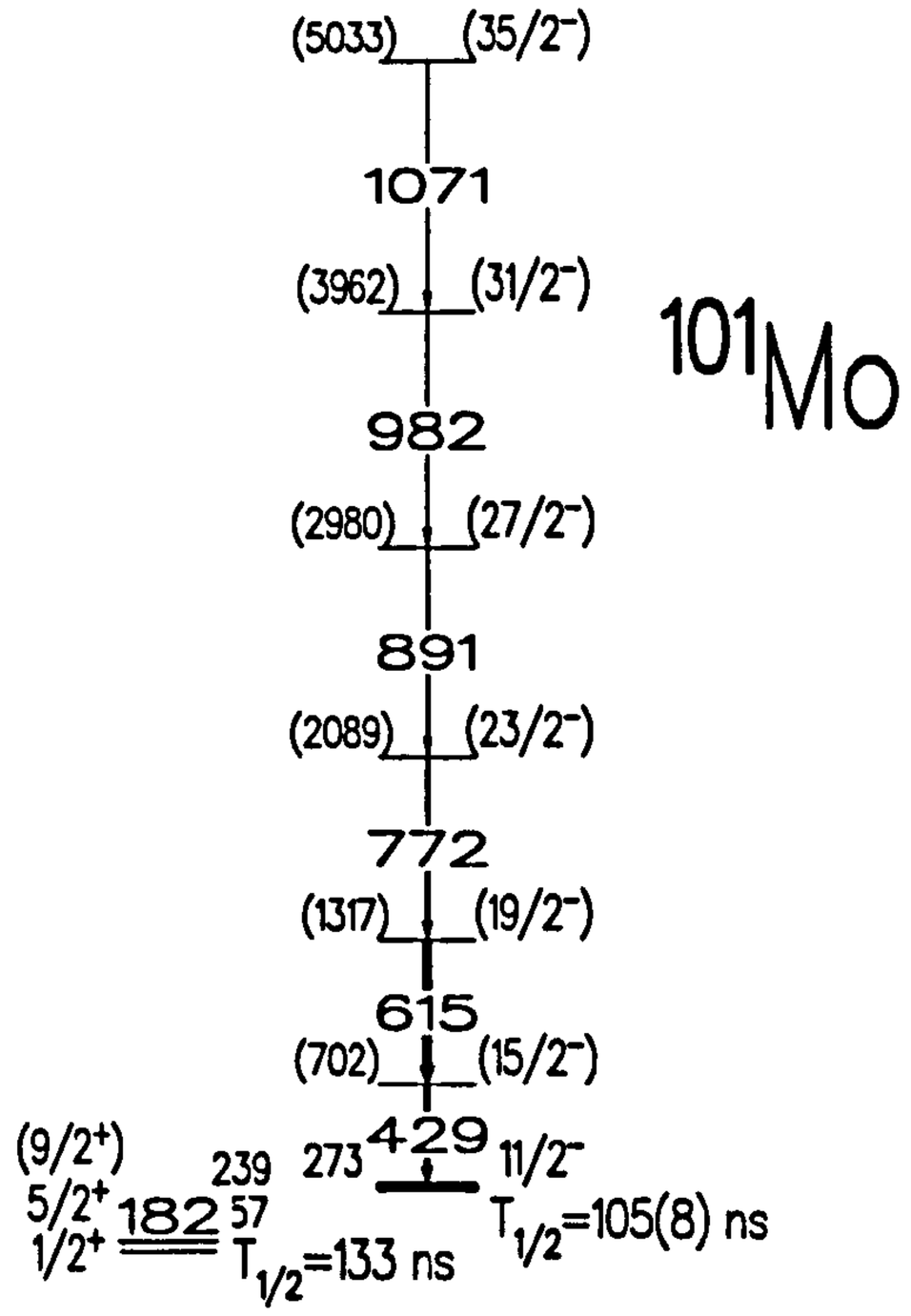

Figure 5.51: Decay Scheme for ^{101}Mo deduced from the deep inelastic gated γ^3 coincidence relations, and the $h_{11/2}$ isomer lifetime deduced from the current work.

Table 5.10: Gamma-ray transitions of ^{101}Mo populated via the quasi-elastic reaction. The γ-ray intensities (in arbitrary units) were taken from a 2-D fit to the $\gamma - \gamma$ coincidence matrix using the program ESCL8R.

E_γ (keV)	I_γ (arb.)	E_i, E_f	$J_i^\pi \rightarrow J_f^\pi$
429.4	—	702,273	$(\frac{15}{2}^-), (\frac{11}{2}^-)$
615.2	100(4)	1317,702	$(\frac{19}{2}^-), \frac{15}{2}^-$
772.0	38(1)	2089,1317	$(\frac{23}{2}^-), (\frac{19}{2}^-)$
890.7	14(1)	2980,2089	$(\frac{27}{2}^-), (\frac{23}{2}^-)$
926.0	3(1)	2243,1317	
1189.1	3(7)	2506,1317	
1370.0	8(2)	2687,1317	

Table 5.11: Gamma-ray transitions of ^{101}Mo populated via the deep inelastic reaction. The γ-ray intensities (in arbitrary units) were taken from a 2-D fit to the $\gamma - \gamma$ coincidence matrix using the program ESCL8R.

E_γ (keV)	I_γ (arb.)	E_i, E_f	$J_i^\pi \rightarrow J_f^\pi$
429.0	—	702,273	$(\frac{15}{2}^-), (\frac{11}{2}^-)$
615.0	100(9)	1317,702	$(\frac{19}{2}^-), \frac{15}{2}^-$
772.0	72(7)	2089,1317	$(\frac{23}{2}^-), (\frac{19}{2}^-)$
890.7	49(6)	2980,2089	$(\frac{27}{2}^-), (\frac{23}{2}^-)$
982.4	21(4)	3962,2980	$(\frac{31}{2}^-), (\frac{27}{2}^-)$
1071.0	13(3)	5033,3962	$(\frac{35}{2}^-), (\frac{31}{2}^-)$

Chapter 6

Discussion and Conclusions

6.1 Phase Changes in Even–N Mo-Isotopes

In the neutron-rich nuclei around mass A $\simeq$ 100, rapid changes in nuclear shape are known to begin as valence nucleons start to fill the $h_{11/2}$ neutron and $g_{9/2}$ proton orbitals. However, the exact location of where these transitions occur and the rapidity of such transitions is still interpreted in a model dependent way, due in part to difficulties in extracting the signs and magnitudes of static quadrupole moments through Coulomb excitation measurements. Nevertheless, details of the band-crossing in these nuclei at high spin can provide useful insights on the Coriolis-driven shape changes, since they are particularly sensitive to the interplay between the single-particle and the shape degrees of freedom. The interpretations offered by the cranked Shell Model (CSM) have been able to provide consistent results in this mass region, and the Cranked-Woods-Saxon-Strutinsky model was subsequently used to calculate the Total Routhian Surface (TRS) for Mo-isotopes and N = 57 isotones in this mass region. the experimental data obtained from both ^{96}Zr + ^{9}Be fusion evaporation and ^{100}Mo + 700 MeV ^{136}Xe binary reaction experi-

ments were compared to the TRS calculations, and the alignment properties of Mo-isotopes and the N = 57 isotones were analysed employing this model. Pauli blocking arguments drawing upon the new information from the odd-N neighbours of ^{102}Ru and ^{100}Mo nuclei were used to prove the role of low-Ω, $\nu h_{11/2}$ orbitals in stabilising their nuclear quadrupole shape.

The analysis of Coriolis-driven particle alignments within the cranked Shell Model formalism often prescribes a rotational approximation to transitional nuclei which may possess quasi-vibrational collectivity at low-spin. Such structural prescription can obscure subtle phase transitional effects as a function of spin, and the interpretations offered by the 'E-Gamma Over Spin' (EGOS) analysis [118] may provide clearer insight to the true nature of the phase changes occurring in the transitional nuclei. Within this EGOS formalism, the γ-ray decay energy of yrast states which differ in spin by 2 $\hbar$, divided by spin (i.e. $R = \frac{E_\gamma}{I}$), as a function of spin then allows to differentiate between the vibrational mode from the rotational nuclear collectivity, since for a

$$vibrator: \quad R = \frac{\hbar\omega}{I} \xrightarrow{I\to\infty} 0, \tag{6.1}$$

$$rotor: \quad R = \frac{\hbar^2}{2J}\left(\frac{4I-2}{I}\right) \xrightarrow{I\to\infty} 4\left(\frac{\hbar^2}{2J}\right), \tag{6.2}$$

where J is the moment of inertia. In the limit of a large value of I, the above formulae 6.1 and 6.2 assume for a perfect harmonic vibrator of $E_\gamma(I \to I-2) = \hbar\omega$, and for a pure rotor, $E_\gamma(I \to I-2) = 4\left(\frac{\hbar^2}{2J}\right)$. When plotted, R increases from $3\left(\frac{\hbar^2}{2J}\right)$ for $I = 2$ to a constant value of $4\left(\frac{\hbar^2}{2J}\right)$ in the rotational case, whereas for a vibrator, R decreases hyperbolically towards zero.

The level structures of even-N Mo-isotopes up to ^{100}Mo (N = 58) are known to exhibit quasi-vibrational characteristics, and their low-lying positive parity levels have been investigated by models incorporating both spherical and deformed degrees of freedom [5, 6, 119, 120]. Most noticeably from

the EGOS-plots in figure 6.1, the lighter members of the Mo-isotopes ($N \leq 58$) indeed follow closely the hyperbolic loci associated with the vibrational structure. Interestingly for the $N = 58$, ^{100}Mo nucleus, where information on the high-spin states are now available, it exhibits a phase change from a vibrator to a constant R-value, suggestive of a rotational structure. This phase change from the vibrational to rotational nuclear collectivity at spin of $\sim$10$-$12 $\hbar$ is often interpreted by the crossing of vibrational ground state (g.s.) structure with an aligned $(\nu h_{11/2})^2_{10+}$ structure [79, 121].

The comparison of experimental alignment properties from different Mo-isotopes allows the identification of chief orbitals responsible for the structural changes frequently observed in this mass region. High-spin experimental results are often presented in a plot of aligned angular momentum (i_x) corrected for the core rotation against the rotational frequency, represented by ω. For the Harris parameterisation required for the analysis of high-spin states in Mo-isotopes, adopted values of $J^0 = 7.0\ \hbar/\text{MeV}^2$ and $J^1 = 15.0\ \hbar^2/\text{MeV}^4$ were used. In figure of 6.1, even-N ^{98}Mo and ^{100}Mo isotopes exhibit a backbend around the same crossing frequencies. This seems to indicate that the same orbital may be responsible for the observed alignment in the even-N Mo-isotopes. For ^{98}Mo and ^{100}Mo isotopes, the phase changes seem to occur at a frequency of $\sim$0.4 MeV, although this critical crossing frequency may be shifted with increasing neutron number, so that between $N = 56$$-$$58$ (^{98,100}Mo), there is a $\sim$0.05 MeV delay in the critical frequency. In addition, the magnitude of alignment gain as a result of the observed backbend may provide some insight into the characteristics of the aligning orbital. In this mass region, both $g_{9/2}$ proton and $h_{11/2}$ neutron orbits can produce a large alignment gain. The amount of aligned angular momentum in ^{100}Mo observed in figure 6.1 is $\sim$10 $\hbar$, and thus prefers the crossing of the

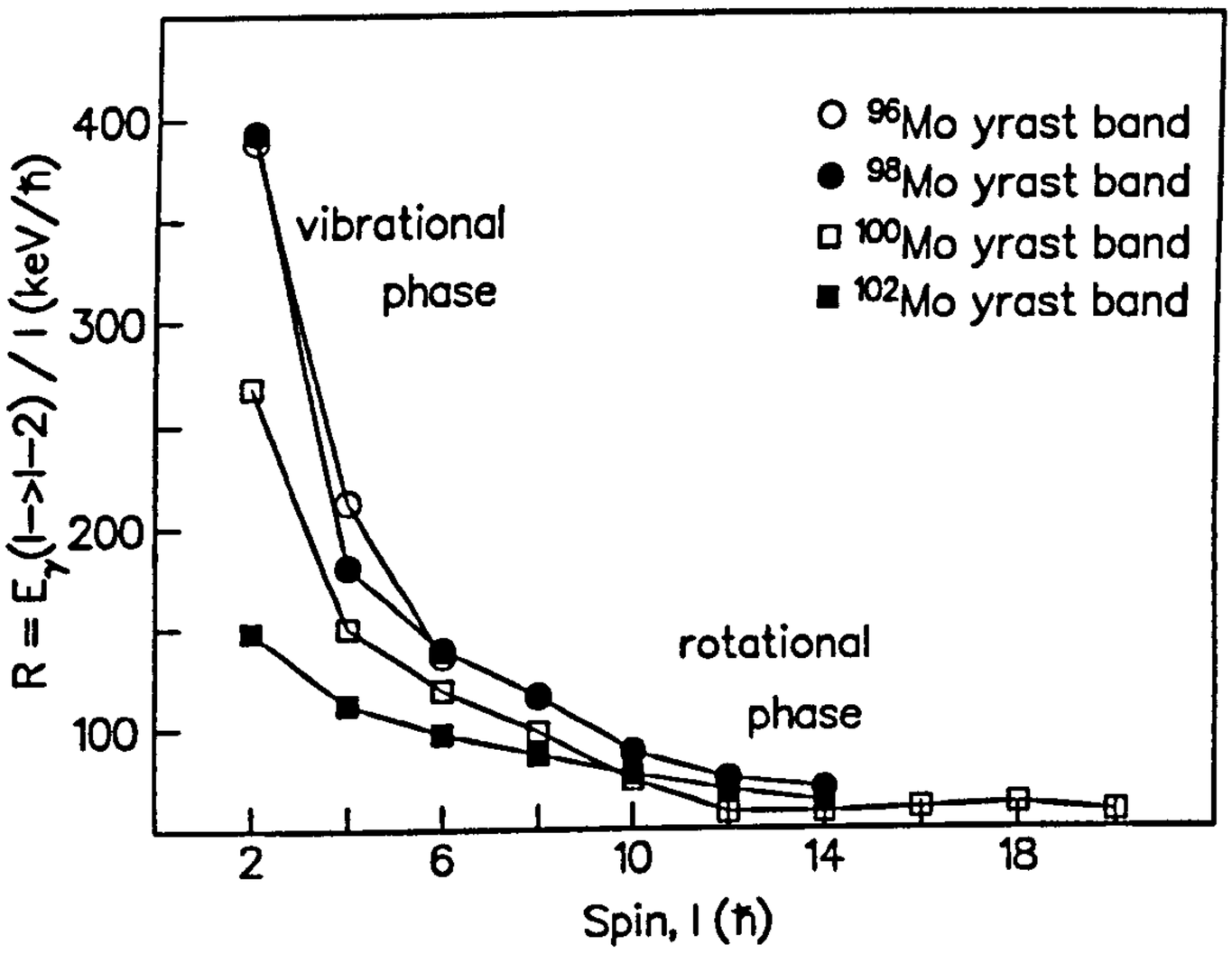

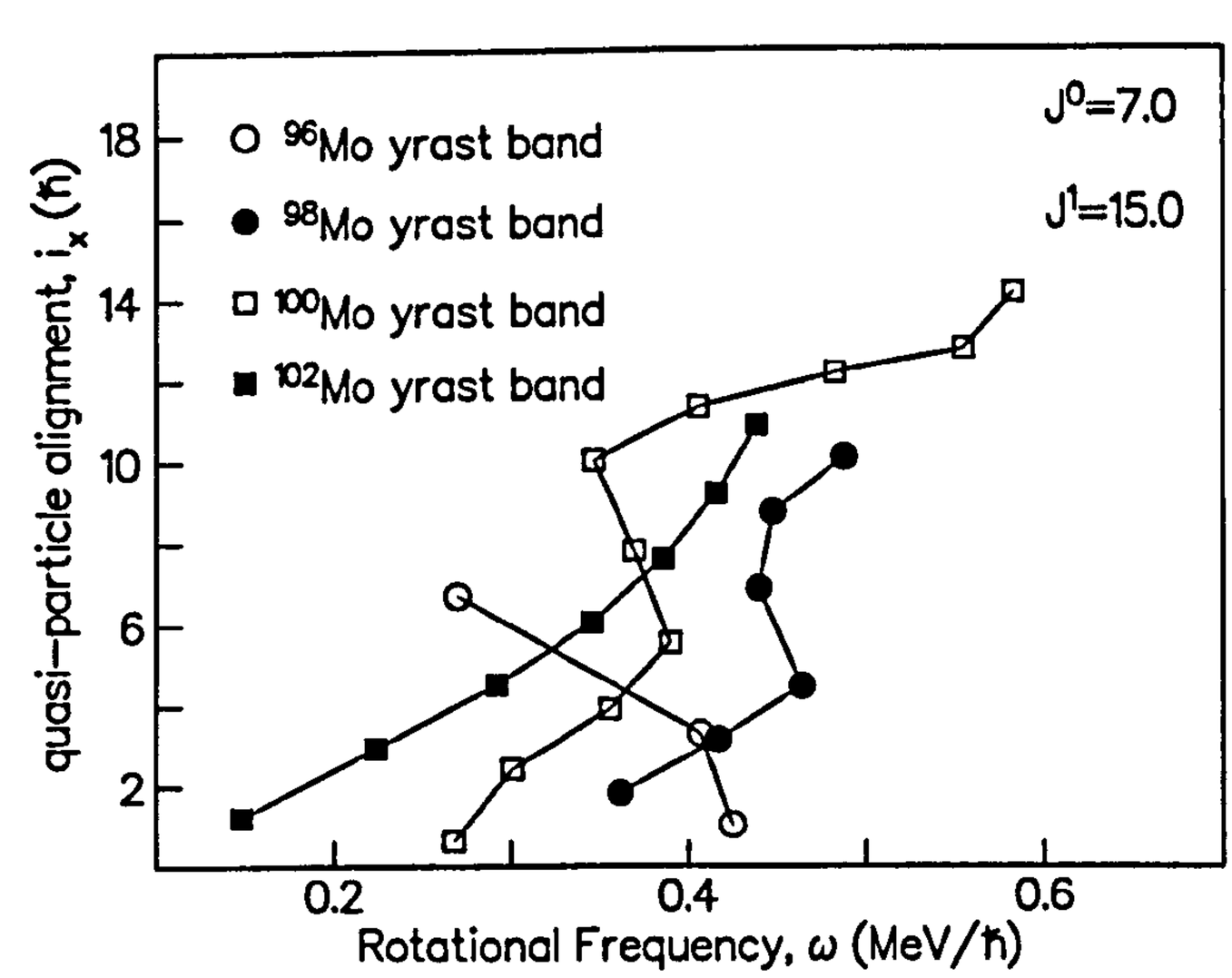

Figure 6.1: (top) EGOS plot for the even-N members of the Mo-isotopes; (below) Deduced quasi-particle alignments for the even-N Mo-isotopes, using the Harris parameters of $\Im^0 = 7.0\ \hbar^2/\mathrm{MeV}$ and $\Im^1 = 15.0\ \hbar^4/\mathrm{MeV}^3$

$(h_{11/2})^2$ neutrons to be the main cause for this alignment.

A theoretical interpretation of such experimental data has been provided by the TRS calculations. An advantage of the TRS calculations is to allow the proton and the neutron contributions to the total aligned angular momentum to be decomposed separately, such that the experimental data on a specific nucleus can be analysed with respect to the changes in both proton and neutron configurations. In figure 6.2, the TRS calculations predict that a pair of neutron quasi-particles align and the quasi-particles are responsible for the first crossing at the critical frequency of $\hbar\omega$ ~0.4 MeV, with the first proton alignment for this configuration not predicted until rotational frequencies of $\hbar\omega$ ~0.6 MeV. Thus the structure of even-N Mo-isotopes, certainly at low to medium spin, are predicted to be dominated by the $(h_{11/2})^2$ neutron configuration. At higher frequencies of ~0.5 MeV, the ^{100}Mo nucleus shows sign of a second alignment, and may suggest that the aligned $g_{9/2}$ proton configurations are favoured at high spin. It is also instructive to compare the experimental results with the Routhian diagram of figures 6.3 and 6.4, plotted for the ^{100}Mo nucleus. According to the diagram, the first 'AB' $(h_{11/2})^2$ neutron alignment can be seen to be favoured over both $(g_{9/2})^2$ proton and $(g_{7/2})^2$ neutron crossing. In figure 6.2, small discrepancies between the location of the first alignment predicted by the CSM and the experimental values that consistently occur at lower frequencies may be realised in the Total Routhian Surface of figure 6.5, which are plotted for the lowest positive parity configurations in the ^{100}Mo. The TRS calculation predicts γ-softness ranging from $\gamma = -20°$ and $\gamma = +20°$. However, in the case of ^{100}Mo in which the ground state levels are followed beyond the first backbend, the TRS calculation describes the ground state band properties well, and predicts a second alignment at $\hbar\omega \approx 0.55$ MeV, in good agreement with the experi-

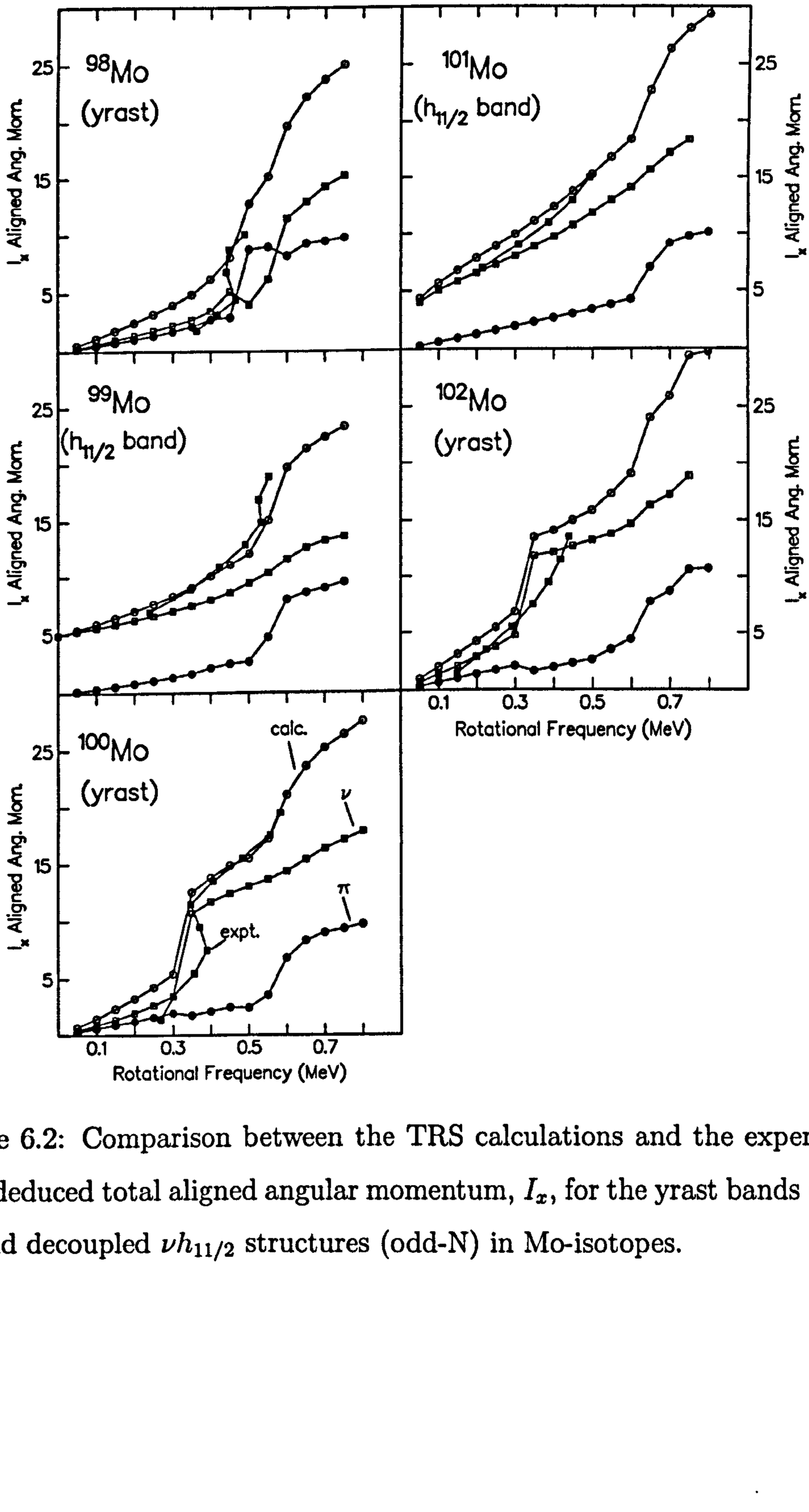

Figure 6.2: Comparison between the TRS calculations and the experimentally deduced total aligned angular momentum, I_x, for the yrast bands (even-N) and decoupled $\nu h_{11/2}$ structures (odd-N) in Mo-isotopes.

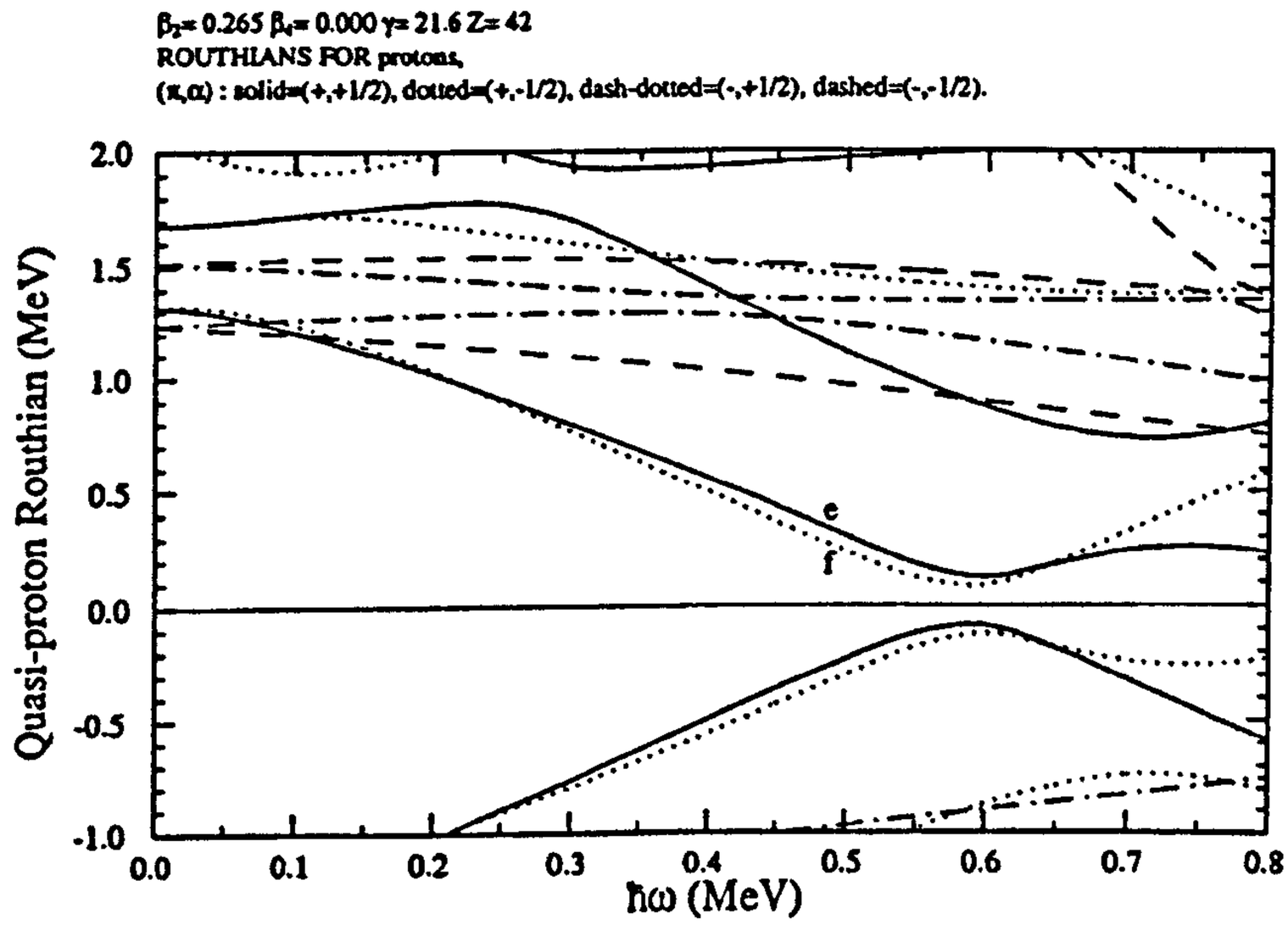

Figure 6.3: The Routhian diagram calculated for the protons in ^{100}Mo. The deformation parameters used were $\beta_2 = 0.265$, $\beta_4 = 0.000$, and $\gamma = 21.6°$.

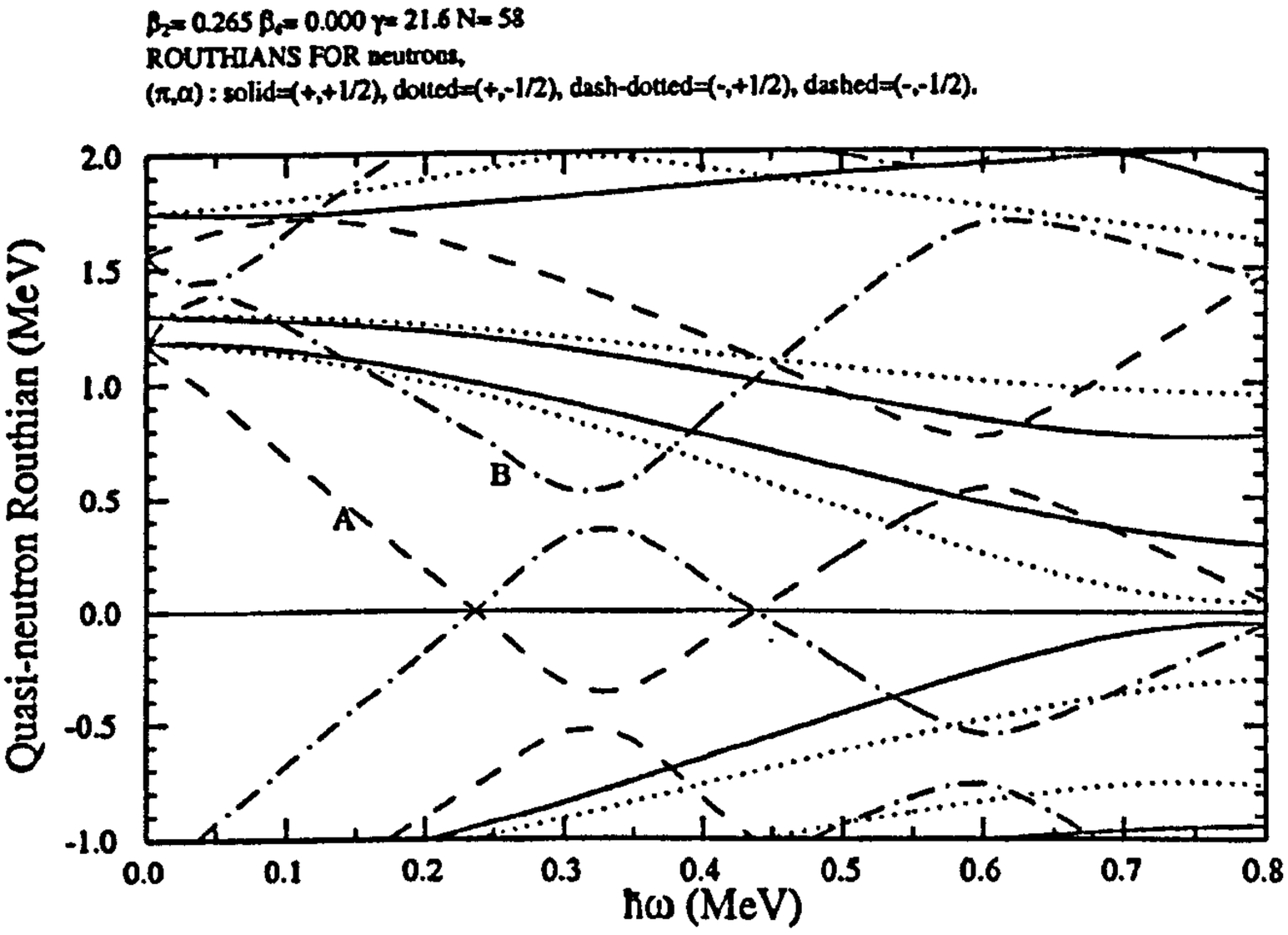

Figure 6.4: The Routhian diagram calculated for the neutrons in ^{100}Mo. The deformation parameters used were $\beta_2 = 0.265$, $\beta_4 = 0.000$, and $\gamma = 21.6°$.

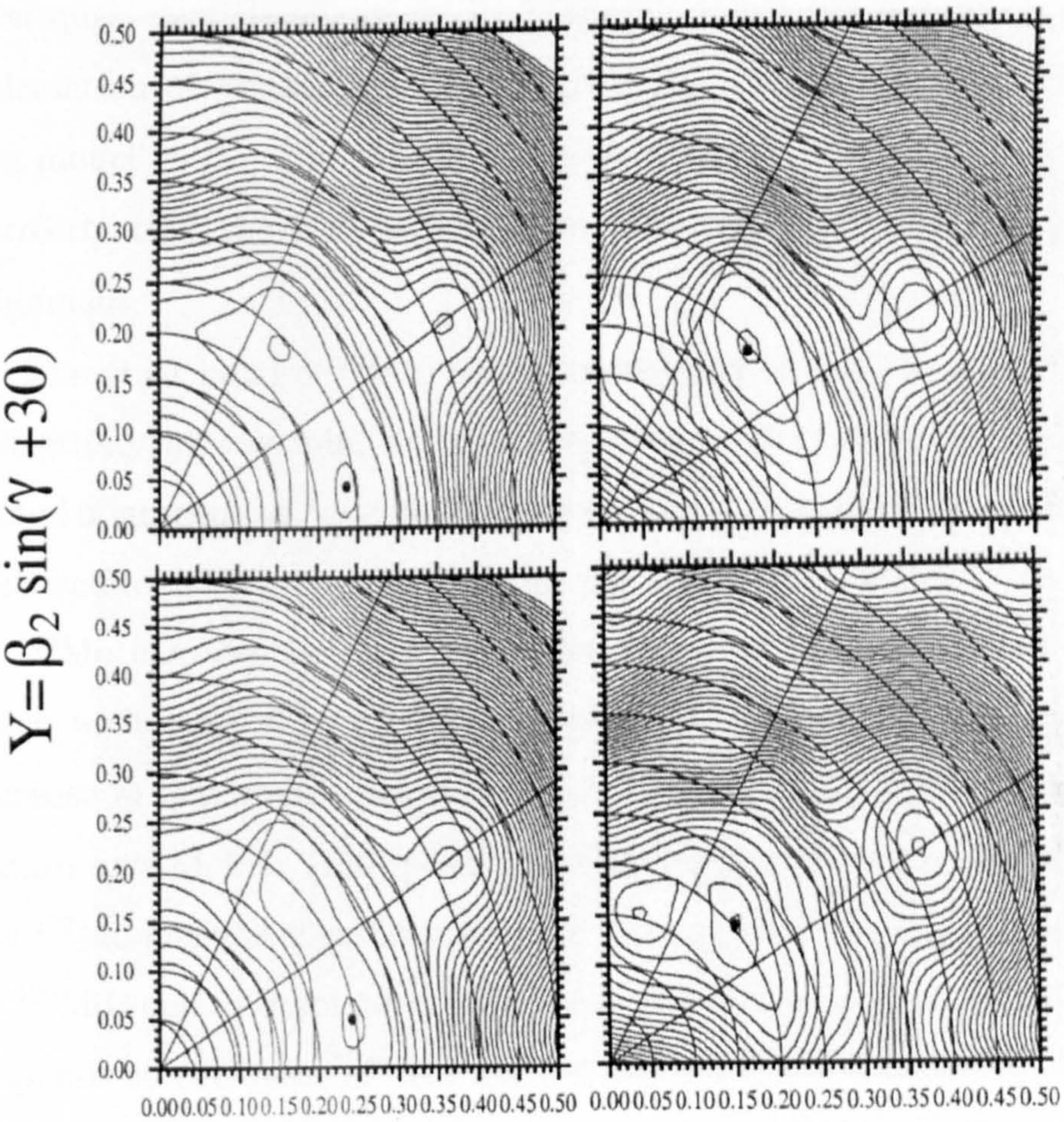

Figure 6.5: Total Routhian Surface calculations for the (0,+) configurations in ^{100}Mo. *upper left*: ω = 0.000 MeV/$\hbar$, (β_2 = 0.239, β_4 = 0.012, γ = -19.8°); *bottom left*: ω = 0.201 MeV/$\hbar$, (β_2 = 0.246, β_4 = 0.017, γ = -18.5°); *upper right*: ω = 0.502 MeV/$\hbar$, (β_2 = 0.246, β_4 = 0.015, γ = 15.2°); *bottom right*: ω = 0.702 MeV/$\hbar$, (β_2 = 0.204, β_4 = 0.004, γ = 13.4°). The energy contour on these calculations is 200 keV.

mental values. The properties of the alignment thus seem quite strongly shape-dependent, and accordingly, the critical backbending frequency for the first quasi-particle alignment in ^{100}Mo of $\sim$0.4 $\hbar\omega$ is well reproduced in the calculation of Mathur and Mukherjee [121], who employed a cranked Nilsson model with pairing and a highly deformed core configuration to predict correctly that the first alignment in ^{100}Mo is due to the $(h_{11/2})^2$ neutron alignment.

The yrast band of ^{102}Mo has been observed to show a markedly different collectivity at low-spin, and remains rotational in character past the predicted alignment at $\hbar\omega \approx 0.30$ MeV, as indicated in figure 6.1 and figure 6.2. This sudden change in structure for the low-lying states in ^{102}Mo compared to ^{100}Mo can also be recognised from the $\sim$0.3 MeV change in the $E(2_1^+)$ value with respect to the ^{100}Mo (see figure 1.4). This suggests a marked increase in quadrupole deformation. Moreover, a IBM-2 calculation of Sambataro and Molnár [120] predicted that the ground state wavefunction for the ^{102}Mo includes significantly more configuration mixing than either ^{98}Mo or ^{100}Mo, and is dominated by two-particle-two-hole excitations. This corresponds to the onset of deformation beyond N = 60, where the $^{90}_{40}Zr_{50}$ core begins to acquire a non-spherical shape. As pointed out by Smith *et. al.* [81], the increased quadrupole moments with spin for the yrast states in ^{102}Mo can also be attributed within the CSM formalism as due to the $h_{11/2}$ neutrons aligning their angular momentum with the rotational axis and causing the minimum in the potential energy surface to move from $\gamma = -20°$ to $\gamma = +20°$ at $\hbar\omega \approx 0.38$ MeV.

It is also interesting to note that at higher rotational frequencies of ω $\sim$0.7 MeV/$\hbar$ (corresponding to aligned spin of $\sim$20–30 $\hbar$), a well-defined superdeformed minimum appears in the potential energy surface for A $\simeq$

100 Mo-isotopes around $\beta \sim 0.4$ (figure 6.5). The current ^{100}Mo + 700 MeV ^{136}Xe experiment chose a beam energy to be approximately 25 % above the Coulomb barrier between the projectile and the target, which corresponds to a maximum expected value of the target-like fragment intrinsic spin of ~25 $\hbar$. This is indeed what was observed in the present experiment, suggesting that a deep inelastic collision using a heavier projectile (e.g. ^{208}Pb) at a similar energy above the Coulomb barrier may be utilised in future for the search of superdeformed structures in the neutron-rich A $\simeq$ 100 Mo-isotopes. Note, that at 25 % above the Coulomb barrier using the lead projectile, the 'rolling limit' of the surface-friction model predicts input spin for the target-like fragments of greater than ~30 $\hbar$.

6.2 Odd-N Mo-Isotopes and The Pauli Blocking Effect

In ^{99}Mo and ^{101}Mo, the high-spin, negative-parity structure can now be determined from the present data, and the changes occurring along the $\nu h_{11/2}$ bands have been interpreted using the TRS calculations. They are studied in the quasi-particle alignment plot in figure 6.2, which also compares them with predictions of the TRS calculations. In comparing these nuclei, and with the ^{97}Mo and ^{103}Mo nuclei, the same values of the Harris parameters were assumed for these Mo-isotopes, and were taken as $\Im^0 = 7.0\ \hbar^2/\mathrm{MeV}$ and $\Im^1 = 15.0\ \hbar^4/\mathrm{MeV}^3$, although the concept of a static moment of inertia reference in the limit of a small deformation and γ-softness may be questionable. In a lower spin regime, the structures of ^{99}Mo and ^{101}Mo are both predicted to have small deformations and to be γ soft, and this is reflected in the observed smooth changes in alignment along the $\nu h_{11/2}$ cascade. For

the ^{99}Mo nucleus, however, a dramatic increase in alignment is observed at $\hbar\omega$~0.5 MeV as an upbend. This is in agreement with the weakening interaction expected for the $(\pi g_{9/2})^2$ crossing associated with the lower Ω orbitals, which reside close to the Fermi surface. As with the observed systematics of the $(\frac{17}{2}^-)$ state in the odd-N Mo-isotopes [122], and in comparison with the $\nu h_{11/2}$ structure presently established in ^{101}Ru, the increased core deformation is probably responsible for pushing the predicted $(\nu g_{7/2})^2$ crossing up to higher crossing, which may explain the lack of $(\nu g_{7/2})^2$ alignment in ^{99}Mo. Note that the highest yrast spins observed in ^{100}Mo show the beginning of a second alignment, and may suggest the start of this $(\nu g_{7/2})^2$ crossing, at a critical frequency of $\hbar\omega$~0.5 MeV.

The backbending behaviour of the various single quasi-particle bands in the odd-N nuclei adjacent to ^{100}Mo and ^{102}Ru perhaps provides a better experimental clarification of orbitals responsible for the alignments and associated shape changes. The alignment of negative parity bands in ^{97,99,101,103}Mo is displayed in figure 6.6, where they are also compared with the alignments of the yrast bands in the neighbouring ^{96,98,100,102}Mo isotopes. The maximum alignment for the even-N yrast Mo-isotopes is about ~10 $\hbar$, consistent for a crossing of the ('AB') $\nu h_{11/2}$ neutron pair. In addition, figure 6.6 also illustrates the clear sign of Pauli-blocking effects manifested in the negative parity, $\nu h_{11/2}$ bands belonging to the ^{99}Mo nucleus at rotational frequencies of $\hbar\omega$~0.4 MeV, where the first alignment has been observed in ^{100}Mo. In addition, the $(\nu h_{11/2})^2$ assignment for the first backbend in ^{98,100}Mo can be almost confirmed by the observation of alignment properties belonging to the negative parity band in ^{100}Mo (figure 5.42). The band built on the (9^-) state is considered to have a significant $(h_{11/2})$ component, so that the band-crossing observed in the yrast band of ^{100}Mo should be blocked for

this negative parity sideband (see figure 6.7). When plotted in the same figure (figure 6.7), the backbending at ~0.4 MeV, which is clearly seen in the yrast band, is indeed blocked for the negative parity band, and the sideband only shows a smooth increase in alignment with increasing rotational frequency. Nevertheless, the first crossing frequency for ^{99}Mo of $\hbar\omega$ ~0.5 MeV is slightly smaller than those values typical for the second crossing in even-N Mo-isotopes, but is consistent with the crossing frequency expected from the cranked Shell Model for a pair of two $g_{9/2}$ protons.

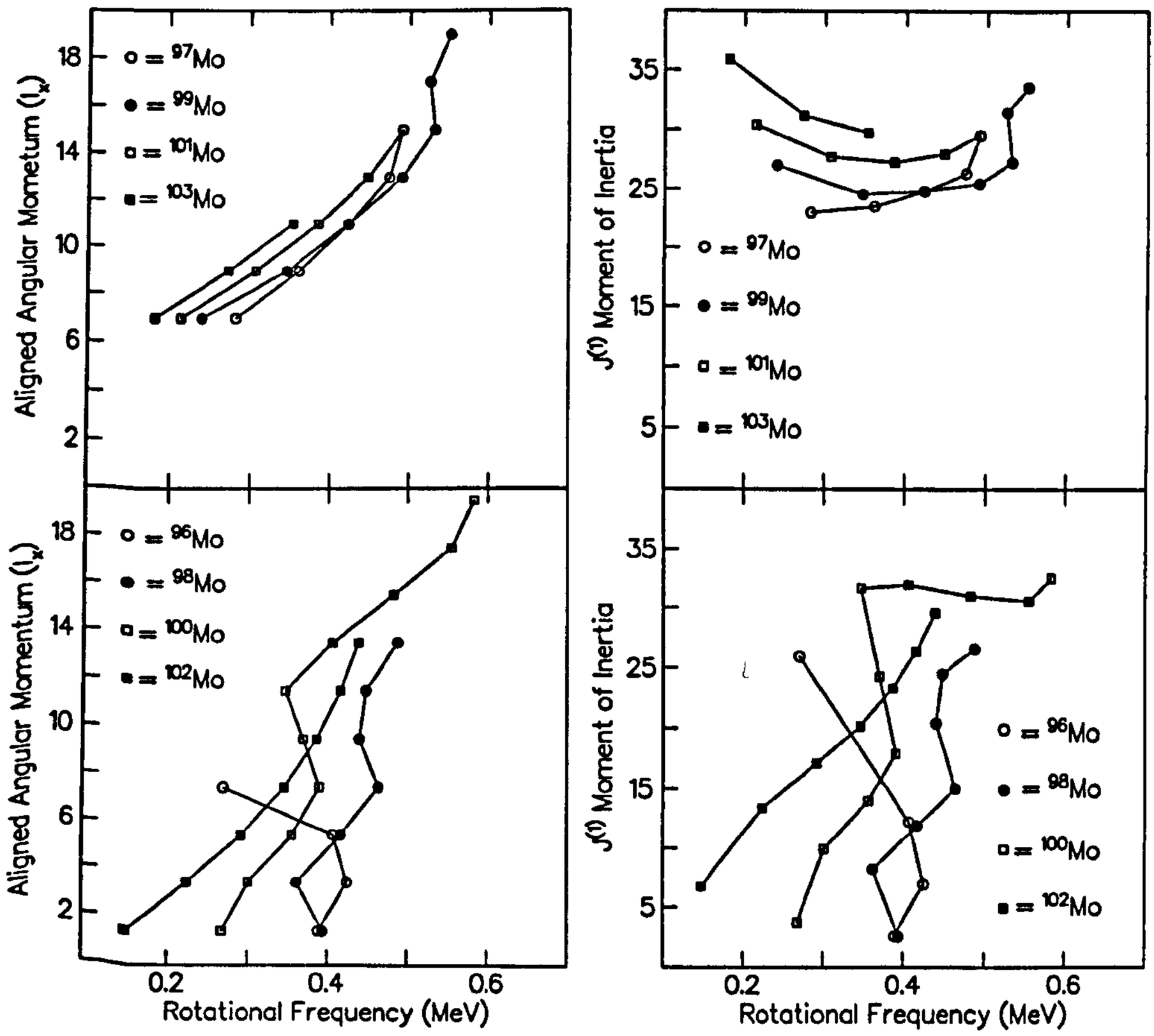

Figure 6.6: Experimental alignment plots of (left) total aligned angular momentum I_x and (right) $J^{(1)}$ moment of inertia for the $\nu h_{11/2}$ bands and the yrast structures in odd-N and even-N Mo-isotopes, respectively.

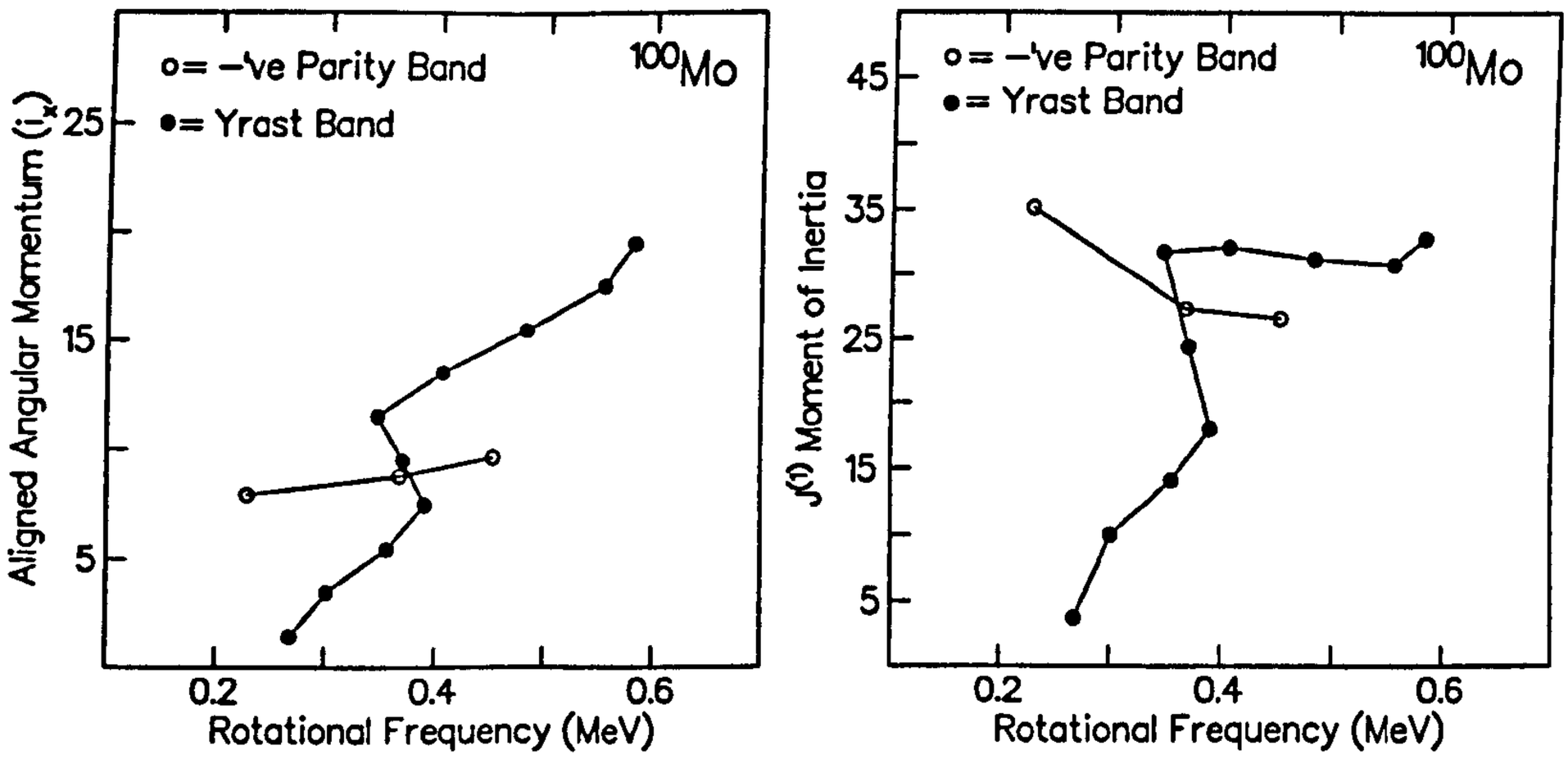

Figure 6.7: Comparison of the experimentally deduced aligned angular momentum (i_x) for the yrast band and a negative-parity, $\nu h_{11/2}$ structure in ^{100}Mo.

Theoretical clarification to the blocking argument is also provided by the Routhian diagram of figures 6.3 and 6.4, where the first neutron alignment ('AB') at $\hbar\omega\sim$0.4 MeV is blocked in the odd-N, ^{99}Mo by the odd neutron, so that the first accessible band-crossing is predicted to be either the ('ef') proton or the ('BC') neutron crossing. The new high spin information on the ^{99}Mo $\nu h_{11/2}$-band and ^{100}Mo yrast band structure demonstrate what seems to be a start of a second alignment at $\hbar\omega\sim$0.5 MeV, and predict this to be the alignment of two $g_{9/2}$ protons.

The first alignment observed in the N = 57 (^{99}Mo) intruder band is similar in frequency with the second in the neighbouring N = 58 (^{100}Mo) yrast band. Similarities are also found between the N = 57 and 58, ^{101}Ru−^{102}Ru pair. The alignment plot of the ^{102}Ru yrast band together with the bands

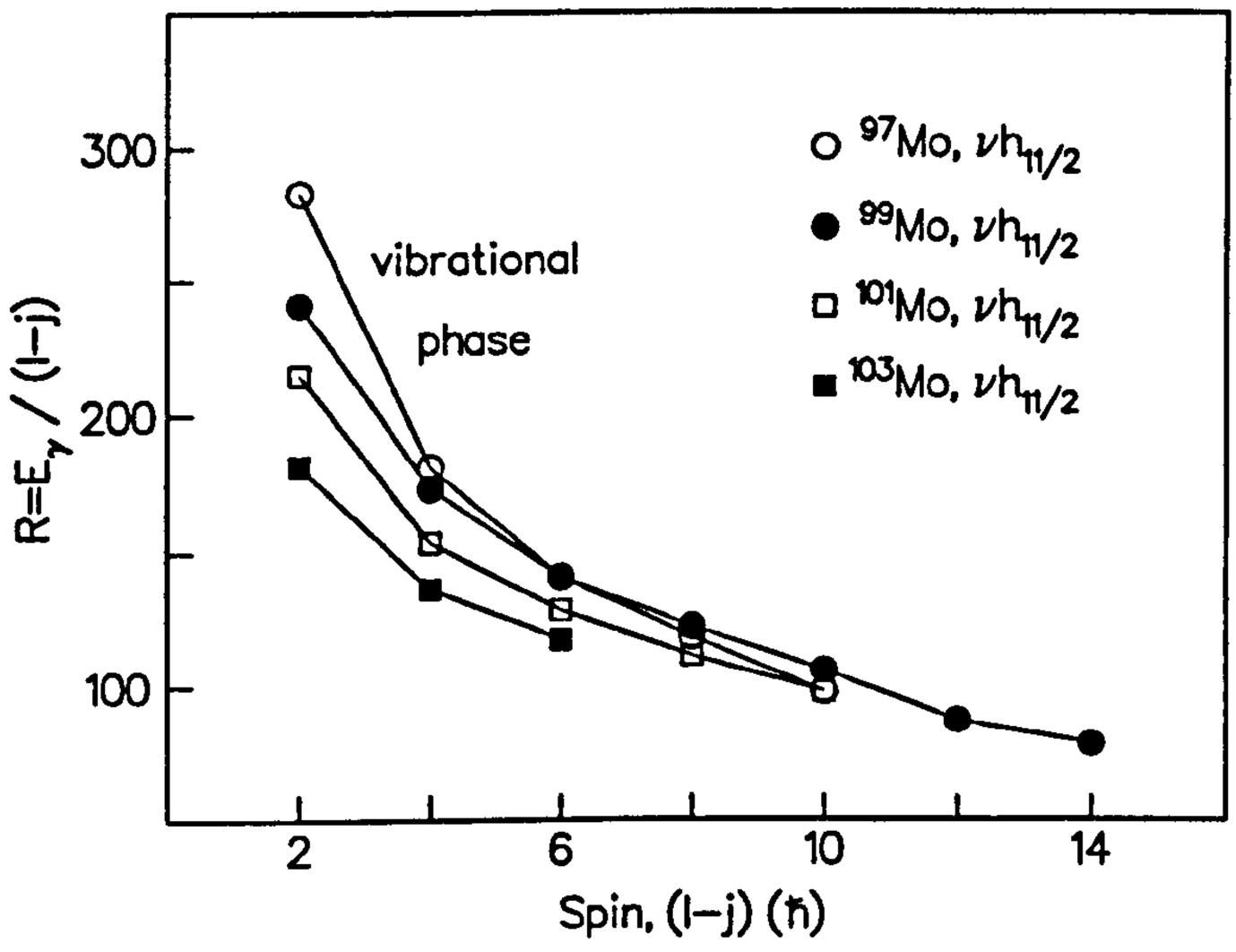

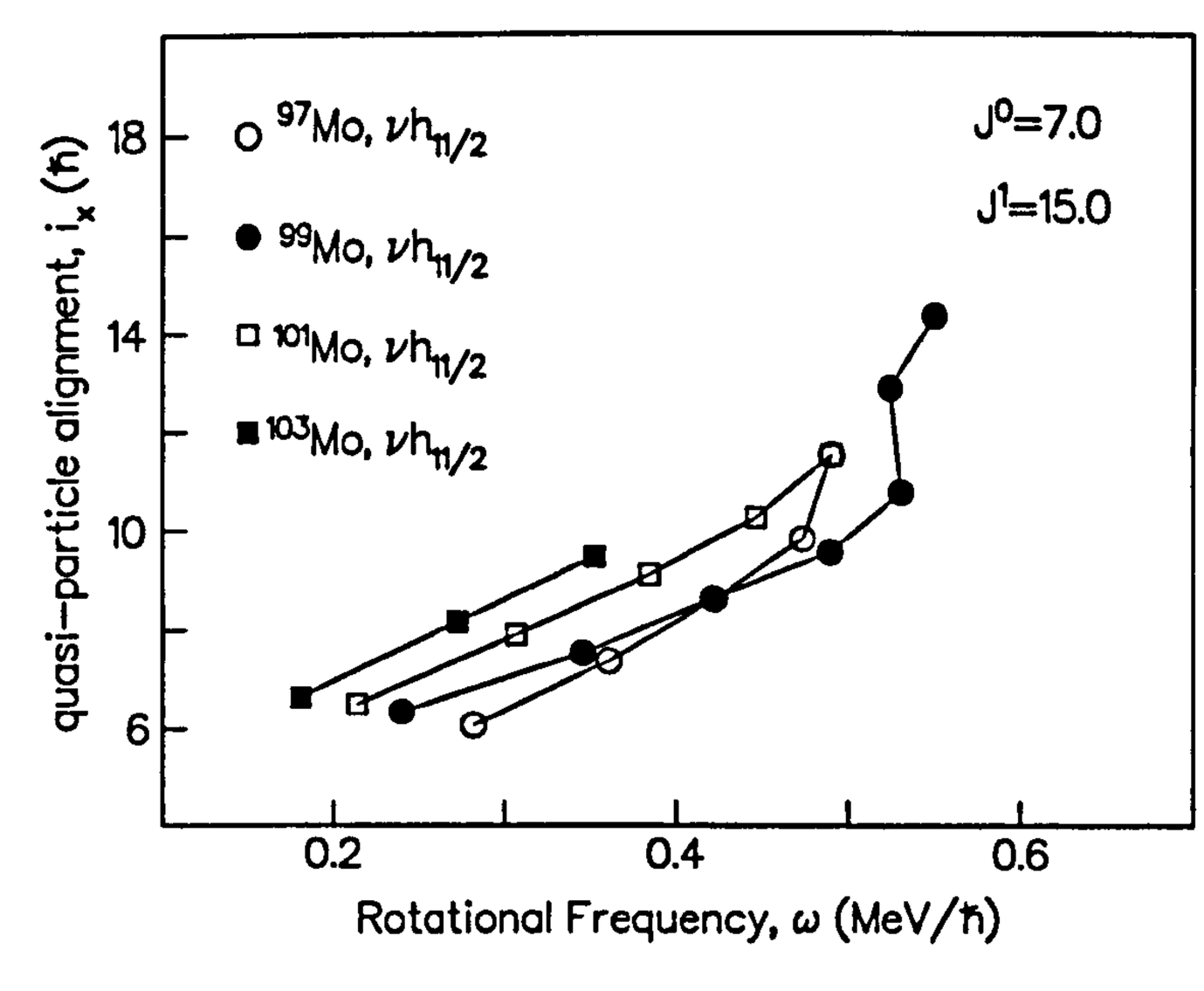

Figure 6.8: (top) An EGOS plot for the odd-N members of Mo-isotopes, and j in this figure refers to the single-particle angular momentum of the bandhead; (below) deduced quasi-particle alignments for the odd-N Mo-isotopes, using the Harris parameters of $\Im^0 = 7.0\ \hbar^2/\mathrm{MeV}$ and $\Im^1 = 15.0\ \hbar^4/\mathrm{MeV}^3$

based on the $d_{5/2}$ neutron, $g_{7/2}$ neutron and $h_{11/2}$ neutron orbitals in ^{101}Ru (see also figure 4.7) are shown in figure 6.9. They exhibit crossings at about the same frequency as the ^{102}Ru yrast band, but, as expected, the one-quasi-particle bands based on the $h_{11/2}$ neutron orbital show no obvious indication of the crossing in this alignment plot. It is worth noting however, that the static picture of deformation may not be appropriate for the detailed, quantitative analysis. With this interpretation of the first backbend, a consistent blocking argument supports the $h_{11/2}$ neutron alignment for ^{102}Ru and ^{100}Mo at rotational frequency of $\hbar\omega\sim$0.4 MeV.

The second alignment seems to have quite different properties from the first one, and is likely to be due to the population of the $g_{9/2}$ proton orbital. The study of the exact details of the effects on the $g_{9/2}$ proton contribution on the alignment properties in this mass region is possible through a systematic investigation of decoupled $\nu h_{11/2}$ intruder bands in N = 57 isotones. The overall picture emerges from this study indeed indicates the increasing importance of the $g_{9/2}$ proton orbital to the alignment, as the decreasing proton numbers towards the Z = 40 subshell from the Z = 50 major shell simultaneously lowers the proton Fermi surface in the $g_{9/2}$-shell, leading to increased quadrupole deformation.

6.3 Intruder Alignment Systematics In N=57 Isotones

Rotational bands in the N = 57 isotones between the shell closures at Z = 40 (Zr) and Z = 50 (Sn) present particularly good laboratories to probe Coriolis-driven alignment effects in weakly deformed nuclei [12, 14, 123, 124, 125, 126, 127, 128]. The odd−A N = 57 isotones systematically exhibit weakly

deformed, decoupled bands associated with the population of $[550]\frac{1}{2}^-$ Nilsson orbital, intruding down from the unique-parity $h_{\frac{11}{2}}$ subshell. In the rotational model, the quasi-particle alignment properties in these bands in $^{103}_{46}$Pd and $^{105}_{48}$Cd have been shown to have a strong dependence on the quadrupole deformation [12]. Specifically the observation of neutron alignments associated with a (predominantly) $g_{\frac{7}{2}}$ pair is proposed to explain the first band–crossing in this structure in ^{105}Cd. In contrast a more complicated scenario has been proposed in ^{103}Pd, where the alignment has been attributed to the simultaneous alignment of both $g_{\frac{7}{2}}$ neutrons and $g_{\frac{9}{2}}$ protons [12].

As the number of valence proton holes increases away from the Z = 50 closed shell, the deformation of the $h_{\frac{11}{2}}$ configuration is expected to increase. This is consistent with the observed proton mid-shell minimisation in the excitation energy of the $\frac{11}{2}^-$ state in the N = 57 isotones, $^{105}_{48}$Cd (1163 keV [128]), $^{103}_{46}$Pd (783 keV [127]), $^{101}_{44}$Ru (527 keV [126]) and ^{99}Mo (684 keV [123]); and the minimum value for the energy of the $\frac{15}{2}^- \rightarrow \frac{11}{2}^-$ transition at ^{101}Ru (431 keV compared to 540 keV, 477 keV and 482 keV and for ^{105}Cd, ^{103}Pd and ^{99}Mo respectively). In ruthenium, this increased quadrupole deformation might be expected to combine with the lowering of the proton Fermi surface in the $g_{\frac{9}{2}}$ shell compared to the palladium and cadmium isotones to produce differing alignment properties at high spins. The situation is further complicated by the calculations which suggest that ruthenium nuclei around N = 60 are expected to possess considerable γ-softness [1].

Figure 6.9 compares the experimental quasi-particle alignments and kinematic moments of inertia for the $h_{\frac{11}{2}}$ decoupled bands in the N = 57 isotones, ^{99}Mo [123, 129], ^{103}Pd [12, 14, 125] and ^{105}Cd [12, 130] with that extracted for the analogous structures observed in the current work on ^{101}Ru. In contrast to the Z = 48 case of ^{105}Cd, the new data for ^{101}Ru shows a distinct

up-bend above $\hbar\omega \approx 0.6$ MeV. Although the $h_{\frac{11}{2}}$ band in ^{103}Pd also shows an increase in alignment in this region, the increase is not so smooth, and has been described in terms of a possible dual alignment of both $g_{\frac{7}{2}}$ neutrons and $g_{\frac{9}{2}}$ protons. The lower frequency of the first alignment in the ^{105}Cd case

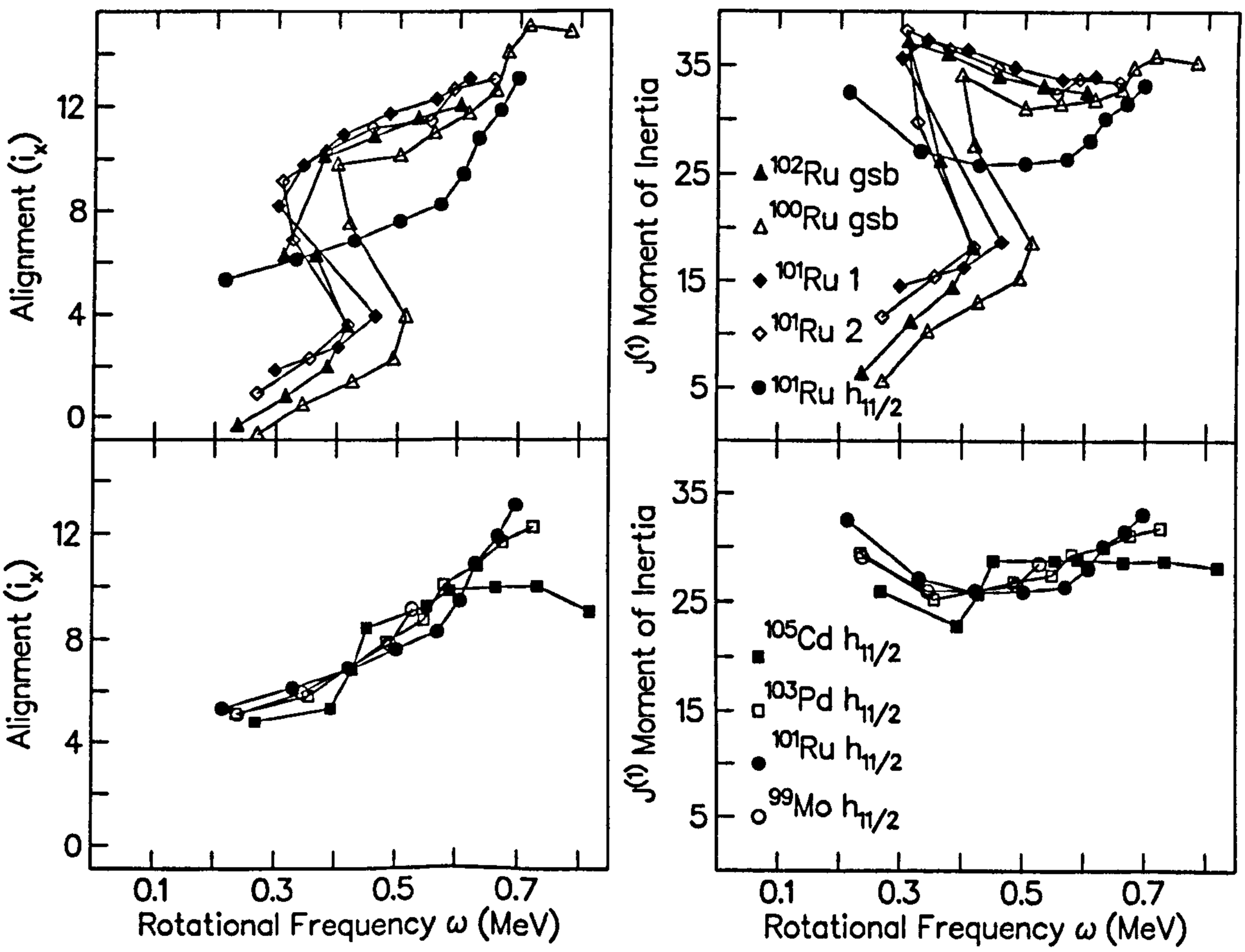

Figure 6.9: Comparison of the experimental (left) quasi-particle alignments and (right) $J^{(1)}$ kinematic moment of inertia for (i) the $h_{11/2}$ structures in he N = 57 isotones (lower figures) and (ii) the yrast bands in ^{100,102}Ru (upper figures).

has been discussed in terms of a $(g_{\frac{7}{2}})^2$ neutron alignment from blocking arguments and by comparison with the yrast structure in ^{106}Cd [131]. However,

as pointed out in reference [12], the theoretically predicted crossing frequencies for these different configurations are highly sensitive to the quadrupole deformation [12].

Figure 6.10 shows the evolution of the excitation energy of the $\frac{11}{2}^-$ yrast bandheads for the N = 57, even-Z isotones from Zr (Z = 40) to Sn (Z = 50). The minimum value for ^{101}Ru is consistent with it having the largest quadrupole deformation at low excitation energy, as is also apparent from the yrast 2^+ energies [132] in the even-even N = 56 and N = 58 isotonic chains. As pointed out in reference [12], for 'axially symmetric' prolate shapes, the CSM predicts the second ('BC') $(h_{\frac{11}{2}})^2$ neutron alignment to become favoured over both the $(g_{\frac{7}{2}})^2$ neutron ('EF') and $(g_{\frac{9}{2}})^2$ ('ab') proton crossings as the core deformation increases. However, the alignment pattern observed for the $h_{\frac{11}{2}}$ band in ^{101}Ru does not show the signature backbending pattern usually associated with the BC alignment in the heavier Cd [133, 134] and Pd [135, 136, 137] nuclei at $\hbar\omega \sim 0.5 \rightarrow 0.6$ MeV. The theoretical quasi−particle routhians for ^{101}Ru shown in figure 6.11 highlight the effect of a substantial positive γ deformation on the rotation frequency of the proton and neutron crossing. These calculations predict an alignment associated with $(g_{\frac{9}{2}})^2$ protons at a frequency of $\hbar\omega \approx 0.6$ MeV for $\gamma = +20°$. This is consistent with the TRS calculations for the lowest negative parity configuration in ^{101}Ru (see figures 6.12 and 6.13), which predict a sudden increase in aligned angular momentum due to a proton crossing in the vicinity of $\hbar\omega = 0.55 \rightarrow 0.6$ MeV. However, quantitative comparison assuming static deformation may not be too accurate for the analysis of different structures, because the differences in alignment frequencies in this figure may result from the use of the same Harris parameters for the moments of inertia ($\Im^0 = 7.0\ \hbar^2/\text{MeV}$ and $\Im^1 = 15.0\ \hbar^4/\text{MeV}^3$). The TRS calculations predict that the $h_{\frac{11}{2}}$, $\beta_2 \approx 0.2$ collective

miminum terminates at $\hbar\omega \approx 0.6$ MeV (see figure 6.12). The TRS calculations also predict a sudden reduction in quadrupole deformation from $\beta_2 \approx 0.2$ to $\beta_2 \approx 0.15$ and thus the sharp increase in the predicted proton total aligned angular momentum, I_x should include both the proton $(g_{\frac{9}{2}})^2$ alignment *and* shape effect. From the quasi-particle Routhians (see figure 6.11), the $(g_{\frac{9}{2}})^2$ proton alignment is predicted to occur around $\hbar\omega = 0.6$ MeV.

The new data on ^{99}Mo show an even more dramatic increase in alignment than that observed for ^{101}Ru, with a backbend observed (rather than an upbend as seen in the heavier isotones). This is consistent with the weaker interaction expected for the $(\pi g_{9/2})^2$ crossing associated with the lower-Ω orbitals, which reside closer to the Fermi surface for ^{99}Mo. As with the $\nu h_{11/2}$ structure in ^{101}Ru, the increased core deformation with respect to ^{105}Cd and ^{103}Pd is responsible for pushing the predicted $(\nu g_{7/2})^2$ crossing up to higher frequencies, which may explain why they are not observed in the current work. It is also of some interest to note that the highest spin transition tenatively deduced for the yrast structure of ^{100}Mo suggests the beginnings of an alignment at a similar frequency to that observed in the $\nu h_{11/2}$ intruder band in neighbouring ^{99}Mo. The Total Routhian Surface calculations for the lowest-lying negative parity sequence in ^{99}Mo are shown in figure 6.14. The predicted quadrupole deformation for this minimum has $\beta \sim 0.2$, but the minimum is soft with respect to both quadrupole and triaxial degrees of freedom. The predicted effect of the $(\pi g_{9/2})^2$ proton alignment is to make this minimum even more $\gamma-$ and $\beta-$soft, resulting in a rather astable, low-deformation configuration. It is perhaps pleasantly surprising then that the rotationally-based CSM calculations reproduced so well the experimental data of many A $\simeq$ 100 nuclei which often appear to show quasi-vibrational structure, however.

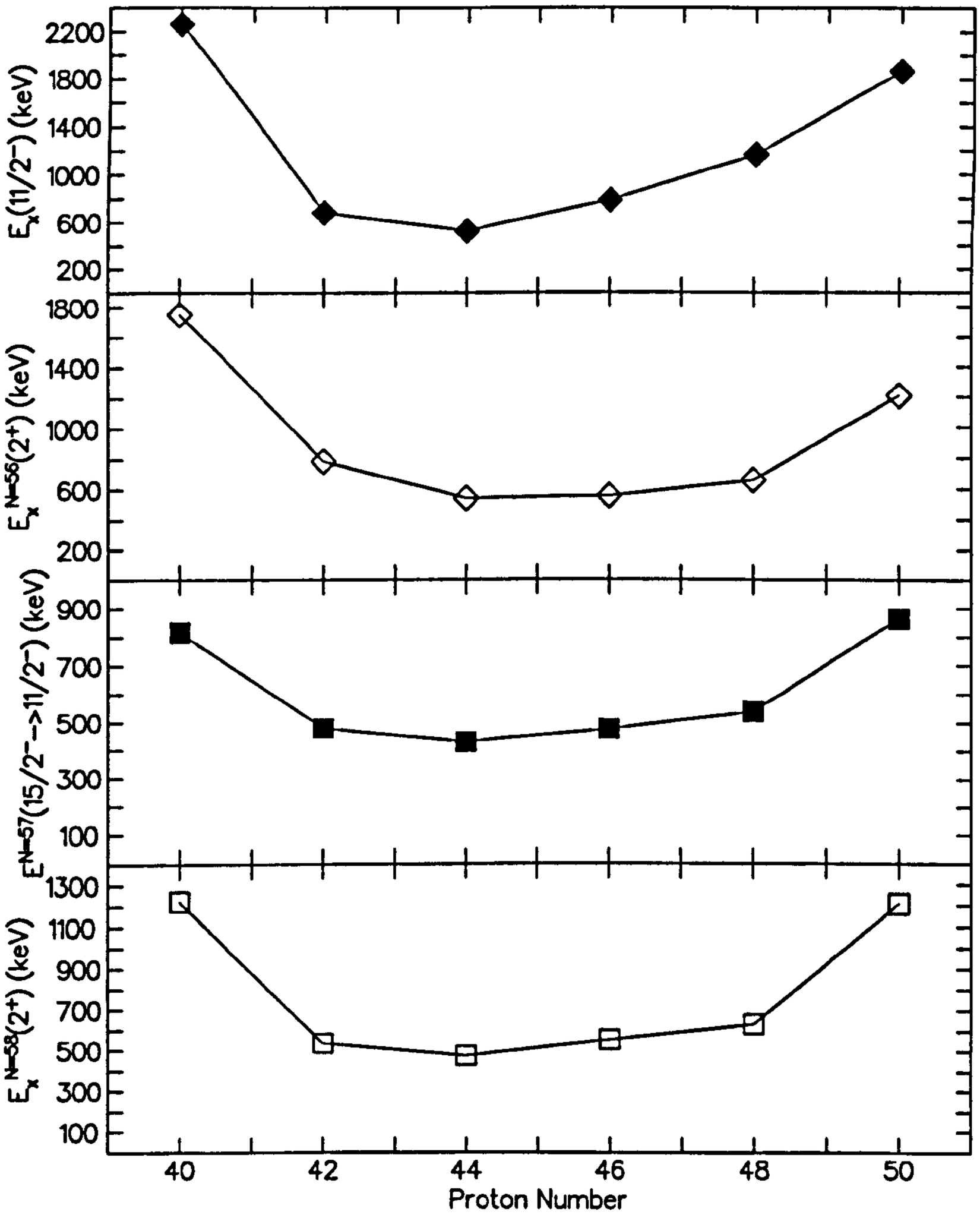

Figure 6.10: Comparison of the excitation energies of the $\frac{11}{2}^-$ bandhead in the even-Z N = 57 isotones and the excitation energies of the lowest 2^+ states in the neighboring even-even N = 56 and N = 58 nuclei. The $\frac{15}{2}^- \rightarrow \frac{11}{2}^-$ transition energy in the decoupled $h_{\frac{11}{2}}$ bands for the N = 57 isotones are also shown. The date for this figure was taken from references [124, 130, 131, 136, 138, 139, 140, 141, 142] respectively.

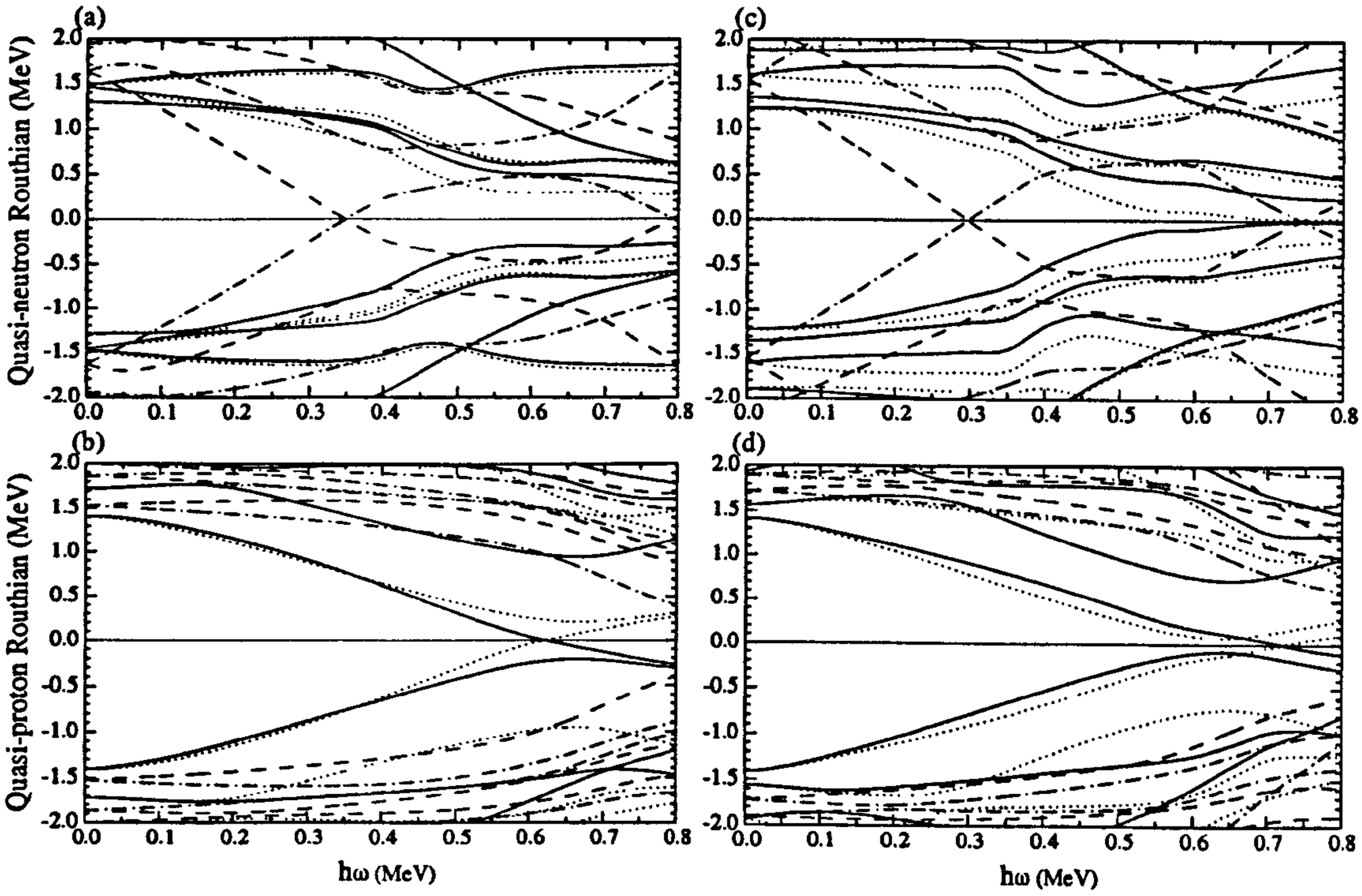

Figure 6.11: Cranked shell model quasi-particle routhians for (a) neutrons and (b) protons in ^{101}Ru with static deformation parameters of $\beta_2 = 0.21$, $\beta_4 = 0.01$ and $\gamma = 0°$. For (c) and (d), the deformation paramenters are the same as for (a) and (b), but with $\gamma = +20°$.

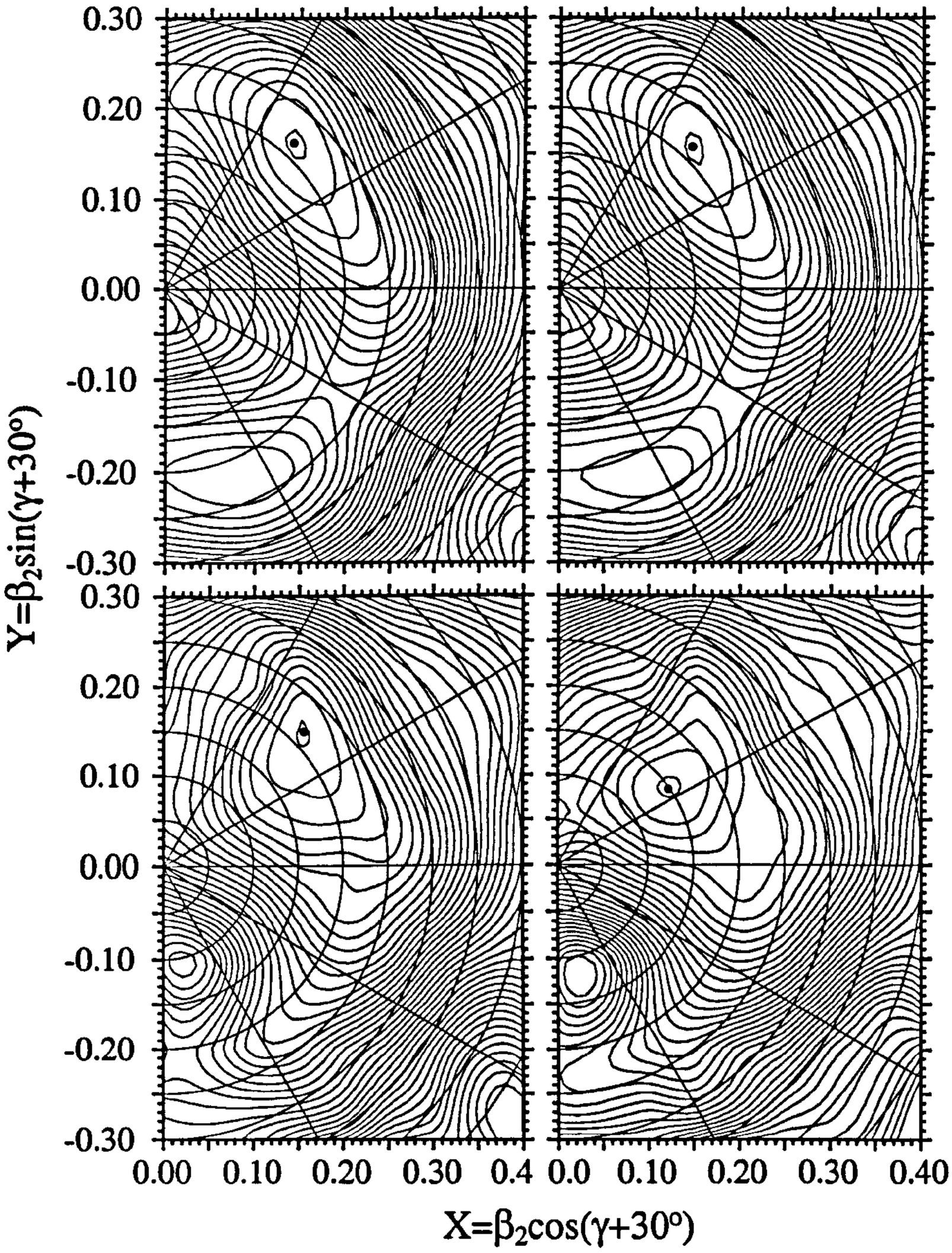

Figure 6.12: TRS calculations for the lowest energy, negative parity, negative signature ($\nu h_{\frac{11}{2}}$) structure in ^{101}Ru. The energy contours are at 200 keV intervals. The deformation parameters for the individual minima are, *upper left*: $\hbar\omega = 0.2$ MeV, $\beta_2 = 0.22$, $\beta_4 = 0.02$, $\gamma = +19°$; *upper right*: $\hbar\omega = 0.3$ MeV, $\beta_2 = 0.22$, $\beta_4 = 0.02$, $\gamma = +17°$; *lower left*: $\hbar\omega = 0.5$ MeV, $\beta_2 = 0.22$, $\beta_4 = 0.02$, $\gamma = +14°$; *lower right*: $\hbar\omega = 0.6$ MeV, $\beta_2 = 0.15$, $\beta_4 = 0.01$, $\gamma = +5°$.

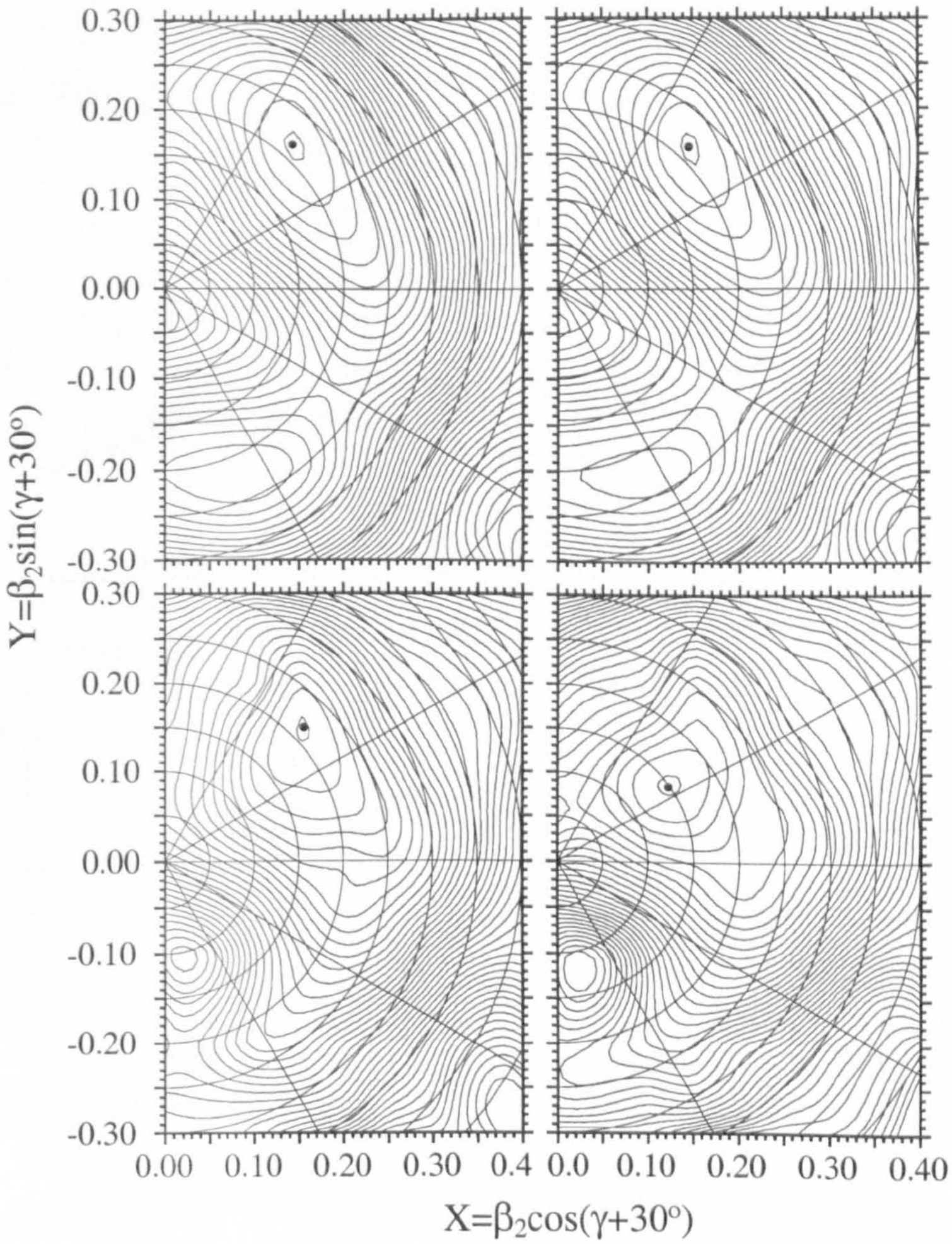

Figure 6.12: TRS calculations for the lowest energy, negative parity, negative signature ($\nu h_{\frac{11}{2}}$) structure in ^{101}Ru. The energy contours are at 200 keV intervals. The deformation parameters for the individual minima are, *upper left*: $\hbar\omega = 0.2$ MeV, $\beta_2 = 0.22$, $\beta_4 = 0.02$, $\gamma = +19°$; *upper right*: $\hbar\omega = 0.3$ MeV, $\beta_2 = 0.22$, $\beta_4 = 0.02$, $\gamma = +17°$; *lower left*: $\hbar\omega = 0.5$ MeV, $\beta_2 = 0.22$, $\beta_4 = 0.02$, $\gamma = +14°$; *lower right*: $\hbar\omega = 0.6$ MeV, $\beta_2 = 0.15$, $\beta_4 = 0.01$, $\gamma = +5°$.

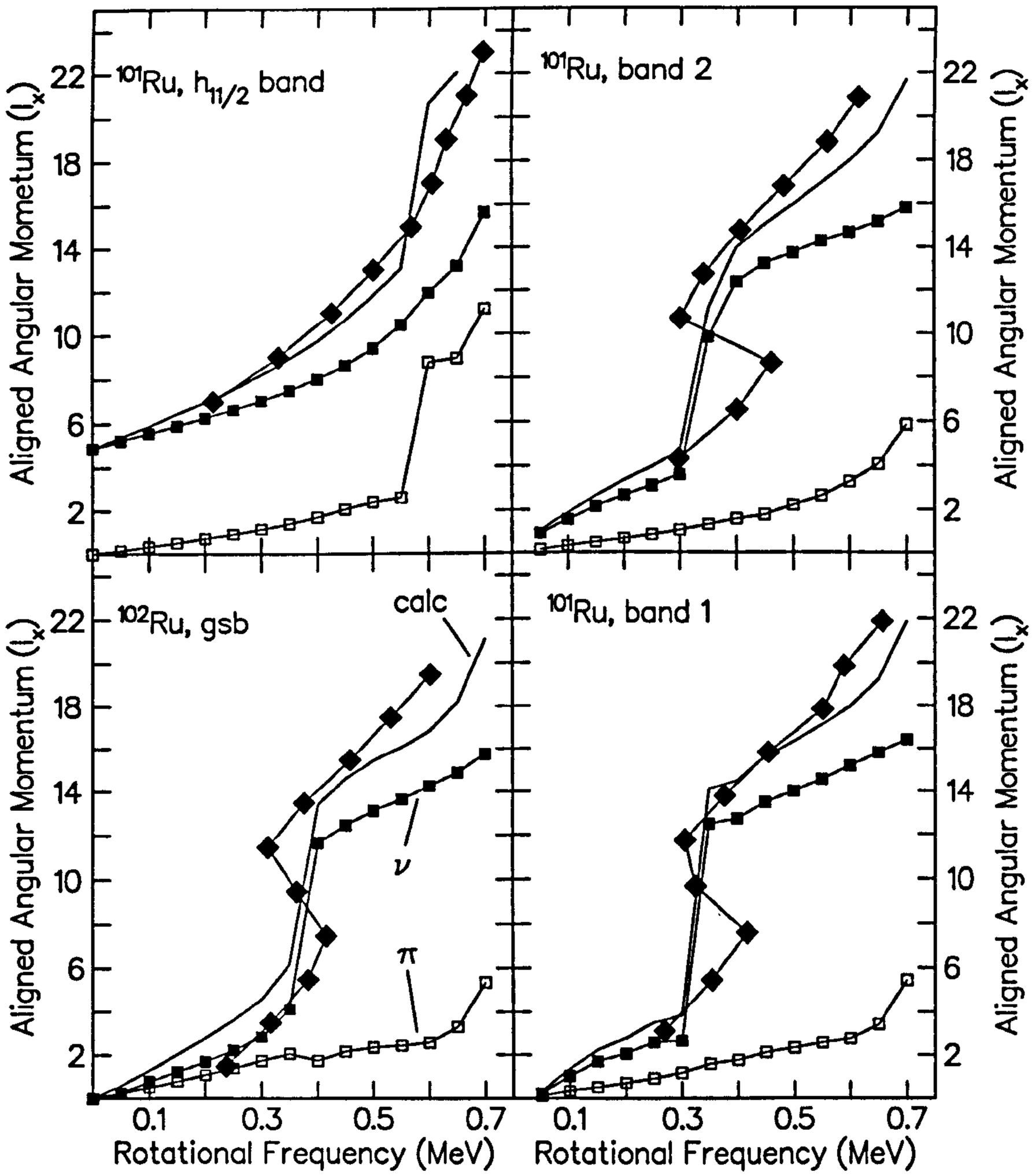

Figure 6.13: Comparison of the experimentally extracted total aligned angular momentum (I_x) for the bands in ^{101}Ru and the ground state band in ^{102}Ru with the results of the TRS calculations. The open squares correspond to proton contributions, with the smaller closed squares representing the predicted neutron contribution. The line is the total I_x value predicted by the TRS calculations and the large black triangles are the values extracted from the experimental data.

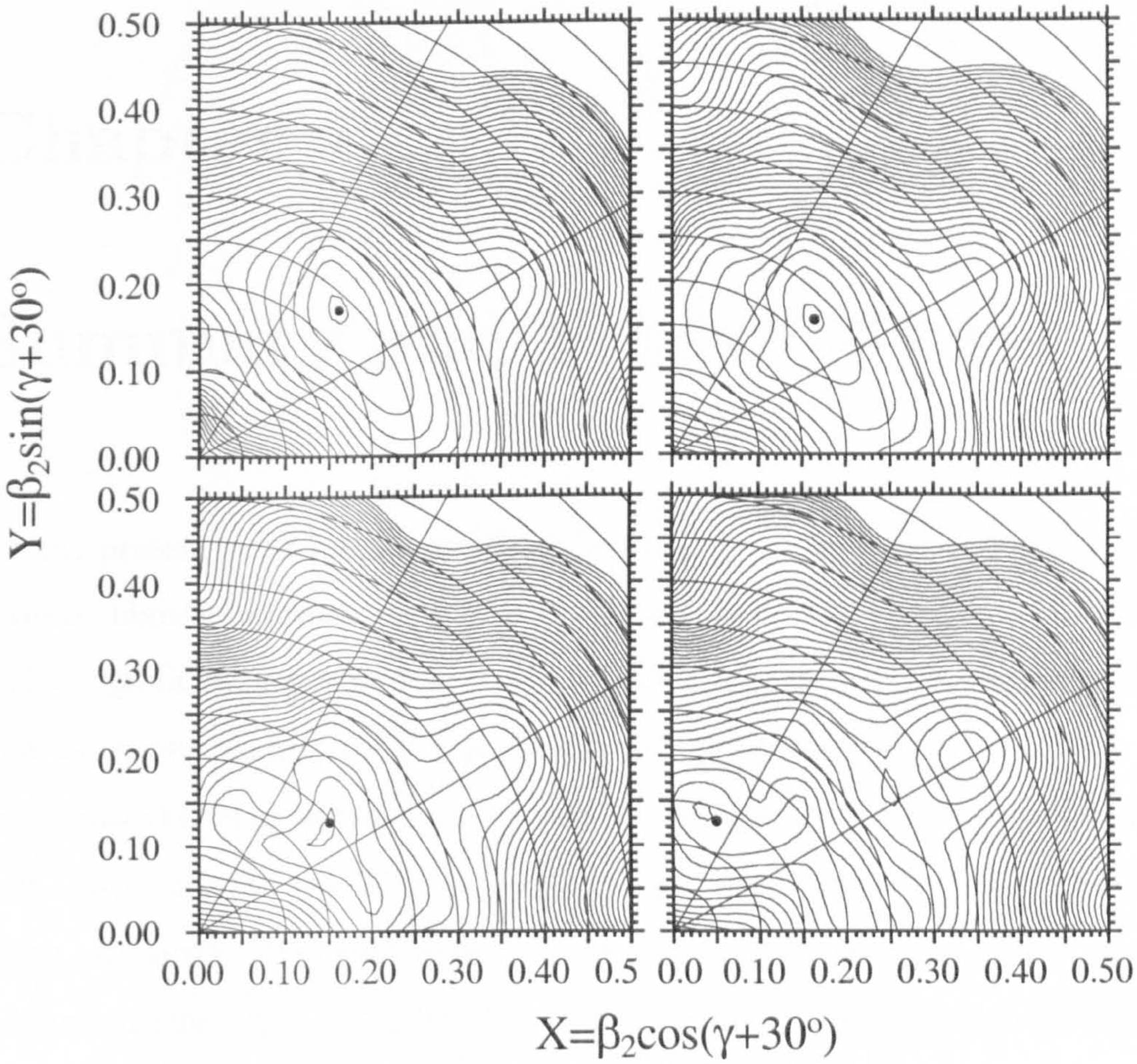

Figure 6.14: Total Routhian Surface calculations for the lowest lying negative parity sequence in ^{99}Mo. (a) $\omega = 0.401$ MeV/$\hbar$, ($\beta_2 = 0.234$, $\beta_4 = 0.019$, $\gamma = +16.3°$); (b) $\omega = 0.502$ MeV/$\hbar$, ($\beta_2 = 0.226$, $\beta_4 = 0.019$, $\gamma = +13.5°$); (c) $\omega = 0.602$ MeV/$\hbar$, ($\beta_2 = 0.197$, $\beta_4 = 0.016$, $\gamma = +10.0°$); (d) $\omega = 0.702$ MeV/$\hbar$, ($\beta_2 = 0.137$, $\beta_4 =$ -0.006, $\gamma = +38.0°$). The energy contour on these calculations is 200 keV.

Chapter 7

Summary and Future Work

For the present experiments involving both fusion-evaporation and binary reactions, high-spin states in slightly neutron-rich nuclei have been populated with a significant cross-section, and a number of previously unreported states have been established. In particular for the binary reaction, both yrast *and* near-yrast states in the reaction fragments were established though the selection of appropriate reaction mechanisms in a large energy-momentum phase space. However, the exact details of the relation between kinematic energy loss and intrinsic spin generated for a given fragment could not be established, due in part to the inability to qualitatively verify the observed Q-value loss to the measured fold distribution for a given exit channel. It is hoped that with better theoretical understanding of the nature of the dissipative process in a binary reaction, together with the improved selectivity in choosing a given exit channel in a large phase space, higher spin and near-yrast states populated in smaller cross-sections can be observed and studied. Nevertheless, the first band-crossing in ^{101,102}Ru and ^{100}Mo have been observed, and has been given a microscopic description using the CSM calculations. Furthermore, the isomer tagging technique allowed to observe the high-spin transitions in

^{99,101}Mo nuclei, and the delayed crossing frequency observed in their $\nu h_{11/2}$ bands with respect to their even-N neighbour, ^{100}Mo, confirmed the $(\nu h_{11/2})^2$ assignment for the first alignment in ^{100}Mo. The above-isomer transitions in ^{101}Mo were observed and the lifetime of its $\nu h_{11/2}$ isomer was established for the first time. The nature of the second alignment in ^{99}Mo has also been discussed, and is thought to be due to $(\pi g_{9/2})^2$ proton alignment. Many new low- to medium-spin states in A $\simeq$ 100 region have been explained by the coupling of valance $g_{9/2}$ protons and $d_{5/2}$, $g_{7/2}$, and $h_{11/2}$ neutrons. In future, a binary reaction using a heavier Pb beam and a ^{100}Mo target should allow the observation of high spin states past the second alignment, and the predicted superdeformed minima in ^{99,100}Mo at $\sim$22 $\hbar$.

Bibliography

[1] J. Skalski, S. Mizutori and W. Nazarewicz, *Nucl. Phys.* **A617** (1997) 282

[2] Richard F. Casten, *Nuclear Structure from a Simple Perspective*, Oxford University Press, Oxford, 1990.

[3] H. Takai *et. al.*, *Phys. Rev.* **C38** (1988) 1247

[4] P. Federman, and S. Pittel, *Phys. Lett.* **77B** (1978) 29

[5] P. Federman, S. Pittel and R. Campos *Phys. Lett.* **82B** (1979) 9

[6] P. Federman, and S. Pittel, *Phys. Rev.* **C20** (1979) 820

[7] E. Kirchuk, P. Federman, and S. Pittel, *Phys. Rev.* **C47** (1993) 567

[8] A. Faessler, J.E. Galonska, U. Gotz and S. Pittel, *Nucl. Phys.* **A326** (1979) 129

[9] P. Bouche, H. Flocard, P.H. Heensen, S.J. Krieger, and W.S. Weiss, *Nucl. Phys.* **A443** (1985) 39

[10] D. Galeriu, D. Bucurescu, and M. Ivacscu, *J. Phys.* **G12** (1986) 329

[11] A. Kumar and M.R. Gunye, *Phys. Rev.* **C32** (1985) 2116

[12] P.H. Regan *et. al.*, *J. Phys.* **G19** (1993) L157

[13] B.M. Nyakó *et. al. Phys. Rev.* **C60** (1999) 024307

[14] D. Jerrestam, *et. al.*, *Nucl. Phys.* **A557** (1993) 411c

[15] L. Genilloud *et. al.*, *Nucl. Phys.* **A662** (2000) 3; erratum, **A669** (2000) 407

[16] N.V. Zamfir and R.F. Casten, *Phys. Lett.* **B260** (1991) 265; L. Wilets and M. Jean, *Phys. Rev.* **102** (1958) 788

[17] K.S. Krane, *Introductory Nuclear Physics*, John Wiley and Sons (1988)

[18] W. Greiner and J.A. Maruhn, *Nuclear Models*, Springer-Verlag (1996)

[19] P.M. Endt, *Atom. Nucl. Data Tables* **23** (1979) 547

[20] P. Ring and P. Schuck, *The Nuclear Many – Body Problem*, ed. W. Beiglböck, Spring-Verlang, New York (1980)

[21] M.G. Mayer, *Phys. Rev.* **78** (1950) 16

[22] I. Talmi, *Rev. Mod. Phys.* **34**, (1962) 704

[23] C.D. O'Leary, *PhD Thesis*, University of Staffordshire (1998)

[24] J.M. Eisenberg and W. Greiner, *Microscopic Theory of Nucleus*, North-Holland Publishing, Amsterdam (1972)

[25] D.L. Hill and J.A. Wheeler, *Phys. Rev.* **89**, (1953) 1102

[26] S.G. Nilsson, *Dan. Mat. Fys. Medd.* **29** (1955) 3

[27] A. deShalit and H. Freshbach, *Theoretical Nuclear Physics*, Vol I, John Wiley and Sons (1974)

[28] E.S. Paul, *Liverpool NSG Postgraduate Lecture Notes*, University of Liverpool (2000)

[29] J. Bardeen, L.N. Cooper and J.R. Schrieffer, *Phys. Rev.* **108** (1957) 1175

[30] A. Bohr, B. R. Mottelson and D. Pines, *Phys. Rev.* **110** (1958) 936

[31] D.R. Inglis, *Phys. Rev.* **96** (1954) 1059

[32] R. Bengtsson and S. Frauendorf, *Nucl. Phys.* **A327** (1979) 139

[33] G.I. Harris *et. al.*, *Phys. Rev.* **139** (1965) 1113

[34] K. Siwek-Wilczyńska and J. Wilczyński, *Nucl. Phys.* **A264** (1976) 115

[35] P. Fröbrich and R. Lipperheide, *Theory of Nuclear Reactions*, Oxford Science Publications, New York (1996)

[36] J. M. Blatt and V. F. Weisskopf, *Theoretical Nuclear Physics* 7th Edition, Wiley (1963)

[37] R. Broda *et. al.*, *Heavy Ion Physics* **7** (1998) 83

[38] W. Krolas *et. al.*, *Acta Polonica* **B25** (1994) 687

[39] R. Broda *et. al.*, *Nucl. Phys.* **A338** (1982) 334

[40] H. Sann *et. al.*, *Phys. Rev. Lett.* **47** (1981) 1248

[41] C.F. Tang, *Physica Scripta* **10** (1974) 90

[42] J. Wilczyński, *Phys. Lett.* **B47** (1973) 484

[43] D.A. Bromley (Ed.), *Treatise on Heavy – Ion Science*, Vol. II, Plenum Press (1984)

[44] J. Wilczyński and K. Siwek-Wilczyńska, *Nukleonika* **21** (1976) 517

[45] D. Bangert and H. Freiesleben, *Nucl. Phys.* **A340** (1980) 205

[46] O. Madelung, *Data in science and technology : semiconductors group V elements and III – V compounds*, Spring-Verlag, New York (1991) extracts from the Landolt-Börnstein New Series

[47] G.F. Knoll, *Radiation Detection and Measurement*, John Wiley and Sons (1989)

[48] I.M. Hibbert, *PhD Thesis*, University of Manchester (1993)

[49] G. Duchene, *Nucl. Instr. Meth. A* **432** (1999) 90

[50] S.L. Shepherd *et. al.*, *Nucl. Instr. Meth. A* **434** (1999) 373

[51] F.A. Beck *et. al.*, *Proceedings of the Int. Conf. on Nucl. Struct. at High Ang. Momentum,* Ottawa (Canada), 1992, p362

[52] C.W. Beausang *et. al.*, *Nucl. Instr. Meth. A* **452** (2000) 431

[53] I.Y. Lee, *Nucl. Phys.* **A520** (1990) p641c

[54] J. Simpson, *Nucl. Phys.* **A654** (1999) p178c

[55] Online website at 'GAMMASPHERE Online Booklet Homepage'; http://nucalf.physics.fsu.edu/ riley/gamma

[56] C.W. Beausang and J. Simpson, *J. Phys.* **G22** (1996) 527

[57] P.J. Nolan, F.A. Beck, and D.B. Fossan, *et. al.*, *Ann. Rev. Nucl. Part. Sci.* **45** (1994) 561

[58] M.W. Simon, *Nucl. Inst. Meth.* **A452** (2000) 205

[59] F. Puhlhofer,*Nucl. Phys.* **A280** (1977) 267

[60] K.S. Krane, R.M. Steffen and R.M. Wheeler, *Nuclear Data Tables* **11** (1973) 351

[61] A. Krämer-Flecken, T. Morek, R.M. Lieder, W. Gast, G. Hebbinghaus, H.M. Jäger and W. Urban, *Nucl. Instr. Meth. Phys. Res.* **A275** (1989) 333

[62] C. Bargholtz and P.E. Tegnér, *Nucl. Instr. Meth. Phys. Res.* **A256** (1987) 513

[63] G. Kajrys, R. Lecomte, S. Landsberger and S. Monaro, *Phys. Rev.* **C28** (1983) 1504

[64] W. Klamra, K. Fransson, B. Sundström, M. Brenner, S. Engman and R. Kvarnström, *Nucl. Phys.* **A376** (1982) 463

[65] W. Nazarewicz, J. Dudek, R. Bengtsson, T. Bengtsson and I. Ragnarsson, *Nucl. Phys.* **A435** (1985) 397

[66] W. Nazarewicz, R. Wyss and A. Johnson, *Phys. Lett.* **225B** (1989) 208

[67] W. Nazarewicz, M.A. Riley and J.D. Garrett, *Nucl. Phys.* **A512** (1990) 61

[68] F.S. Stephens, R.M. Diamond, J.R. Leigh, T. Kammuri and K. Nakai, *Phys. Rev. Lett.* **29** (1972) 438

[69] H. Dejbakhsh and S. Bouttchenko, *Phys. Rev.* **C52** (1995) 1810

[70] C.M. Lederer, J.M. Jaklevic, and J.M. Hollander, *Nucl. Phys.* **A185** (1971) 449

[71] P.K. Bindal, D.H. Youngblood, R.L. Kozub, and P.H. Hoffmann-Pinther, *Phys. Rev.* **C12** (1975) 390

[72] T. Ishimatsu *et. al.*, *Nucl. Phys.* **A185** (1972) 273

[73] D.C. Radford, *Nucl. Inst. Meth. Phys. Res.* **A361** (1995) 297

[74] W. Urban, *ANA software*, private communication, University of Manchester.

[75] N. Fotiades *et. al.*, *Phys. Rev.* **C65** (2002) 044303

[76] J.H. Hamilton, *Int. Conf. on Exotic Nuclei and Atomic Masses*, Arles (France), 1995, eds. M. de Saint Simon and O. Sorlin, p487

[77] J.M. Chatterjee, M. Saha-Sarkar, S. Bhattacharya, P. Banerjee, S. Sarkar, R.P. Singh, and S. Murulithar, *Nucl. Phys.* **A678** (2000) 367

[78] J. Barrette, M. Barrette, A. Boutard, R. Haroutuian, G. Lamoureux and S. Monaro, *Phys. Rev.* **C6** (1972) 1339

[79] P.H. Regan *et. al.*, *Phys. Rev.* **C55** (1997) 2305

[80] J.J. Valiente-Dobón, *Phys. Rev.* **C**, submitted.

[81] A.G. Smith *et. al.*, *Phys. Rev. Lett.* **77** (1996) 1711

[82] L.K. Peker, *Nucl. Data Sheets* **73** (1994) 1

[83] I. Deloncle *et. al.*, *Eur. Phys. J.* **A8** (2000) 177

[84] A.A. Sonzogni, *Nucl. Data Sheets* **98** (2003) 515

[85] W.P. Jones, *Phys. Rev.* **C4** (1971) 580

[86] J.K. Tuli, *Nucl. Data Sheets* **71** (1994) 71

[87] R.C. Deihl, *Phys. Rev.* **C1**, (1970) 2132

[88] G. Lhersonneau, *Phys. Rev.* **C54**, (1996) 1117

[89] J. Wilczyński, K. Siwek-Wilczyńska, J.S. Larsen, J.C. Acquadro, and P.R. Christensen, *Nucl. Phys.* **A244** (1975) 147

[90] W. von Oertzen, In *Nuclear Spectroscopy* (J. Cerny, Ed.), Academic Press, New York (1975)

[91] S.E. Vigdor, *Proc. Symposium Macroscopic Features of Heavy – Ion Collisions* Argonne, 1976, Report ANL/PHY-76-2, Vol.1, p.95.

[92] L.B.J. Goldfarb, and W. von Oertzen, *Heavy Ion Collisions* (R. Bock, Ed.), North-Holland, Amsterdam (1979) Vol. I, p. 215.

[93] M. Zielińska *et. al.*, *Nucl. Phys.* **A712** (2002) 3

[94] Y.S. Kim and B.L. Cohen, *Phys. Rev.* **142** (1966) 788

[95] J. Eichler, *Z. Phys.* **219** (1969) 114

[96] E.R. Flynn, F. Ajzenberg-Selove, R.E. Brown, J.A. Cizewski and J.W. Sunier, *Phys. Rev.* **C24** (1981) 2475

[97] K.R. Pohl *et. al.*, *Phys. Rev.* **C53** (1996) 2682

[98] J. Suhonen and G. Lhersonneau, *Phys. Rev.* **C64**, (2001) 014315

[99] M.A. Choudhury, W. Booth and R.N. Glover, *Nuovo Cimento* **A99** (1988) 701

[100] S.J. Mundy, W. Gelletly, J. Lukasiak, W.R. Philips and B.J. Varley, *Nucl. Phys.* A441 (1985) 534

[101] D. Hook, J.L. Durell, W. Gelletly, J. Lukasiak and W.R. Philips, *J. Phys. G: Nucl. Phys.* **12** (1986) 1277

[102] J.L. Durrel, in *Proc. Int. Conf. on Spectroscopy of Heavy Nuclei,* Crete, 1989, eds. J.F. Sharpey-Schafer and L.D. Sypuras, IoP Conf. Pro. No. 105 (Institute of Physics), London, 1990, p307

[103] H. Ahrens, N. Kaffrel, N. Trautmann and G. Herrmann, *Phys. Rev.* **C14** (1976) 211

[104] R.F. Casten, E.R. Flynn, O. Hansen and T.J. Mulligan, *Nucl. Phys.* **A184** (1972) 357

[105] E.R. Flynn, R.E. Brown, J.A. Cizewski, J.W. Sunier, W.P. Alford, E. Sugarbaker and D. Ardouin, *Phys. Rev.* **C22** (1980) 43

[106] R. Estep, R.K. Sheline, D.J. Decman, E.A. Henry, L.G. Mann, R.A. Mayer, W. Stoeff, L.E. Ussery and J. Kentele, *Phys. Rev.* **C39** (1989) 76

[107] J. Koenig, H. Bohn, T. Faestermann, P.Kienle, H.J. Körner, W.A. Mayer, D. Piereira, K.E. Rehm and H.J. Scheerer, *Phys. Rev.* **C24** (1981) 2076

[108] S. Ohya, M. Kanazawa, N. Mutsuro, T. Tamura and Z. Matumoto, *J. Phys. Soc. Jpn.* 50 (1981) 1057

[109] G. Battistuzzi, K. Kawade, H. Lawin, K. Shizuma and K. Sistemich, *Z. Phys. A.* **306** (1982) 113

[110] G. Lhersonneau *et. al.*, *Z. Phys. A.* **358** (1997) 317

[111] S.A. Hjorth and B.L. Cohen, *Phys. Rev.* **B135** (1964) 920

[112] R.C. Diehl, B.L. Cohen, R.A. Moyer and L.H. Goldman, *Phys. Rev.* **C1** (1970) 2132

[113] J. Dubuc, G. Kairys, P. Lariviére, S. Pilotte, W. Del Bianco and S. Monaro, *Phys. Rev.* **C37** (1988) 954

[114] H. Weigmann, S. Raman, J.A. Harvey, R.L. Macklin and G.G. Slaughter, *Phys. Rev.* **C20** (1979) 115

[115] H. Seyfarth *et. al.*, *Z. Phys. A.* **339** (1991) 269

[116] W.L. Sievers, D.A. Close, C.J. Umbarger, R.C. Bearse and F.W. Prosser, Jr., *Phys. Rev.* **C6** (1972) 1001

[117] W. Booth, S.M. Dalgliesh, K.C. McLean, R.N. Glover and F.R. Hudson, *Phys. Lett.* **30B** (1969) 335

[118] P. Regan *et. al.*, *Phys. Rev. Lett* **90** (2003) 152502

[119] H. Dejbakhsh, D. Latypov, G. Ajupova, and S. Sholmo, *Phys. Rev.* **C46** (1992) 2326

[120] M. Sambataro and G. Molnár, *Nucl. Phys.* **A376** (1982) 201

[121] T. Mathur and S. Mukherjee, *Phys. Rev.* **C44** (1991) 909

[122] D. Bucurescu, Ghe. Cata-Danil, I Cata-Danil, M Ivascu, N Marginean, and C.A. Ur, *Phys. Rev.* **C63** (2000) 014306

[123] P.H. Regan, T.M. Menezes, C.J. Pearson, W. Gelletly, C.S. Purry, P.M. Walker, S. Juutinen, R. Julin, P.A. Butler, G. Jones and P. Greenlees, *Phys. Rev.* **C55** (1997) 2305

[124] D.R. Haenni, H. Dejbakhsh, R.P. Schmitt and G. Mouchaty, *Phys. Rev.* **C33** (1986) 1543(R)

[125] B.M. Nyakó *et. al.*, *Phys. Rev.* **C60** (1999) 024307

[126] Jean Blachot, *Nucl. Data Sheets* **83** (1998) 1; **62** (1991) 305

[127] D. de Frenne and E. Jacobs, *Nucl. Data Sheets* **93** (2001) 447

[128] D. de Frenne and E. Jacobs, *Nucl. Data Sheets* **68** (1993) 935

[129] G. Lhersonneau *et. al.*, *Z. Phys.* **A358** (1997) 317

[130] D. Jerrestam *et. al. Nucl. Phys.* **A593** (1995) 162

[131] P.H. Regan *et. al.*, *Nucl. Phys.* **586** (1995) 351

[132] L. Grodzins, Phys. Lett. **2**, 88 (1962); L. Goettig and W. Nazarewicz, J. Phys. **G16** (1990) L51

[133] N. Fotiades *et. al.*, *Phys. Rev.* **C61** (2000) 064326

[134] P.H. Regan *et. al.*, *Phys. Rev.* **C49** (1994) 1885

[135] K.R. Pohl, P.H. Regan, J.E. Bush, P.E. Raines, D.P. Balamuth, D. Ward, A. Galindo-Uribarri, V.P. Janzen, S.M. Mullins and S. Pilotte, *Phys. Rev.* **C53** (1996) 2682

[136] A.O. Macchiavelli *et. al.*, *Phys. Rev.* **C38** (1988) 1088

[137] M. Houry *et. al.*, *Eur. Phys. J.* **A6** (1999) 43

[138] D. Jerrestam, W. Klamra, B. Fogelberg, R. Bark, A. Gizon, J. Gizon, E. Ideguchi, S. Mitarai, M. Piiparinen, G. Sletten, *Nucl. Phys.* **A603** (1996) 203

[139] G. Lhersonneau, P. Dendooven, S. Hankonen, A. Honkanen, M. Huhta, R. Julin, S. Juutinen, M. Oinonen, H. Penttila, A. Savelius,

S. Törmänen, J. Aystö, P.A. Butler, J.F.C. Cocks, P.M. Jones, J.F. Smith , *Phys. Rev.* **C54** (1996) 1117

[140] S. Juutinen, E. Makela, R. Julin, M. Piiparinen, S. Törmänen, A. Virtanen, E. Adamides, A. Atac, J. Blomqvist, B. Cederwall, C. Fahlander, E. Ideguchi, A. Johnson, W. Karczmarczyk, J. Kownacki, S. Mitarai, L.-O. Norlin, J. Nyberg, R. Schubart, D. Seweryniak, G. Sletten **Nucl. Phys. A617** (1997) 74

[141] J. Blachot, *Nucl. Data. Sheets.* **89** (2000) 213

[142] D. Cline *Acta Phys. Pol.* **C30** (1999) 1291

Appendix A

List of Publications

1. *Deviations from Axial Symmetry in* ^{181}Os

Zs. Podolyak, S. Al-Garni, R.F. Casten, J.R. Cooper, D.M. Cullen, A. Dewald, R. Krucken, H. Newman, J.N. Orce, C.J. Pearson, C. Ur, R. Venturelli, S. Vincent, C. Wheldon, P.M. Walker, F.R. Xu, **A.D. Yamamoto**, N.V.Zamfir, *Phys. Rev.* **C66** (2002) 011304

2. *High-j Proton and Neutron Alignments in Gamma-Soft* ^{101}Ru

A.D. Yamamoto, P.H. Regan, C.W. Beausang, F.R. Xu, M.A. Caprio, R.F. Casten, G. Gurdal, A.A. Hecht, C. Hutter, R. Krucken, S.D. Langdown, D. Meyer, J.J. Ressler, N.V. Zamfir, *Phys.Rev.* **C66** (2002) 024302

3. *Signature for Vibrational to Rotational Evolution Along the Yrast Line*

P. H. Regan, C. W. Beausang, N. V. Zamfir, R. F. Casten, J.-y. Zhang, **A. D. Yamamoto**, M. A. Caprio, G. Grdal, A. A. Hecht, C.Hutter, R. Krcken, S. D. Langdown, D. A. Meyer, and J. J. Ressler, *Phys. Rev. Lett.* **90** (2003) 152502

4. *In-Beam Thin-Target Fragmentation of* ^{197}Au.

P.H. Regan, S.D. Langdown, K. Gladnishki, S.M. Mullins, Zs. Podolyák, M. Benatar, E. Gueorguieva, P. Kwinana, J.J. Lawrie, G.K. Mabala, S. Mukherjee, R.T. Newman, C.J. Pearson, J.F. Sharpey-Schafer, R. Smit, S.M. Vincent, **A.D. Yamamoto**, *in press* The Proceedings of the International Conference on Nuclear Structure: Mapping the Triangle, Jackson Lake Lodge, Grand Teton National Park, Wyoming, USA, 22-25 May 2002, *AIP Conf. Proc.* **638** (2002) p43-49

5. *Multi-Quasiparticle States in* ^{184}W *via 14-Nucleon Transfer*

C. Wheldon, J.J. Valiente-Dobón, P.H. Regan, C.J. Pearson, C.Y. Wu, J.F. Smith, A.O. Macchiavelli, D. Cline, R.S. Chakrawarthy, R. Chapman, M. Cromaz, P. Fallon, S.J. Freeman, A. Görgen, W. Gelletly, A. Hayes, H. Hua, S.D. Langdown, I.Y. Lee, X. Liang, Zs. Podolyák, R. Teng, D. Ward, D.D. Warner, **A.D. Yamamoto**, *Submitted to Eur. Phy. J. A*

6. *Transition from the Seniority Regime to Collective Motion*

J.J. Ressler, R.F. Casten, N.V. Zamfir, C.W. Beausang, R.B. Cakirli, H. Ai, H. Amro, M.A. Caprio, A.A. Hecht, A. Heinz, S.D. Langdown, E.A. McCutchan, D.A. Meyer, C. Plettner, P.H. Regan, **A.D. Yamamoto**, *Submitted to Phys. Rev. Lett.*

7. *Low-Lying Structure of* ^{210}Ra *and* ^{209}Ra

J.J. Ressler, C.W. Beausang, H. Ai, H. Amro, M.A. Caprio, R.F. Casten, A.A. Hecht, S.D. Langdown, E.A. McCutchan, D.A. Meyer, P.H. Regan, J.S. Sciacchitano, **A.D. Yamamoto**, N.V. Zamfir, *Submitted to Phys. Rev. C*

8. *Low Spin States in ^{162}Yb and First Order Phase/Shape Transitions*
E.A. McCutchan, N.V. Zamfir, M.A. Caprio, R.F. Casten, H. Amro, C.W. Beausang, D.S. Brenner, A.A. Hecht, C. Hutter, S.D. Langdown, D.A. Meyer, P.H. Regan, J.J. Ressler, **A.D. Yamamoto**, *Submitted to Phys. Rev. C*

9. *Binary Reaction Spectroscopy of $^{99,100}Mo$: Intruder Alignment Systematics in $N = 57$ and $N = 58$ Isotones*
P.H. Regan, **A.D. Yamamoto**, F.R. Xu, C.Y. Wu, A.O. Macchiavelli, D. Cline, J.F. Smith, S.J. Freeman, J.J. Valiente-Dobón, K. Andgren, R.S. Chakrawarthy, M. Cromaz, P. Fallon, W. Gelletly, A. Görgen, A. Hayes, H. Hua, S.D. Langdown, I.Y. Lee, C.J. Pearson, Zs. Podolyák, R. Teng, C. Wheldon, *Accepted for publication in Phys. Rev. C*

10. *Study of ^{136}Ba via Deep Inelastic Collisions: Identification of the $(\nu h_{\frac{11}{2}})^{-2}_{10^+}$*
J.J. Valiente-Dobón, P.H. Regan, C. Wheldon, C.Y. Wu, N. Yoshinaga, K. Higashiyama, J.F. Smith, D. Cline, R.S. Chakrawarthy, R. Chapman, M. Cromaz, P. Fallon, S.J. Freeman, A. Görgen, W. Gelletly, A. Hayes, H. Hua, S.D. Langdown, I.Y. Lee, X. Liang, A.O. Macchiavelli, Zs. Podolyák, R. Teng, D. Ward, D.D. Warner, **A.D. Yamamoto**, *Submitted to Phys. Rev. C*

11. *The Highs and the Lows of the A=100 Region: Vibration-to-Rotation Evolution in Mo and Ru Isotopes.*
P.H. Regan, A.D. Yamamoto, C.W. Beausang, N.V. Zamfir, R.F. Casten, Jing-Ye Zhang, **A.D. Yamamoto**, M.A. Caprio, G. Gürdal, A.A. Hecht, C. Hutter, R. Krücken, S.D. Langdown, D. Meyer, J.J. Ressler, *in press* The Proceedings of the International Conference on Frontiers of Nuclear Struc-

ture, Berkeley, California, USA 29 July-2 August 2002 *AIP Conf. Proc.* **656** (2003) p422-428.

Appendix B

Oral and Poster Presentations

1. Oral: *Search for the Decays in ^{71}Br / ^{71}Kr Mirror Pair*

North-West Europe Nuclear Physics Conference, Bergen, April 2001

2. Oral: *Search for the Decays in ^{71}Br / ^{71}Kr Mirror Pair*

EPSRC Postgraduate Summer School, University of Bangar, September 2001

3. Oral: *A Search for the Superdeformed Minima in ^{100}Mo*

Division of Nuclear Physics 2002 Fall Meeting, American Physical Society, October 2002

4. Poster: *A Search for the Superdeformed Minima in ^{100}Mo*

Nuclear Structure Theory Workshop, University of Surrey, Guildford, January 2003

5. Oral: *A Search for the Superdeformed Minima in ^{100}Mo*

Nuclear Physics Conference, Institute of Physics, Glasgow, April 2003